Imidoyl Amidine Ligands: A Versatile Framework to Build Homo and Heterometallic Complexes

Luis Raúl Castañeda-Perea

A Thesis Submitted in Partial Fulfillment of the Requirements for the

Doctorate in Philosophy Degree in Chemistry

Ottawa-Carleton Chemistry Institute

University of Ottawa

Candidate

Luis Raúl Castañeda-Perea

Supervisor

Jaclyn Brusso

Abstract

Ligand design in general enables the formation of coordination compounds with multiple functionalities within a single framework. To date, two of the most widely studied ligands are 2,2′:6′,2″-terpyridine (terpy) and acetylacetone (acac), whose tridentate and bidentate coordination pockets, respectively, enables the formation of metallic complexes with various geometries. The Brusso group had been incorporating imidoyl amidine (ImAm) ligands to build different materials such as organic radicals and fluorescent materials. In particular, the ligands *N*-2-pyridylimidoyl-2-pyridylamidine (Py_2ImAm) and *N*-2-pyrimidylimidoyl-2-pyrimidylamidine (Pm_2ImAm) were recently synthesized and have great appeal to build metallic complexes, as they poses two coordination sites similar to those in terpy and acac. The work presented herein represents the first studies involving the coordination of Py_2ImAm and Pm_2ImAm as discrete ligands. Our results demonstrate the versatility of these ligand frameworks, in which discrete mononuclear complexes, homometallic and heterometallic polynuclear complexes may be realized.

Chapter one serves as a brief introduction to transition metal chemistry and has a comprehensive review of the coordination chemistry of the ImAm ligand framework. In chapter two, the selective coordination of first row transition metals into the bidentate or tridentate sites of Py_2ImAm is explored. The formation of these mononuclear complexes is acid-base driven, where a weak acid induces coordination to the tridentate site and a weak base leads to coordination in the bidentate site. Coordination to both sides of Pm_2ImAm with manganese or iron is explored in chapter three. The results show the formation of unusual tetranuclear complexes with the metal ions in both low spin and high spin configurations. Chapter four covers the coordination to cobalt, and the formation of polynuclear complexes with different geometries using Pm_2ImAm. The magnetochemistry of these cobalt polynuclear complexes is also presented and reveal a single molecule magnet behaviour for one of the complexes. Finally, in chapter five, a one-pot synthesis of copper-manganese heterometallic complexes is presented. Overall, these imidoyl amidine ligands are able to build complexes with different geometries, different electronic configurations (i.e. low or high spin), and different metal ions. These results show a great versatility of ImAm ligands and suggest the future use of these ligands by other research groups.

Foreword

The majority of the content in chapter 2 was published in the reference below. The only exception is section 2.5 and the crystal structure of **[Co^{III}(Py$_2$ImAm)$_3$]·MeCN** that was included for completeness.

Chapter 2 reference: Castañeda, R.; Hollingshead, A.; Gabidullin, B.; Brusso, J. L., Probing the Coordination Chemistry of *N*-2-Pyridylimidoyl-2-pyridylamidine: A Versatile Ligand with Multiple Coordination Sites. *Crystal Growth & Design* **2017,** *17* (12), 6572-6578.

Contributions: The synthesis of all compounds with the exception of **[Mn^{III}(Py$_2$ImAm)$_3$]·DCM** and **[Fe^{III}(Py$_2$ImAm)$_3$]·DCM** was performed by Luis Raúl Castañeda Perea. The synthesis of **[Mn^{III}(Py$_2$ImAm)$_3$]·DCM** and **[Fe^{III}(Py$_2$ImAm)$_3$]·DCM** was performed by Andrew Hollingshead. The IR, UV-vis and PXRD characterization in all the compounds was performed by Luis Raúl Castañeda Perea. The SCXRD data was collected and refined by Luis Raúl Castañeda Perea, with the supervision of Dr. Bulat Gabidullin. The entire manuscript was written by Luis Raúl Castañeda Perea, with relevant corrections and edition by Dr. Jaclyn L. Brusso. All figures in this manuscript were prepared by Luis Raúl Castañeda Perea.

Chapter 3 reference: Castañeda, R.; Harriman, K. L. M.; Wong, J. W. L.; Gabidullin, B.; Murugesu, M.; Brusso, J. L., Rational Design of Tetranuclear Complexes Employing N-Imidoylamidine Based Ligands. *Eur. J. Inorg. Chem.* **2019**, (7), 963-972.

Contributions: The synthesis of all compounds was performed by Luis Raúl Castañeda Perea. The IR, and PXRD characterization for all the compounds was performed by Luis Raúl Castañeda Perea. The measurement and fit of the magnetic data was performed by Katie Lois Marie Harriman and Dr. Muralee Murugesu. The Mössbauer spectrum was collected and fitted by Dr. Joanne Wong. The SCXRD data was collected and refined by Luis Raúl Castañeda Perea with the supervision of Dr. Bulat Gabidullin. The manuscript was written by Luis Raúl Castañeda Perea, with only the exception of the magnetic description that was written by Katie Lois Marie Harriman. Relevant corrections and editions to the entire manuscript were done by Dr. Jaclyn L. Brusso. Figures in this manuscript were prepared by Luis Raúl Castañeda Perea, except for the magnetic susceptibility figures that were prepared by Katie Lois Marie Harriman.

The information from chapter 4 was accepted in Journal of Materials Chemistry C and will appear online in 2020. The information from the journal article was adjusted to the thesis format.

Chapter 4 reference: Castañeda, R.; Rouzières, M. Mathieu; Clérac, R.; Brusso, J. L., Controlling the nuclearity and topology of cobalt complexes through hydration at the ppm level, *J. Mat. Chem. C.* **2020**.

Contributions: The synthesis of all compounds was performed by Luis Raúl Castañeda Perea. The IR, and PXRD characterization in all the compounds was performed by Luis Raúl Castañeda Perea. The measurement and fit of the magnetic data was performed by Mathieu Rouzières, and Dr. Rodolphe Clérac. The SCXRD data was collected and refined by Luis Raúl Castañeda Perea. The manuscript was written by Luis Raúl Castañeda Perea, with the only exception of the magnetic description that was written by Dr. Jaclyn L. Brusso and Dr. Rodolphe Clérac. Relevant corrections and editions to the entire manuscript were done by Dr. Jaclyn L. Brusso. Figures in this manuscript were prepared by Luis Raúl Castañeda Perea, except for the magnetic susceptibility figures that were prepared by Mathieu Rouzières, and Dr. Rodolphe Clérac.

The research presented in chapter 5 has not yet been published, but we are in the process of preparing a manuscript.

Contributions: The synthesis of all compounds was done by Luis Raúl Castañeda Perea. The IR, and PXRD characterization in all the compounds was performed by Luis Raúl Castañeda Perea. The single crystal structures were collected and refined by Luis Raúl Castañeda Perea. The EPR data was collected and interpreted by Luis Raúl Castañeda Perea. The magnetic data was collected by Dr. Rodolphe Clérac. The entire chapter was written by Luis Raúl Castañeda Perea and revised by Jaclyn L. Brusso. Figures in this manuscript were prepared by Luis Raúl Castañeda Perea, except for the magnetic susceptibility figures that were prepared by Dr. Rodolphe Clérac.

Notes

All figures, charts and schemes in chapter 1 are original artwork and have not been copied from any article, book, thesis or any other document.

If a compound appears in more than one chapter, it is assigned a new number to make each chapter self contained. With the purpose to avoid confusion between numbers of ligands and metal complexes, the ligands have the letter “a” after the number, while the complexes have the letter “b” after the number.

Acknowledgements

Along the journey I took to get here, I passed through different institutions and places. Different people inspired me not only in university, but also at congresses, workshops and seminars. I would like to acknowledge everyone who has inspired me to study chemistry.

To Jaclyn, a person who always look at the bright side and pushes me to be a better person, and better chemist

To Rodolphe Clérac, whose contributions are priceless

To Katie and Muralee, stars in the sky and I always can find them if I look carefully at the sky

To Florence Williams and Ratmir Derda, a short stay but lots learned

To the American Crystallographic Association, because it is thanks to them that I can consider myself a crystallographer

To Tatiana Timofeeva and Yulia Getmanenko, for all the opportunities and learning I received from them

To the family Fuentes Montero, for all the support and inspiration they have given me

Dedication

To my family and my beloved country, *Mexico*

Table of Contents

List of Charts

List of Schemes

List of Figures

List of Tables

List of Abbreviations

ImAm	Imidoyl Amidine
CFT	Crystal Field Theory
Δ	Crystal Field Splitting
H.S.	High Spin
L.S.	Low Spin
NMR	Nuclear Magnetic Resonance
ZFS	Zero Field Splitting
EPR	Electron Paramagnetic Resonance
MCD	Magnetic Circular Dichroism
IR	Infrared Spectroscopy
MP	Meting Point
SCXRD	Single Crystal X-Ray Diffraction
PXRD	Powder X-Ray Diffraction
MLCT	Metal to Ligand Charge Transfer

List of Ligand Abbreviations

1.1a	acac	Acetylacetone
1.2a	terpy	2,2′:6′,2″-Terpyridine
1.3a	Py_2ImAm	*N*-2-pyridylimidoyl-2-pyridylamidine
1.4a	Pm_2ImAm	*N*-2-pyrimidylimidoyl-2-pyrimidylamidine
1.5a	en	Ethylenediamine
1.6a	Py	Pyridine
1.7a	biPy	2,2′-Bipyridine
1.8a	nacnac	1,3-diketimine
1.9a	bca	Bis(carbonyl)amide
1.10a	ImAm	Imidoyl amidine
1.11a	bacac	Bis(acetylacetone)
1.12a	pdpb	2,4-Pentanedione, 3,3'-(1,3-phenylene)bis-
1.13a	bacacPy	2,6-Bis(acetoacetyl)pyridine
1.14a	bPy_2ca	Bis(2-pyridylcarbonyl)amine
1.15a	bPm_2ca	Bis(2-pyrimidylcarbonyl)amide
1.16a	TEMPO	(2,2,6,6-Tetramethylpiperidin-1-yl)oxyl
1.17a	Pz	Pyrazole
1.18a	Pz_2ImAm	*N*-1-pyrazolylimidoyl-1-pyrazolylamidine
1.19a	Tz	1,3,5-Triazine
1.20a	Py_3Tz	2,4,6-Tris((2-pyridyl)-1,3,5-triazine
1.21a	Pm_3Tz	2,4,6-Tris((2-pyrimidyl)-1,3,5-triazine
1.22a	$(C_3F_7)_2Ph_2ImAm$	Butanimidamide, 2,2,3,3,4,4,4-heptafluoro-*N*-[2,2,3,3,4,4,4-heptafluoro-1-(phenylimino)butyl]-*N*-phenyl-
1.23a	$(C_3F_7)_2(F_5Ph)_2ImAm$	Butanimidamide, 2,2,3,3,4,4,4-heptafluoro-*N*-[2,2,3,3,4,4,4-heptafluoro-1-[(2,3,4,5,6-pentafluorophenyl)imino]butyl]-*N*'-(2,3,4,5,6-pentafluorophenyl)-

1.24a	$(C_3F_7)_2(Cl_2Ph)_2$ImAm	Butanimidamide, *N*-(2,6-dichlorophenyl)-*N*'-[1-[(2,6-dichlorophenyl)imino] -2,2,3,3,4,4,4-heptafluorobutyl]-2,2,3,3,4,4,4-heptafluoro-
1.25a	$(C_3F_7)_2(Dipp)_2$ImAm	Butanimidamide, 2,2,3,3,4,4,4-heptafluoro-*N*-[2,2,3,3,4,4,4-heptafluoro-1-[(2,4,6-trimethylphenyl)imino]butyl]-*N*'-(2,4,6-trimethylphenyl)-
1.26a	Ph_3ImAm	Benzenecarboximidamide, *N*-(iminophenylmethyl)-*N*'-phenyl-
1.27a	$Ph_2(4\text{-}(NO_2)Ph)$ImAm	Benzenecarboximidamide, *N*-(iminophenylmethyl)-4-nitro-*N*'-phenyl-
1.28a	Ph_4ImAm	Benzenecarboximidamide, *N*'-phenyl-*N*-[phenyl(phenylamino)methylene]-, [*C*(*Z*),*N*(*E*)]-
1.24a	PmAm	Pyrimidine-2-carboxamidine
2.1a	biPy	2,2'-bipyridine
2.2a	phen	1,10-Phenanthroline
2.3a	terpy	2,2';6',2''-Terpyridine
2.4a	Py_4Pz	Tetra-2-pyridyl-1,4-pyrazine
2.5a	Py_2ImAm	*N*-2-pyridylimidoyl-2-pyridylamidine
2.6a	[HPy_2ImAm]Cl	*N*-2-pyridylimidoyl-2-pyridylamidine hydrochloride
3.1a	Py_2ImAm	*N*-2-pyridylimidoyl-2-pyridylamidine
3.2a	Pm_2ImAm	*N*-2-pyrimidylimidoyl-2-pyrimidylamidine
3.3a	Py_3Tz	2,4,6-Tris((2-pyridyl)-1,3,5-triazine
3.4a	Pm_3Tz	2,4,6-Tris((2-pyrimidyl)-1,3,5-triazine
4.1a	acac	Acetylacetone
4.2a	nacnac	1,3-diketimine
4.3a	terpy	*N*-2-pyridylimidoyl-2-pyridylamidine
4.4a	Pz_2ImAm	*N*-1-pyrazolylimidoyl-1-pyrazolylamidine
4.5a	Py_2ImAm	*N*-2-pyridylimidoyl-2-pyridylamidine
4.6a	Pm_2ImAm	*N*-2-pyrimidylimidoyl-2-pyrimidylamidine
5.1a	Py_2ImAm	*N*-2-pyridylimidoyl-2-pyridylamidine
5.2a	Pm_2ImAm	*N*-2-pyrimidylimidoyl-2-pyrimidylamidine

5.3a Pz_2ImAm *N*-1-pyrazolylimidoyl-1-pyrazolylamidine

List of Metal Complex Abbreviations

1.1b **$[Ni(bPy_2ca)_2]$**

1.2b **$[Fe(bPy_2ca)_2]$**

1.3b **$[Cu^{II}(MeO_2ImAm)_2]$**

1.4b **$[Cu^{II}_3(Pz_2ImAm)_2(Pz)_2(4ClO_4)]$**

1.5b **$[Cu^{II}(Pz_2ImAm)_2]$**

1.6b **$[Ni^{II}(Pz_2ImAm)_2]$**

1.7b **$[Cu^{II}_3(Py_2ImAm)_2{\cdot}2OAc](ClO_4)_2$**

1.8b **$[Tl^{I}(C_3F_7)_2(Dipp)_2ImAm]$**

1.9b **$[Zn^{II}((C_3F_7)_2(Dipp)_2ImAm)Et]$**

1.10b **$[Zn^{II}((C_3F_7)_2(Cl_2Ph)_2ImAm)Et]$**

1.11b **$[Zn^{II}((C_3F_7)_2(cHex)_2ImAm)Et]$**

1.12b **$[Zn^{II}((C_3F_7)_2(Dipp)_2ImAm)EtO^-]$**

1.13b **$[Zn^{II}((C_3F_7)_2(Cl_2Ph)_2ImAm)EtO^-]$**

1.4b **$[Zn^{II}((C_3F_7)_2(cHex)_2ImAm)EtOO^-]$**

1.15b **$F_2Ph_2(4\text{-}NO_2)BTA$**

1.16b **$[Pt^{II}(Ph_3ImAm)_2]$**

2.1b **$[Mn^{III}(Py_2ImAm)_3]$**

2.2b **$[Fe^{III}(Py_2ImAm)_3]$**

2.3b **$[Co^{III}(Py_2ImAm)_3]$**

2.4b **$[Mn^{II}(Py_2ImAm)Cl_2]$**

2.5b **$[Fe^{III}(Py_2ImAm)Cl_3]$**

2.6b **$[Co^{II}(Py_2ImAm)Cl_2]$**

3.1b **$[Mn^{II}_2(\mu\text{-}Cl)_2(Pm_2ImAm)_2Cl_2]$**

3.2b **$[Mn^{III}Mn^{II}_3(Pm_2ImAm)_3Cl_6]$**

3.3b **$[Fe^{III}(Pm_2ImAm)Cl_3]$**

3.4b **$[Fe^{III}_4(Pm_2ImAm)_3Cl_9]$**

4.1b **$[Co^{II}_3(Pm_2ImAm)_2Cl_4]$**

4.2b **$[Co^{II}_6(\mu\text{-}Cl)_2(Pm_2ImAm)_4Cl_8]$**

4.3b **$[Co^{II}(Py_2ImAm)_2]$**

4.4b **$[Co^{II}_2(\mu\text{-}Cl)_2(Pm_2ImAm)_2Cl_2$**

5.1b **$[Mn^{II}_2Cu^{II}(Pm_2ImAm)_2Cl_4]\cdot 2H_2O$**

5.2b **$[Mn^{II}_4Cu^{II}_2(\mu\text{-}Cl)_2(Pm_2ImAm)_4Cl_6]\cdot 2MeOH\cdot 2DCM$**

5.3b **$[Cu^{II}(Py_2ImAm)_2]$**

Chapter 1

Introduction

1.1 Overview

The focus of the present thesis represents the first step towards understanding the coordination chemistry of imidoyl amidine (**1.1a**; ImAm; Chart 1.1) ligands, which possess both bidentate and tridentate coordination sites. Studying the coordination of a ligand with two distinctive coordination sites is attractive because it allows the coordination of two metal ions into different chemical environments. For example, within the same complex it is possible to have two metal ions with different electronic configurations. In particular, this thesis focusses on the development of coordination complexes employing *N*-2-pyridylimidoyl-2-pyridylamidine (**1.2a**; Py_2ImAm) and *N*-2-pyrimidylimidoyl-2-pyrimidylamidine (**1.3a**; Pm_2ImAm) ligands with first row transition metal ions. In this introductory chapter, relevant information regarding coordination chemistry such as crystal field theory, high spin vs. low spin configurations and chelation will be addressed. Following this brief discussion of coordination concepts, relevant ligands that possess similar features to the imidoyl amidine framework are presented, along with some mention of their application when pertinent to this thesis. Interestingly, prior to this study, the majority of reported ImAm-based complexes were obtained via metal assisted transformations, where the ligand was prepared in situ. These complexes are discussed in detail, along with the unique properties they might have. As well, imidoyl amidines can be prepared through organic synthetic approaches, and all such strategies are presented in this chapter with emphasis on the efficient and reproducible methodology used to isolate Py_2ImAm and Pm_2ImAm. The main objective of this introductory chapter is to bring light to the ImAm ligand framework, as it has been significantly less studied than analogous ligands yet has tremendous potential in the synthesis of future materials and catalysts.

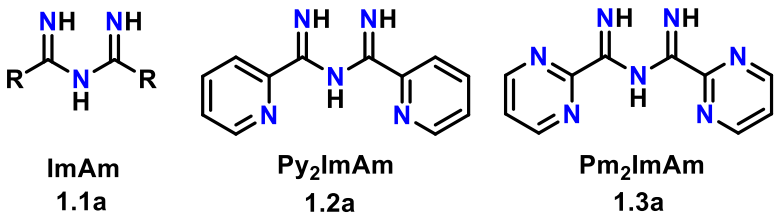

Chart 1.1. Key ligand frameworks of relevance to this thesis.

1.2 Coordination Chemistry

Coordination chemistry involves the study of the interactions between metals and ligands, and is a very exciting and relevant topic as metal complexes are key to our everyday lives, being found in applications such as textile dyes[1] or light emitting diodes,[2] are prevalent in biological systems in the form of metalloproteins,[3] and are key components in catalysis.[4, 5] In a very simplistic way, metallic complexes have two distinctive components with specific roles. While metals are normally found as cations with differing oxidation states, ligands typically act as neutral or anionic donors to the metal ions. In solution, coordination complexes are flexible frameworks, and can possess various conformations. Additionally, many complexes are known to exists as a racemic mixture in solution. On the other hand, in the solid-state coordination complexes can have different forms, as for example different polymorphs or solvates.

Nowadays high-level *ab initio* calculations provide very valuable information of metallic complexes,[6] and this information is often used as a starting point to explain the behaviour of metal complexes. Although very valuable, for large polynuclear complexes high-level *ab initio* calculations are very computationally demanding and can be very costly with respect to time; the more atoms involved in a metal complex within a given symmetry, the more computationally expensive the calculations become. On the other hand, a simplified way to explain metallic complexes involves the use of crystal field theory (CFT). In combination with magnetochemistry and UV-vis spectroscopy, CFT can be very helpful in defining the splitting energy levels in metallic complexes. In short, CFT assumes ligands to be negative point charges that experience repulsive forces between one another and, in order to interact with the metal ions, need to overlap with the *d*-orbitals on the metal centre. This overlap can be constructive, destructive or a combination of the two, depending on which of the five *d*-orbitals on the metal ion the ligand

orbitals interact with. The results of these interactions lead to changes in the relative energy levels of the metal ion *d*-orbitals in the coordination complex compared to the free ion. For example, in a spherical field all the *d*-orbitals have the same degree of attraction and repulsion, therefore all the orbitals have the same energy (Figure 1.1). As ligands approach the metal ion, the electrons from the ligand will be closer to some *d*-orbitals than others causing a loss of this degeneracy and a splitting of the *d*-orbitals. The degree of splitting, defined as crystal field splitting (Δ), and relative energy levels of the five *d*-orbitals is geometry dependent, as highlighted in Figure 1.1. In other words, complexes with a given coordination number normally have different energy levels depending on the geometry. An example of this is the four-coordinate tetrahedral and square planar geometries that have very different energy level diagrams with respect to one another. Another factor that effects crystal field splitting is the coordination number; typically, higher coordination numbers result in larger Δ (e.g. $\Delta_{tet} < \Delta_{oct}$).

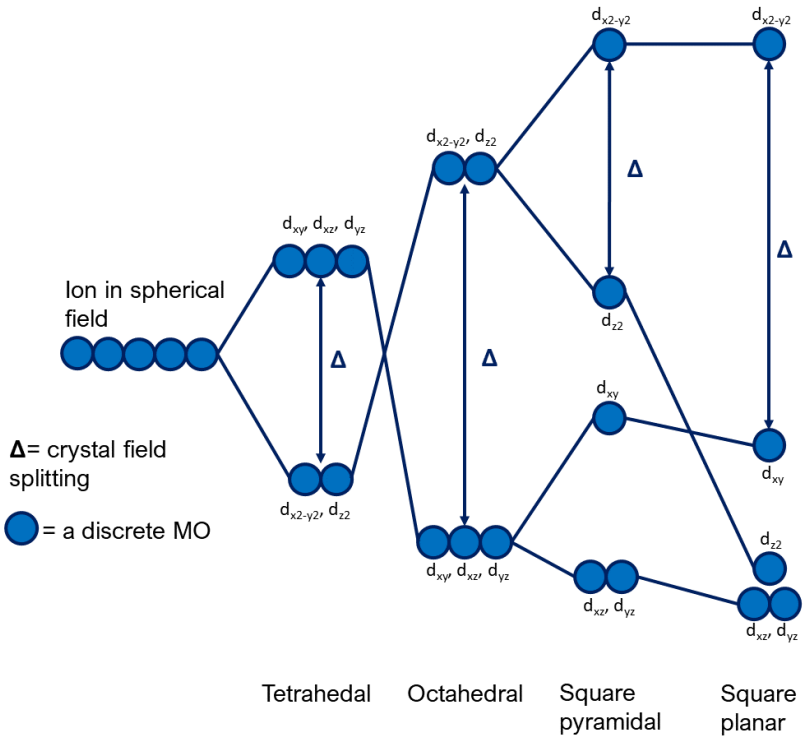

Figure 1.1. CFT diagrams for coordination geometries encountered in this thesis.

Although CFT treats ligands as negative point charges, in reality ligands can vary significantly and can therefore have a strong effect on the metal ion, which can lead to a dramatic influence on Δ. Some ligands will lead to a small Δ, while others will produce a large Δ. This phenomenon can

be explained by ligand field theory, which categorizes ligands based on their ability to act as electron donors or acceptors. This classification, also known as the spectrochemical series, orders ligands based on their ability to enhance Δ. For example, ligands that have little influence on the energy levels of the metal ion *d*-orbitals are known as weak field ligands. Metal complexes comprised of exclusively weak field ligands typically have small Δ values. Conversely, ligands that are better electron donors are considered strong field ligands and increase the Δ value. A comprehensive list of ligands ranging from weak field to strong field can be seen in Chart 1.2. It should be noted that the list in Chart 1.2 represents a general trend, as the effect of the ligand also depends on how hard or soft a metal ion is. Another factor affecting Δ is the oxidation state of the metal ion, an increase in a positive oxidation state increases Δ. Although this thesis focusses on first row transition metals, it is worth mentioning that second and third row transition metals have relatively large Δ.

$$\text{Halides} < OH^- < C_2O_4^{-2} < H_2O < NCS^- < \text{Py} < NH_3 < \text{en} < \text{biPy} < NO_2^- < PPh_3 < CN^- < CO$$

Chart 1.2. Spectrochemical series for common ligands. Ethylene diamine is abbreviated as en, pyridine as Py, and 2,2′-bipyridine as biPy.

CFT can be very useful as a first approach to identifying the electronic configuration of metal centres. Assuming a d^7 tetrahedral cobalt(II) complex (T_d point group) where Δ is expected to be small, each *d*-orbital would first be half filled before spin pairing. Each orbital is half filled first because there is energy required for the transition of two electrons in different orbitals (i.e. ↑ ↑) to paired electrons in single orbital (i.e. ↑↓), and this concept is defined as "Spin-Pairing Energy". The overall spin would be $S = 3/2$ (Figure 1.2a), and this corresponds to the highest number of unpaired electrons possible for a d^7 ion and is thus defined as "High Spin" (H.S.). A second example would be to assume the same d^7 metal centre, although with square planar geometry (D_{4h} point group). Square planar geometries normally have a larger Δ than the spin-pairing energy, therefore the electrons will fill the lower energy *d*-orbitals before occupying the higher energy ones (Figure 1.2b). This results in a lower number of unpaired electrons ($S = ½$) and is defined as "Low Spin" or L.S. It worthwhile mentioning that L.S. tetrahedral complexes are extremely rare, regardless of the metal centre,[7] and likewise square planar H.S. complexes are rare.[8] Unfortunately,

metallic complexes frequently deviate from ideal geometries, often possessing intermediate geometries (e.g. distorted tetrahedral and/or square planar). In such cases, magnetic measurements and Mössbauer experiments are extremely helpful in identifying the spin state of the complex (e.g. H.S. *vs*. L.S.).

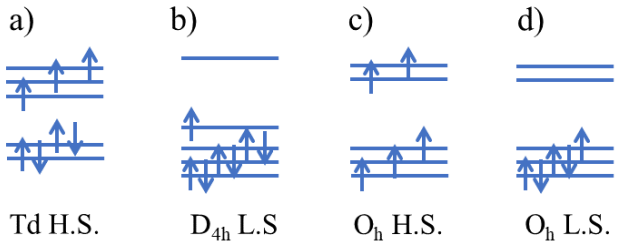

Figure 1.2. Examples of different H.S. and L.S. electronic configurations in metal complexes with tetrahedral (Td), square planar (D_{4h}) and octahedral geometry (O_h).

Octahedral complexes are notorious for possessing H.S. and L.S. configurations, and one of the main factors that can shift the balance between a H.S. or L.S. state is the ligand field strength. For example, consider an Fe(III) complex surrounded by six chloride anions ($[FeCl_6]^{-3}$). Since chloride is a weak field ligand, Δ is anticipated to be lower than the spin pairing energy and therefore each of the five electrons should be placed into individual *d*-orbitals (Figure 1.2c). In this example, $[FeCl_6]^{-3}$ has a H.S. configuration with $S = 5/2$. However, if the same metal ion is surrounded by six strong field ligands such as cyanide anions ($[Fe(CN)_6]^{-3}$), Δ can become much larger than the spin pairing energy resulting in a large Δ that induces a L.S. configuration with $S = ½$ (Figure 1.2d).

1.3 Organic Ligands and the Chelate Effect

Organic ligands can coordinate metal ions with different bonding orbitals, such as non-bonding orbitals (or lone pairs), or π bonds. The bonding between a ligand and a metal ion can be ionic, due the attraction of a negative charge and a positive charge, or covalent due to constructive overlap of non-bonding orbitals in the ligands and the frontier *d*-orbitals of metal ions. In the case of covalent bonding there is the opportunity to have electron donation from the ligand to the metal, which can decrease the energy in both the ligand and the metal *d*-orbitals. Simple examples of organic ligands include ammonia and ethylene. In the case of ammonia (NH_3), the nitrogen atom

has a single lone pair, which can act as sigma donor and coordinate metal ions. Likewise, organic molecules can have many functional groups or substituents that are capable of coordinating to different metal centres, some examples include alcohols, carboxylic acids, nitrogen or oxygen containing heterocycles, amines, phosphines, olefins, thiols, thiocarbamates, carbenes, etc. Like ammonia, the aforementioned examples all possess lone pairs thus can also act as sigma donors. A ligand with a single coordination group is referred as "monodentate", whereas ligands with more than one coordination site are referred to as polydentate (e.g. two, three and four coordination groups in a single ligand are referred to as bidentate, tridentate and tetradentate, respectively); organic ligands often fall into the latter category. For a given coordination group, polydentate ligands form more stable complexes than monodentate ligands due to the "chelate effect". The stabilization enabled by the chelate effect is typically described as a result of two main factors, the increase of entropy of the system and the higher rate of formation associated with complexes comprised of polydentate ligands. For example, consider the substitution of ammonia ligands in $[Co^{II}(NH_3)_4]^{2+}$ for bidentate ethylenediamine ligands (**1.4a**; en Figure 1.3); as en replaces NH_3, there is an increase of the number of molecules (i.e. three reactant molecules afford five product molecules) resulting in a larger entropy term. Additionally, when an amino group in $[Co^{II}(en)_2]^{2+}$ dissociates, the bidentate ligand still has another amino moiety connected to the metal ion. In that case, restoration of the bidentate complex requires an intramolecular reaction, which would be faster than the bimolecular reaction that would occur if substitution for two ammonia ligands takes place.

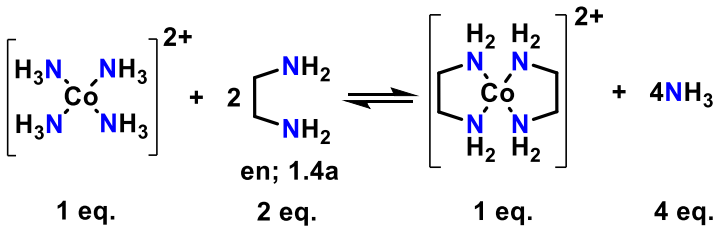

Figure 1.3. Ligand exchange of ammonia for en in a cobalt(II) complex. The substitution result in a higher number of individual molecules.

1.4 Acetyl Acetone (acac) and Related Ligands

Bidentate ligands in general are very common, and perhaps one of the most studied bidentate frameworks is based on the acetylacetone ligand **(1.5a**; acac; Chart 1.3). Not surprisingly, acac ligands can be found in a variety of applications including redox flow batteries,[9] low emission polyurethane catalysts,[10] oxidation of π systems,[11, 12] and decarbonylation of cinnamamides,[13] to name a few. A number of research groups have taken advantage of the two functional groups in acac (i.e. R^1 and R^2), substituting these sites with a diverse range of moieties such as hydrophobic chains,[14] electron withdrawing groups,[15, 16] or additional coordination pockets.[17] Ligands with multiple coordination sites are able to coordinate more than a single metal ion, a highly desirable quality since metals can act in a cooperative manner with each other.[18] A few examples of acac based ligands with multiple coordination pockets can be seeing in Chart 1.3, although a more comprehensive list can be found in the review of Brock *et al*.[17] Taking advantage of the additional coordination sites, a number of research groups have reported the synthesis of polynuclear complexes with topologies ranging from triangles, squares and cubes to helicates and tetrahedrons.[17] Interestingly, these polynuclear complexes also include many examples of heterometallic systems.[17]

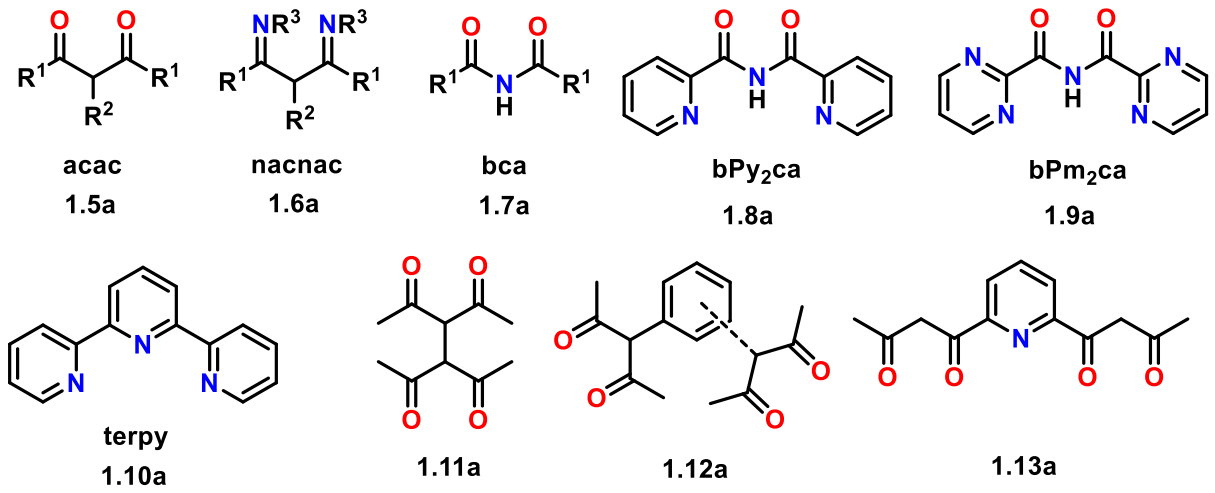

Chart 1.3. Examples of commonly employed ligands with bidentate and/or tridentate coordination sites.

Another route to functionalize acac is through substitution of oxygen for nitrogen, as demonstrated in 1,3-diketimine (**1.6a**; nacnac; Chart 1.3), a ligand widely used in catalysis.[19] The

introduction of imino groups in nacnac brings a third functionalization position at the nitrogen atoms (i.e. R^3; Chart 1.3). This additional functionalization site offers a big advantage over acac, as R^3 can be used to increase sterics around the metal ions, giving rise to highly active low coordinate metal ions that do not form dimers.[19]

On the other hand, substitution of the central α-carbon in acac for nitrogen affords the bis(carbonyl)amide ligand (**1.7a**; bca; Chart 1.3), which has been employed in coordination complexes for a variety of applications in materials chemistry including single chain magnets,[20, 21] spin crossover materials,[22] metal organic frameworks (MOFs),[23, 24] and luminescent complexes.[25, 26] In part, bca ligands are attractive for materials chemistry due to the addition of pyridyl (**1.8a**; bPy_2ca; Chart 1.3) or pyrimidyl (**1.9a**; bPm_2ca; Chart 1.3) rings at the R^1 position, thereby forming an additional tridentate coordination pocket that resembles the coordination environment of 2,2';6',2''-terpyridine (**1.10a**; terpy; Chart 1.3), a widely employed non-innocent ligand with different uses in catalysis[27] and material chemistry.[28] It is important to emphasize that the two distinct coordination pockets within the ligand framework of bPy_2ca and bPm_2ca are very different to one another, with the bidentate pocket possessing a weaker ligand field compared to the tridentate site due to the presence of the nitrogen atoms, which tend to have higher ligand field strength compared with oxygen. The difference between the coordination environments in both bPy_2ca and bPm_2ca facilitates the stepwise synthesis of heteronuclear complexes with various metal ions, or the development of homonuclear systems with the metal ions in different electronic configurations. The idea behind a stepwise synthesis is to first prepare a mononuclear complex coordinated in the tridentate pocket of bPy_2ca with nickel **(1.1b**; **$[Ni(bPy_2ca)_2]$**)[29] or iron **(1.2b**; **$[Fe(bPy_2ca)_2]$**),[22] and then using these mononuclear complexes as starting materials to subsequently coordinate to a second metal ion (e.g. lanthanides).[21] Alternatively, in the case of **$[Fe(bPy_2ca)_2]$**,[22] which has a low spin configuration, coordination to a high spin iron ion in the bidentate pocket of bPy_2ca affords a coordination polymer with a 1:1 mixture of low spin Fe(II) and high spin Fe(III) ions.[30] These types of complexes with a single metal in different electronic configurations are neither naturally occurring nor easy to achieve with inorganic ligands.

1.5 Complexes with Imidoyl Amidine Ligands

Imidoyl amidine ligands (ImAm; Chart 1.1) are essentially the triaza version of acac. From a historic perspective, while acac has been used in metallic complexes for over a century,[31] nacnac since 1968,[32] and bca since 1976,[33] the first ImAm complex did not appear until 1984.[34] This may be due to the preparative method for ImAm, which was first reported *via* a metal assisted transformation when acetamidine was reacted in the presence of nickel to make methylimidoyl-methylamidine *in situ*.[34] Subsequent work led to other metal assisted transformations to afford ImAm frameworks, such as the nucleophilic addition of methanol to dicyanamide in the presence of copper(II) nitrate to make the complex bis[di(methoxycarbimido)aminato]copper(II) **(1.3b**; **[Cu^{II}(MeO$_2$ImAm)$_2$]**).[35] The mechanism of formation of **1.3b** was studied by DFT calculations,[35] and involves bending of the dicyanamide with coordination to copper(II) (Scheme 1.1). Following coordination to Cu(II), nucleophilic addition of methanol to the nitrile moieties thereby releasing the molecular strain affording the copper(II) square planar complex **1.3b**.

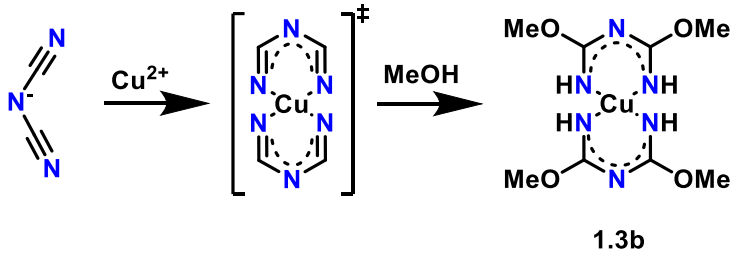

1.3b

Scheme 1.1. Reaction mechanism of the metal assisted transformation of dicyanamide into **1.3b**, as reported by Boča *et al*.[35]

Inspired by the metal assisted transformation reported by Boča *et al*.,[35] a number of copper complexes with alkoxy substituents (e.g. methoxy, ethoxy, propoxy, iso-propoxy, and sec-butoxy) at the R^1 position were synthesized with the intent to apply them as catalysts in the oxidation of alcohols to aldehydes.[36] Although a wide list of oxidants are able to catalyze the oxidation of alcohols into aldehydes, some examples include NaOCl, $KMnO_4$, and $Cr_2O_7^{-2}$, the majority of these oxidants are not selective and tend to give undesired by-products and lead to overoxidation. The aforementioned copper complexes prepared by Kopylovich *et al.*[36] offer an attractive alternative as they were shown to catalyze the oxidation of alcohols by using oxygen, a green oxidant, and (2,2,6,6-Tetramethylpiperidin-1-yl)oxyl (TEMPO). In this case, oxygen is not able to

overoxidize the products, resulting a cleaner synthesis. It should be noted that copper and TEMPO by themselves are able to push the oxidation of alcohols to aldehydes, as was first reported by Semmelback;[37] however, organic ligands made this reaction more reproducible and more robust to various conditions, representing an important step forward in this research field. More recently, [38] ImAm complexes with different alkoxy substituents have been employed to catalyze the oxidation of cyclohexane with hydrogen peroxide as oxidant.

Kitagawa's group, inspired by the synthesis of **1.3b**, carried out the nucleophilic addition of pyrazole (**1.14a**; Scheme 1.2; Pz) to dicyanamide in the presence of copper(II) (Scheme 1.2),[39] generating *N*-1-pyrazolylimidoyl-1-pyrazolylamidine (**1.15a**; Pz_2ImAm) *in situ*. This ligand is particularly attractive as it has an additional tridentate coordination site similar to that in terpy, bPy_2ca and bPm_2ca. As a result, copper can coordinate both the tridentate and bidentate pockets, making a linear trinuclear complex (**1.4b**; **$[Cu^{II}_3(Pz_2ImAm)_2(Pz)_2(4ClO_4)]$**; Scheme 1.2).[39] Interestingly the ligand Pz_2ImAm was shown to act as a ferromagnetic coupler between the central and outer copper ions in **1.4b**.[39] Importantly, this reaction afforded a relatively high yield (56% - 78%), which enabled its use as a starting material for subsequent complexes (Scheme 1.2). For example, Kamiyama *et al.* removed the peripheryl copper ions by employing EDTA[40] leading to the mononuclear copper square planar complex **$[Cu^{II}(Pz_2ImAm)_2]$** (**1.5b**). Isolation of **$[Cu^{II}(Pz_2ImAm)_2]$** allowed the coordination to a second metal ion (M= Mn^{II}, Co^{II}, Ni^{II}, or Cu^{II}) in the tridentate site of Pz_2ImAm, making a linear trinuclear complexes with the formula **$[M_2Cu^{II}(Pz_2ImAm)_2][ClO_4]_4$** (Scheme 1.2).[40] Similar to the homometallic linear trinuclear copper complex, Pz_2ImAm acts as ferromagnetic coupler in the heterometallic complexes reported by Kamiyama *et al.*[40] It should be noted that the synthesis of **$[M_2Cu^{II}(Pz_2ImAm)_2][ClO_4]_4$** (where M = Mn, Co) is very inefficient, due being a multi-step synthesis with very low yields in the final step of the reaction.[40]

The first report of a free ImAm ligand also involved the use of **1.4b** as starting material, and was achieved by using $(NH_4)_2S$ to precipitate the copper ions (Scheme 1.2).[41] Afterwards, Pz_2ImAm was used to synthesize the square planar complexes with copper (**1.5b**) and nickel (**1.6b**; **$[Ni^{II}(Pz_2ImAm)_2]$**).[41] From **1.5b** and **1.6b**, the synthesis of heterometallic complexes with cobalt or nickel was finally realized after four steps, resulting in three new linear trinuclear heterometallic complexes with the metal combinations Co^{II}-Cu^{II}-Co^{II}, Ni^{II}-Cu^{II}-Ni^{II}, and Ni^{II}-Ni^{II}-Ni^{II}.[41] Overall,

the yields after four steps are low, between 25% and 5%. It worth mentioning that manganese also catalyzes the nucleophilic addition of pyrazole to dicyanamide to make Pz_2ImAm.[42]

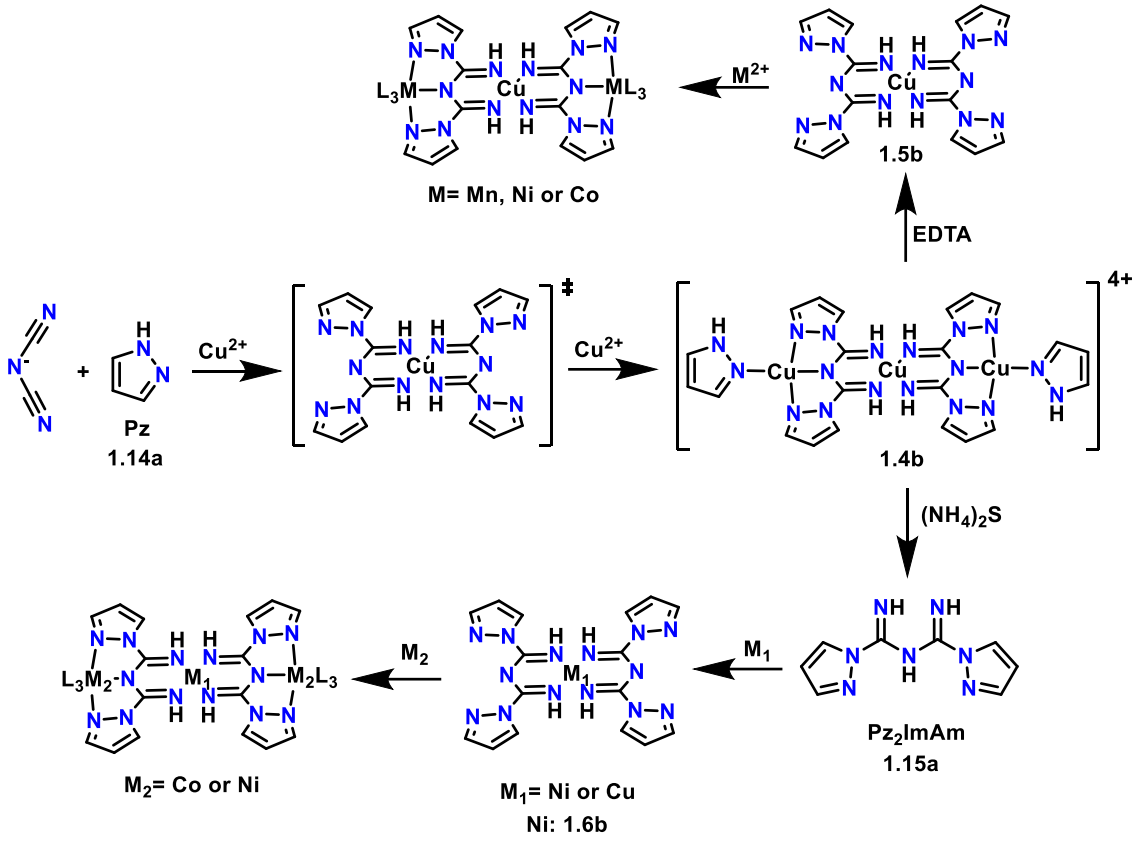

Scheme 1.2. Synthesis of different complexes that take advantage of the nucleophilic addition of pyrazole to dicyanamide.

1.5.1 Synthesis of ImAm Complexes by the Decomposition of a Triazine

ImAm ligand frameworks have also been reported through the decomposition of triazines such as 1,3,5-triazine (**1.16a**; Tz, Chart 1.4), 2,4,6-tris((2-pyridyl)-1,3,5-triazine (**1.17a**; Py_3Tz; Chart 1.4) and 2,4,6-tris((2-pyrimidyl)-1,3,5-triazine (**1.18a**; Pm_3Tz; Chart 1.4) in the presence of a metal. For example, hydrolysis of Pm_3Tz in presence of copper(II) nitrate affords a square planar complex with bPm_2ca, which represents the first bca-based complex to be reported.[33] In the same manner, copper(II) can catalyze the decomposition of Tz, Py_3Tz, and Pm_3Tz to make various ImAm complexes,[43-45] demonstrating that in the presence of a metal salt triazines can be hydrolyzed to make either bca-based ligands or react *via* ring opening to generate ImAm ligands.

Previous studies have shown that the metal ions play an important role in this reactivity, such that copper(II) can hydrolyze Py_3Tz while copper(I) cannot.[46]

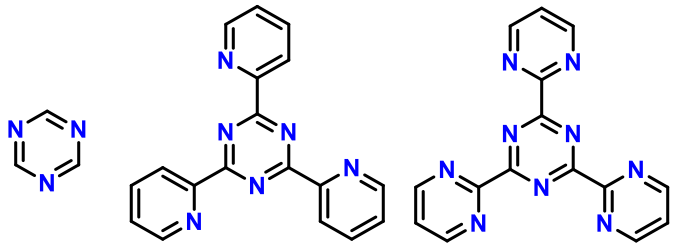

Chart 1.4. Examples of triazine base ligands with multiple coordination pockets.

Decomposition of Py_3Tz in presence of copper(II) salts represents the first report of a coordination complex employing Py_2ImAm ligands, where the ligand framework is again generated *in situ*. Similar to Pz_2ImAm, Py_2ImAm possesses both a bidentate and tridentate coordination site, which enables the formation of a 1-D coordination polymer of the general formula **$[Cu^{II}_3(Py_2ImAm)_2(OAc)_2][ClO_4]_2$** (**1.7b**; Figure 1.4a). The complex **1.7b** has two crystallographic independent copper(II) ions, Cu1 located in an inversion centre and coordinated to the bidentate pocket of Py_2ImAm, and Cu2 located in general position and coordinated into the tridentate pocket. The geometry around Cu1 was described as elongated octahedral, as the perchlorate anions are weakly interacting with Cu1 with long Cu-O distance equal to 2.777(5) Å. On the other hand, the geometry around Cu2 is described as square pyramidal, with acetate acting as a bridging ligand to a second Cu2 ion (Figure 1.4a). Interestingly, ferromagnetic interactions were observed between Cu1 and Cu2, and these interactions were explained as resulting from the orthogonality in the $d_{x^2-y^2}$ orbitals of Cu1 and Cu2 (Figure 1.4b). This observation is consistent with other reports in which ImAm ligands act to ferromagnetically couple Cu ions in polynuclear copper ImAm complexes,[39, 40, 45] validating the explanation of Kajiwara *et al*.[44] to some extent.

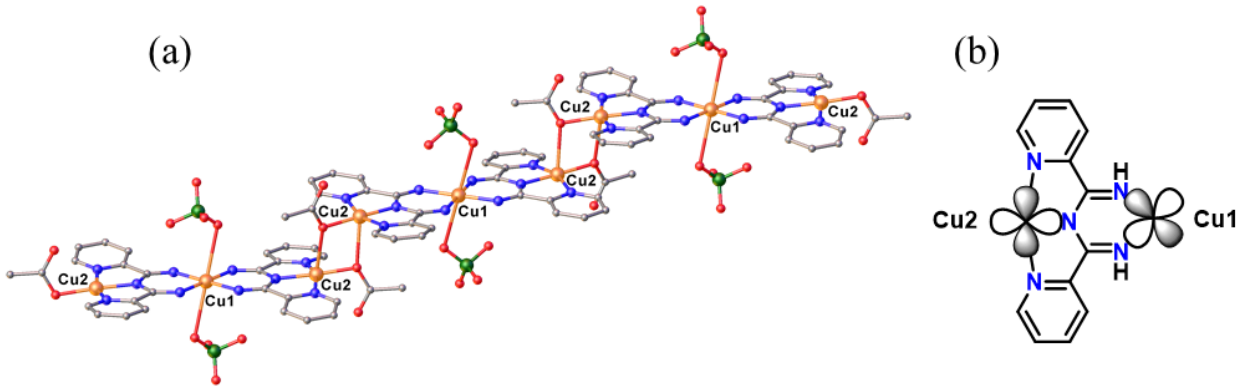

Figure 1.4. (a) Crystal diagram of a 1-D coordination chain within **1.7b**. Hydrogen atoms had been omitted for clarity. The figure was drawn from the cif file deposited in the CCDC.[47] (b) Orthogonal overlap of the $d_{x^2-y^2}$ orbitals of Cu1 and Cu2 in **1.7b**.

1.5.2 Ketoxime-Mediated Synthesis of Imidoyl Amidine Complexes with Nickel(II) or Palladium(II)

Another interesting metal assisted transformation affording ImAm ligands involves the reaction between a nitrile and oxime in presence of either nickel(II) or palladium(II) salts resulting in the synthesis of several ImAm complexes with various substituents at the R^1 position, as shown in Chart 1.5. This strategy, reported by Kopylovich *et al.*,[48-51] consists of nitrile activation via the oxime (e.g. 2-propanone oxime, 2-butanone oxime) affording both carboxylic acids and amidines.[49] The amidine then reacts with another nitrile thereby generating a square planar complex with an ImAm ligand (Chart 1.5). In the case of palladium, three different square planar complexes were obtained and tested as Suzuki and Heck catalysts.[50]

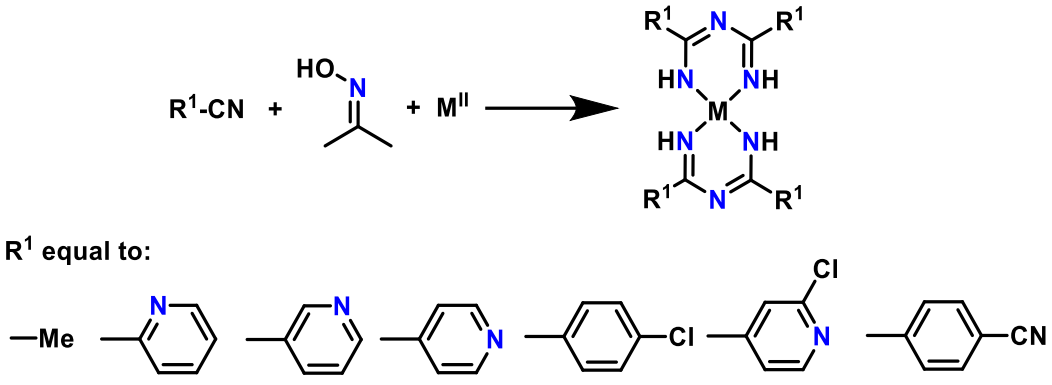

Chart 1.5. Ketoxime-mediated synthesis of ImAm complexes. M is equal to Ni^{II} or Pd^{II}.

1.5.3 Synthesis of ImAm Ligands with Perfluoro Alkyl Chains at the R^1 Position

Starting with the ligand in hand is very advantageous as it allows some degree of control over the functional groups at the R^1 and R^3 positions of imidoyl amidines. While the R^1 position can be tailored to include a tridentate pocket, the R^3 site can be used to add steric bulk. Bulky substituents such as phenyl (Ph) can influence the geometry and coordination number around metal ions. For instance, Siedle *et al.*[52] synthesized a ligand with the R^1 = C_3F_7 and R^3 = Ph (**1.19a**; $(C_3F_7)_2Ph_2$ImAm; Scheme 1.3), that is able to coordinate a cobalt(II) ion in a tetrahedral configuration due to the bulky phenyl substituents. Since the tetrahedral configuration is enforced by the ligand, the cobalt(II) ion was found to be in the high spin configuration, something that is not energetically favorable in cobalt(II) complexes with ImAm ligands;[53] the favorable configuration is low spin square planar cobalt(II). The synthesis of $(C_3F_7)_2Ph_2$ImAm starts with thermolysis of perfluorotributylamine at 140 °C to remove one perfluorobutyl chain, resulting in the imine **1.20a** (Scheme 1.3).[52] **1.20a** was subsequently reacted with excess aniline affording the desired $(C_3F_7)_2Ph_2$ImAm ligand. Although different ImAm ligands can be made following the reaction in Scheme 1.3, the high temperatures of this reaction and the leaving group HF are typically a lab safety concern to synthesize these ligands.

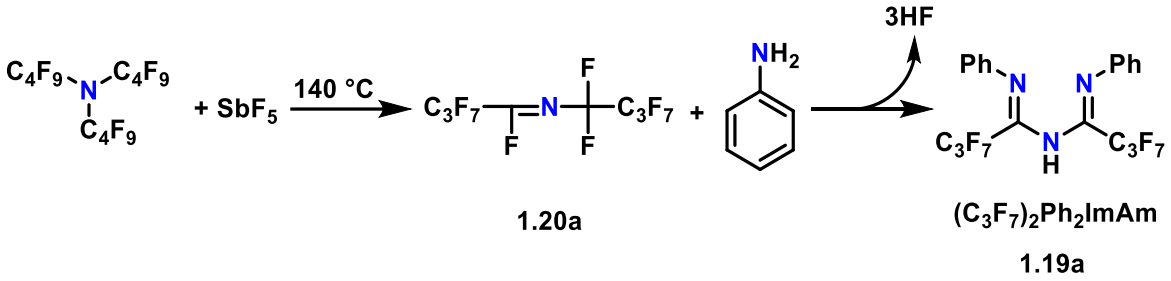

Scheme 1.3. Synthesis of $(C_3F_7)_2Ph_2ImAm$.

Later publications were inspired by the synthesis of **1.19a**, and used this synthetic strategy to obtain other ImAm ligands.[54-58] In particular, compounds possessing bulky substituents at the R^3 position were targeted, which can be prepared by two potential routes related to Scheme 1.3; the first by changing the source of perfluoroalkyl amine, while the second option involves changing the source of aniline. The latter route was employed with the starting materials 2,6-(diisopropyl)aniline,[54] 2,4,6-tris(methyl)aniline,[55] pentafluoroaniline,[56] 2-fluoro,6-(trifluoromethyl)aniline,[56] 2,6-bis(chloro)aniline,[59] 2-(trifluoromethyl)aniline,[58] 2-(nitro)aniline,[58] 4-(nitro)aniline,[58] and cyclohexylamine[60] to have different substituents at the R^3 position of **1.19a**. The abbreviation for these substituents can be seen in Chart 1.6.

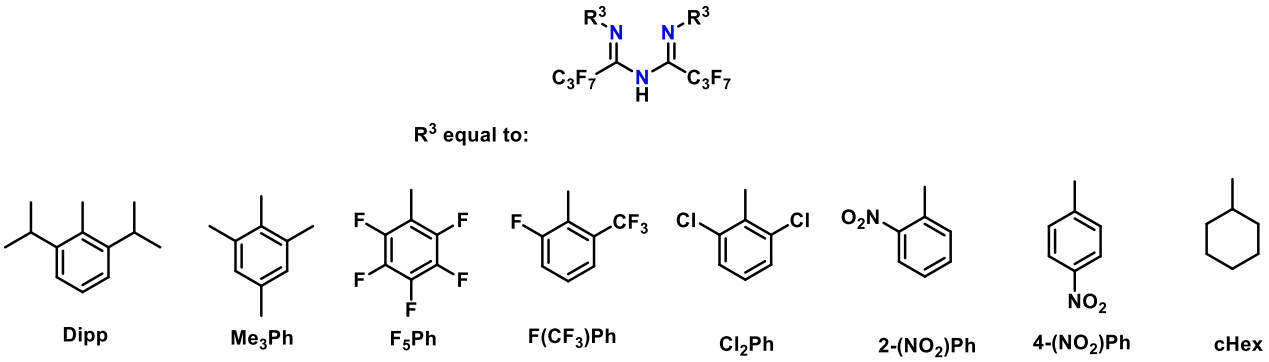

Chart 1.6. List of different R^3 substituents used in the synthesis of fluorinated imidoyl amidine ligands.

Interestingly using a ligand with pentafluorophenyl substituents at the R^3 position of **1.19a** (**1.21a**; $(C_3F_7)_2(F_5Ph)_2ImAm$; Chart 1.7) made possible to synthesize stable low coordinate copper(I)-carbonyl (**1.8b**, **$[Cu^I((C_3F_7)_2(F_5Ph)_2ImAm)\cdot CO]\cdot MeCN$**; Chart 1.8) and copper(I)-ethylene (**1.9b**, **$[Cu^I((C_3F_7)_2(F_5Ph)_2ImAm)\cdot(C_2H_4)]$**; Chart 1.8) complexes.[56] Such complexes are

typically not stable with first row transition metal ions as carbon monoxide and ethylene tend to abandon the metal centres. An advantage of highly fluorinated ligands such as **1.21a** is the tendency to stabilize metallic complexes at higher temperatures and lower pressures. In the case of **1.9b**, a stabilization was observed to the point that the complex could be placed at low pressures in a Schlenk line and remain intact. The same group later used a dichlorophenyl (Cl_2Ph) substituted ligand (**1.22a**; $(C_3F_7)_2(Cl_2Ph)_2$ImAm; Chart 1.7) to developed a copper(I)-ethylene (**1.10b**, **[Cu^I($(C_3F_7)_2(Cl_2Ph)_2$ImAm)·(C_2H_4)]**; Chart 1.8) and a gold(I)-ethylene (**1.11b**, **[Au^I($(C_3F_7)_2(Cl_2Ph)_2$ImAm)·(C_2H_4)]**; Chart 1.8) complexes.[59] These metal-ethylene complexes (**1.9b**-**1.11b**) have the same coordination environment around the metal ions in as shown in Figure 1.5, with the ligand connected in a bidentate fashion and ethylene coordinated in η^2 fashion. Interestingly, both copper(I) and gold(1) ethylene complexes catalyze the carbene transfer reaction of ethyl diazoacetate (a widely used carbene source) to saturated and unsaturated hydrocarbons.[59]

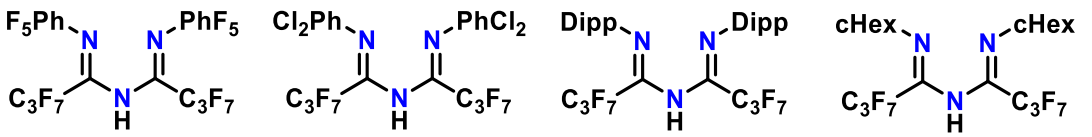

Chart 1.7. Structures of ImAm ligand with perfluoro alkyl chains. The abbreviation for the substituents at the R^3 position can be found in Chart 1.6.

Thus far, the examples described involve ImAm ligands that coordinate metal ions in bidentate or tridentate fashion. Although rare, there are a few examples of ImAm ligands acting as monodentate ligands. One of these peculiar examples employs a ligand with the substituents R^1 = C_3F_7 and R^3 = 2,6-diisopropylphenyl (Dipp), which can be abbreviated as $(C_3F_7)_2(Dipp)_2$ImAm (**1.23a**; Chart 1.7). This ligand was used to make a mononuclear Tl(I) complex (**1.12b**; **[$Tl^I(C_3F_7)_2(Dipp)_2$ImAm]**; Chart 1.8),[55] where the Tl(I) ion is coordinated exclusively to the central nitrogen atom of **1.23a**. It worth mentioning that monocoordinated complexes Tl(I) are very rare. Typically, ImAm ligands coordinate to metal ions in a bidentate fashion through the imino groups (i.e. Figure 1.5) with the central nitrogen atom in the opposite direction to the metal ion in a conformation that is often described as the U-conformation. On the other hand, when ImAm ligands are coordinated in a monodentate fashion, the ligand can have a different

conformation to the U-shape, which is the case for **1.12b**. This can be referred to as a W-shape ligand, with the three nitrogen atoms pointing in the same direction to the metal.

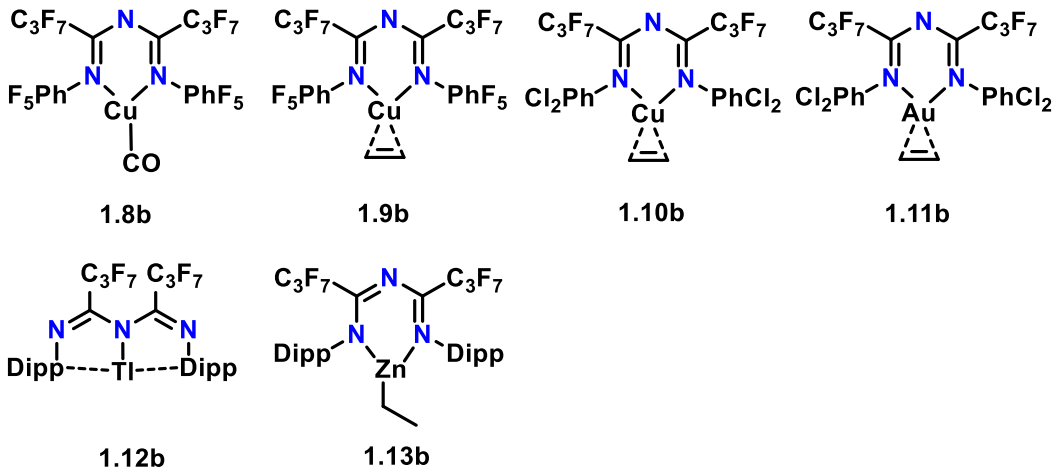

Chart 1.8. Structure of carbonyl and ethylene complexes with imidoyl amidine ligands.

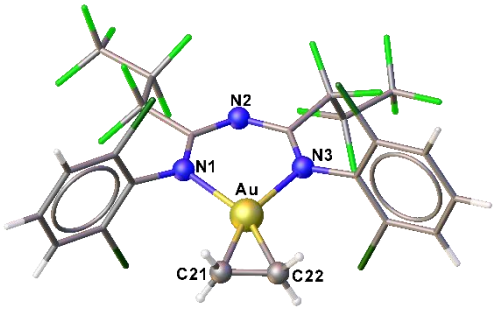

Figure 1.5. Crystal diagram of **1.11b**. The figure was drawn from a cif file deposited in the CCDC.[59]

Other examples of monodentate coordination of ImAm ligands can be found in the publication of Flores *et al.*,[57] in which they study the coordination of **1.21a** and **1.22a** to Ag^{I} with the purpose to thermally stabilize two, three and four coordinated complexes. The synthetic strategy to obtain these low coordinate complexes is rather interesting, coordination of anions such as nitrates, chlorides or perchlorates can be avoided by using AgO as the metal source, therefore improving the chances of obtaining low coordinate complexes. These Ag(I) complexes have been patented for their antimicrobial activity.[61]

More recently, Kulkarni *et al.*[60] used the ligands **1.22a**, **1.23a**, and $(C_3F_7)_2(cHex)_2ImAm$ (**1.24a**; Chart 1.7) to synthesize three Zin(II)-ethyl complexes as catalyst of the Tishchenko reaction. The three complexes reported (**1.13b**; **[Zn^{II}($(C_3F_7)_2$(Dipp)$_2$ImAm)Et]**, **1.14b**; **[Zn^{II}($(C_3F_7)_2$(Cl_2Ph)$_2$ImAm)Et]**, and **1.15b**; **[Zn^{II}($(C_3F_7)_2$(cHex)$_2$ImAm)Et]**) can be obtained by reacting diethyl Zinc(II) with their respective ligands at 80 °C in toluene. In the specific case of **1.13b**, it was crystallized and single crystal XRD revealed a trigonal planar complex (Chart 1.8). These Zinc(II)-ethyl complexes are very sensitive to air and moisture, and, even in the solid state, the ethyl group gradually oxidizes. By controlling the exposure of **1.13b**-**1.15b** to dry air it was possible to oxidize them into two ethoxy complexes **[Zn^{II}($(C_3F_7)_2$(Dipp)$_2$ImAm)EtO^-]** (**1.16b**) and **[Zn^{II}($(C_3F_7)_2$(Cl_2Ph)$_2$ImAm)EtO^-]** (**1.17b**), and a rare ethylperoxyde complex **[Zn^{II}($(C_3F_7)_2$(cHex)$_2$ImAm)$EtOO^-$]** (**1.18b**). The Tishchenko reaction, which involves the dimerization of two aldehydes to make a carboxylic ester, has be known about a century,[62] and is of special interest due its atom efficiency.[62] Common Zinc(II) compounds such as $Zn(II)Et_2$, $Zn(II)Cl_2$, $Zn(II)_2(OAc)_2$ and $Zn(II)(OTf)_2$[*] do not catalyze the Tishchenko reaction at 80°C with benzaldehyde as substrate,[60] whereas the three aforementioned Zinc(II)-ethyl complexes are able to catalyze the Tishchenko reaction at 80 °C in a solvent free environment. Furthermore, increasing the temperature of reaction to 140 °C with **[Zn^{II}($(C_3F_7)_2$(Dipp)$_2$ImAm)Et]** can push the reaction to full conversion of benzaldehyde into phenyl benzoate.[60] Finally, Kulkarni *et al.*[60] used **[Zn^{II}($(C_3F_7)_2$(cHex)$_2$ImAm)$EtOO^-$]** to oxidize *trans*-chalcone into an epoxide, a process that is normally difficult in electron deficient olefins such as *trans*-chalcone.

1.5.4 Synthesis of ImAm Ligands by a Classic Organic Synthesis Approach

The fluorinated ImAm derivatives previously mentioned form coordination complexes that typically enhance stability due to the presence of fluorine atoms in the ligand framework as well as protecting the metal centre with bulky substituents. However, a major drawback of these fluorinated complexes is the use of perfluorotributylamine as starting material (Scheme 1.3), as it is a very potent greenhouse gas. Previous studies have shown that perfluorotributylamine has warming properties more than 7,000 times that of carbon dioxide over a 100 year period.[63] Nonetheless, there are other routes to obtain ImAm ligands with bulky substituents at the R^3

[*] OTf is a common abbreviation for triflate anion

position. As an example, two different synthetic approaches to make tertiary and quaternary ImAm ligands has been reported by Häger *et al*.[64] The first route results in tertiary ImAm ligands, and consists of reacting an imidoyl chloride with an amidine (Scheme 1.4). The second route reported by Häger *et al.*[64] is a two-step synthesis that involves the reaction of an imidoyl chloride with an imidoyl ethyl ester, followed by substitution of the ester with an amine in the second step (Scheme 1.5).

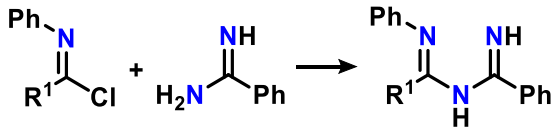

Scheme 1.4. Synthesis of tertiary ImAm ligands. Substituents at R^1 = Ph or 4-(NO_2)Ph.

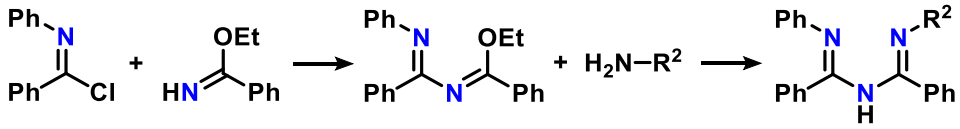

Scheme 1.5. Synthesis of quaternary ImAm ligands. Substituents at R^2 = Ph or *t*Bu.

In addition to synthesizing imidoyl amidine derivatives, Häger also used Ph_3ImAm (**1.25a**; Chart 1.9), Ph_2(4-(NO_2)Ph)ImAm (**1.26a**), and Ph_4ImAm (**1.27a**) to coordinate different transition metals as well as boron difluoride. In the case of tertiary ligands such as **1.25a** and **1.26a**, a single Ph group did not hinder the coordination of Ni^{II} or Pd^{II} to form near ideal square planar complexes. On the other hand, the quaternary ligand Ph_4ImAm does affect the geometry of a Cu(II) ion, inducing a more tetrahedral configuration when compared to Ph_3ImAm. With respect to the coordination of nitrogen to boron, this is very interesting topic because in recent years these nitrogen-boron compounds had been studied for their sharp fluorescence peaks,[65] high thermal resistance,[66] strong UV-absorption[67] and excellent stability under different solvents.[67] Interestingly, two examples of materials with a 1,3,5,2-triazaborinine ring (i.e. boratriazine; BTA) were reported with the ligands **1.26a**, and **1.27a**.[64] In the case of the BTA adduct with **1.26a** (**1.19b**; **F_2Ph_2(4-(NO_2)Ph)BTA**; Chart 1.9) its fluorescence properties were investigated.[64]

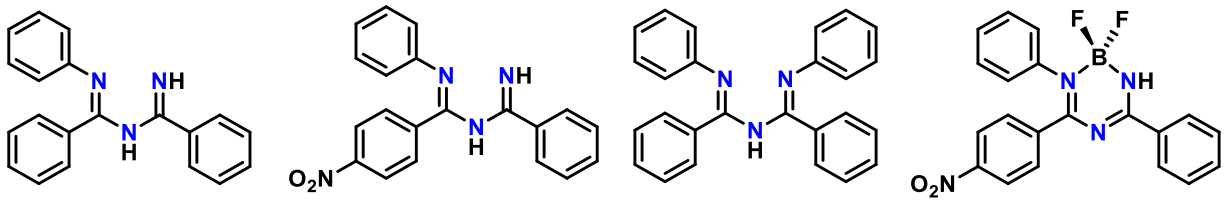

Chart 1.9. ImAm ligands used by Häger *et al*. to make coordination complexes.

It worthwhile mentioning that a fluorescent material with an ImAm framework was reported before **$F_2Ph_2(4\text{-}NO_2)BTA$**, but it was made by a metal assisted transformation with Pt(II).[68] In such example, a near ideal square planar Pt(II) complex with two anionic Ph_3ImAm ligands was isolated (**1.20b**; **$[Pt^{II}(Ph_3ImAm)_2]$**; Figure 1.6), and featured a very interesting pH dependent fluorescence.[68] While in acidic media, complete quenching of the emission of **$[Pt^{II}(Ph_3ImAm)_2]$** occurred, whereas fluorescence was observed in basic and neutral conditions. This interesting behavior is related to the conjugation of the lone pair in central nitrogen atom. In general, deprotonation of ImAm occurs first at the central nitrogen atom rather than the imino hydrogen atoms. This deprotonation is intuitive since the negative charge can be delocalized over two imino groups. The delocalization of the charge in the central nitrogen results in a partial sp^2 hybridization of this nitrogen, and evidence of the change in hybridization can be seen in the contraction of the C-N distance from 1.38-1.39 Å to 1.34 Å. The pH dependent luminescence of **$[Pt^{II}(Ph_3ImAm)_2]$** was explained in relation to the protonation, or deprotonation, of the central nitrogen atom. At neutral or basic pH the complex is neutral and the central nitrogen atom is not protonated (Figure 1.6), and therefore the negative charge can be delocalized into the Pt(II) ion. On the other hand, in acidic media, the central nitrogen atom is protonated and has more sp^3 character. As a result, the fluorescence is quenched due changes in the distribution of electron density in the complex. This experimental finding was confirmed by adding a methyl group to the central nitrogen in **$[Pt^{II}(Ph_3ImAm)_2]$**, and therefore enforcing the equivalent to a protonated version, resulting in the quenching of the luminescence.

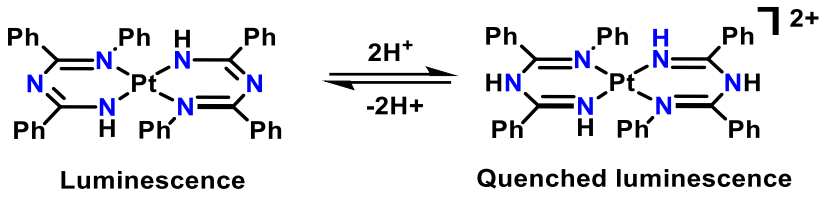

Figure 1.6. Quenching of the luminescence of **[Pt^{II}(Ph$_3$ImAm)$_2$]** at acidic pH. This complex was reported by Pombeiro *et al.*[68]

1.5.5 Synthesis of ImAm Ligands with Pyridyl or Pyrimidyl Substituents

The synthetic routes reported in Schemes 1.4 and 1.5 are very interesting, as they can lead to asymmetric ImAm derivatives with four potential substituents and enable the inclusion of bulky substituents that can protect the metal centre in catalytic cycles. However, overall yields reported in both reactions are poor, between 23% and 12%.[64] In addition to poor yields, the starting materials are not commercially available thus must be synthesized. On the other hand, the Brusso group at the University of Ottawa developed a high yielding one-pot metal free synthetic procedure for Py$_2$ImAm and Pm$_2$ImAm starting from the commercially available starting materials 2-pyridinecarbonitrile and 2-pyrimidinecarbonitrile, respectively. The synthesis of both ligands involves the reaction of ammonia gas with the appropriately substituted nitriles (Scheme 1.6). In the case of Py$_2$ImAm, the reaction is carried under pressure affording a 63% yield,[69] while Pm$_2$ImAm is isolated by allowing 2-pyrimidinecarbonitrile to react slowly with ammonia over two weeks at room temperature and atmospheric pressure,[70] resulting in a 76% yield.

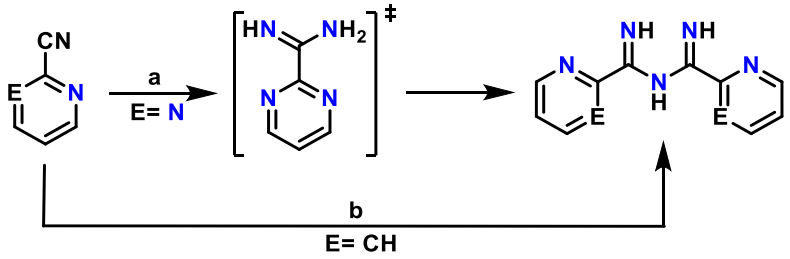

Scheme 1.6. Synthesis of Py$_2$ImAm and Pm$_2$ImAm. *Reagents and conditions*: (a) NH_3, MeCN, RT. (b) 2-cyanopyridine, MeCN, 110 °C.

Similar to acac and nacnac, ImAm ligands can exhibit tautomerism in the imino and amino groups. An interesting example of this tautomerism was observed in the solid state of Py$_2$ImAm

and Pm_2ImAm, which exist in different tautomeric forms in solid state; Py_2ImAm crystallizes in the amino-imino tautomer, while Pm_2ImAm crystallizes in the imino-imino form (Chart 1.10). In solution, Pm_2ImAm exist as an equilibrium of the two tautomeric forms, whereas Py_2ImAm exists as a single tautomer.[58, 70]

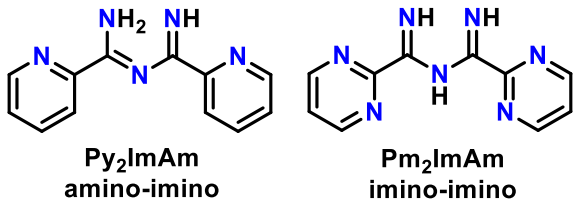

Chart 1.10. Tautomeric forms observed in the single crystals and powder of Py_2ImAm and Pm_2ImAm as observed by SC-XRD and PXRD.

1.6 Thesis Outline

This introductory chapter covers all the main research avenues that employ ImAm ligands. It is clear the use of imidoyl amidines as ligands is not exhaustive, and they have been much less studied compared to their acac and nacnac analogs. The main objective of this thesis is to study the coordination chemistry of Py_2ImAm and Pm_2ImAm, as having the ligands in hand in large quantities enables their investigation without restraint. As the first step towards exploring the coordination chemistry of these ligands, first row transition metals were chosen due to their applicability in a number of applications including coupling reaction catalysts,[4] water splitting,[71] memory devices,[72] spin-crossover systems,[72] luminescent materials,[73] and MRI contrast agents[74] to name a few. It worth mentioning that other members of the group had previously probed the coordination of these ImAm ligands with main group elements such as sulfur, selenium, and boron. During the course of the thesis a bottom up approach had been used, developing first mononuclear complexes, then afterwards investigating more unique polynuclear complexes. To elucidate the electronic configuration and or the interactions between metal centres, many of these complexes have been characterized by FT-IR and NMR spectroscopy, UV-vis spectroscopy, single crystal (SC) and powder X-ray diffraction (P-XRD), magnetometry, EPR spectroscopy and Mössbauer spectroscopy.

In the second chapter, selective coordination of Py_2ImAm with first row transition metal was explored, establishing a protocol to exclusively bind in a bidentate or tridentate fashion. This was achieved by controlling the pH of the solution, which directs coordination of the metal ion. Two main frameworks were obtained, the first molecular framework occurs when the metal ion coordinates in a bidentate fashion, resulting in mononuclear complexes with a nearly ideal octahedral configuration of the general formula **$[M^{III}(Py_2ImAm)_3]$** (M= Mn, Fe or Co). Coordinating the metal ion in a terpy-like fashion results in either a pentacoordinate or hexacoordinate environment about the metal centre of the general formula **$[M^{II}(Py_2ImAm)Cl_2]$** (M= Mn or Co) or **$[Fe^{III}(Py_2ImAm)Cl_3]$**. In some cases, it was also observed a shift in the coordination of the metal ion from the tridentate to bidentate site of Py_2ImAm upon addition of a base such as NaOH. In addition to the synthesis of these mononuclear complexes the single crystal characterization of these complexes is also presented in this chapter.

The third chapter describes the establishment of polynuclear complexes in which the metal ions are coordinated in both the bidentate and tridentate sites of Pm_2ImAm. In particular, manganese and iron homometallic tetranuclear complexes were prepared. These tetranuclear complexes were characterized by single crystal X-ray diffraction, magnetometry, and in the case of the iron tetranuclear complex, by Mössbauer spectroscopy. The magnetochemistry of these tetranuclear complexes was understood by comparing with the individual mononuclear complexes described in Chapter 2. These studies reveal a central metal ion with low spin configuration surrounded by three outer metal ions in a high spin configuration. Complexes such as these, with the same metal ion in two different electronic configurations, are not common and in the case of manganese the complex reported is unique as octahedral manganese(III) low spin ions are very rare. This therefore represents the first complex reported with both manganese(III) low spin and manganese(II) high spin. The synthesis and single crystal characterization of these tetranuclear complexes is also presented in this chapter.

Following the same vein as the third chapter, in the fourth chapter cobalt was coordinated into both coordination pockets of Pm_2ImAm. Interestingly, two different complexes were obtained, a linear trinuclear complex with the formula **$[Co^{II}_3(Pm_2ImAm)_2Cl_4]$** and a hexanuclear complex (**$[Co^{II}_6(\mu\text{-}Cl)_2(Pm_2ImAm)_4Cl_8]$**) that consists of two linear trinuclear moieties linked together through two bridging chloride ions. Despite both **$[Co^{II}_3(Pm_2ImAm)_2Cl_4]$** and **$[Co^{II}_6(\mu$-**

Cl)$_2$(Pm$_2$ImAm)$_4$Cl$_8$] having basically the same asymmetric unit, they greatly differ in the crystal packing and magnetochemistry. For example, the crystal lattice of **[Co$^{II}_3$(Pm$_2$ImAm)$_2$Cl$_4$]** has extended columnar solvent channels, while **[Co$^{II}_6$(μ-Cl)$_2$(Pm$_2$ImAm)$_4$Cl$_8$]** does not. Like the tetranuclear complexes, the magnetochemistry was understood by studying the individual mononuclear cobalt complexes with Py$_2$ImAm reported in Chapter 2. Single molecule magnet behavior was observed in **[Co$^{II}_6$(μ-Cl)$_2$(Pm$_2$ImAm)$_4$Cl$_8$]** yet was not observed for **[Co$^{II}_3$(Pm$_2$ImAm)$_2$Cl$_4$]**. Interestingly, the factor that conduce to a linear trinuclear or hexanuclear complex is not the solvent used for the crystallization nor the source of the weak acid, but rather the content of water in the methanol used.

The fifth chapter covers the one-pot synthesis of copper-manganese heterometallic complexes. Like the cobalt complexes in Chapter 4, depending of the water content of the metal used two molecular frameworks were obtained, a linear trinuclear with the formula **[Mn$^{II}_2$Cu^{II}(Pm$_2$ImAm)$_2$Cl$_4$]** and a hexanuclear complex with the formula **[Mn$^{II}_4$Cu$^{II}_2$(μ-Cl)$_2$(Pm$_2$ImAm)$_4$Cl$_8$]**. The single crystal structures of **[Mn$^{II}_2$Cu^{II}(Pm$_2$ImAm)$_2$Cl$_4$]**, and **[Mn$^{II}_4$Cu$^{II}_2$(μ-Cl)$_2$(Pm$_2$ImAm)$_4$Cl$_8$]** are analogous to the structures of the cobalt complexes presented in the chapter 4.In both complexes, copper(II) is coordinated in bidentate fashion to two Pm$_2$ImAm ligands with a square planar geometry. The manganese dichloride located at the periphery of the molecules and is coordinated into the tridentate pocket of Pm$_2$ImAm for both complexes. For the first time, a one-pot synthesis had been employed to synthesize heterometallic complexes with imidoyl amidine ligands, and this strategy has great potential to combine different metal ions in the development heterometallic complexes.

The last chapter covers the conclusions and future work. The chemistry of Py$_2$ImAm and Pm$_2$ImAm is summarized with the main factors that direct the coordination of bidentate or tridentate sites. Because the mononuclear and polynuclear complexes were synthesized in different chapters, a brief summary of the main factors that affect the synthesis of mononuclear *vs* polynuclear is presented in this chapter. Complexes from different chapters are also compared in terms of common electronic configurations (i.e. H.S. or L.S.). Base on the success of the synthesis of heterometallic complexes in chapter 5, a short discussion of new opportunities to synthesize new heterometallic complexes is provided. Finally, a list of future works that will be completed by our co-workers at university of Ottawa and abroad is presented. This future research involves

testing complexes obtained during the course of this thesis for different purposes. The imidoyl amidine ligands presented here can form a variety of architectures and have a unique reactivity with first-row transition metals.

1.6 References

[1] El-Wakiel, N. A.; Rizk, H. F.; Ibrahim, S. A., *Appl. Organomet. Chem.* **2017,** 31, (10), e3723.

[2] Montes, V. A.; Pohl, R.; Shinar, J.; Anzenbacher Jr, P., *Chem.: Eur. J.* **2006,** 12, (17), 4523-4535.

[3] Lu, Y.; Yeung, N.; Sieracki, N.; Marshall, N. M., *Nature* **2009,** 460, (7257), 855-862.

[4] Zweig, J. E.; Kim, D. E.; Newhouse, T. R., *Chem. Rev.* **2017,** 117, (18), 11680-11752.

[5] Miao, J.; Ge, H., *Eur. J. Org. Chem.* **2015,** , (36), 7859-7868.

[6] Ghosh, A., *Coord. Chem. Rev.* **2009,** 253, (5), 523-525.

[7] Byrne, E. K.; Richeson, D. S.; Theopold, K. H., *ChemComm* **1986**, (19), 1491-1492.

[8] Pascualini, M. E.; Di Russo, N. V.; Thuijs, A. E.; Ozarowski, A.; Stoian, S. A.; Abboud, K. A.; Christou, G.; Veige, A. S., *Chem. Sci* **2015,** 6, (1), 608-612.

[9] Suttil, J. A.; Kucharyson, J. F.; Escalante-Garcia, I. L.; Cabrera, P. J.; James, B. R.; Savinell, R. F.; Sanford, M. S.; Thompson, L. T., *J. Mater. Chem. A* **2015,** 3, (15), 7929-7938.

[10] Sridaeng, D.; Limsirinawa, A.; Sirojpornphasut, P.; Chawiwannakorn, S.; Chantarasiri, N., *J. Appl. Polym. Sci.* **2015,** 132, (31).

[11] Pereira, C.; Silva, J. F.; Pereira, A. M.; Araújo, J. P.; Blanco, G.; Pintado, J. M.; Freire, C., *Catal. Sci. Technol.* **2011,** 1, (5), 784-793.

[12] Charleton, K. D. M.; Prokopchuk, E. M., *J. Chem. Educ.* **2011,** 88, (8), 1155-1157.

[13] Gao, R.-X.; Luan, X.-Q.; Xie, Z.-Y.; Yang, L.; Pei, Y., *Org. Biomol. Chem.* **2019,** 17, (21), 5262-5268.

[14] Hargreaves, R. N.; Truter, M. R., *J. Chem. Soc. A*, **1969**, (0), 2282-2287.

[15] Corain, B.; Basato, M.; Visentin, G.; Zanotti, G., *Dalton Trans.* **1983**, (7), 1217-1223.

[16] Galland, M.; Riobé, F.; Ouyang, J.; Saleh, N.; Pointillart, F.; Dorcet, V.; Le Guennic, B.; Cador, O.; Crassous, J.; Andraud, C.; Monnereau, C.; Maury, O., *Eur. J. Inorg. Chem.* **2019,** 2019, (1), 118-125.

[17] Brock, A. J.; Clegg, J. K.; Li, F.; Lindoy, L. F., *Coord. Chem. Rev.* **2018,** 375, 106-133.

[18] Matsunaga, S.; Shibasaki, M., *ChemComm* **2014,** 50, (9), 1044-1057.

[19] Webster, R. L., *Dalton Trans.* **2017,** 46, (14), 4483-4498.

[20] Kajiwara, T.; Nakano, M.; Kaneko, Y.; Takaishi, S.; Ito, T.; Yamashita, M.; Igashira-Kamiyama, A.; Nojiri, H.; Ono, Y.; Kojima, N., *J. Am. Chem. Soc.* **2005,** 127, (29), 10150-10151.

[21] Madalan, A. M.; Bernot, K.; Pointillart, F.; Andruh, M.; Caneschi, A., *Eur. J. Inorg. Chem.* **2007,** 2007, (35), 5533-5540.

[22] Wocadlo, S.; Massa, W.; Folgado, J.-V., *Inorganica Chim. Acta* **1993,** 207, (2), 199-206.

[23] Kamiyama, A.; Noguchi, T.; Kajiwara, T.; Ito, T., *Angew. Chem. Int. Ed.* **2000,** 39, (17), 3130-3132.

[24] Cowan, M. G.; Miller, R. G.; Southon, P. D.; Price, J. R.; Yazaydin, O.; Lane, J. R.; Kepert, C. J.; Brooker, S., *Inorg. Chem.* **2014,** 53, (22), 12076-12083.

[25] Zebret, S.; Dupont, N.; Bernardinelli, G.; Hamacek, J., *Chem.: Eur. J.* **2009,** 15, (14), 3355-3358.

[26] Zebret, S.; Torres, E.; Terreno, E.; Guénée, L.; Senatore, C.; Hamacek, J., *Dalton Trans.* **2011,** 40, (16), 4284-4290.

[27] Wei, C.; He, Y.; Shi, X.; Song, Z., *Coord. Chem. Rev.* **2019,** 385, 1-19.

[28] Launay, J.-P.; Launay, J. P.; Verdaguer, M.; Verdaguer, M., *Electrons in Molecules: From Basic Principles to Molecular Electronics*. ed.; Oxford University Press: 2013.

[29] Kamiyama, A.; Noguchi, T.; Kajiwara, T.; Ito, T., *Inorg. Chem.* **2002,** 41, (3), 507-512.

[30] Kajiwara, T.; Watanabe, I.; Kaneko, Y.; Takaishi, S.; Enomoto, M.; Kojima, N.; Yamashita, M., *J. Am. Chem. Soc.* **2007,** 129, (41), 12360-12361.

[31] Vigato, P. A.; Peruzzo, V.; Tamburini, S., *Coord. Chem. Rev.* **2009,** 253, (7), 1099-1201.

[32] Bonnett, R.; Bradley, D. C.; Fisher, K. J., *ChemComm* **1968**, (15), 886-887.

[33] Lerner, E. I.; Lippard, S. J., *J. Am. Chem. Soc.* **1976,** 98, (17), 5397-5398.

[34] Norrestam, R., *Acta Cryst. C* **1984,** 40, (6), 955-957.

[35] Boča, R.; Hvastijová, M.; Kožíšek, J.; Valko, M., *Inorg. Chem.* **1996,** 35, (16), 4794-4797.

[36] Kopylovich, M. N.; Karabach, Y. Y.; Guedes da Silva, M. F. C.; Figiel, P. J.; Lasri, J.; Pombeiro, A. J. L., *Chem.: Eur. J.* **2012,** 18, (3), 899-914.

[37] Semmelhack, M. F.; Schmid, C. R.; Cortes, D. A.; Chou, C. S., *J. Am. Chem. Soc.* **1984,** 106, (11), 3374-3376.

[38] Nesterova, V. O.; Kopylovich, N. M.; Nesterov, S. D., *Inorganics* **2019,** 7, (7).

[39] Tong, M.-L.; Wu, Y.-M.; Tong, Y.-X.; Chen, X.-M.; Chang, H.-C.; Kitagawa, S., *Eur. J. Inorg. Chem.* **2003,** , (13), 2385-2388.

[40] Igashira-Kamiyama, A.; Kajiwara, T.; Konno, T.; Ito, T., *Inorg. Chem.* **2006,** 45, (16), 6460-6466.

[41] Zheng, L.-L.; Zhang, W.-X.; Qin, L.-J.; Leng, J.-D.; Lu, J.-X.; Tong, M.-L., *Inorg. Chem.* **2007,** 46, (23), 9548-9557.

[42] Arroyo, M.; Gómez-Iglesias, P.; Martín-Alvarez, J. M.; Alvarez, C. M.; Miguel, D.; Villafañe, F., *Inorg. Chem.* **2012,** 51, (11), 6070-6080.

[43] Turnbull, M. M.; Wei, M. Y.; Willett, R. D., *J. Coord. Chem.* **1995,** 35, (1-2), 11-17.

[44] Kajiwara, T.; Kamiyama, A.; Ito, T., *ChemComm* **2002**, (12), 1256-1257.

[45] Glaser, T.; Theil, H.; Liratzis, I.; Weyhermüller, T.; Bill, E., *Inorg. Chem.* **2006,** 45, (13), 4889-4891.

[46] Zhou, X.-P.; Li, D.; Zheng, S.-L.; Zhang, X.; Wu, T., *Inorg. Chem.* **2006,** 45, (18), 7119-7125.

[47] Groom, C. R.; Bruno, I. J.; Lightfoot, M. P.; Ward, S. C., *Acta Cryst. B* **2016,** 72, (2), 171-179.

[48] Kopylovich, M. N.; Tronova, E. A.; Haukka, M.; Kirillov, A. M.; Kukushkin, V. Y.; Fraústo da Silva, J. J. R.; Pombeiro, A. J. L., *Eur. J. Inorg. Chem.* **2007,** 2007, (29), 4621-4627.

[49] Kopylovich, M. N.; Haukka, M.; Kirillov, A. M.; Kukushkin, V. Y.; Pombeiro, A. J. L., *Chem.: Eur. J.* **2007,** 13, (3), 786-791.

[50] Kopylovich, M. N.; Lasri, J.; Guedes da Silva, M. F. C.; Pombeiro, A. J. L., *Dalton Trans.* **2009**, (16), 3074-3084.

[51] Kopylovich, M. N.; Kirillov, A. M.; Tronova, E. A.; Haukka, M.; Kukushkin, V. Y.; Pombeiro, A. J. L., *Eur. J. Inorg. Chem.* **2010,** , (16), 2425-2432.

[52] Siedle, A. R.; Webb, R. J.; Behr, F. E.; Newmark, R. A.; Weil, D. A.; Erickson, K.; Naujok, R.; Brostrom, M.; Mueller, M.; Chou, S.-H.; Young, V. G., *Inorg. Chem.* **2003,** 42, (4), 932-934.

[53] Starikova, A. A., *Chem. Pap.* **2018,** 72, (4), 821-828.

[54] Dias, H. V. R.; Singh, S., *Inorg. Chem.* **2004,** 43, (19), 5786-5788.

[55] Dias, H. V. R.; Singh, S.; Cundari, T. R., *Angew. Chem. Int. Ed.* **2005,** 44, (31), 4907-4910.

[56] Dias, H. V. R.; Singh, S.; Flores, J. A., *Inorg. Chem.* **2006,** 45, (22), 8859-8861.

[57] Flores, J. A.; Kobayashi, Y.; Dias, H. V. R., *Dalton Trans.* **2011,** 40, (40), 10351-10359.

[58] Adiraju, V. A. K.; Flores, J. A.; Yousufuddin, M.; Dias, H. V. R., *Organometallics* **2012,** 31, (22), 7926-7932.

[59] Flores, J. A.; Dias, H. V. R., *Inorg. Chem.* **2008,** 47, (11), 4448-4450.

[60] Kulkarni, N. V.; Das, A.; Ridlen, S. G.; Maxfield, E.; Adiraju, V. A. K.; Yousufuddin, M.; Dias, H. V. R., *Dalton Trans.* **2016,** 45, (11), 4896-4906.

[61] Dias, H. V. R.; van Waasbergen, L. G.; Flores, J. A. Poly-halogenated triazapentadiene compositions. 2010.

[62] Törmäkangas, O. P.; Koskinen, A. M. P., *Org. Process Res. Dev.* **2001,** 5, (4), 421-425.

[63] Hong, A. C.; Young, C. J.; Hurley, M. D.; Wallington, T. J.; Mabury, S. A., *Geophys. Res. Lett.* **2013,** 40, (22), 6010-6015.

[64] Häger, I.; Fröhlich, R.; Würthwein, E.-U., *Eur. J. Inorg. Chem.* **2009,** , (16), 2415-2428.

[65] Loudet, A.; Burgess, K., *Chem. Rev.* **2007,** 107, (11), 4891-4932.

[66] Li, F.; Yang, S. I.; Ciringh, Y.; Seth, J.; Martin, C. H.; Singh, D. L.; Kim, D.; Birge, R. R.; Bocian, D. F.; Holten, D.; Lindsey, J. S., *J. Am. Chem. Soc.* **1998,** 120, (39), 10001-10017.

[67] Bañuelos, J., *Chem. Rec.* **2016,** 16, (1), 335-348.

[68] Sarova, G. H.; Bokach, N. A.; Fedorov, A. A.; Berberan-Santos, M. N.; Kukushkin, V. Y.; Haukka, M.; Fraústo da Silva, J. J. R.; Pombeiro, A. J. L., *Dalton Trans.* **2006**, (31), 3798-3805.

[69] Leitch, A. A.; Korobkov, I.; Assoud, A.; Brusso, J. L., *ChemComm* **2014,** 50, (38), 4934-4936.

[70] Yousaf, M.; Yutronkie, N. J.; Castañeda, R.; Klein, J. A.; Brusso, J., *New J Chem* **2017,** 41, (20), 12218-12224.

[71] Nesterov, S. D.; Nesterova, V. O., *Catalysts* **2018,** 8, (12).

[72] Pedersen, K. S.; Bendix, J.; Clérac, R., *ChemComm* **2014,** 50, (34), 4396-4415.

[73] Pamei, M.; Puzari, A., *Nano-Structures & Nano-Objects* **2019,** 19, 100364.

[74] Morrow, J. R.; Tóth, É., *Inorg. Chem.* **2017,** 56, (11), 6029-6034.

Chapter 2

Probing the Coordination Chemistry of *N*-2-pyridylimidoyl-2-pyridylamidine: A Versatile Ligand with Multiple Coordination Sites

Authorship disclosure: A portion of this chapter was published in *Crystal Growth & Design* as "Probing the coordination chemistry of *N*-2-pyridylimidoyl-2-pyridylamidine: a versatile ligand with multiple coordination sites" R. Castañeda, A. Hollingshead, B. Gabidullin, J. L. Brusso, *Cryst. Growth Des.* **2017**, *17*, 6572-6578. The synthesis of all compounds with exception of **[Mn^{III}(Py$_2$ImAm)$_3$]·DCM** and **[Fe^{III}(Py$_2$ImAm)$_3$]·DCM** was performed by Luis Raúl Castañeda Perea. The synthesis of **[Mn^{III}(Py$_2$ImAm)$_3$]·DCM** and **[Fe^{III}(Py$_2$ImAm)$_3$]·DCM** was performed by Andrew Hollingshead. All crystals structures presented in this chapter were collected and refined by Luis Raúl Castañeda Perea with consultation of Bulat Gabidullin.

2.1 Introduction

Polypyridines such as 2,2'-bipyridine (**2.1a**; biPy; Chart 2.1), phenanthroline (**2.2a**; phen; Chart 2.1), 2,2';6',2"-terpyridine (**2.3a**; terpy; Chart 2.1), and tetra-2-pyridyl-1,4-pyrazine (**2.4a**; Py$_4$Pz; Chart 2.1) represent a diverse family of ligands extensively studied for a wide variety of applications such as catalysis,[1] photoluminescence,[2] photoredox,[3] spintronics,[4] and molecular switches,[5] to name a few. Considering the versatility of polypyridines, and the ability to tailor the properties of the resulting metal complexes through the attachment of functional groups, research efforts towards the development of new derivatives through reliable and economic processes continues to garner attention. In that regard, the Brusso group recently developed the synthesis of *N*-2-pyridylimidoyl-2-pyridylamidine (**2.5a**; Py$_2$ImAm; Chart 2.1),[6] a ligand that possesses both a bidentate and tridentate coordination pockets. The presence of two coordination environments facilitates the development of a variety of metal complexes in which we can take advantage of the versatility of Py$_2$ImAm. Furthermore, employing a ligand such as **2.5a**, and developing the synthetic methodology in which nuclearity and topology can be controlled, tailor-made polynuclear homo and heterometallic clusters may be realized.[7-9] While many clusters are known, the formation of such systems often rely on serendipitous reaction pathways,[4, 10-13] which can lead to unexpected or unpredictable materials. The approach presented herein provides an avenue towards achieving these goals by exploiting the attributes of our polypyridine-based compounds.

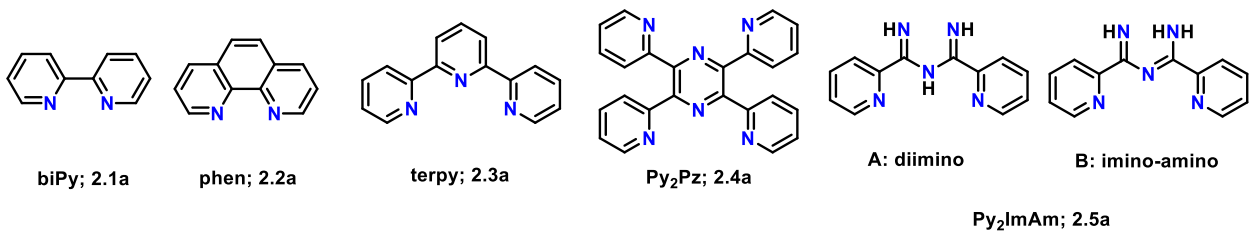

Chart 2.1. Examples of polypyridines.

Although the preparation of Py_2ImAm has only recently been elucidated, coordination complexes of **2.5a** with copper,[14] palladium,[15] and manganese[16] have been reported; however, these complexes were all prepared in one pot synthetic procedures through metal-assisted transformations. In other words, the reaction between a metal salt and a pyridyl synthon led to the formation of Py_2ImAm *in situ*. Unfortunately, these metal assisted transformations cannot be carried out with every metal ion, and often lead to multi-step synthesis with poor yields.

The first example of a complex with Py_2ImAm was a copper coordination polymer, isolated after the thermal decomposition of tris(2-pyridyl)triazine in the presence of copper (II) acetate.[14] In this study, the authors demonstrate that the Py_2ImAm ligand acts to ferromagnetically couple the adjoining Cu^{II} ions, which alternate between square planar and octahedral coordination environments within the one-dimensional chain. In addition to magnetic studies, complexes bearing the Py_2ImAm ligand have also been investigated for their catalytic activity towards Suzuki–Miyaura and Heck cross-coupling reactions.[15] In particular, a square planar Pd^{II} complex in which two Py_2ImAm ligands coordinate to the metal centre in a bidentate fashion, was isolated upon reacting palladium (II) chloride with 2-cyanopyridine. And finally, when manganese (II) fluoride is reacted with pyridine-2-amidoxime, **2.5a** is generated *in situ* affording a Mn^{III} complex in which the metal ion adopts a distorted octahedral environment bound to three anionic Py_2ImAm ligands in a bidentate fashion.[16] Interestingly, a redox reaction occurs in this example leading to oxidation of the metal ion.

Since all previous reports of coordination complexes involving the Py_2ImAm ligand consist of one pot synthesis involving metal-assisted transformations, their formation relied on serendipitous reaction pathways. As such, the nuclearity and topology were difficult to control. Starting with the ligand already in hand enables tailoring of the reaction conditions, such that accessing the bidentate and/or tridentate coordination pockets of Py_2ImAm should be feasible.

Such influence on the metal environment is important, as it can lead to metallic complexes with significant differences in their properties. For example, since previous studies suggest Py_2ImAm acts as a ferromagnetic coupler, as was observed in the aforementioned copper complex,[14] it is anticipated that unique magnetic exchange may be feasible through the development of homo and heterometallic polynuclear complexes employing Py_2ImAm as a ligand. In addition, the development of Py_2ImAm based coordination complexes may find significant use in catalysis, as demonstrated with the palladium complex.[15] Interestingly, a metal complex coordinated exclusively in the tridentate site of Py_2ImAm has yet to be realized. Considering the vast use of terpy-based complexes in catalysis, isolation of a terpy analog employing **2.5a** provides an avenue with significant potential.

As a first step towards exploring the ligating attributes of Py_2ImAm, we sought to develop the methodology in which the coordination environment of the metal ion could be controlled. To that end, presented herein are a number of manganese, iron and cobalt complexes, in which the various reaction conditions employed specifically enable coordination to either the bidentate or tridentate coordination pockets of Py_2ImAm. In particular, when carried out under basic or neutral conditions, M^{III} coordination complexes are isolated in which the metal ion adopts a distorted octahedral environment bound to three anionic Py_2ImAm ligands in a bidentate fashion affording tris(*N*-2-pyridylimidoyl-2-pyridylamidinate) manganese(III) (**2.1b**; **$[Mn^{III}(Py_2ImAm)_3]$**), tris(*N*-2-pyridylimidoyl-2-pyridylamidinate)iron(III) (**2.2b**; **$[Fe^{III}(Py_2ImAm)_3]$**) and tris(*N*-2-pyridylimidoyl-2-pyridylamidinate) cobalt(III) (**2.3b**; **$[Co^{III}(Py_2ImAm)_3]$**). By changing to acidic conditions, it is possible to access the tridentate coordination pocket of Py_2ImAm, leading to the formation of coordination complexes **$[Mn^{II}(Py_2ImAm)Cl_2]$** (**2.4b**), **$[Fe^{III}(Py_2ImAm)Cl_3]$** (**2.5b**) and **$[Co^{II}(Py_2ImAm)Cl_2]$** (**2.6b**). These studies demonstrate that the key factor in controlling the coordination site is the presence (or absence) of a weak acid. Although the choice of solvent does not appear to influence the coordination environment, it has been shown to affect the crystal packing and, in some cases presented here, various solvates were obtained.

2.2 Structural Analysis of Py_2ImAm

While the synthesis of Py_2ImAm was reported earlier by other members of the Brusso group,[6] the single crystal characterization of this ligand is studied in this thesis. In general *N*-imidoylamidines can exist in two tautomeric forms (i.e. diimino *vs*. imino-amino; Chart 2.1), but interestingly NMR studies shows that Py_2ImAm primarily exists as the diimino tautomer in solution (Figure 2.1). In particular, the ^1H NMR spectrum reveals two singlets at 11.39 ppm and 9.55 ppm, which integrate in a 1:2 ratio, and the number of signals indicates a symmetrical molecule. Interestingly, in the solid state Py_2ImAm exists in the other tautormeric form, as confirmed through single crystal X-ray analysis (Figure 2.2). This may be attributed to the planarity of the molecular framework, which would lead to allylic strain between the N-H of the central nitrogen atom and the C-H of the pyridyl rings if a hydrogen atom was located on the central nitrogen of Py_2ImAm. Since Py_2ImAm crystallizes as the imino-amino tautomer, the allylic strain can be avoided. In the solid state, crystals of Py_2ImAm belong to the $P2_1/c$ space group and the asymmetric unit consists of two independent molecules. Discrete hydrogen bonded dimers are observed between independent Py_2ImAm molecules, which pack in a herringbone motif with C-H···N inter-stack hydrogen bonds (Figure 2.2).

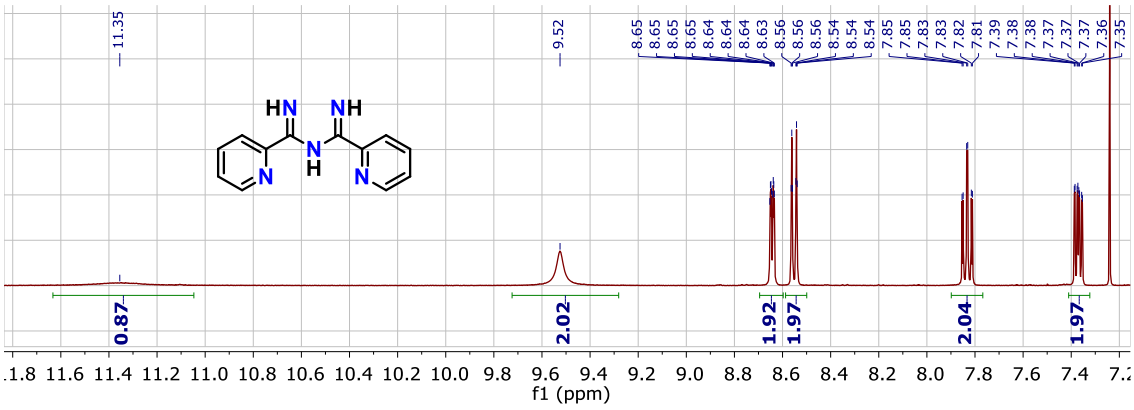

Figure 2.1. Expansion of the aromatic region in the ^1H NMR of Py_2ImAm. $CDCl_3$ was used as solvent.

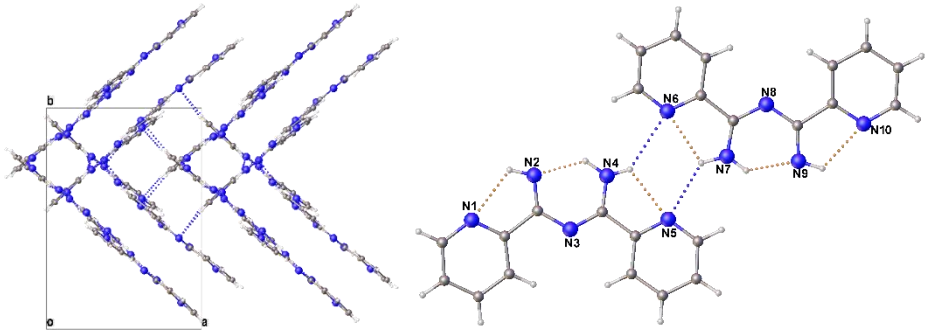

Figure 2.2. Structural diagram of Py_2ImAm illustrating the hydrogen bonded dimer (right) and a view of the crystal packing along the 001 plane (left). Intermolecular hydrogen bonds are denoted as blue dotted lines and intramolecular hydrogen bonds as orange dotted lines.

2.3 Synthesis and Structural Analysis of Complexes Coordinated to Py_2ImAm in a Bidentate Fashion

With Py_2ImAm in hand, its treatment with manganese, iron and cobalt was explored. In general, a solution of Py_2ImAm in common organic solvents (e.g. acetonitrile (MeCN), dichloromethane (DCM), chloroform) was layered or stirred with an alcoholic solution of a metal salt (e.g. $MnCl_2$, $FeCl_3$, $Co(OAc)_2$; Scheme 2.1). After several days under atmospheric conditions, crystals suitable for X-ray analysis were obtained, confirming the identity of **$[Mn^{III}(Py_2ImAm)_3]$**, (**$[Fe^{III}(Py_2ImAm)_3]$**) and (**$[Co^{III}(Py_2ImAm)_3]$**). Initially, basic conditions were employed through the addition of triethylamine (Et_3N) to the ligand solution; however, this was found to be unnecessary to access the **$[M^{III}(Py_2ImAm)_3]$** complexes because Py_2ImAm ligand can act as the base or proton sponge in the reaction. Although Et_3N is not necessary, without its use the yield obtained is approximately half of that when Et_3N is utilized during the synthesis.

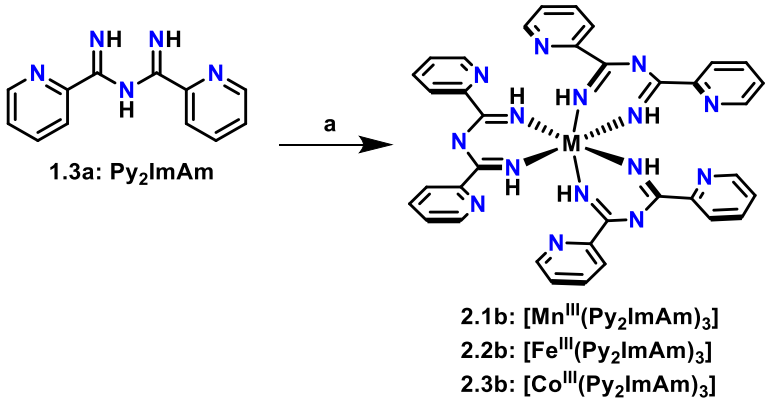

Scheme 2.1. Synthesis of tris(*N*-2-pyridylimidoyl-2-pyridylamidinate) manganese(III) (**[Mn^{III}(Py$_2$ImAm)$_3$]**), tris(*N*-2-pyridylimidoyl-2-pyridylamidinate) iron(III) (**[Fe^{III}(Py$_2$ImAm)$_3$]**) and tris(*N*-2-pyridylimidoyl-2-pyridylamidinate) cobalt(III) (**[Co^{III}(Py$_2$ImAm)$_3$]**). *Reagents and conditions*: (a) $MnCl_2$, $FeCl_3$ or $Co(OAc)_2$ in EtOH./MeCN, EtOH./DCM, EtOH./dichloroethane, EtOH./chloroform or EtOH./chlorobenzene; with or without Et_3N.

In all the coordination complexes obtained following the reaction conditions outlined in Scheme 2.1, the metal ion adopts a distorted octahedral environment bound to three anionic Py$_2$ImAm ligands in a bidentate fashion (Figure 2.3). Based on charge balance, the metal ions possess an oxidation state of +3, thus suggesting a redox process occurs in the case of the manganese and cobalt reactions. It should be pointed out that O_2 has higher oxidation potential at alkaline pH when compared to neutral or acidic.[17] Frequently the presence of Et_3N (or other weak bases) assist the oxidation of Mn^{2+} to Mn^{3+}. These structures are similar to the previously reported octahedral complex tris(*N*-2-pyridylimidoyl-2-pyridylamidinate) manganese(III) (**[Mn^{III}(Py$_2$ImAm)$_3$]·MeCN**),[16] obtained *via* the one-pot reaction between pyridine-2-amidoxime and an Mn^{II} salt. Interestingly, the metal ion in the previously reported analog also undergoes oxidation from Mn^{II} to Mn^{III}.

Due to the solubility of Py$_2$ImAm, a variety of solvents may be employed (e.g. MeCN, DCM, dichloroethane, chloroform, chlorobenzene) to dissolve the ligand. To probe the effect of solvent, a number of reactions with $MnCl_2$ and $FeCl_3$ were carried out, leading to an array of bidentate octahedral complexes. Crystalline material was obtained when DCM, dichloroethane, chloroform and chlorobenzene were used to dissolve the ligand, which were subsequently layered with

ethanolic solutions of $MnCl_2$ or $FeCl_3$; the resulting crystals were characterized by IR spectroscopy and unit cell checks. Regardless of the solvate, the IR spectra were consistent for each manganese and iron complex. While the IR stretching frequencies are quite similar, the unit cell parameters differ significantly (See Appendix B; Table B.1), indicative of the influence of the solvent on the lattice parameters. Presented here are the solvates with MeCN and DCM.

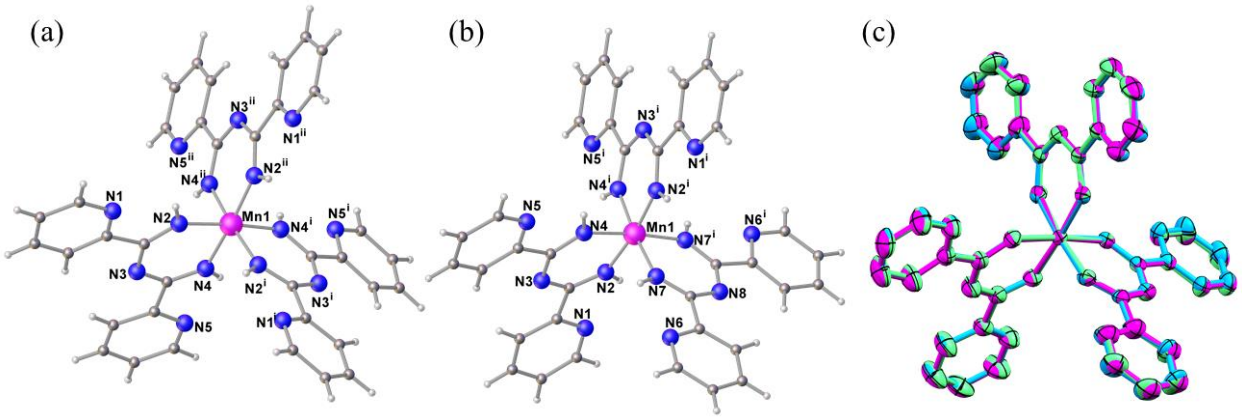

Figure 2.3. (a) Structural diagram of **[Mn^{III}(Py$_2$ImAm)$_3$]·MeCN**, (b) structural diagram of **[Mn^{III}(Py$_2$ImAm)$_3$]·DCM** and (c) overlay of complexes **[Mn^{III}(Py$_2$ImAm)$_3$]·DCM** (pink), **[Fe^{III}(Py$_2$ImAm)$_3$]·DCM** (green) and **[Co^{III}(Py$_2$ImAm)$_3$]·DCM** (light blue; bottom). Solvent molecules have been omitted for clarity and symmetry related positions are labeled with the superscript i.

In regards to the MeCN solvates **[Mn^{III}(Py$_2$ImAm)$_3$]·MeCN**,[16] **[Fe^{III}(Py$_2$ImAm)$_3$]·MeCN**, and **[Co^{III}(Py$_2$ImAm)$_3$]·MeCN** single crystal analysis reveals these complexes are isomorphic, crystallizing in the trigonal space group *R*-3. In these complexes, the molecules sit on a C_3 axis (Figure 2.3a), thus possess essentially equidistant N-M bond lengths within each individual complex (Table 2.1). It worth mentioning there is a contraction in the N-M distances from manganese to cobalt (Table 2.1). The pyridyl rings of the *N*-imidoylamidine ligands are involved in intramolecular hydrogen bonding (e.g. N-H···N; Table B.5), similar to that observed in Py$_2$ImAm. The molecular complexes in these MeCN solvates stack along the *c*-axis and possess a number of C-H···N and π-π interactions between neighbouring molecules (Figure 2.4 *left*). In these solvates, the MeCN was found to occupy voids in the lattice with only weak interactions existing between the complex and the solvent molecules.

Table 2.1. Nitrogen to metal distances in the MeCN solvates

Bond	**$[Mn^{III}(Py_2ImAm)_3]\cdot MeCN$** Length (Å)	**$[Fe^{III}(Py_2ImAm)_3]\cdot MeCN$** Length (Å)	**$[Co^{III}(Py_2ImAm)_3]\cdot MeCN$** Length (Å)
N2-M1	1.95932(3)	1.915(4)	1.9133(3)
N4-M1	1.94117(4)	1.925(4)	1.8945(3)

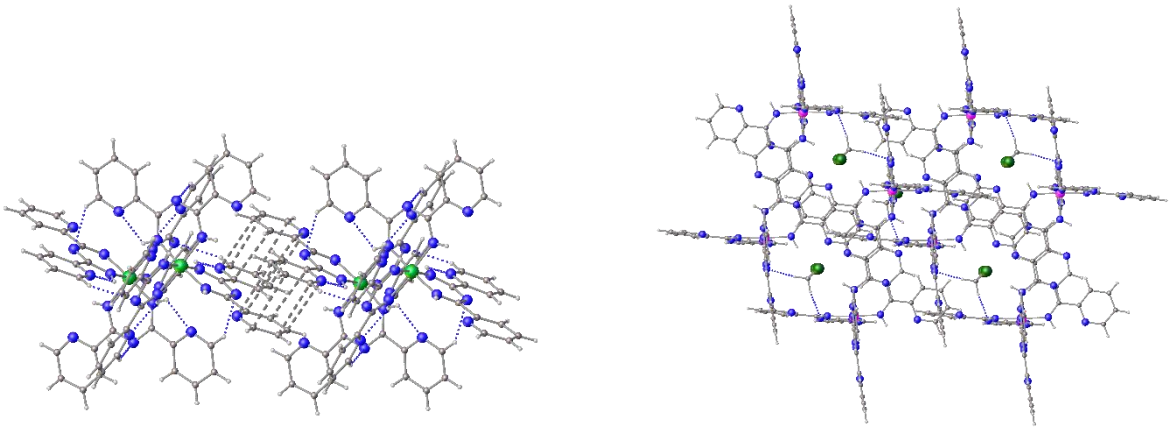

Figure 2.4. Crystal packing of **$[Fe^{III}(Py_2ImAm)_3]\cdot MeCN$** (left), and **$[Mn^{III}(Py_2ImAm)_3]\cdot DCM$** (right). Solvent molecules had been omitted for clarity. Hydrogen bonds are shown as blue doted lines. The π-π interactions are denoted as gray dashed lines.

In addition to the MeCN solvates, DCM solvates of **$[Mn^{III}(Py_2ImAm)_3]\cdot DCM$**, **$[Fe^{III}(Py_2ImAm)_3]\cdot DCM$** and **$[Co^{III}(Py_2ImAm)_3]\cdot DCM$** were fully characterized through single crystal X-ray diffraction. These three new structures are isomorphic, crystallizing in the monoclinic space group *C*2/c; the similarity between the molecular framework of these complexes is highlighted in the overlay of the three structures shown in Figure 2.3c. Similar to the MeCN solvates, here the pyridyl rings are also involved in intramolecular hydrogen bonding with the imino hydrogen atoms leading to a planar arrangement of the ligands. As well, the N-M distances within each individual complex are essentially equidistant (Table 2.2). When the N-M distances in a complex are equidistant, as for example for both MeCN and DCM solvates, it is assumed there is no Jahn Teller distortion in these complexes. Nevertheless, both MeCN and DCM solvates sit around a symmetry of operation as it can be seeing in the asymmetric unit of these complexes (Figure 2.3), and therefore these equidistant distances can be related to an averaging of the N-M bond lengths. Jahn Teller distortions can be a useful tool to determine whether a complex is L.S. or H.S. For example, if **$[Mn^{III}(Py_2ImAm)_3]$** and **$[Co^{III}(Py_2ImAm)_3]\cdot DCM$** are L.S. a Jahn Teller

distortion should not be present as these complexes lack of the required degeneracy. In the other hand if **[Mn^{III}(Py$_2$ImAm)$_3$]** and **[Co^{III}(Py$_2$ImAm)$_3$]·DCM** are H.S. the degeneracy in these complexes would induce a Jahn Teller distortion in these complexes. This Jahn Teller distortion can be observed as a contraction or expansion of one axis (normally along the d_z^2 orbital). Although base on crystallography we cannot conclude if these complexes are either H.S. or L.S., it should be noted that in Chapter 3 the magnetochemistry of these complexes is provided, confirming L.S. configurations for these complexes.

Although numerous molecular similarities exist between the MeCN and DCM solvates (i.e. **[M^{III}(Py$_2$ImAm)$_3$]·MeCN** *vs*. **[M^{III}(Py$_2$ImAm)$_3$]·DCM**), rather significant differences are observed in their respective crystal packing as a result of the role of the solvent within the crystal lattice. For example, the solvent in the acetonitrile complexes **[M^{III}(Py$_2$ImAm)$_3$]·MeCN** simply occupies a void, thus enabling π-π interactions to exist between ligands of neighbouring complexes (Figure 2.4 *left*). In the case of **[M^{III}(Py$_2$ImAm)$_3$]·DCM** complexes, the central nitrogen atom (N3) acts as hydrogen bond acceptor for the DCM molecule (Figure 2.5). Since DCM is located on a C_2 axis, this leads to hydrogen bonds with two independent metal complexes. Another role of DCM in the intermolecular interactions of these complexes is the N6···Cl1 halogen bond,[†] which also involves two independent molecular complexes (Figure 2.5). Due to these solvent-complex interactions, and the position of DCM in the lattice, less complex-to-complex interactions exist, compared to the MeCN solvates. As a result, the only meaningful complex-to-complex interactions in **[M^{III}(Py$_2$ImAm)$_3$]·DCM** are weak C-H···N hydrogen bonds (See Appendix B; Table B.5).

[†] The N6···Cl1 distances are equal to 3.12472(9) Å, 3.09710(6) Å, and 3.0723(2) Å for **[Mn^{III}(Py$_2$ImAm)$_3$]·DCM**, **[Fe^{III}(Py$_2$ImAm)$_3$]·DCM**, and **[Co^{III}(Py$_2$ImAm)$_3$]·DCM** respectively. The C19-Cl1···N6 angles are 163.4518(6)°, 163.2097(4)°, and 163.1290(16)° for **[Mn^{III}(Py$_2$ImAm)$_3$]·DCM**, **[Fe^{III}(Py$_2$ImAm)$_3$]·DCM**, and **[Co^{III}(Py$_2$ImAm)$_3$]·DCM** respectively.

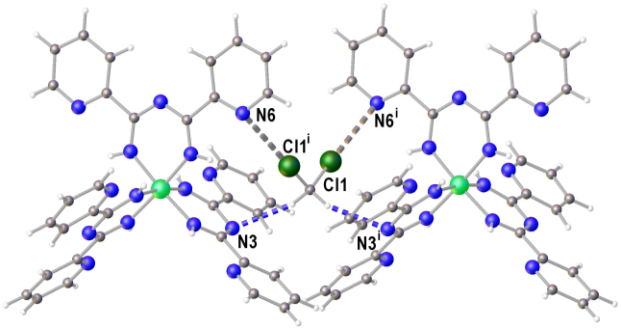

Figure 2.5. Intermolecular interactions of DCM in the crystal lattice of **[Fe^{III}(Py$_2$ImAm)$_3$]·DCM**. Hydrogen bonds are denoted by blue dotted lines; N-Cl halogen contacts are denoted by gray dashed lines; symmetry related positions are labeled with the superscript i.

Table 2.2. Nitrogen to metal distances (Å) in the DCM solvates

Bond	**[Mn^{III}(Py$_2$ImAm)$_3$]·DCM**	**[Fe^{III}(Py$_2$ImAm)$_3$]·DCM**	**[Co^{III}(Py$_2$ImAm)$_3$]·DCM**
N2-M1	1.9495(1)	1.9270(1)	1.8981(1)
N4-M1	1.9428(1)	1.9229(1)	1.9006(2)
N7-M1	1.9592(1)	1.9208(1)	1.9118(1)

2.4 Synthesis and Structural Analysis of Complexes Coordinated to Py$_2$ImAm in a Tridentate Fashion

Starting with the ligand prepared prior to coordination with metal salts provides several advantages over the previously reported methods to develop coordination complexes with Py$_2$ImAm; namely, the ability to vary the solvent choice during the reaction and crystallization process. Such control over the reaction conditions enables numerous variations to the synthetic procedures and facilitates the development of synthetic methodology in which the nuclearity and topology of complexation can be controlled. For example, all previous reports of coordination complexes involving the Py$_2$ImAm ligand consist of a one pot synthesis with a metal salt and the corresponding pyridyl synthon (i.e. tris(2-pyridyl)triazine, 2-cyanopyridine or pyridine-2-amidoxime), thus solvent choice was limited due to solubility and reactivity of the reagent to form Py$_2$ImAm *in situ*. Here, we have the ligand already in hand, which expands the solvent choices available, and consequently enables tailoring of the reaction conditions.

As described above, carrying out the reaction under basic or neutral conditions afforded M^{III} coordination complexes in which the metal ion adopts a distorted octahedral environment bound

to three anionic Py_2ImAm ligands in a bidentate fashion. By changing to acidic conditions, it is possible to access the tridentate coordination pocket of Py_2ImAm. For example, mixing a methanolic solution of *N*-2-pyridylimidoyl-2-pyridylamidine hydrochloride (**2.6a**; $[HPy_2ImAm]Cl$), generated through treatment of Py_2ImAm with $HCl_{(g)}$, to a solution of a metal salt (e.g. $MnCl_2$, $FeCl_3$, $CoCl_2$) in ethanol, afforded the corresponding coordination complexes **[$Mn^{II}(Py_2ImAm)Cl_2$]**, **[$Fe^{III}(Py_2ImAm)Cl_3$]** and **[$Co^{II}(Py_2ImAm)Cl_2$]**, respectively (Scheme 2.2), as single crystals suitable for X-ray analysis (*vide infra*). Thus, by employing the hydrochloride salt of the *N*-imidoylamidine, tridentate coordination may be achieved. This is attributed to the additional proton in $[HPy_2ImAm]Cl$, which is most likely positioned between the two imine nitrogen atoms, thus blocking the bidentate coordination site. Deprotonation of the central nitrogen atom preferentially leads to the imino-amino tautomer, which leaves the tridentate pocket free to coordinate to the metal ion.

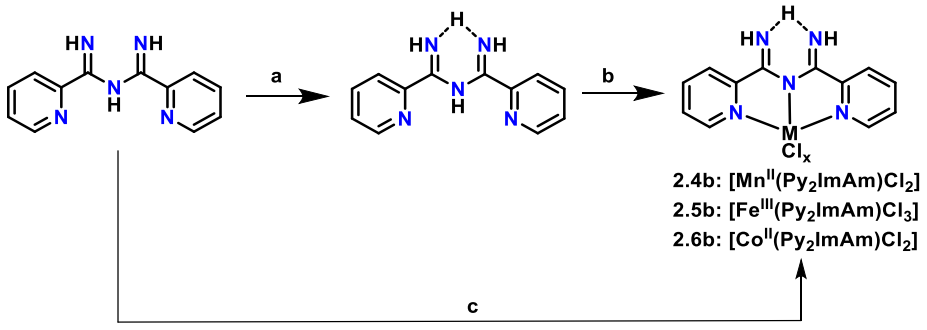

Scheme 2.2. Synthesis of **[$Mn^{II}(Py_2ImAm)Cl_2$]**, **[$Fe^{III}(Py_2ImAm)Cl_3$]** and **[$Co^{II}(Py_2ImAm)Cl_2$]**. *Reagents and conditions:* (a) $HCl_{(g)}$, MeCN, RT; (b) $MnCl_2$, $FeCl_3$ or $CoCl_2$ in EtOH, RT; (c) $[PyH][FeCl_4]$, $[PyH][MnCl_3{\cdot}H_2O]$ or $[PyH]_2[CoCl_4]$ in MeCN or DCM, RT.

Although employing the hydrochloride salt of Py_2ImAm facilitates coordination in a tridentate fashion, the use of $[HPy_2ImAm]Cl$ limits the solvent choice due to its limited solubility. As well, since the tridentate complexes are not very soluble in EtOH, albeit large crystal are obtained but in relatively poor yields (e.g. 25 – 46 %). In order to improve yields, and facilitate variation in reaction conditions, pyridinium metal salts were prepared, enabling the use of acidic conditions with solvents other than ethanol. To that end, MeCN and DCM solutions of pyridinium trichloromanganate(II) monohydrate (**$[PyH]{\cdot}[MnCl_3{\cdot}H_2O]$**),[18] pyridinium tetrachloroferrate(III) (**$[PyH]{\cdot}[FeCl_4]$**)[19] and bis(pyridinium) tetrachlorocobaltate(II) (**$[PyH]_2{\cdot}[CoCl_4]$**)[20] were

combined with Py_2ImAm dissolved in MeCN or DCM, affording pure **[$Mn^{II}(Py_2ImAm)Cl_2$]**, **[$Fe^{III}(Py_2ImAm)Cl_3$]** and **[$Co^{II}(Py_2ImAm)Cl_2$]**, respectively. Due to the insolubility of these coordination complexes in organic solvents, these conditions led to much larger yields (70 – 96%) of a crystalline material with a single phase, as confirmed by PXRD (See Appendix B; Figures B.4-B.6) within 20 minutes.

In contrast to the bidentate materials, the ligand is neutral in the tridentate coordination complexes, and the oxidation state of the metal remains consistent with the starting material – i.e. no oxidation is observed in the reaction with $MnCl_2$ or $CoCl_2$. This may be attributed to the lower oxidation potential of oxygen in acidic media, as well as the speed with which the complexes crystallize out of solution. As such, the key difference between these three pincer-type complexes is the oxidation state of the metal ion, which is +3 for iron and +2 for manganese and cobalt. As a result, the topology is dependent on the oxidation state of the metal. For example, in **[$Fe^{III}(Py_2ImAm)Cl_3$]** a distorted octahedral meridional complex is obtained, which crystallizes in the monoclinic *C*2/c space group (See Appendix B; Table B.4). Since there is a hydrogen atom located between the two imino groups (i.e. N3 and $N3^{i}$) in **[$Fe^{III}(Py_2ImAm)Cl_3$]**, which has half occupancy as the molecule resides on a C_2 axis that runs along the Cl2-Fe1-N2 line (Figure 2.6), the ligand should be neutral. This, coupled with the presence of three chloride ligands, suggests an oxidation state of +3 for the iron centre. ^{1}H NMR spectroscopic studies in DMSO-d_6 further supports this assignment of the hydrogen atom and oxidation state (Figure 2.7). In the solid state, intermolecular N-H···Cl and C-H···Cl interactions exists between neighbouring **[$Fe^{III}(Py_2ImAm)Cl_3$]** molecules (See Appendix B; Table B.5), which pack in a layered-like array along the *b*-plane.

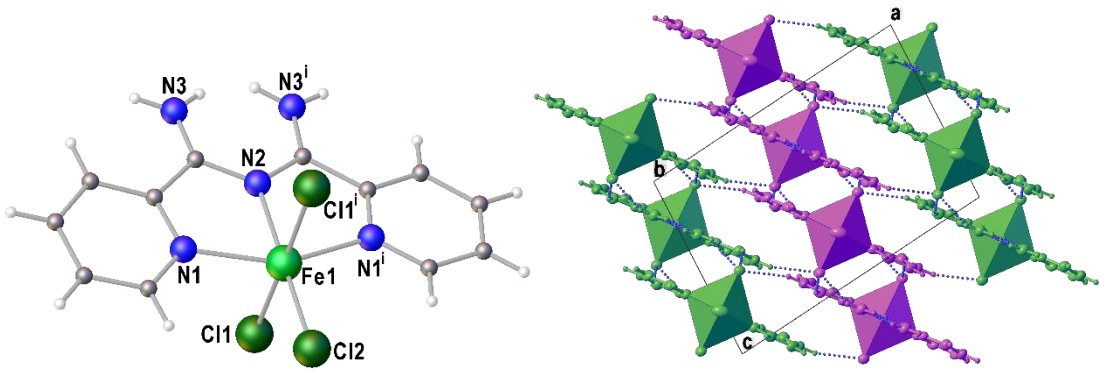

Figure 2.6. Structure diagram of **[Fe^{III}(Py$_2$ImAm)Cl$_3$]** (left) and packing along the 010 plane for **[Fe^{III}(Py$_2$ImAm)Cl$_3$]** (right). Symmetry related positions are labeled with the superscript i and hydrogen bonds are denoted as blue dotted lines.

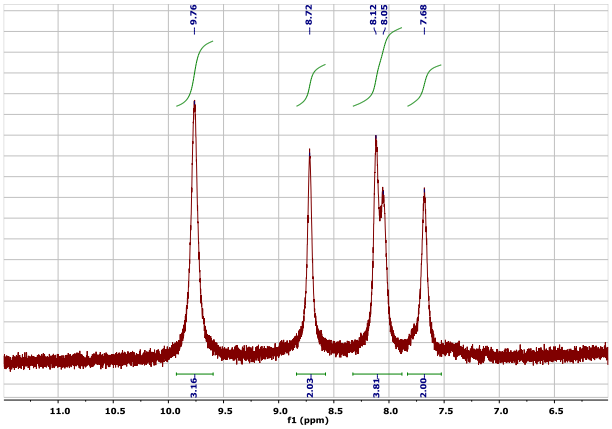

Figure 2.7. Expansion of the aromatic region in the ^{1}H NMR of **[Fe^{III}(Py$_2$ImAm)Cl$_3$]**. Deuterated DMSO was used as solvent.

Complexes **[Mn^{II}(Py$_2$ImAm)Cl$_2$]** and **[Co^{II}(Py$_2$ImAm)Cl$_2$]** are isomorphic, and belong to the monoclinic $P2_1/n$ space group. Similar to **[Fe^{III}(Py$_2$ImAm)Cl$_3$]** both complexes have a neutral ligand, with a hydrogen atom located in a single imino group (i.e. N2; Figure 2.8); however, contrary to the iron tridentate complex, the oxidation state of Mn and Co in **[Mn^{II}(Py$_2$ImAm)Cl$_2$]** and **[Co^{II}(Py$_2$ImAm)Cl$_2$]**, respectively, is +2 based on charge balance (i.e. two chloride ligands and a neutral ligand about each metal centre). Although these isomorphic structures possess very similar lattice parameters (See Appendix B; Table B.4), small differences exist between these complexes, which can be seen in the overlay of the two structures (Figure 2.8). These differences may be attributed to the smaller N-M and Cl-M distances of **[Co^{II}(Py$_2$ImAm)Cl$_2$]** compare to

[Mn^{II}(Py$_2$ImAm)Cl$_2$] (Table 2.3). Nonetheless, the coordination environment about the metal centres are best described as square pyramidal with τ parameters of 0.05 and 0.23 for **[Mn^{II}(Py$_2$ImAm)Cl$_2$]** and **[Co^{II}(Py$_2$ImAm)Cl$_2$]**, respectively.

Table 2.3. Nitrogen to metal and chlorine to metal bond lengths (Å) for **[Mn^{II}(Py$_2$ImAm)Cl$_2$]** and **[Co^{II}(Py$_2$ImAm)Cl$_2$]**

[Mn^{II}(Py$_2$ImAm)Cl$_2$]		[Co^{II}(Py$_2$ImAm)Cl$_2$]	
Mn1-N1	2.243(1)	Co1-N1	2.159(5)
Mn1-N3	2.190(1)	Co1-N3	2.020(5)
Mn1-N5	2.222(1)	Co1-N5	2.116(5)
Mn1-Cl1	2.373(1)	Co1-Cl1	2.302(2)
Mn1-Cl2	2.371(7)	Co1-Cl2	2.314(2)

Because **[Mn^{II}(Py$_2$ImAm)Cl$_2$]** and **[Co^{II}(Py$_2$ImAm)Cl$_2$]** are isomorphic, only the crystal packing for **[Mn^{II}(Py$_2$ImAm)Cl$_2$]** is shown, although the respective distances for both complexes are given. Crystal packing for these complexes is composed of parallel dimers forming chain-like ribbons perpendicular to the 010 plane (Figure 2.9). Each ribbon is held together by the N4-H4A···Cl1 hydrogen bonds (Figure 2.9). Lateral interactions between ribbons are C-H···Cl and N-H···Cl hydrogen bonds (See Appendix B; Table B.5). Weak π-π interactions between the two independent pyridine rings with 3.64 Å and 3.60 Å centroid to centroid distance were observed in **[Mn^{II}(Py$_2$ImAm)Cl$_2$]** and **[Co^{II}(Py$_2$ImAm)Cl$_2$]** respectively.

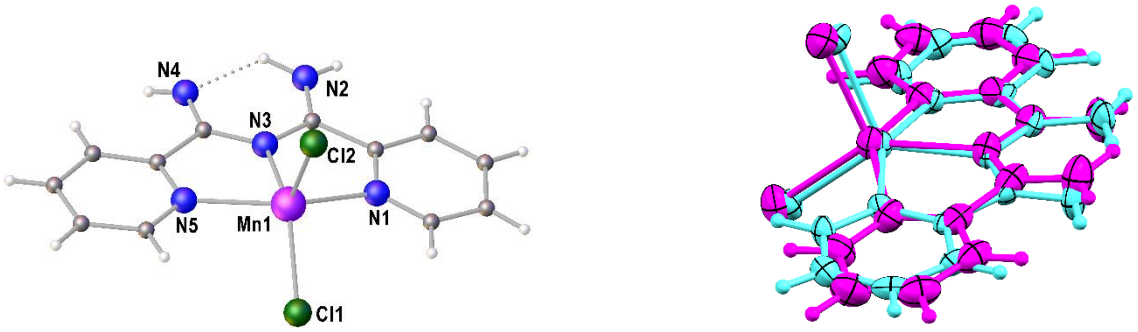

Figure 2.8. Structure diagram of **[Mn^{II}(Py$_2$ImAm)Cl$_2$]** (left), overlay of complexes **[Co^{II}(Py$_2$ImAm)Cl$_2$]** (light blue) and **[Mn^{II}(Py$_2$ImAm)Cl$_2$]** (pink; right). Hydrogen bonds are denoted with gray dotted lines. For the overlay image, root-mean-square deviation is 0.0985.

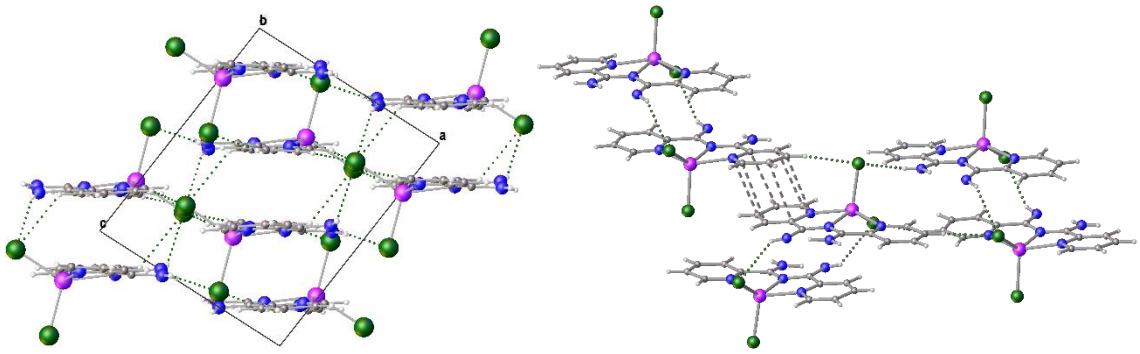

Figure 2.9. Crystal packing view along the 010 plane for **[$Mn^{II}(Py_2ImAm)Cl_2$]** (left), and view of main crystal lattice interactions in **[$Mn^{II}(Py_2ImAm)Cl_2$]** (right). Hydrogen bonds are denoted as green doted bonds, and π-π interactions as a gray dashed line.

2.5 Acid or Base Effect in Shifting Coordination Sites

In addition to selectively coordinating a metal into the bidentate or tridentate pockets of **2.5a**, the possibility of shifting the metal ion from one coordination site to another was also explored. Fortunately for us, the bidentate complexes **[$Fe^{III}(Py_2ImAm)_3$]** and **[$Mn^{III}(Py_2ImAm)_3$]** are very dark coloured, especially when compared to their tridentate analogs **[$Fe^{III}(Py_2ImAm)Cl_3$]** and **[$Mn^{II}(Py_2ImAm)Cl_2$]**, which are pale yellow as can been seen in the crystal photo of these complexes (Figure 2.10). Given this difference in colour, facile probing of the change in coordination can be achieved. The one exception is **[$Co^{III}(Py_2ImAm)_3$]** a yellow solid (Figure 2.10c), which is not radically different to the green complex **[$Co^{II}(Py_2ImAm)Cl_2$]** (Figure 2.10f). The yellow colour observed in **[$Co^{III}(Py_2ImAm)_3$]** can be attributed to the absence of d-d transitions, which are forbidden, because **[$Co^{III}(Py_2ImAm)_3$]** is diamagnetic as shown by NMR (Figure 2.11). The colour of the Py_2ImAm ligand is pale yellow, thus the colour of the crystals in **[$Co^{III}(Py_2ImAm)_3$]** **[$Fe^{III}(Py_2ImAm)Cl_3$]**, **[$Mn^{II}(Py_2ImAm)Cl_2$]**, and **[$Co^{II}(Py_2ImAm)Cl_2$]** can be primarily attributed to the ligand absorption.

In terms of solubility, the bidentate complexes (**2.1b**-**2.3b**) differ compared to their tridentate analogs (**2.4b**-**2.6b**). While the later are very soluble in water, the former are only sparingly soluble in chlorinated solvents such as dichloromethane, dichloroethane, chlorobenzene and chloroform. Interestingly, in the case of manganese and iron complexes the shift of coordination from the tridentate pocket of Py_2ImAm to the bidentate site is possible, and can be done by reacting an

aqueous solution of **[Fe^{III}(Py$_2$ImAm)Cl$_3$]** and **[Mn^{II}(Py$_2$ImAm)Cl$_2$]** with two equivalents of NaOH. A gradual colour change from pale yellow for both complexes, to deep red for **[Fe^{III}(Py$_2$ImAm)Cl$_3$]** and deep violet for **[Mn^{II}(Py$_2$ImAm)Cl$_2$]** was observed. Following the change in colour of the solutions, two main products precipitate from the aqueous solution, the desired bidentate complexes (**2.1b** and **2.2b**) along with Fe(OH)$_3$ or Mn(OH)$_2$, respectively. This latter byproduct of these reactions forms as a result of the non-stochiometric reaction conditions and was identified by IR spectroscopy. The identity of the bidentate complexes **2.1b** and **2.2b** was confirmed by IR, UV-vis, and a unit cell check of the crystals obtained, thereby confirming the shift in coordination from the tridentate to bidentate pocket of Py$_2$ImAm.

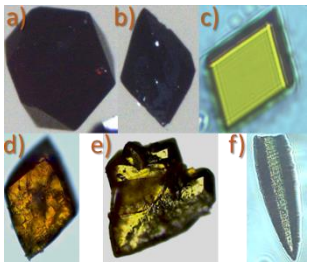

Figure 2.10. A single crystal photo of the complexes: (a) **[Fe^{III}(Py$_2$ImAm)$_3$]**; (b) **[Mn^{III}(Py$_2$ImAm)$_3$]**; (c) **[Co^{III}(Py$_2$ImAm)$_3$]**; (d) **[Fe^{III}(Py$_2$ImAm)Cl$_3$]**; (e) **[Mn^{II}(Py$_2$ImAm)Cl$_2$]**; (f) **[Co^{II}(Py$_2$ImAm)Cl$_2$]**.

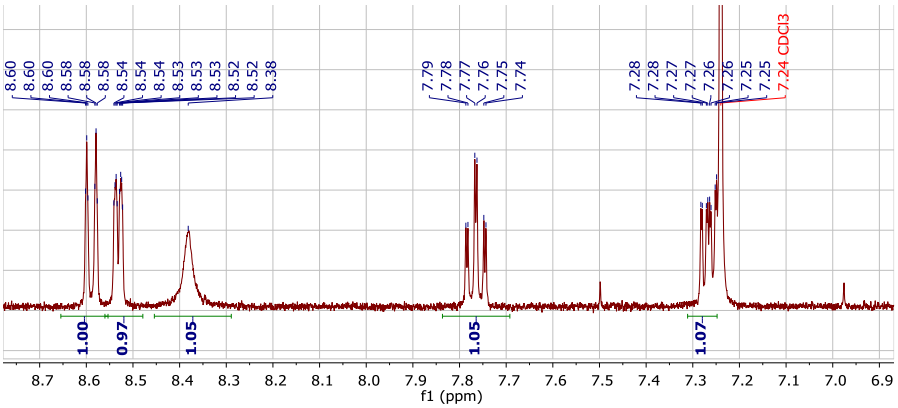

Figure 2.11. Expansion of the aromatic region of the ^{1}H NMR of **[Co^{III}(Py$_2$ImAm)$_3$]**. NMR was prepared in a saturated solution of the complex in CDCl$_3$.

Conversely, the change in coordination of the metal ion from the bidentate to tridentate site after the addition of an acid was more elusive, which may be attributed to the poor solubility of

2.1b and **2.2b** (<1 mg per mL in any chlorinated solvent), preventing the isolation of crystalline solids. Nevertheless, UV-vis studies were conducted on **2.1b** and **2.2b** in an attempt to confirm the shift in coordination geometry. As it can be seen in Figure 2.12, the UV-vis of the complexes **2.1b** and **2.2b** has an absorption band at 611 nm and 578 nm, respectively, and these absorption bands are attributed to the complex since such an absorption is not present in the absorption spectra of neither the metal salt nor the free ligand. After the addition of 10 equivalents of formic acid to a DCM solution of **2.1b** and **2.2b** a change in colour is observed, and these absorption bands at 611 nm and 578 nm disappear (Figure 2.12). The reaction vials for this reaction can be seen in Figure 2.13.

The transition observed in Figure 2.13 upon the addition of an acid to **2.1b** and **2.2b** can be related to protonation of the anionic ligand to afford the neutral ligand; however, it is not possible to conclude whether there is a shift in the coordination geometry of the metal ion or not. This is due to the ability of Py_2ImAm to be protonated while coordinated to the metal ion in a bidentate fashion. This was observed in the complex of **[Pt^{II}(Ph_3ImAm)$_2$]**,[21] discussed earlier in section **1.5.1**. The complex **[Pt^{II}(Ph_3ImAm)$_2$]** has phenyl rings instead pyridyl rings, and protonation of the central nitrogen of the ImAm framework was demonstrated upon treatment with an acid. Following protonation of **[Pt^{II}(Ph_3ImAm)$_2$]**, the metal to ligand charge transfer band (MLCT) was quenched. Likewise to **[Pt^{II}(Ph_3ImAm)$_2$]**, the absorption bands at 611 nm and 578 nm in **2.1b** and **2.2b**, respectively, could be due to a charge transfer process, which would explain the intense colour of the crystals **2.1b** and **2.2b**. These absorption bands in **2.1b** and **2.2b** could be then quenched by protonation of the central nitrogen. Nevertheless, it is safe to conclude that **2.1b** and **2.2b** react with an acid, to make a different complex to the starting material, as shown by UV-vis.

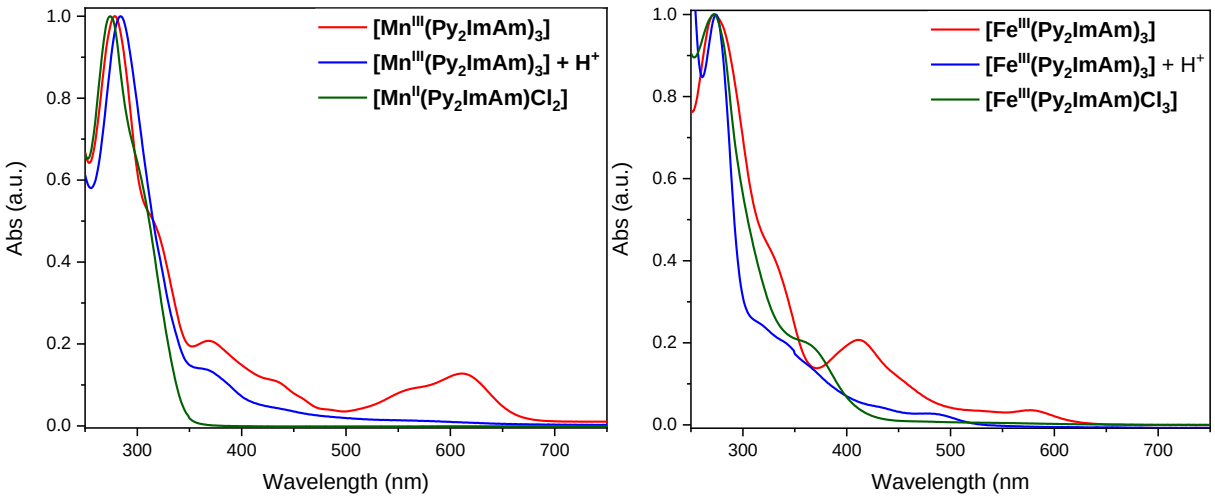

Figure 2.12. UV-vis spectra of **2.1b** and **2.2b** in red, **2.4b** and **2.5b** in green. The blue plots are the samples of **2.1b** and **2.2b** after the addition of formic acid.

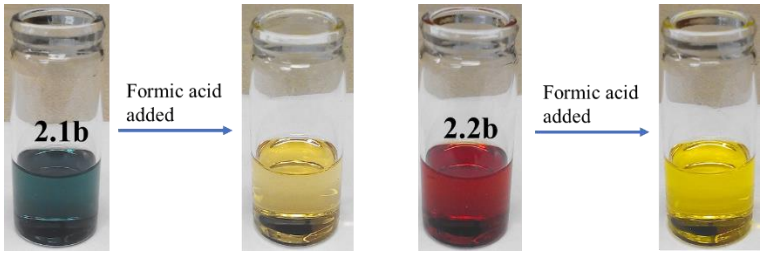

Figure 2.13. View of the reaction of **2.1b** and **2.2b** with formic acid.

2.6. Conclusions

In summary, we have developed the synthetic methodology to control the topology of several coordination complexes employing the Py$_2$ImAm ligand with manganese, iron and cobalt. In particular, we found the presence or absence of a weak acid affects the pathway for metal coordination, leading to complexes in which the metal ion is bound to the bidentate or tridentate site of Py$_2$ImAm, respectively. While octahedral complexes were obtained with or without the presence of a weak base such as triethylamine, the use of a mild acid alters the coordination environment from the bidentate imino side of the Py$_2$ImAm ligand to the tridentate terpy-like coordination pocket. Interestingly, the choice of transition metal or solvent selection does not appear to play a significant role in directing coordination. This is underlined by the set of three isomorphic structures obtained with different metal ions but using very similar synthetic

conditions. Furthermore, in the specific case of the terpy-like complexes, the metal ion can shift to the bidentate pocket of the ligand by adding a base, which suggests that coordination is not only selective, but also reversible under certain conditions.

Having resolved the necessary conditions to coordinate to specific sites in Py_2ImAm, in the following chapters we begun to probe the development of polynuclear complexes, not only with the metals described here, but also exploring other transition metals such as nickel and copper. Furthermore, this strategy was also employed with other *N*-imidoylamidine ligands. Finally, in the following chapters, the magnetochemistry of select mononuclear complexes described here was studied, with the goal to help in the understanding of the spin states of polynuclear complexes employing the imidoylamidine ligand framework.

2.7. Experimental Section

General procedures. All solvents were reagent grade and used without further purification. ^{1}H NMR spectra were recorded in $CDCl_3$ or $(CD_3)_2SO$ on a Bruker Advance 400 MHz spectrometer. IR spectra were recorded on an Agilent Technologies Cary 630 FT-IR spectrometer. A single crystalline phase for the complexes described here was assessed by comparison of the PXRD patterns with predicted patterns from single crystal data, the results of which are included in Appendix.

Synthesis of the pyridinium counter ions:

Synthesis of pyridinium tetrachloroferrate(III) ([PyH]·[FeCl$_4$]). **[PyH]·[FeCl$_4$]** was prepared according to the previously described synthesis of Weiland *et al*.[19] Identity of **[PyH]·[FeCl$_4$]** was confirmed through the unit cell parameters, which are the same as the isomorphic structure with pyridinium tetrachloroaluminate.[22] To the best of our knowledge, single crystal X-ray diffraction of **[PyH]·[FeCl$_4$]** has never been performed. The crystals were pale yellow plates. Unit cell was found to be orthorhombic with the space group *Cmcm* and the lattice parameters at 200 K are a = 9.154(4), b = 8.116(4), c = 14.134(6). IR (cm^{-1}): ν 3257.7 (m), 3185.7 (m), 3134.5 (m), 3078.8 (w), 2964.2 (w), 2865.9 (w), 1850.0 (w)1832.7 (m), 1604.3 (s), 1535.8 (s), 1485.5 (s), 1385.1 (m), 1328.6 (m), 1262.1 (w), 1238.5 (w), 1199.4 (w), 1188.1 (w), 1050.8

(w), 1023.1 (w), 982.2 (w), 862.9 (m), 812.1 (w), 734.9 (s), 666.5 (s). H^1 NMR (400 MHz, ACN-d_3): 7.55-9.81 (brm, 5H), 13.78 (s, 1H). MP. 130 °C.

Synthesis of pyridinium trichloromanganate(II) monohydrate ([PyH]·[$MnCl_3$·H_2O]). **[PyH]·[$MnCl_3$·H_2O]** was prepared according to the previously described synthesis of Richards *et al*.[18] and recrystallized from acetonitrile to afford pink needle-like crystals. The unit cell parameters of the pink needles match those reported by Caputo *et al*.[23] IR (cm^{-1}): *v* 3432.7 (br), 3341.6 (br), 3213.5 (m), 3152.9 (m), 3103.0 (m), 3062.3 (s), 2956.4 (m), 2894.1 (m), 1870.6 (w), 1633.1 (m), 1601.7 (s), 1531.1 (s), 1481.7 (s), 1369.0 (w), 1327.8 (m), 1240.1 (m), 1193.7 (m), 1052.8 (m), 1027.8 (m), 894.5 (m), 471.3 (s), 671.5 (s).

Synthesis of bis(pyridinium) tetrachlorocobaltate (II) ([PyH]$_2$·[$CoCl_4$]). Pyridine (1.33 mL, 16.54 mmol) was added dropwise to a solution of $Co^{II}Cl_2$·$6H_2O$ (1.9699 g, 8.27 mmol) in HCl (1.38 mL, 12M) and methanol (6 mL) cooled in an ice bath. Following the addition of pyridine, the reaction flask was left in the ice bath with stirring for another 30 minutes. After the methanol was removed under reduced pressure, 50 mL of acetonitrile was added to the resulting blue residue. A crystalline blue solid (2.487 g) was obtained upon removal of the acetonitrile under reduced pressure. A final yield of 83.3% was obtained. Unit cell parameters match those reported by Felloni *et al*.[20] IR (cm-1): ν 3209.5 (m), 3149.0 (m), 3101.3 (m), 6067.3 (s), 1632.8 (m), 1601.6 (m), 1523.5 (s), 1478.8 (s), 1365.2 (w), 1324.3 (w), 1048.8 (m), 1026.9 (w), 990.3 (m), 908.6 (m), 889.8 (s), 745.2 (s), 672.9 (s).

General synthesis of tris(*N*-2-pyridylimidoyl-2-pyridylamidinate) metal (III) dichloromethane solvates ([M^{III}(Py_2ImAm)$_3$]·DCM)

An alcoholic solution of the metal salt (0.15 mmol) was layered on top of a DCM (10 mL) solution of Py_2ImAm (99.0 mg, 45 mmol) and triethylamine (1.5 mL, 10.7 mmol) in a sealed reaction flask. After several days block-like crystals of **[M^{III}(Py_2ImAm)$_3$]·DCM** were obtained.

Specific details for [Mn^{III}(Py_2ImAm)$_3$]·DCM. $MnCl_2$·$4H_2O$ was dissolved in 2 mL of ethanol. Yield 48.1%. Black block-like crystals were obtained. IR (cm^{-1}): *v* 3287 (m), 3268 (m), 3051 (m), 2996 (w), 1590 (w), 1573 (m), 1525 (m), 1485 (w), 1468 (m), 1427 (s), 1411 (s), 1262 (m), 1221 (m), 1139 (w), 1056 (m), 997 (m), 904 (w), 831 (w), 801 (m), 781 (m), 744 (s), 709 (s).

Specific details for [$Fe^{III}(Py_2ImAm)_3$]·DCM. $FeCl_3$ was dissolved in 2 mL ethanol. Yield 76.1%. Black block-like crystals were obtained. IR (cm^{-1}): *v* 3287 (m), 3268 (m), 3051 (m), 2996 (w), 1590 (w), 1573 (m), 1525 (m), 1485 (w), 1468 (m), 1427 (s), 1411 (s), 1262 (m), 1221 (m), 1139 (w), 1056 (m), 997 (m), 904 (w), 831 (w), 801 (m), 781 (m), 744 (s), 709 (s).

Specific details for [$Co^{III}(Py_2ImAm)_3$]·DCM. $Co(H_3CCO_2)\cdot 4H_2O$ was dissolved in 5 mL ethanol. Orange block-like crystals were obtained. IR (cm^{-1}): *v* 3305 (m), 3290 (m), 3056 (w), 2999 (w), 1601 (w), 1577 (s), 1552 (s), 1508 (m), 1410 (s), 1292 (w), 1262 (w), 1181 (w), 1138 (w), 1098 (w), 905 (w), 815 (m), 795 (m), 744 (s), 705 (s).

Synthesis of [$Mn^{III}(Py_2ImAm_3)$]·MeCN. A solution of $Mn(OAc)_2\cdot 4H_2O$ (24.5 mg, 0.1 mmol) in 2-methoxyethanol (2 mL) was stirred with a solution consisting of Py_2ImAm (67.5 mg, 2.48 mmol) in MeCN (2 mL). Black block-like crystals were obtained after four days. Yield 29.1 mg (0.04 mmol, 40.0%). IR (cm^{-1}): *v* 3288 (m), 3270 (m), 3050 (m), 2998 (w), 1590 (w), 1574 (m), 1486 (w), 1468 (w), 1426 (s), 1411 (s), 1262 (m), 1221 (m), 1139 (w), 1057 (s), 997 (m), 904 (w), 831 (w), 799 (m), 782 (m), 745 (s), 709 (s).

Synthesis of [$Fe^{III}(Py_2ImAm_3)$]·MeCN. A solution of $FeCl_3$ (134.5 mg, 0.82 mmol) in methanol (8 mL) was layered on top of a solution consisting of Py_2ImAm (560.2 mg, 2.48 mmol) and triethylamine (1 mL) in MeCN (15 mL). Red plate-like crystals were obtained after two months. Yield 341.1 mg (0.468 mmol, 57.1%). IR (cm^{-1}): *v* 3331 (br), 3290 (m), 3269 (m), 3054 (w), 3002 (w), 1575 (m), 1536 (m), 1498 (w), 1470 (w), 1422 (s), 1260 (m), 1222 (m), 1182 (w), 1139 (m), 1098 (w), 1058 (s), 1034 (w), 995 (m), 939 (w), 901 (w), 810 (m), 786 (m), 743 (s), 707 (s).

Synthesis of [$Co^{III}(Py_2ImAm_3)$]·MeCN. The crystals collected of **[$Co^{III}(Py_2ImAm)_3$]·DCM** were covered in a MeCN solution. After two weeks there is solvent exchange in the crystal lattice from DCM to MeCN. IR (cm^{-1}): *v* 3303 (m), 3278 (s), 3055 (m), 3003 (w), 1602 (m), 1578 (s), 1553 (s), 1512 (s), 1476 (s), 1417 (s), 1269 (w), 1261 (m), 1224 (m), 1182 (w), 1138 (m), 1099 (w), 1089 (w), 1058 (s), 1035 (w), 996 (s), 943 (m), 902 (w), 811 (w), 795 (s), 743 (s), 723 (w), 706 (s).

Synthesis of [Mn^{II}(Py_2ImAm)Cl_2]. Route A: A solution of $MnCl_2 \cdot 4H_2O$ (81.0 mg., 4 mmol) in ethanol (4 mL) was combined with a solution of [HPy_2ImAm]Cl (107.1 mg, 0.41 mmol) in ethanol (4 mL). After stirring for 30 min, the resulting reaction was left to stand for several days. After two days, yellow block-like crystals of **[Mn^{II}(Py_2ImAm)Cl_2]** were obtained. Yield 36.8 mg (0.1 mmol, 25.6%). **Route B:** Upon combining a solution of Py_2ImAm (0.5072 g; 2.25 mmol) in MeCN (14 mL) with a hot solution of **[PyH]·[$MnCl_3$]·H_2O**, (0. 5812 g; 2.25 mmol) in methanol (10 mL), a bright yellow precipitate of **[Mn^{II}(Py_2ImAm)Cl_2]** formed, which was filtered, washed with methanol and dried in air. Yield 0.6460 g (1.84 mmol, 73.8%). IR (cm^{-1}): *v* 3277 (s), 3067 (w), 1630 (s), 1594 (s), 1581 (s), 1566 (s), 1492 (m), 1466 (m), 1435 (s), 1356 (s), 1298 (m), 1258 (m), 1201 (m), 1183 (s), 1139 (m), 1111 (w), 1015 (s), 1003 (s), 898 (m), 820 (m), 782 (s), 753 (s), 702 (m), 686 (m).

Synthesis of [Fe^{III}(Py_2ImAm)Cl_3]. Route A: A solution of $FeCl_3$ (21.6 mg, 0.133 mmol) in ethanol (2 mL) was combined with a solution of [HPy_2ImAm]Cl (0.133 mmol, 34.9 mg) in ethanol (2 mL). After stirring for 30 min, the resulting reaction was left to stand for several days. After two days, yellow plate-like crystals of **[Fe^{III}(Py_2ImAm)Cl_3]** were obtained. Yield 24.1 mg (0.062 mmol, 46.6%). **Route B:** A solution of Py_2ImAm (1.5413 g; 6.84 mmol) in DCM (25 mL) was added dropwise to a solution of **[PyH]·[$FeCl_4$]** (1.899 g; 6.84 mmol) in DCM (25 mL). The immediate orange precipitate was filtered, washed with methanol and dried to obtain **[Fe^{III}(Py_2ImAm)Cl_3]** as a pale yellow solid. Yield 1.8641 g (4.81 mmol, 70.3%). ^{1}H NMR (δ, $(CD_3)_2SO$, 400 MHz): 9.76 (s, 3H), 8.72 (s, 2H), 8.12 (brm, 4H), 7.68 (s, 2H). IR (cm^{-1}): *v* 3271(s), 3062 (w), 3021 (w), 2021 (w), 1630 (s), 1602 (s), 1590 (s), 1570 (w), 1501(m),1478 (m), 1433 (s), 1353 (s), 1300 (m), 1299 (m), 1262 (m), 1200 (m), 1182 (w), 1171 (w), 1136 (m), 1097 (m), 1058 (m), 1027 (s), 1110 (s), 904 (m), 867 (s), 830 (m), 802 (s), 752 (s), 703 (m).

Synthesis of [Co^{II}(Py_2ImAm)Cl_2]. Route A: A solution of $CoCl_2 \cdot 6H_2O$ (96.9 mg, 0.407 mmol) in ethanol (4 mL) was combined with a solution of [HPy_2ImAm]Cl (106.6 mg, 0.407 mmol) in ethanol (4 mL). Small green plate-like crystals of **[Co^{II}(Py_2ImAm)Cl_2]** began to grow within minutes. Yield 52.8 mg (0.14 mmol, 36.5%). **Route B:** A solution of Py_2ImAm (0.4747 g; 2.10 mmol) in MeCN (22 mL) was added to a solution of **[PyH]$_2$·[$CoCl_4$]** (0.7668 g; 2.12 mmol) in MeCN (22 mL). The solution was stirred for 20 minutes, producing **[Co^{II}(Py_2ImAm)Cl_2]** as a green precipitate. The solid was filtered, washed with DCM followed by isopropanol and dried in

air. Yield 0.7197g (2.02 mmol, 96.1%). ^{1}H NMR (δ, $(CD_3)_2SO$, 400 MHz): 9.74, 8.70, 8.11, 7.68. IR (cm^{-1}): *v* 3260 (m), 1635 (s), 1586 (s), 1567 (m), 1493 (m), 1467 (w), 1438 (s), 1359 (s), 1294 (m), 1260 (m), 1200 (m), 1183 (m), 1038 (m), 1048 (w), 1024 (s), 1009 (s), 902 (m), 822 (w), 784 (s), 754 (s), 704 (m), 684 (w).

X-ray crystallography. Data collection for the single crystals studied here (See Appendix B; Table B.1-B.4) was obtained on Bruker SMART APEX-II CCD diffractometer (graphite monochromated Mo K_α radiation, λ = 0.71073 Å, ω-scans with a 0.5° step in ω) at 200 K. Absorption corrections were applied by using the semiempirical method of the SADABS program[24] for all samples reported. The structures were solved by SHELXT[25] and refined by full-matrix least-squares methods on F^2 with SHELXL-2015[26] in anisotropic approximation for all non-hydrogen atoms. Hydrogens atoms on the pyridine and pyrimidine rings were constrained to ride on their parent atoms with C—H = 0.95 A˚ and U_{iso} = 1.2U_{eq}(C), while imino N—H hydrogens were refined isotropically for all complexes. SADI restrain was used to associate the N-H distances with a 0.02 standard deviation in the data sets of **[Fe^{III}(Py$_2$ImAm)Cl$_3$]** and **[Mn^{III}(Py$_2$ImAm)$_3$]·DCM**. DIFIX was applied in the complex **[Co^{II}(Py$_2$ImAm)Cl$_2$]** to restrain the N-H distances to 0.88 Å using 0.02 as standard deviation. In the rest of the complexes the position of the imino hydrogen was freely refined.

Powder X-ray diffraction (PXRD) was performed on a Rigaku Ultima IV diffractometer, with Cu K_α monochromatic radiation (λ = 1.54056 Å) and θ–2θ geometry. The lattice parameters and space group obtained from single crystal were used as a starting point to do a Pawley fit of each complex in order to verify a single crystalline phase present (See Appendix C; Figures C.1-C.6). Very minor deviations from the lattice parameters from PXRD comparing to the lattice parameters of single crystal were observed.

2.8 References

[1] Winter, A.; Newkome, G. R.; Schubert, U. S., *ChemCatChem* **2011,** 3, (9), 1384-1406.

[2] Eryazici, I.; Moorefield, C. N.; Newkome, G. R., *Chem. Rev.* **2008,** 108, (6), 1834-1895.

[3] Porras, J. A.; Mills, I. N.; Transue, W. J.; Bernhard, S., *J. Am. Chem. Soc.* **2016,** 138, (30), 9460-9472.

[4] Pedersen, K. S.; Bendix, J.; Clérac, R., *ChemComm* **2014,** 50, (34), 4396-4415.

[5] Seo, K.; Konchenko, A. V.; Lee, J.; Bang, G. S.; Lee, H., *J. Am. Chem. Soc.* **2008,** 130, (8), 2553-2559.

[6] Leitch, A. A.; Korobkov, I.; Assoud, A.; Brusso, J. L., *ChemComm* **2014,** 50, (38), 4934-4936.

[7] Kanady, J. S.; Tsui, E. Y.; Day, M. W.; Agapie, T., *Science* **2011,** 333, (6043), 733.

[8] Hernández Sánchez, R.; Zheng, S.-L.; Betley, T. A., *J. Am. Chem. Soc.* **2015,** 137, (34), 11126-11143.

[9] Lee, Y.; Sloane, F. T.; Blondin, G.; Abboud, K. A.; García-Serres, R.; Murray, L. J., *Angew. Chem. Int. Ed.* **2015,** 54, (5), 1499-1503.

[10] Steel, P. J., *Acc. Chem. Res.* **2005,** 38, (4), 243-250.

[11] Dul, M.-C.; Pardo, E.; Lescouëzec, R.; Journaux, Y.; Ferrando-Soria, J.; Ruiz-García, R.; Cano, J.; Julve, M.; Lloret, F.; Cangussu, D.; Pereira, C. L. M.; Stumpf, H. O.; Pasán, J.; Ruiz-Pérez, C., *Coord. Chem. Rev.* **2010,** 254, (19), 2281-2296.

[12] Manoli, M.; Inglis, R.; Manos, M. J.; Nastopoulos, V.; Wernsdorfer, W.; Brechin, E. K.; Tasiopoulos, A. J., *Angew. Chem. Int. Ed.* **2011,** 50, (19), 4441-4444.

[13] Furukawa, S.; Reboul, J.; Diring, S.; Sumida, K.; Kitagawa, S., *Chem. Soc. Rev.* **2014,** 43, (16), 5700-5734.

[14] Kajiwara, T.; Kamiyama, A.; Ito, T., *ChemComm* **2002**, (12), 1256-1257.

[15] Kopylovich, M. N.; Lasri, J.; Guedes da Silva, M. F. C.; Pombeiro, A. J. L., *Dalton Trans.* **2009**, (16), 3074-3084.

[16] Duros, V.; Sartzi, H.; Teat, S. J.; Sanakis, Y.; Roubeau, O.; Perlepes, S. P., *Inorg. Chem. Commun.* **2014,** 50, 117-121.

[17] Bohu, T.; Santelli, C. M.; Akob, D. M.; Neu, T. R.; Ciobota, V.; Rösch, P.; Popp, J.; Nietzsche, S.; Küsel, K., *Front. Microbiol.* **2015,** 6, 734.

[18] Richards, P. M.; Quinn, R. K.; Morosin, B., *J. Chem. Phys.* **1973,** 59, (8), 4474-4477.

[19] Weinland, R. F.; Kissling, A., *Z. Anorg. Allg. Chem.* **1921,** 120, (1), 209-231.

[20] Felloni, M.; Hubberstey, P.; Wilson, C.; Schroder, M., *CrystEngComm* **2004,** 6, (19), 87-95.

[21] Sarova, G. H.; Bokach, N. A.; Fedorov, A. A.; Berberan-Santos, M. N.; Kukushkin, V. Y.; Haukka, M.; Fraústo da Silva, J. J. R.; Pombeiro, A. J. L., *Dalton Trans.* **2006**, (31), 3798-3805.

[22] Zaworotko, M. J.; Cameron, T. S.; Linden, A.; Sturge, K. C., *Acta Crystallogr., Sect. C: Cryst. Struct. Commun.* **1989,** C45, (7), 996-1002.

[23] Caputo, R.; Willett, R. D.; Morosin, B., *J. Chem. Phys* **1978,** 69, (11), 4976-4983.

[24] Sheldrick, G. M. *SADABS*, V.2.0.3, Bruker/Siemens area detector absorption correction program; Bruker AXS: Madison, WI, 2003.

[25] Sheldrick, G., *Acta Cryst. A* **2015,** 71, (1), 3-8.

[26] Linden, A., *Acta Crystallogr. Sect. C* **2015,** 71, (1), 1-2.

Chapter 3

Rational Design of Tetranuclear Complexes Employing *N*-imidoylamidine Based Ligands

Authorship disclosure: A version of this chapter was published in *European Journal of Inorganic Chemistry* as "Rational design of tetranuclear complexes employing N-imidoylamidine based ligands" R. Castañeda, K. L. M. Harriman, J. W. L. Wong, B. Gabidullin, M. Murugesu, J. L. Brusso, *European Journal of Inorganic Chemistry* **2019**, 963-972. The synthesis of all compounds was performed by Luis Raúl Castañeda Perea. The measurement and fit of the magnetic data was performed by Katie Lois Marie Harriman and Dr. Muralee Murugesu. The Mössbauer spectrum was collected and fitted by Joanne Wong. All crystallography was collected and refined by Luis Raúl Castañeda Perea.

3.1 Introduction

Ligand design and the development of polynuclear complexes holds great appeal for a variety of applications, due in large part to the properties afforded to polynuclear complexes. For example, they have the capacity for stepwise multielectron redox chemistry,[1-3] or one can access tunable electronic, magnetic or photophysical properties.[4, 5] Nature exploits these desirable attributes tremendously by employing polynuclear cofactors to effect small molecule activation in enzymatic processes (e.g. photosystem II, nitrogenase).[6] From a materials perspective, the development of coordination polymers relies on polynuclear complexation, and, although not necessary, polynuclear complexes have proven to be highly desirable in the design of molecular magnets.[5]

From a synthetic point of view, the formation of many polynuclear complexes often relies on serendipitous reaction pathways,[7] which can lead to unexpected or unpredictable materials. As such, the design and synthesis of polydentate ligands in which nuclearity and topology can be controlled provides an avenue towards achieving tailor-made polynuclear homo and heterometallic complexes, polymers and networks. In that regard, *N*-imidoylamidines such as *N*-2-pyridylimidoyl-2-pyridylamidine (**3.1a**; Py_2ImAm; Chart 3.1) and *N*-2-pyrimidylimidoyl-2-pyrimidylamidine (**3.2a**; Pm_2ImAm; Chart 3.1) are particularly attractive due to the presence of two distinct coordination environments within a single rigid ligand framework. Accessing and controlling coordination to the bidentate and/or tridentate sites within Py_2ImAm or Pm_2ImAm would facilitate the development of a variety of metal complexes. Although *N*-imidoylamidines

are ideal for the development of polynuclear complexes, few examples exist in literature.[8-12] This is due in large part to the generation of these ligands, which until recently were only prepared in one pot synthetic procedures through metal-assisted transformations. In other words, Py_2ImAm and Pm_2ImAm were prepared using a metal salt and a pyridyl or pyrimidyl synthon. For example, a copper coordination polymer or dimer can be isolated following decomposition of either tris(2-pyridyl)triazine[11] (**3.3a**) or tris(2-pyrimidyl)triazine (**3.4a**),[12] respectively, in the presence of copper (II) salts. In both copper complexes, the *N*-imidoylamidine ligand acts to ferromagnetically couple the adjoining Cu^{II} ions, which alternate between different coordination environments. Alternatively, the Py_2ImAm ligand has also been reported through the *in situ* reaction between 2-cyanopyridine and butan-2-on oxime with $PdCl_2$ to make a palladium(II) square planar complex,[9] or pyridine-2-amidoxime with MnF_2 resulting in a manganese(III) octahedral complex.[8] Since these reports all consisted of one pot synthesis involving metal-assisted transformations, their formation relied on serendipitous reaction pathways. As such, the nuclearity and topology were difficult to control.

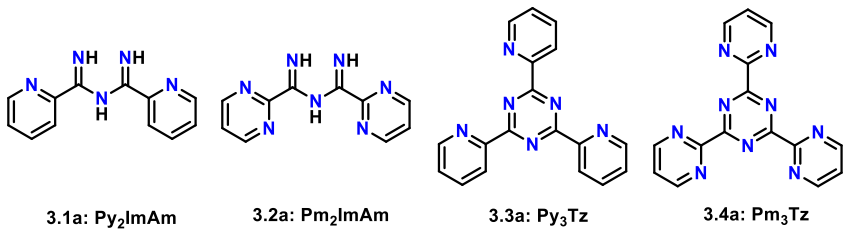

Chart 3.1. Structure of Py_2ImAm**,** Pm_2ImAm, Py_3Tz, and Pm_3Tz.

As described in the introductory chapter, our group recently reported the synthesis of both Py_2ImAm[13] and Pm_2ImAm,[14] which enables tailoring of the reaction conditions such that selective coordination in a bidentate and/or tridentate fashion can be achieved. To that end, in the second chapter we have also developed the synthetic methodology to control the topology of several coordination complexes employing the Py_2ImAm ligand with first row transition metal ions (e.g. Mn, Fe, Co). In particular, coordination complexes in which the metal ion adopts a distorted octahedral environment bound to three anionic Py_2ImAm ligands in a bidentate fashion can be achieved when the reactions are carried out under basic or neutral conditions. By changing to acidic conditions, it is possible to access the tridentate coordination pocket of Py_2ImAm. In the second chapter it was also demonstrated that the key factor in controlling the coordination site is the

presence (or absence) of a weak acid. Having resolved the necessary conditions to coordinate to specific sites in Py_2ImAm, we can now begin to probe the versatility of this ligand framework in the development of polynuclear complexes, not only with Py_2ImAm, but also exploring other *N*-imidoylamidine ligands (e.g. Pm_2ImAm).

To that end, presented herein are the synthesis, structural analysis and magnetic characterization of two tetranuclear complexes employing the Pm_2ImAm ligand with manganese and iron. To help elucidate the electronic structure of the polynuclear complexes, the structural and magnetic properties of mononuclear species, which represent molecular moieties within the polynuclear complexes, are also described. Due to the similarities between the tetranuclear complexes and their mononuclear components, we can take advantage of these features to gain a better understanding of the magnetic interactions within these materials. These results reveal a unique combination of spin states within the complex, namely a low spin M^{III} central ion and high spin metal ions (M^{II} or M^{III}) at the periphery.

3.2 Synthesis and Structural Analysis of $[Mn^{II}_2(\mu\text{-}Cl)_2(Pm_2ImAm)_2Cl_2]$

As shown in the second chapter, the coordination environment of first row transition metals in either a bidentate or tridentate fashion with Py_2ImAm can be controlled by tailoring the reaction conditions. Following a similar procedure, coordination to the tridentate pocket of the pyrimidyl analogue Pm_2ImAm can also be achieved. Here, a methanolic (MeOH) solution of pyridinium trichloromanganate(II) monohydrate (**$[PyH][Mn^{II}Cl_3H_2O]$**), was combined with a solution of Pm_2ImAm in acetonitrile (MeCN; Scheme 3.1). After leaving the resulting solution to stand overnight, crystals suitable for X-ray analysis were obtained confirming the identity of **$[Mn^{II}_2(\mu\text{-}Cl)_2(Pm_2ImAm)_2Cl_2]$** (**3.1b**). In this complex, which crystallizes in the triclinic space group *P*-1, the asymmetric unit contains one Mn^{II} ion coordinated in *mer*-fashion to a neutral Pm_2ImAm ligand (Figure 3.1). The asymmetric unit is completed with two chloride ions, one of which is bridging to a second Mn^{II} ion (e.g. Mn1'). As such, the metal ions adopt a six-coordinate arrangement with two μ-Cl^- anions between the two metal centres resulting in geometries that are best described as distorted octahedron, as determined using the SHAPE[15] software (Figure 3.1 and Table 3.1). Interestingly, when the pyrimidyl ligand is employed a dimeric complex with bridging chloride ions is isolated, contrary to a mononuclear complex that was obtained with Py_2ImAm in

the second chapter (i.e. **[Mn^{II}(Py$_2$ImAm)Cl$_2$]**); however, similar to the pyridyl analogue, the Mn^{II} ions coordinate exclusively in a tridentate fashion to Pm$_2$ImAm under acidic conditions. As well, the *N*-imidoylamidine ligand in **[Mn$^{II}_2$(μ-Cl)$_2$(Pm$_2$ImAm)$_2$Cl$_2$]** is neutral, since there is a hydrogen atom located at the imino nitrogen atom N5, which was refined isotropically without any constraints. Thus, based on charge balance the oxidation state of the manganese ions are +2 (i.e. two chloride ligands and a neutral Pm$_2$ImAm ligand about each metal centre), which is consistent with the previously reported analogue.

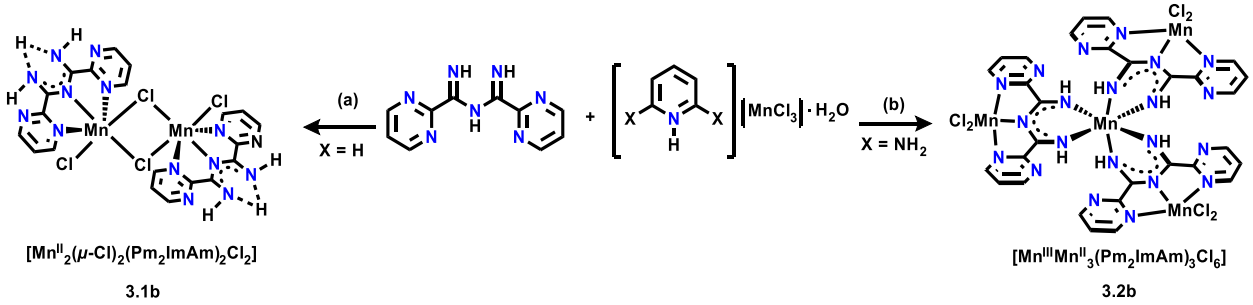

Scheme 3.1. Synthesis of complexes **[Mn$^{II}_2$(μ-Cl)$_2$(Pm$_2$ImAm)$_2$Cl$_2$]** and **[Mn^{III}Mn$^{II}_3$(Pm$_2$ImAm)$_3$Cl$_6$]** employing the **Pm$_2$ImAm** ligand. Reagents and conditions: (a) X = H, MeOH/MeCN; (b) X = NH$_2$ MeOH/MeCN.

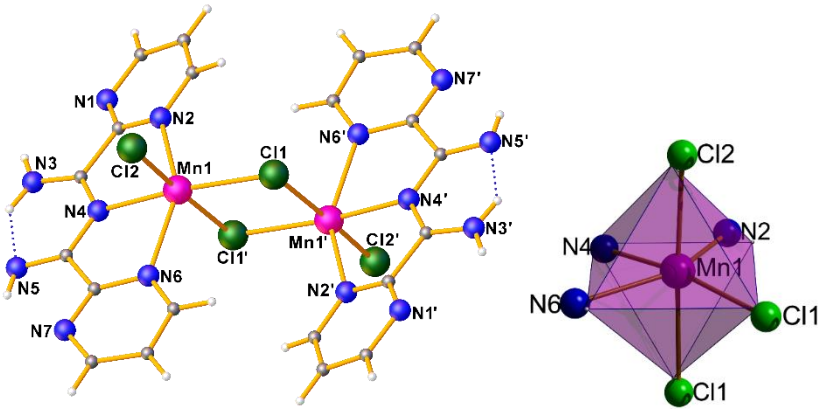

Figure 3.1. Structural diagram of **[Mn$^{II}_2$(μ-Cl)$_2$(Pm$_2$ImAm)$_2$Cl$_2$]** on the left, and Shape analysis of this complex on the right.

Table 3.1. Results from Shape analysis for octahedral environment

Structure ML_6	Metal Centre	HP-6	PPY-6	OC-6	TPR-6	JPPY-6
$[Mn^{II}_2(\mu\text{-}Cl)_2(Pm_2ImAm)_2Cl_2]$	**Mn1**	33.0213	21.9051	3.0496	13.1415	25.1129
$[Mn^{III}Mn^{II}_3(Pm_2ImAm)_3Cl_6]$	**Mn1**	32.2971	26.6744	0.4319	12.8321	30.1063
$[Fe^{III}(Pm_2ImAm)Cl_3]$	**Fe1**	34.0579	25.1044	1.7171	14.6982	28.3952
$[Fe^{III}_4(Pm_2ImAm)_3Cl_9]$	**Fe1**	32.3181	28.8192	0.0521	15.4895	32.2957
	Fe2	33.4483	23.0784	1.9465	12.0613	26.5821
	Fe3	33.8745	24.5474	1.7518	14.1244	27.9600

HP-6: D_{6h}, Hexagon; PPY-6: C_{5v}, Pentagonal pyramid; OC-6: *Oh*, Octahedron; TPR-6: D_{3h}, Trigonal prism; JPPY-6: C_{5v}, Johnson pentagonal pyramid J2

3.3 Role of a Less Acidic Counter Ion to Synthesize $[Mn^{III}Mn^{II}_3(Pm_2ImAm)_3Cl_6]$

Interestingly, by changing to a less acidic counter ion, polynuclear complexes can be isolated. For example, reacting a solution of 2,6-diaminopyridinium trichloromanganate(II) monohydrate (**$[(NH_2)_2PyH][Mn^{II}Cl_3{\cdot}H_2O]$**) in MeOH with a MeCN solution of Pm_2ImAm affords the tetranuclear complex **$[Mn^{III}Mn^{II}_3(Pm_2ImAm)_3Cl_6]$** (**3.2b**), as confirmed through single crystal X-ray analysis (Figure 3.2). This difference in reactivity may be attributed to a change in the speed with which the product precipitates out of solution. For example, by employing a less acidic counter ion such as the diaminopyridinium salt, the rate of precipitation is supressed, thereby enabling oxidation of the central manganese and crystallization of the tetranuclear complex **$[Mn^{III}Mn^{II}_3(Pm_2ImAm)_3Cl_6]$**. When the more acidic pyridinium counter ion is used, the dinuclear complex **$[Mn_2(\mu\text{-}Cl)_2(Pm_2ImAm)_2Cl_2]$** quickly precipitates from the reaction mixture, thereby inhibiting the formation of the tetranuclear complex. In **$[Mn^{III}Mn^{II}_3(Pm_2ImAm)_3Cl_6]$**, which crystallizes in the monoclinic *C2/c* space group, each ligand is anionic and coordinates to two Mn ions resulting in two distinct Mn moieties – one coordinated in a bidentate fashion, the other in the tridentate pocket of the ligand. The central Mn ion, which is bound to three anionic Pm_2ImAm ligands in a bidentate fashion, adopts a nearly ideal octahedral environment (Figure 3.3) that is very similar to that of the mononuclear complex **$[Mn^{III}(Py_2ImAm)_3]$** reported in the second chapter, as highlighted in the overlay of the two structures (Figure 3.4). Comparing the Mn–N distances of the central metal in **$[Mn^{III}Mn^{II}_3(Pm_2ImAm)_3Cl_6]$** to those of **$[Mn^{III}(Py_2ImAm)_3]$** reveal a slight elongation of these bond lengths upon development of the polynuclear complex (e.g. 1.94227(4) – 1.95932(3) Å for **$[Mn^{III}(Py_2ImAm)_3]$**; 1.954(4) – 1.969(5) for

[$Mn^{III}Mn^{II}_3(Pm_2ImAm)_3Cl_6$]). This minimal elongation of the Mn–N distances suggests the metal ion remains in the same oxidation state for both complexes (i.e. +3). Moreover, the absence of a Jahn-Teller elongation in these complexes indicates that the Mn^{III} adopts a rare low spin configuration, which is further supported by magnetic measurements (*vide infra*).

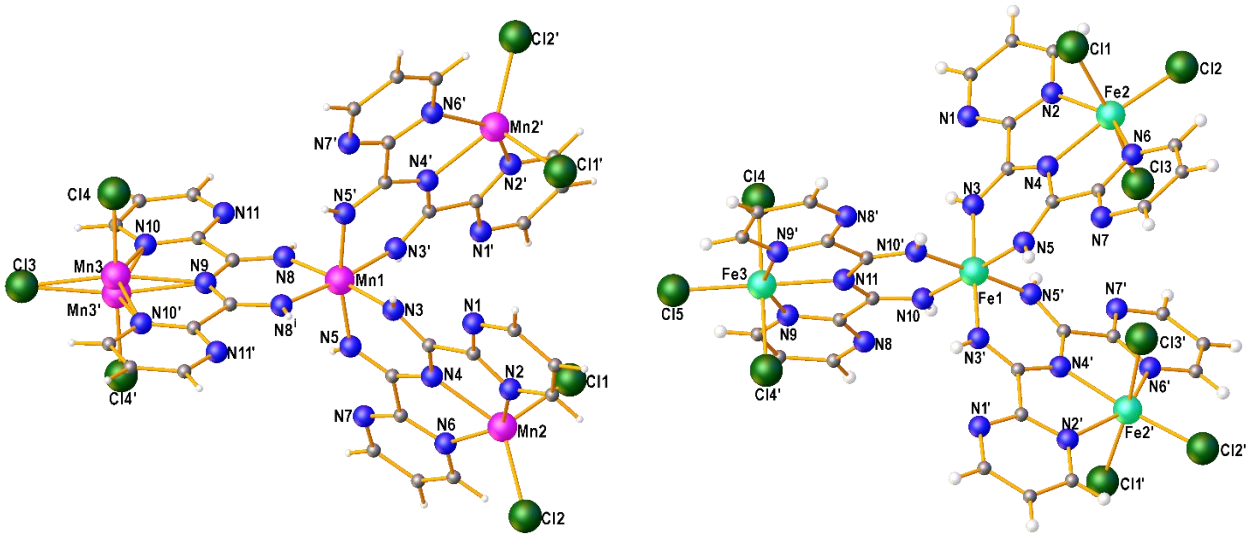

Figure 3.2. Structural diagram of **[$Mn^{III}Mn^{II}_3(Pm_2ImAm)_3Cl_6$]** (left) and **$Fe^{III}_4(Pm_2ImAm)_3Cl_9$]** (right).

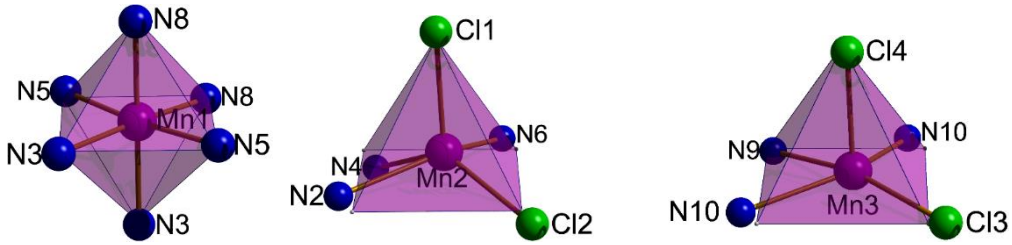

Figure 3.3. Deviation from ideal octahedron or square pyramidal environment about the manganese atoms of **[$Mn^{III}Mn^{II}_3(Pm_2ImAm)_3Cl_6$]** complex.

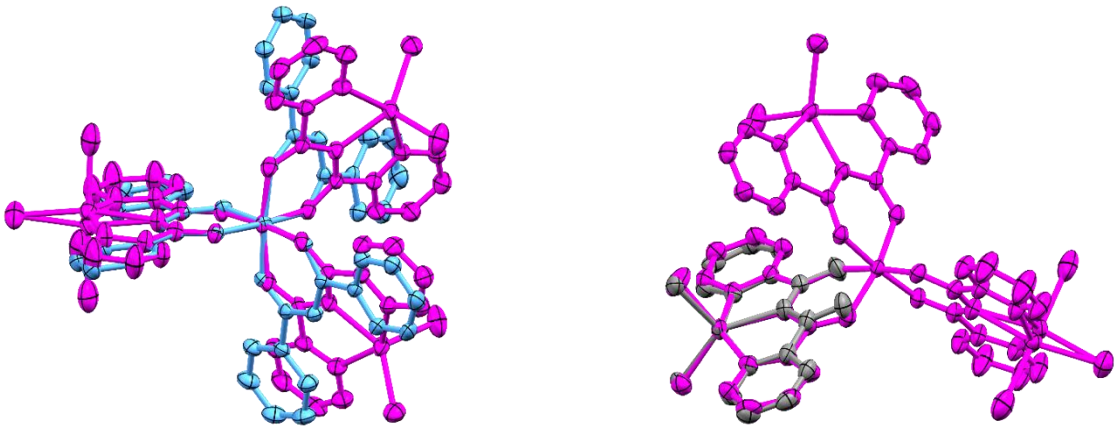

Figure 3.4. Structural overlay of mononuclear **[$Mn^{III}(Py_2ImAm)_3$]** (blue) with tetranuclear **[$Mn^{III}Mn^{II}_3(Pm_2ImAm)_3Cl_6$]** (magenta) on the left and mononuclear **[$Mn^{II}(Py_2ImAm)Cl_2$]** (gray) with **[$Mn^{III}Mn^{II}_3(Pm_2ImAm)_3Cl_6$]** (magenta) on the right. Hydrogen atoms have been omitted for clarity.

The asymmetric unit of **[$Mn^{III}Mn^{II}_3(Pm_2ImAm)_3Cl_6$]** contains three crystallographically independent metal ions, resulting from the complex sitting on a C_2 axis. The outer metal ions (Mn2 and Mn3) are pentacoordinate with the metal ion residing within the plane of the tridentate Pm_2ImAm ligand. The remaining metal coordination environment is filled by two Cl anions above and below the plane of the ligand framework, leading to a coordination geometry that is best described as square pyramidal rather than trigonal bipyramidal (Figure 3.3 and Table 3.2). Although similar, the geometries of Mn2 and Mn3 differ slightly. In the case of Mn2, since it is located in a general position, it is reproduced by symmetry (e.g. Mn2'). In the second chapter it was discussed the tridentate mononuclear complex **[$Mn^{II}(Py_2ImAm)Cl_2$]**, which has the same coordination environment as Mn2, as highlighted in the overlay of both structures shown in Figure 3.4. On the other hand, Mn3 is unique and located on the C_2 axis. As such, the coordination environment of Mn3 is dissimilar to the previously reported complex, which results in a chloride ion (Cl4) being disordered over two symmetry equivalent positions around the C_2 axis. The coordination environment about the Mn3 is therefore closer to square pyramidal than Mn2 (Figure 3.3).

Table 3.2. Results from shape analysis and *tau* parameters for the pentacoordinate environment.

Structure ML_5	Metal Centre	PP-5	vOC-5	TBPY-5	SPY-5	JTBPY-5	τ
$[Mn^{III}Mn^{II}_3(Pm_2ImAm)_3Cl_6]$	**Mn2**	31.0900	5.1798	3.9712	2.6451	7.7897	0.14
	Mn3	29.0025	3.0990	7.5800	2.9694	9.0626	0.40

PP-5: D_{5h}, Pentagon; vOC-5: C_{4v}, Vacant octahedron; TBPY-5: D_{3h}, Trigonal bipyramidal; SPY-5: C_{4v}, Square pyramidal; JTBPY-5: D_{3h}, Johnson trigonal bipyramid J12

3.4 Synthesis and Structural Analysis of $[Fe^{III}(Pm_2ImAm)Cl_3]$

Mononuclear **$[Fe^{III}(Pm_2ImAm)Cl_3]$** (**3.3b**) was synthesized using the same approach as its pyridyl analogue **$[Fe^{III}(Py_2ImAm)Cl_3]$** discussed in the second chapter, by reacting a DCM solution of Pm_2ImAm with a DCM solution of pyridinium tetrachloroferrate(III) (**[PyH][FeCl₄]**), as outlined in Scheme 3.2. Here, the acidic environment achieved through the use of **[PyH][FeCl₄]** affords **$[Fe^{III}(Pm_2ImAm)Cl_3]$**, as confirmed through single crystal X-ray analysis (Figure 3.5). In **$[Fe^{III}(Py_2ImAm)Cl_3]$**, which crystallizes in the monoclinic *P2/c* space group (See Appendix B; Table B.6), the metal ion adopts a distorted octahedral topology (Figure 3.5) with the Pm_2ImAm ligand coordinated in *mer*-fashion. The hydrogen atom located between the two imino groups (i.e. N3 and N3') in **$[Fe^{III}(Pm_2ImAm)Cl_3]$** has half occupancy, as the molecule resides on a C_2 axis that runs along the Cl2-Fe1-N2 line (Figure 3.5a). The ligand is therefore neutral, suggesting an oxidation state of +3 for the iron centre due to the presence of the three chloride ligands. This oxidation state is further supported by the Fe–N distances that are very similar to the pyridyl analogue **$[Fe^{III}(Py_2ImAm)Cl_3]$** discussed in the second chapter (Table 3.3), along with magnetic analysis (*vide infra*). An overlay of the molecular structures of **$[Fe^{III}(Py_2ImAm)Cl_3]$** and **$[Fe^{III}(Pm_2ImAm)Cl_3]$** illustrates the minimal differences between these structures (Figure 3.5b).

Table 3.3. Comparison of metal distances in **$[Fe^{III}(Py_2ImAm)Cl_3]$** and **$[Fe^{III}(Pm_2ImAm)Cl_3]$**. Both molecules reside in a C_2 axis.

$[Fe^{III}(Py_2ImAm)Cl_3]$		**$[Fe^{III}(Pm_2ImAm)Cl_3]$**	
Atoms	Distance (Å)	Atoms	Distance (Å)
Fe1-N1	2.119(4)	Fe1-N2	2.132(2)
Fe1-N2	2.096(5)	Fe1-N4	2.132(3)
Fe1-Cl1	2.403(1)	Fe1-Cl1	2.372(1)
Fe1-Cl2	2.240(2)	Fe1-Cl2	2.246(1)

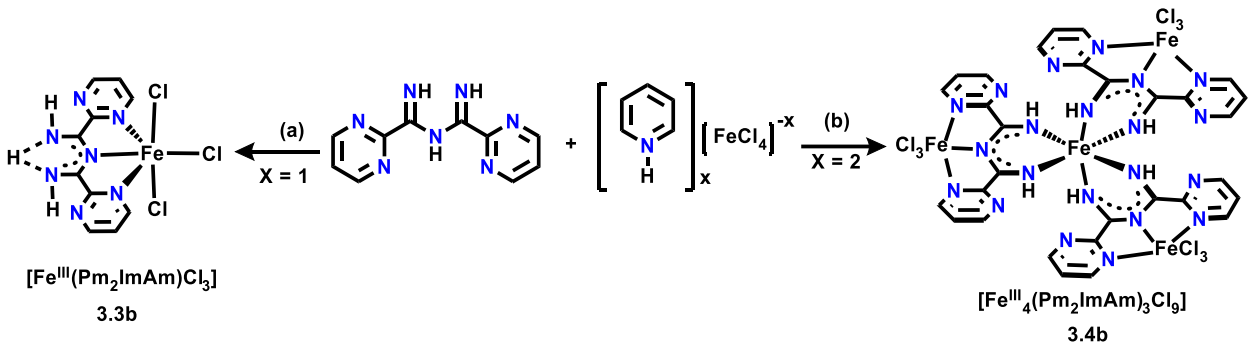

Scheme 3.2. Synthesis of complexes **[Fe^{III}(Pm$_2$ImAm)Cl$_3$]** and **[Fe$^{III}_4$(Pm$_2$ImAm)$_3$Cl$_9$]** employing the Pm$_2$ImAm ligand. Reagents and conditions: (a) X = 1, DCM; (b) X = 2, DMSO/CHCl$_3$.

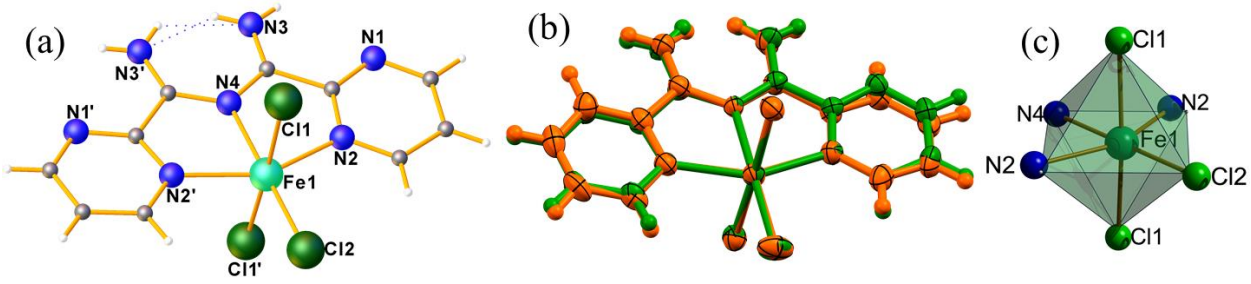

Figure 3.5. (a) Structural diagram of **[Fe^{III}(Pm$_2$ImAm)Cl$_3$]**. Symmetry related positions are labeled with the prime symbol. (b) Structural overlay of **[Fe^{III}(Py$_2$ImAm)Cl$_3$]** (orange) and **[Fe^{III}(Pm$_2$ImAm)Cl$_3$]** (green). The hydrogen atom located at N3 has half occupancy as the molecule resides on a C2 axis. (c) Deviation from ideal octahedron of **[Fe^{III}(Py$_2$ImAm)Cl$_3$]**.

3.5 Synthesis and Structural Analysis of [Fe$^{III}_4$(Pm$_2$ImAm)$_3$Cl$_9$]

Contrary to the manganese analogue, isolation of the tetranuclear iron complex did not require a less acidic pyridinium counter ion. Instead, the polynuclear iron complex was achieved *via* alteration of both the solvent system along with the oxidation state of the metal salt employed – namely, *bis*(pyridinium) tetrachloroferrate(II) (**[PyH]$_2$[FeCl$_4$]**). In this case, crystals of **[Fe$^{III}_4$(Pm$_2$ImAm)$_3$Cl$_9$]** (**3.4b**) suitable for X-ray analysis were obtained by layering a dimethyl sulfoxide (DMSO) solution of **[PyH]$_2$[FeCl$_4$]** over a solution of Pm$_2$ImAm in chloroform. It should be noted that while **[Fe$^{III}_4$(Pm$_2$ImAm)$_3$Cl$_9$]** can be achieved with either *bis*(pyridinium) tetrachloroferrate(II) (**[PyH]$_2$[FeCl$_4$]**) or pyridinium tetrachloroferrate(III) (**[PyH][FeCl$_4$]**),

employing **[PyH]$_2$[FeCl$_4$]** resulted in the formation of larger crystals of **[Fe$^{III}_4$(Pm$_2$ImAm)$_3$Cl$_9$]**. Furthermore, tiny crystals of the mononuclear complex **[Fe^{III}(Pm$_2$ImAm)Cl$_3$]** were also formed as a by-product regardless of whether **[PyH]$_2$[FeCl$_4$]** or **[PyH][FeCl$_4$]** was used as the iron source. Thus, formation of the larger crystals of **[Fe$^{III}_4$(Pm$_2$ImAm)$_3$Cl$_9$]** using **[PyH]$_2$[FeCl$_4$]** enabled isolation of pure **[Fe$^{III}_4$(Pm$_2$ImAm)$_3$Cl$_9$]** through density separation methods using chloroform.

Perhaps unsurprisingly, the crystal structure of **[Fe$^{III}_4$(Pm$_2$ImAm)$_3$Cl$_9$]** has many similarities to **[Mn^{III}Mn$^{II}_3$(Pm$_2$ImAm)$_3$Cl$_6$]**. For instance, both complexes crystallize in the same monoclinic space group (*C2/c*), with both complexes sitting on a C_2 axis. As a result, the asymmetric unit of **[Fe$^{III}_4$(Pm$_2$ImAm)$_3$Cl$_9$]** contains three independent iron atoms in the same manner as **[Mn^{III}Mn$^{II}_3$(Pm$_2$ImAm)$_3$Cl$_6$]**, with Fe1 being the central metal, Fe2 located in a general position and Fe3 situated along a C_2 axis (Figure 3.2). The coordination environment of the central iron atom in **[Fe$^{III}_4$(Pm$_2$ImAm)$_3$Cl$_9$]** is analogous to the mononuclear complex **[Fe^{III}(Py$_2$ImAm)$_3$]** discussed in the second chapter (Figure 3.6), having nearly ideal octahedral configurations and only minor elongation of the Fe–N distances from 1.915(4) – 1.925(4) Å in **[Fe^{III}(Py$_2$ImAm)$_3$]** to 1.9191(2) – 1.9426(2) Å in **[Fe$^{III}_4$(Pm$_2$ImAm)$_3$Cl$_9$]**. These similarities suggest an oxidation state of +3 for the central iron ion, consistent with the mononuclear complex. In the case of the peripheral iron atoms Fe2 and Fe3, both possess distorted octahedral topologies (Figure 3.7) with minimal differences in their Fe–N and Fe–Cl distances. Visual comparison between the outer iron atoms in **[Fe$^{III}_4$(Pm$_2$ImAm)$_3$Cl$_9$]** to the mononuclear complex **[Fe^{III}(Pm$_2$ImAm)Cl$_3$]**, highlights the nearly identical coordination geometry between these moieties (Figure 3.6).

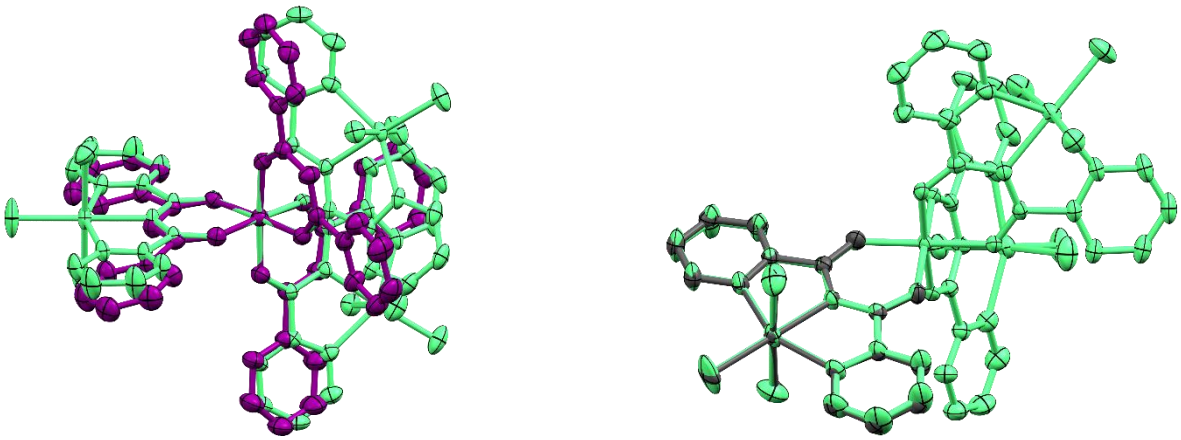

Figure 3.6. Structural overlay of mononuclear **[Fe^{III}(Py$_2$ImAm)$_3$]** (purple) with tetranuclear **[Fe$^{III}_4$(Pm$_2$ImAm)$_3$Cl$_9$]** (green) on the left and mononuclear **[Fe^{III}(Pm$_2$ImAm)Cl$_3$]** (gray) with **[Fe$^{III}_4$(Pm$_2$ImAm)$_3$Cl$_9$]** (green) on the right. Hydrogen atoms have been omitted for clarity.

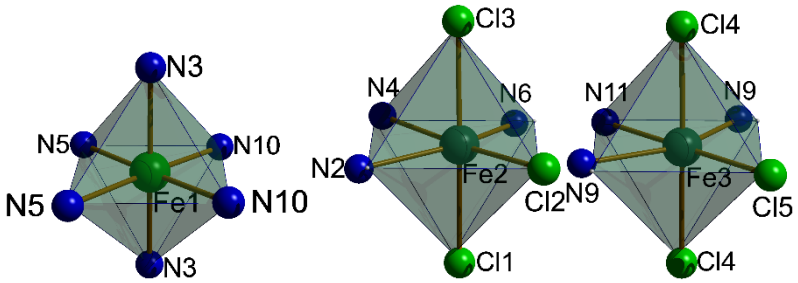

Figure 3.7. Deviation from ideal octahedral environment about the iron atoms of **[Fe$^{III}_4$(Pm$_2$ImAm)$_3$Cl$_9$]**.

3.6 Structural Comparison of Tetranuclear Mn and Fe Complexes

Although coordination of the central metal ion is near to perfect octahedron in both tetranuclear complexes presented here, neither tetranuclear complex possesses the D_3 point group as their individual mononuclear counterparts do. This is attributed to the tilting direction of the *N*-imidoylamidine ligands, two of which fold towards each other while leaning away from the third Pm$_2$ImAm ligand (Figure 3.8). As a consequence, the interplanar angles between the ligands close to each other are 68° and 70° for **[Mn^{III}Mn$^{II}_3$(Pm$_2$ImAm)$_3$Cl$_6$]** and **[Fe$^{III}_4$(Pm$_2$ImAm)$_3$Cl$_9$]**, respectively. In the case of the manganese derivative, this folding makes possible the formation of parallel stacks of ligands, which is reinforced by C-H···Cl, C-H···N and N-H···Cl hydrogen bonding (Figure 3.9 and Table B.7). Conversely, the crystal packing of **[Fe$^{III}_4$(Pm$_2$ImAm)$_3$Cl$_9$]**

consists of a less dense array of molecules, which affords extended solvent channels and limited intermolecular interactions consisting of weaker C-H···Cl hydrogen bonds (Figure 3.9 and Table B.7).

Due to the twisted nature of the ligands with respect to one another, which prevents dense packing of the molecules, structural voids with differing volumes exist in both tetranuclear complexes. In the case of **[$Mn^{III}Mn^{II}_3(Pm_2ImAm)_3Cl_6$]**, a structure void volume of 17.4% was found, while **[$Fe^{III}_4(Pm_2ImAm)_3Cl_9$]** has solvent channels that occupy 43.8% of the unit cell volume (Figure 3.9). These structural void volumes were generated using a probe radius of 1.2 in Mercury while excluding solvent molecules during the calculation.[16] The large discrepancy between the porosity of these structures, and therefore the presence of extended solvent channels in **[$Fe^{III}_4(Pm_2ImAm)_3Cl_9$],** is likely due to the lower number of intermolecular hydrogen bonds in **[$Fe^{III}_4(Pm_2ImAm)_3Cl_9$]** compared to **[$Mn^{III}Mn^{II}_3(Pm_2ImAm)_3Cl_6$]** (See Appendix B; Table B.7).

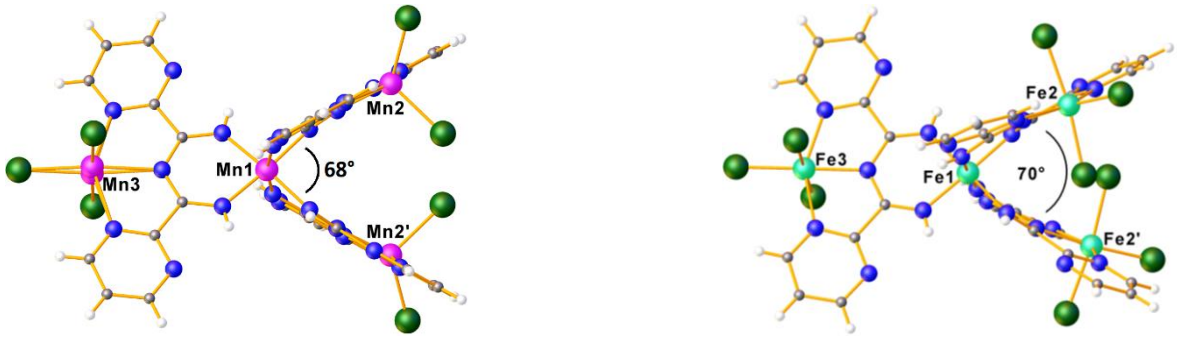

Figure 3.8. Structural diagram of **[$Mn^{III}Mn^{II}_3(Pm_2ImAm)_3Cl_6$]** (left) and **[$Fe^{III}_4(Pm_2ImAm)_3Cl_9$]** (right) showing the folding of the tetranuclear complexes. Ligands connected to M2 fold close to each other. Symmetry related positions are labeled with a prime symbol.

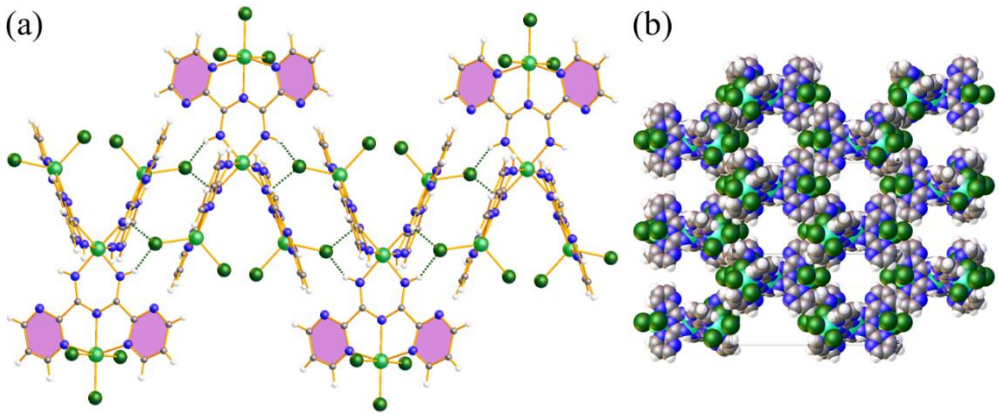

Figure 3.9. (a) Packing view of **[$Mn^{III}Mn^{II}_3(Pm_2ImAm)_3Cl_6$]** with a single stack of tetranuclear complexes. C-H···N hydrogen bonds are denoted as blue dotted lines and N-H···Cl as green dotted lines. (b) View of solvent channels along the 101 plane in **[$Fe^{III}_4(Pm_2ImAm)_3Cl_9$]**.

3.7 Magnetic Characterization

In order to gain insight into the oxidation states and electronic configuration of the metal centres, magnetic susceptibility studies were completed for both **[$Mn^{III}Mn^{II}_3(Pm_2ImAm)_3Cl_6$]** and **[$Fe^{III}_4(Pm_2ImAm)_3Cl_9$]**; full experimental details are provided in the section 3.10. For completeness, magnetic susceptibility studies were also performed on **[$Mn^{II}_2(\mu\text{-}Cl)_2(Pm_2ImAm)_2Cl_2$]**, revealing characteristic behaviour for a high spin dinuclear Mn^{II} complex.[17-19] The variable temperature magnetic susceptibility measurements of **[$Mn^{II}_2(\mu\text{-}Cl)_2(Pm_2ImAm)_2Cl_2$]** yielded a χT product of 8.71 cm^3 K mol^{-1} at 300 K (g_{exp} = 1.98), indicative of two non-interacting S = 5/2 ions (χT_{calc} = 8.75 cm^3 K mol^{-1}, assuming g = 2.00). Weak ferromagnetic interactions between spin carriers results in a gradual increase in the χT value upon decreasing temperature. This interaction was quantified by fitting the experimental data to the spin Hamiltonian (See Appendix F; Equations F.1-F.2, F.5, F.7) with PHI software,[20] yielding a coupling constant of J_1 = +0.289 cm^{-1}. Full fitting parameters are provided in Table 3.4. This ferromagnetic interaction results in a maximum χT product of 11.74 cm^3 K mol^{-1} at 2.4 K which is in good agreement with the non-zero ground state arising from the S_T = 5 coupled spin. At temperatures lower than 2.4 K, the χT product experiences a decrease (11.37 cm^3 K mol^{-1} at 1.8 K), preventing the system from reaching the maximum susceptibility for an S_T = 5 system (15.00 cm^3 K mol^{-1}). This slight downturn of the χT product at low temperature may be ascribed to intermolecular interactions, which were effectively accounted for in the fit of the susceptibility (zJ

= -0.0079 cm^{-1}). The weak nature of these interactions are supported by the intermolecular Mn^{II}---Mn^{II} distances of 8.00 and 8.09 Å. The values obtained from the fit of the susceptibility also adequately reproduce the experimental magnetization data (Figure 3.10).

Table 3.4. Selected magnetic parameters for complexes **$[Mn^{II}_2(\mu\text{-}Cl)_2(Pm_2ImAm)_2Cl_2]$, $[Mn^{III}(Py_2ImAm)_3]$**, **$[Fe^{III}(Py_2ImAm)_3]$**, and **$[Fe^{III}(Pm_2ImAm)Cl_3]$**.

	$[Mn^{II}_2(\mu\text{-}Cl)_2(Pm_2ImAm)_2Cl_2]$	$[Mn^{III}(Py_2ImAm)_3]$	$[Fe^{III}(Py_2ImAm)_3]$	$[Fe^{III}(Pm_2ImAm)Cl_3]$
S	$S_1 = S_2 = 5/2$	1	1/2	5/2
g[a]	1.98	1.97	1.83	1.99
D[a]	---	+8.55 cm^{-1}	+14.47 cm^{-1}	+4.32 cm^{-1}
zJ[a]	-0.0079 cm^{-1}	-0.608 cm^{-1}	---	-0.103 cm^{-1}
J_1[a]	+0.289 cm^{-1}	---	---	---
λ[a]	---	---	+4.05 cm^{-1}	---

[a] Obtained from the fit of the experimental data to the Hamiltonians described in the ESI with PHI software.[20]

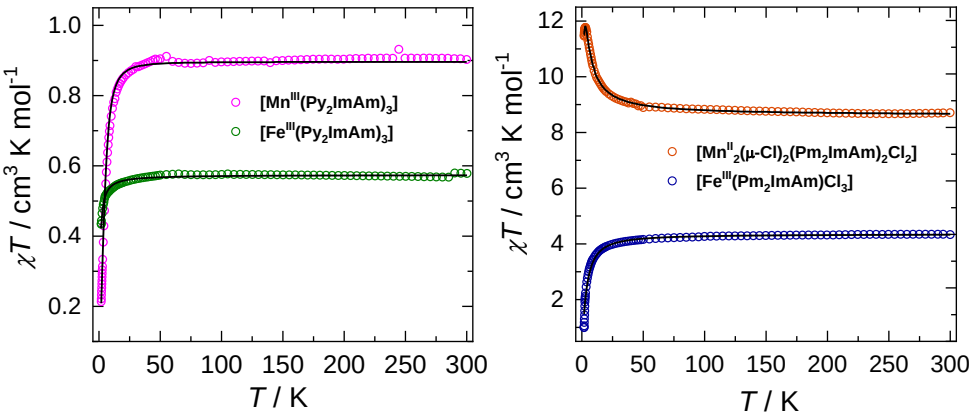

Figure 3.10. Temperature dependence of the χT product for **$[Mn^{II}_2(\mu\text{-}Cl)_2(Pm_2ImAm)_2Cl_2]$** (orange), **$[Mn^{III}(Py_2ImAm)_3]$** (pink), **$[Fe^{III}(Py_2ImAm)_3]$** (green), and **$[Fe^{III}(Pm_2ImAm)Cl_3]$** (blue) with χ being the molar magnetic susceptibility per molecule as defined by M/H. Experimental data was collected under an applied dc field of 1000 Oe and it is represented by hollow circles while the best-fits to the data are depicted as black solid lines.

With the goal of understanding the spin states and coupling in the tetranuclear compounds, the mononuclear compounds **$[Mn^{III}(Py_2ImAm)_3]$**, **$[Fe^{III}(Py_2ImAm)_3]$**, and **$[Fe^{III}(Pm_2ImAm)Cl_3]$** were also investigated through magnetic susceptibility measurements, as they display isostructural components with the tetranuclear species. Due to the structural similarities, these mononuclear compounds have provided additional insight into the properties of the tetranuclear systems. Although the ligand utilized in **$[Mn^{III}(Py_2ImAm)_3]$** and

[Fe^{III}(Py$_2$ImAm)$_3$] varies slightly with the tetranuclear complexes, the presence of hard donor atoms (N-atoms) and their bidentate binding modes with the respective metal ions would suggest that the ligand field effect is near identical, leading to minimal differences in their crystal fields. Thus, these systems serve as ideal models in order to determine the spin state of the central metal ion in each of the tetranuclear compounds without the effects of intramolecular coupling between spin carriers.

Variable temperature magnetic susceptibility studies on **[Mn^{III}(Py$_2$ImAm)$_3$]** and **[Fe^{III}(Py$_2$ImAm)$_3$]** reveal χT products of 0.90 and 0.58 cm^3 K mol^{-1}, respectively, at 300K (Figure 3.10). For **[Mn^{III}(Py$_2$ImAm)$_3$]**, the experimentally obtained room temperature χT value is close to the expected value of 1.00 cm^3 K mol^{-1} for a low spin Mn^{III} ion (i.e. S = 1). Upon lowering the temperature, the χT product remains relatively constant until 25 K, where a decrease in the χT product is observed until it reaches 0.21 cm^3 K mol^{-1} at 1.8 K. This decrease at low temperature is likely due to weak antiferromagnetic intermolecular interactions between spin-carriers, which is further supported by the close intermolecular Mn^{III}---Mn^{III} distance of 5.69 Å. These interactions were accounted for in the fit of the susceptibility (Table 3.4). Further examination into the structural metrics of **[Mn^{III}(Py$_2$ImAm)$_3$]** reveals a trigonal distortion in the octahedral geometry of the Mn^{III} ion along the C_3 axis. Not only is this reminiscent of previous examples of low spin Mn^{III} compounds, but it should also be noted that there are only a small number of complexes that exhibit this spin state for an Mn^{III} ion.[21-27] This distortion results in slight changes to the energy levels of the *d*-orbitals (Figure 3.11), such that the orbital contribution to the magnetic moment for an S = 1 system should be quenched. However, considerable zero field splitting (ZFS) parameters have been obtained for the related low spin Mn^{III} ion in **[Tp$_2$Mn^{III}]$^+$** (Tp = hydridotris(pyrazolyl)borate anion) and its derivatives (D = +14.60 - +18.07 cm^{-1}, method dependent), where such findings were supported by magnetic circular dichroism (MCD), magnetic susceptibility and high-field electron paramagnetic resonance (EPR) studies.[21, 28] With respect to **[Mn^{III}(Py$_2$ImAm)$_3$]**, the variable temperature susceptibility was fit using the PHI[20] program, with the best fit parameters revealing a *g*-factor of 1.97 and a D-value of +8.55 cm^{-1} (Table 3.4). Considering the lack of orbital moment from the ground state S= 1 configuration of **[Mn^{III}(Py$_2$ImAm)$_3$]** it is reasonable to assume the primary contributor to the D parameter is a low-lying triplet excited state (Figure 3.11). While this is difficult to conclude exactly without electronic structure calculations, it was found that the D value increases as the energy of the triplet

excited state decreases in the **[Tp$_2$Mn^{III}]$^+$** family.[17] With respect to the fitting, any attempts to restrain $D < 0$, did not accurately reproduce the data. Additionally, the *g*-factor obtained is only marginally smaller than what is expected for a truly isotropic system (i.e. 2.00), which is reasonable for the $S = 1$ ground state with minimal population of the excited state. Thus, the low temperature magnetic behaviour of **[Mn^{III}(Py$_2$ImAm)$_3$]** may be best explained by a mix of the ZFS effects and antiferromagnetic coupling between nearest neighbours.

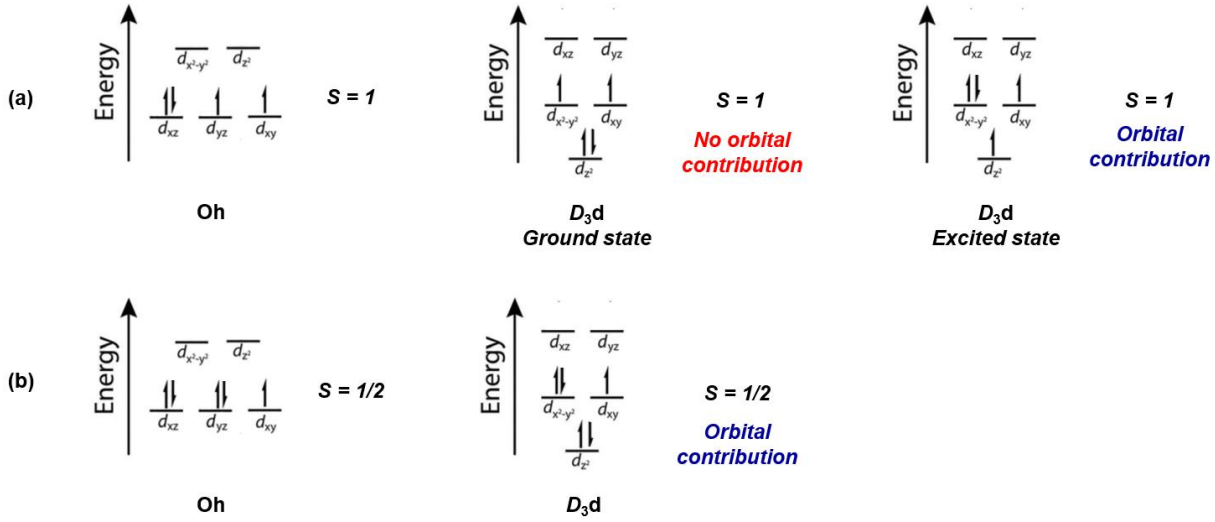

Figure 3.11. *d*-orbital splitting diagrams for Oh symmetry (left) and a trigonally distorted octahedron with D_3d symmetry (middle) and the excited state configuration for D_3d (right).[29] The electronic configurations are representative of (a) Mn^{III} ($S = 1$) and (b) Fe^{III} ($S = 1/2$) ions in a strong ligand field (low spin configuration).

Due to the isomorphic nature of **[Mn^{III}(Py$_2$ImAm)$_3$]** and **[Fe^{III}(Py$_2$ImAm)$_3$]**, the effects of a trigonal distortion also needs to be considered in the evaluation of the spin state of **[Fe^{III}(Py$_2$ImAm)$_3$]**. The strong ligand field provided by the **Py$_2$ImAm** ligand results in a low spin state of the Fe^{III} ion, and combined with the distorted octahedral environment, results in an orbital contribution to the observed magnetic moment (Figure 3.11). This is reflected in the χT *vs*. T plot of **[Fe^{III}(Py$_2$ImAm)$_3$]**, as the experimental χT product at 300 K is larger than what is expected from the spin-only formalism (0.58_{exp} *vs*. 0.38_{calc} cm^3 K mol^{-1}; assuming $g = 2.00$). The χT product persists with decreasing temperature until 10 K, at which point a decrease is observed until the χT product reaches 0.44 cm^3 K mol^{-1} at 1.8K. Using this entire data range, the data was fit to obtain a *g*-factor and a *D*-value, as well as a spin-orbit coupling term (λ), which was needed in order to

account for the unquenched orbital angular momentum (See Appendix F; Equations F.1-F.4). It is noteworthy that the best fit parameters of g = 1.83 and D = +14.47 cm^{-1} are similar to those obtained for **[$Mn^{III}(Py_2ImAm)_3$]**, although the spin state for the Fe analogue is smaller (S = ½ *vs.* 1).

The spin state of the peripheral Fe^{III} ions (Fe2, Fe2', and Fe3) in **[$Fe^{III}_4(Pm_2ImAm)_3Cl_9$]** have also been evaluated by analyzing the structurally analogous **[$Fe^{III}(Pm_2ImAm)Cl_3$]** mononuclear compound. With respect to **[$Fe^{III}(Pm_2ImAm)Cl_3$]**, a χT product of 4.33 cm^3 K mol^{-1} is obtained at 300 K, which corresponds to the expected spin-only (assume g = 2.00) value of 4.38 cm^3 K mol^{-1} for an S = 5/2 ion. Here, the presence of three weak-field chloride anions allows for the high spin state to be achieved for **[$Fe^{III}(Pm_2ImAm)Cl_3$]** compared to the low spin state, which is observed for **[$Fe^{III}(Py_2ImAm)_3$]**. For **[$Fe^{III}(Pm_2ImAm)Cl_3$]**, the profile of the χT plot with decreasing temperature is characteristic of an isolated spin-system, with little-to-no deviation from the Currie constant (Figure 3.11). Below 50 K, the χT product gradually deceases until it reaches 10 K, upon which a rapid decrease to 1.00 cm^3 K mol^{-1} at 1.8 K is observed. Fitting the data yielded the expected isotropic g-factor of 1.99 with a D-value of +4.32 cm^{-1}, consistent with a high spin isotropic Fe^{III} ion. In order to account for the low temperature downturn of the χT product, inter-complex magnetic interactions (zJ) were needed to accurately reproduce the experimental data. These interactions were treated in the mean-field approximation (See Appendix F; Equation F.7), revealing a weak antiferromagnetic interaction of -0.103 cm^{-1}.

Given the above information, the variable temperature magnetic susceptibility of the tetranuclear compounds were analyzed (Figure 3.12). The χT product at 300 K of both **[$Mn^{III}Mn^{II}_3(Pm_2ImAm)_3Cl_6$]** and **[$Fe^{III}_4(Pm_2ImAm)_3Cl_9$]** were slightly smaller than the values expected using the spin-only formalism assuming g= 2.00 (12.40_{exp} *vs.* 14.12_{calc} cm^3 K mol^{-1}, and 12.69_{exp} *vs.* 13.50_{calc} cm^3 K mol^{-1}, respectively). This is not surprising given that antiferromagnetic interactions between the central (Mn1 and Fe1) and peripheral metal ions may already be present at 300 K, as can be seen by the high temperature profile of the χT *vs.* T plot. In other words, no saturation of the χT product was observed, even at room temperature. Upon cooling, the χT product of **[$Mn^{III}Mn^{II}_3(Pm_2ImAm)_3Cl_6$]** gradually decreases to 11.04 cm^3 K mol^{-1} at 65 K, at which point a drastic increase in the susceptibility occurs, reaching a maximum at 2.6 K of 20.52 cm^3 K mol^{-1}. This rise in the χT product can be attributed to spin alignment of the peripheral Mn^{II} ions, resulting

from the dominant intramolecular antiferromagnetic interaction between the central Mn^{III} and the peripheral Mn^{II} ions (Figure 3.13). The obtained maximum is in good agreement with this antiferromagnetic model, as it is close to the expected spin-only value of 24.38 cm^3 K mol^{-1} for a spin ground state of $S_T = 13/2$. Below 2.6 K, the observed decrease in the χT product down to 19.91 cm^3 K mol^{-1} at 1.8 K can be attributed to intermolecular antiferromagnetic interactions. As shown in Figure 3.9 there are few short intermolecular Mn-Mn distances in the crystal lattice of **$[Mn^{III}Mn^{II}_3(Pm_2ImAm)_3Cl_6]$** (e.g. Mn1-Mn2= 5.713(1) Å) that could result in the intermolecular interactions observed.

With respect to **$[Fe^{III}_4(Pm_2ImAm)_3Cl_9]$**, the χT product steadily decreases with cooling from 300 K, where below 50 K there is more notable decrease of the χT product followed by a rapid decrease below 20 K. The final value of 3.05 cm^3 K mol^{-1} is achieved at 1.8 K (Figure 3.12). The overall profile of this χT *vs.* T plot is unlike that of the manganese congener, as the effect of spin alignment between the outer peripheral ions is not observable for **$[Fe^{III}_4(Pm_2ImAm)_3Cl_9]$**. This may be attributed to stronger intermolecular magnetic interactions in **$[Fe^{III}_4(Pm_2ImAm)_3Cl_9]$** compared to **$[Mn^{III}Mn^{II}_3(Pm_2ImAm)_3Cl_6]$**, which were effectively accounted for in the fit of the experimental data (Table 3.5). Alternatively, this downturn in the χT product can be ascribed to the central Fe^{III} ion, which is highly anisotropic (as evidenced by the unquenched first order orbital angular momentum of the metal centre in **$[Fe^{III}(Py_2ImAm)_3]$**).

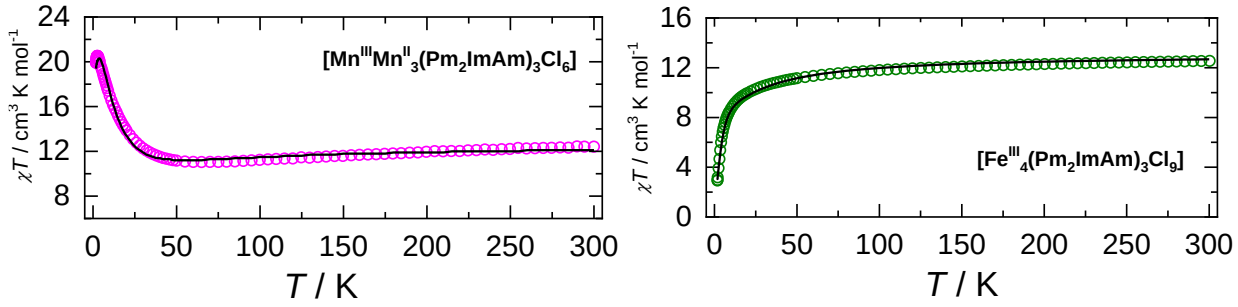

Figure 3.12. Temperature dependence of the χT product for **$[Mn^{III}Mn^{II}_3(Pm_2ImAm)_3Cl_6]$** (left, pink), and **$[Fe^{III}_4(Pm_2ImAm)_3Cl_9]$** (right, green) with χ being the molar magnetic susceptibility per molecule as defined by M/H. Experimental data was collected under an applied dc field of 1000 Oe and is represented by hollow circles while the best-fits to the data are depicted as black solid lines.

Table 3.5. Selected magnetic parameters for **[$Mn^{III}Mn^{II}_3(Py_2ImAm)_3Cl_6$]** and **[$Fe^{III}_4(Pm_2ImAm)_3Cl_9$]**.

	[$Mn^{III}Mn^{II}_3(Py_2ImAm)_3Cl_6$]	**[$Fe^{III}_4(Pm_2ImAm)_3Cl_9$]**
S_1	1	1/2
S_2	5/2	5/2
g_1 [a]	1.89	1.83
g_2 [a]	1.89	1.95
J_2 [a]	-3.14 cm^{-1}	-2.39 cm^{-1}
D [a]	+1.37 cm^{-1}	+0.49 cm^{-1}
zJ [a]	---	-0.14 cm^{-1}

[a] Obtained from the fit of the experimental data to the Hamiltonians described in the text with PHI software.[20]

Utilizing the information gleaned from the fits of the magnetic susceptibilities of **[$Mn^{III}(Py_2ImAm)_3$]**, **[$Fe^{III}(Py_2ImAm)_3$]**, and **[$Fe^{III}(Pm_2ImAm)Cl_3$]**, the variable temperature magnetic susceptibilities of **[$Mn^{III}Mn^{II}_3(Pm_2ImAm)_3Cl_6$]** and **[$Fe^{III}_4(Pm_2ImAm)_3Cl_9$]** were then subsequently fit to quantify the strength of the exchange interactions present. Within these molecules the strength of the exchange coupling term (J_2) between the central metal ion and the peripheral metal ions is assumed to be predominant, and any interactions between the peripheral ions were assumed negligible (Figure 3.13). The parameters for the central metal ions, Mn1 and Fe1 of **[$Mn^{III}Mn^{II}_3(Pm_2ImAm)_3Cl_6$]** and **[$Fe^{III}_4(Pm_2ImAm)_3Cl_9$]**, respectively, were restrained to the values obtained from the mononuclear compounds as outlined in Table 3.4, and all other parameters were varied as free terms in order to prevent over parameterization. Thus, in order to accurately reproduce the experimental data of **[$Mn^{III}Mn^{II}_3(Pm_2ImAm)_3Cl_6$]**, an exchange Hamiltonian combined with the Zeeman and axial zero field splitting (ZFS) components was needed (See Appendix F; Equation F.1-F.3, F.6); the best fit parameters are summarized in Table 3.5. From the best fit, an exchange coupling constant of -3.14 cm^{-1} was achieved. A coupling constant of this strength is comparable with other multinuclear Mn-based clusters.[19, 30] In addition, the satisfactory fit obtained for the one *J*-model accurately reproduces the data, further demonstrating that any interactions between the peripheral metal ions is minimal.

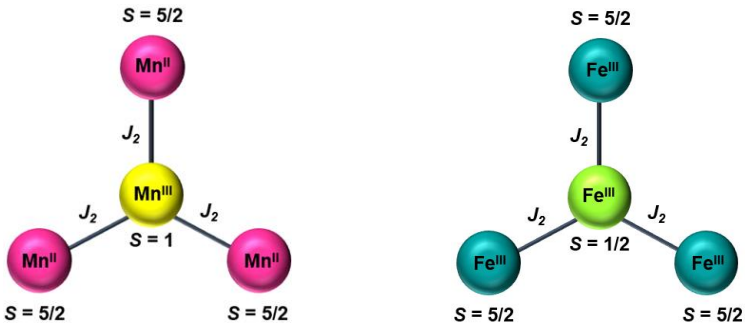

Figure 3.13. Magnetic structure representation of **[$Mn^{III}Mn^{II}_3(Pm_2ImAm)_3Cl_6$]** (left) and **[$Fe^{III}_4(Pm_2ImAm)_3Cl_9$]** (right). J_2 represents the magnetic exchange constant determined from the fit of the experimental data to the exchange Hamiltonian (See Appendix F; Equation F.6).

The values obtained for **[$Fe^{III}_4(Pm_2ImAm)_3Cl_9$]** are comparable to those from the fit of **[$Mn^{III}Mn^{II}_3(Pm_2ImAm)_3Cl_6$]**, with the exception of the inclusion of an intermolecular magnetic interaction constant, *zJ* (See Appendix F; Equation F.7), thus making the spin Hamiltonian for this species the sum of the exchange, Zeeman, axial ZFS, and intermolecular Hamiltonians (See Appendix F; Equation F.1-F.3, F.6). The obtained *zJ* for **[$Fe^{III}_4(Pm_2ImAm)_3Cl_9$]** is the same order of magnitude as **[$Fe^{III}(Pm_2ImAm)Cl_3$]**, and effectively represents the downturn of the χT product at low temperature. In addition, a g_2 value of 1.95 is obtained, representing the average *g*-value for the peripheral Fe^{III} ions. This finding correlates well with the parameters from **[$Fe^{III}(Pm_2ImAm)Cl_3$]**, which demonstrates that by including weaker field ligands such as chloride ions, the metal ion adopts a high spin state that is largely isotropic in nature, thereby leading to a *g*-value relatively close to 2.00. Lastly, J_2 was found to be antiferromagnetic in nature, again corroborating with the exchange model developed for these tetranuclear compounds. Overall, the magnitude of this interaction remains consistent with previously reported clusters.[31, 32] It is also worth noting that while the *D* parameters remain positive for these systems, the *D* values for **[$Mn^{III}Mn^{II}_3(Pm_2ImAm)_3Cl_6$]** and **[$Fe^{III}_4(Pm_2ImAm)_3Cl_9$]** are either one or two orders of magnitude smaller than their mononuclear derivatives. These findings suggest the superexchange pathways *via* the *N*-imidoylamidine ligand results in dominant antiferromagnetic interactions between the central and peripheral metal ions. This ultimately leads to ferromagnetic spin alignment of the outer spins, thus leading to stabilization of non-negligible spin ground states.

3.8 Mössbauer Spectroscopy

To support the oxidation assignment for the iron centres in **[Fe_4^{III}(Pm_2ImAm)$_3$$Cl_9$]**, the electronic structure of each of the Fe atoms was determined by Mössbauer spectroscopy at 80 K revealing the presence of two distinct Fe species (Figure 3.14). The central Fe atom with a relative area of 26% has an isomer shift of δ = 0.11 mm s^{-1} and quadruple splitting of ΔE_Q = 2.06 mm s^{-1} corresponding to a low spin Fe^{III} species. The three peripheral Fe atoms with a relative area of 74% have an isomer shift of δ = 0.46 mms^{-1} and quadruple splitting of ΔE_Q = 0.87 mms^{-1}. While the spin-state of the peripheral iron atoms (i.e. low spin Fe^{II} *vs.* high spin Fe^{III}) cannot be determined strictly by Mössbauer spectroscopy, magnetic measurements and charge balance were also used to determine the spin-states as high spin Fe^{III} unambiguously.

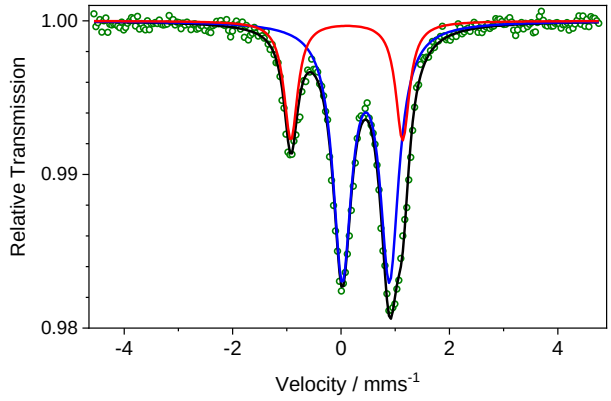

Figure 3.14. Zero-field Mössbauer spectrum of **[Fe_4^{III}(Pm_2ImAm)$_3$$Cl_9$]** recorded at 80 K; experimental data collected is indicated as green circles. The blue line corresponds to the fit of the outer high spin Fe^{III} ions, while the red line corresponds to the fit of the central low spin Fe^{III} ion. The overall sum of the iron ions is represented by the black line.

3.9 Conclusions

Herein, we have demonstrated the versatility of the *N*-2-pyrimidylimidoyl-2-pyrimidylamidine ligand framework, which provides an ideal platform in the development of polynuclear complexes. More specifically, we have synthesized tetranuclear Mn and Fe complexes, in which coordination to the bidentate and tridentate sites within the *N*-imidoylamidine ligands was achieved. The spin states of the metal ions in these tetranuclear complexes were elucidated by SQUID magnetometry and Mössbauer spectroscopy, which reveal a unique combination of low and high spin states for the metal centres within the cluster aggregates. More

specifically, the central metal ion in both complexes adopts an oxidation state of +3 with octahedral geometry to six N-donor atoms, resulting in a low spin state. Conversely, the peripheral ions exhibit either +2 or +3 oxidation states, depending on the metal chosen (Mn *vs*. Fe), and adopt high spin states as a consequence of the ligand field associated with three N-donor and two/three terminal halides.

The design strategy implemented here through the use of these *N*-imidoylamidine ligands provides an avenue to further explore the formation of polynuclear species with differing spin states. In that regard a similar strategy was used in chapter 4 to build homometallic complexes with cobalt(II), that also have a combination of different geometries and spin configurations. As well, employing a new strategy that elaborates on the one described here led to the development of heterometallic complexes as outlined in chapters 5.

3.10 Experimental Section

General Procedures. All solvents and reagents were reagent grade and used without further purification. Pyridinium tetrachloroferrate(III) (**[PyH][FeCl$_4$]),** pyridinium trichloromanganate(II) monohydrate (**[PyH][MnCl$_3$]·H$_2$O**) and *N*-2-pyrimidylimidoyl-2-pyrimidylamidine (**Pm$_2$ImAm**) were synthesized according to literature procedures.[33, 34,13] IR spectra were recorded on an Agilent Technologies Cary 630 FT-IR spectrometer. A single crystalline phase was confirmed by comparison of the experimental PXRD patterns with those calculated from the single crystal data (See Appendix D; Figures D.1-D.3).

Synthesis of *bis*(pyridinium) tetrachloroferrate(II) ([PyH]$_2$[FeCl$_4$]). After dissolving $FeCl_2 \cdot 4H_2O$ (10.79 g, 54.27 mmol) in a solution of concentrated hydrochloric acid (10 mL) and methanol (20mL), the reaction was cooled to 0 °C and pyridine (8.8 mL, 113.29 mmol) was added dropwise with stirring. After stirring for 20 min, the solvent was removed under reduced pressure affording an orange residue that was crystallized from 50 mL acetone affording **[PyH]$_2$[FeCl$_4$]** as pale-yellow needles. Yield: 13.14 g (36.71 mmol, 67.6%). Unit cell parameters of the yellow needles belong to the triclinic system and are *a*= 7.590(7) Å, *b*= 8.027(7) Å, *c*= 12.60(1) Å, α= 88.81(1), β= 83.21(2), γ= 79.24(2). These unit cell parameters match those of three different yet related compounds *bis*(pyridinium) tetrachloromaganate(II), *bis*(pyridinium) tetrachlorocobaltate(II), and *bis*(pyridinium) tetrachlorozincate(II).[35-37] Note: After exposing **[PyH]$_2$[Fe^{II}Cl$_4$]** to air it slowly oxidizes into **[PyH]$_4$[Fe$^{III}_2$OCl$_6$]Cl$_2$**. IR (cm^{-1}): *ν* 3208 (w), 2957

(w), 3105 (m), 3076 (m), 2957 (w), 1600 (m), 1529 (s), 1484 (s), 1442 (s), 1327 (w), 1213 (m), 1194 (m), 1166 (m), 1064 (m), 1039 (m), 1010 (m), 884 (m), 757 (m), 739 (s), 697 (s), 672 (s).

Synthesis of 2,6-diaminopyridinium trichloromanganate(II) monohydrate ([(NH$_2$)$_2$PyH][MnCl$_3$·H$_2$O]). After dissolving $MnCl_2·(H_2O)_4$ (5.85 g, 29.57 mmol) in concentrated hydrochloric acid (3 mL) and methanol (15 mL), the reaction was cooled to RT and a solution of 2,6-diaminopyridine (3.24 g, 29.66 mmol) in methanol (20 mL) was slowly added dropwise with stirring. After stirring for 30 min, the solvent was removed under reduced pressure and the resulting residue was suspended in 150 mL of MeCN, filtered and dried in vacuo. Yield: 5.69 g (19.67 mmol, 66.5%) of **[(NH$_2$)$_2$PyH][MnCl$_3$]·H$_2$O** as pale pink solid. IR (cm^{-1}): *ν* 3543 (br), 3418 (s), 3328 (s), 3214 (s), 3156 (m), 3005 (w), 1745 (w), 1646 (s), 1626 (s), 1598 (s), 1487 (w), 1380 (m), 1300 (s), 1174 (s), 1122 (w), 1056 (w), 997 (w), 774 (s), 750 (m), 689 (s).

Synthesis of di-*μ*-chloro-bis[chloro(*N*-2-pyrimidylimidoyl-2-pyrimidylamidine)manganese] (3.1b). A hot solution of **[PyH][MnCl$_3$·H$_2$O]**, (0.65 g; 2.50 mmol) in methanol (5 mL) was added to a hot solution of **Pm$_2$ImAm** (0.58 g; 2.55 mmol) in MeCN (15 mL). After cooling to room temperature, a pale-yellow precipitate formed. The solid was filtered, washed with DCM followed by methanol and dried in air. Yield: 0.30 g (0.84 mmol, 33.5%). IR (cm^{-1}): *ν* 3293 (m), 3261 (m), 3071 (m), 3049 (w), 1637 (s), 1596 (w), 1569 (s), 1508 (w), 1439 (w), 1393 (s), 1365 (s), 1278 (w), 1236 (m), 1206 (s), 1117 (m), 1108(m), 1070 (m), 1021 (m), 1007 (s), 917 (w), 887 (m), 834 (m), 821 (s), 806 (m), 722 (m), 669 (s).

Synthesis of trichloro(*N*-2-pyrimidylimidoyl-2-pyrimidylamidine)iron(III) (3.3b). A solution of **[PyH]$_2$[FeCl$_4$]** (0.14 g; 0.50 mmol) in DCM (7 mL) was added to a solution of **Pm$_2$ImAm** (0.12 g; 0.50 mmol) in DCM (7 mL). Immediately a bright yellow precipitate formed, which was filtered, washed with methanol and dried in air. Yield: 0.16 g (0.41 mmol, 79.8%). IR (cm^{-1}): *ν* 3252 (w), 3223 (s), 3095 (m), 3059 (m), 1644 (s), 1604 (w), 1576 (s), 1554 (m), 1394 (s), 1354 (s), 1231 (w), 1215 (m), 1128 (m), 1104 (m), 1030 (m), 1014 (s), 932 (s), 898 (w), 820 (s), 804 (m), 727 (s), 674 (s).

Synthesis of [Mn^{III}Mn$^{II}_3$(Pm$_2$ImAm)$_3$Cl$_6$]. A solution of **[(NH$_2$)$_2$PyH][Mn^{II}Cl$_3$·H$_2$O]** (0.62 g; 2.15 mmol) in methanol (10 mL) was added to a solution of **Pm$_2$ImAm** (0.36 g; 1.60 mmol) in MeCN (27 mL). After eight hours, green plate crystals formed, which were filtered, rinsed with ethanol and DCM, then dried in air. Yield: 0.33 g (0.29 mmol, 54.4%). IR (cm^{-1}): *ν* 3400 (br), 3220

(m), 3085 (w), 1612 (w), 1579 (w), 1557 (s), 1527 (w), 1459 (m), 1436 (w), 1404 (s), 1270 (m), 1222 (w), 1193 (m), 1097 (m), 1056 (m), 1015 (m), 982 (m), 820 (m), 710 (s).

Synthesis of $[Fe^{III}_4(Pm_2ImAm)_3Cl_9]$. A solution of **$[PyH]_2[FeCl_4]$** (0.28 g, 0.078 mmol) in DMSO (0.5 mL) was layered on top of a solution of **Pm_2ImAm** (0.12 g, 0.52 mmol) in chloroform (6 mL). After 5 days, black needle-like crystals formed, which were filtered, rinsed with chloroform, then dried in air. Yield: 0.055 g (0.045 mmol, 25.9%). Note: outside a chloroform environment, crystals of **$[Fe^{III}_4(Pm_2ImAm)_3Cl_9]$** degrade after a few hours due to solvent loss from the crystal lattice. IR (cm^{-1}): *v* 3259 (br), 3071 (br), 2989 (br), 2918 (br), 2851 (w), 1698 (m), 1612 (m), 1572 (w), 1557 (s), 1465 (m), 1404 (s), 1393 (w), 1271 (m), 1195 (m), 1098 (m), 1050 (m), 1022 (m), 998 (m), 950 (w), 800 (m), 740 (s), 704 (s), 668 (w).

X-ray crystallography. Data collection for the single crystals studied here (See Appendix B; Table B.6) were obtained on Bruker SMART APEX-II CCD diffractometer (graphite monochromated Mo K_α radiation, λ = 0.71073 Å, ω-scans with a 0.5° step in ω). Single crystals of **$[Mn^{III}Mn^{II}_3(Pm_2ImAm)_3Cl_6]$** and **$[Fe^{III}_4(Pm_2ImAm)_3Cl_9]$** were collected at 200 K while **$[Mn_2(\mu\text{-}Cl)_2(Pm_2ImAm)_2Cl_2]$** was collected at 210 K and **$[Fe^{III}(Pm_2ImAm)Cl_3]$** was collected at 239 K. Absorption corrections were applied by using the semi-empirical method of the SADABS program[38] for all samples with the exception of **$[Mn_2(\mu\text{-}Cl)_2(Pm_2ImAm)_2Cl_2]$** as it was twin and therefore TWINABS was applied instead. The structures were solved by SHELXT[39] and refined by full-matrix least-squares methods on F^2 with SHELXL-2015[40] in anisotropic approximation for all non-hydrogen atoms. Hydrogen atoms on the pyridine and pyrimidine rings were constrained to ride on their parent atoms with C—H = 0.95 A˚ and U_{iso} = 1.2U_{eq}(C), while imino N—H hydrogens were refined isotropically for all complexes. SADI restrain was used to associate the imino N-H distances with a 0.02 standard deviation in the all data sets. Part of the electron density contribution of solvent was removed using *Squeeze* protocol in crystal structures **$[Mn^{III}Mn^{II}_3(Pm_2ImAm)_3Cl_6]$** and **$[Fe^{III}_4(Pm_2ImAm)_3Cl_9]$**.[41]

Magnetic Measurements. To prevent solvent loss some samples were filtered immediately prior to sample preparation for the magnetic measurements. Samples of **$[Mn_2(\mu\text{-}Cl)_2(Pm_2ImAm)_2Cl_2]$** and **$[Fe^{III}(Pm_2ImAm)Cl_3]$** do not contain solvent in the crystal lattice and therefore the measurements were performed on a dry sample, and the molecular weight used was taken from the cif file. As explain in chapter 2, the octahedral bidentate complexes have numerous

solvates, so the complexes used for the measurements were **$[Mn^{III}(Py_2ImAm_3)]\cdot MeCN$** and **$[Fe^{III}(Py_2ImAm_3)]\cdot MeCN$** as they retain the crystallinity for longer periods of time when compared to the other solvates. Both **$[Mn^{III}(Py_2ImAm_3)]\cdot MeCN$** and **$[Fe^{III}(Py_2ImAm_3)]\cdot MeCN$** were filtered prior the measurements, and the molecular weight used was taken from the cif file. While **$[Mn^{III}Mn^{II}_3(Pm_2ImAm)_3Cl_6]$** is stable outside the mother liquor, **$[Fe^{III}_4(Pm_2ImAm)_3Cl_9]$** loses the crystallinity within 10 minutes exposed to air. In the case of **$[Mn^{III}Mn^{II}_3(Pm_2ImAm)_3Cl_6]$** dry sample was used for the measurements and the molecular weight was taken from the cif file. The solvent content in **$[Fe^{III}_4(Pm_2ImAm)_3Cl_9]$** was estimated by the number of electrons removed from the hkl file, as this complex was *squeezed*. The electrons removed were assumed to be the main solvent of the reaction (chloroform). The solvent estimation was included in the final molecular weight of **$[Fe^{III}_4(Pm_2ImAm)_3Cl_9]$**. Magnetic susceptibility measurements were performed with the use of a Quantum Design SQUID magnetometer MPMS-XL7 operating between 1.8 and 300 K for applied fields ranging from 0 to 7 T. Direct current (dc) magnetic susceptibility studies were performed on polycrystalline samples of **$[Mn^{III}(Py_2ImAm)_3]$** (10.5 mg), **$[Fe^{III}(Py_2ImAm)_3]$** (10.6 mg), **$[Fe^{III}(Pm_2ImAm)Cl_3]$** (10.4 mg), **$[Mn^{III}Mn^{II}_3(Pm_2ImAm)_3Cl_6]$** (16.4 mg), and **$[Fe^{III}_4(Pm_2ImAm)_3Cl_9]$** (11.7 mg). All samples were wrapped in a polyethylene membrane and silicon grease was utilized to restrain **$[Mn^{III}(Py_2ImAm)_3]$** and **$[Fe^{III}(Pm_2ImAm)Cl_3]$**. The magnetization data was collected at 100 K to check for ferromagnetic impurities, which were absent in all samples. Diamagnetic corrections were applied for the sample holder and the inherent diamagnetism of the sample was estimated with the used of Pascal's constants.

Mössbauer Spectroscopy. Mössbauer spectrum was recorded with a ^{57}Co source in an Rh matrix using an alternating constant acceleration Wissel mössbauer spectrometer operated in the transmission mode and equipped with a Janis closed-cycle helium cryostat. Isomer shifts are given relative to the iron metal at ambient temperature. Simulation of the experimental data was performed with the Mfit program: E. Bill, Max-Planck Institute for Chemical Energy Conversion, Mülheim/Ruhr, Germany.

3.11 References

[1] Ferreira, R. B.; Cook, B. J.; Knight, B. J.; Catalano, V. J.; García-Serres, R.; Murray, L. J., *ACS Catal.* **2018**, 7208-7212.

[2] Siedschlag, R. B.; Bernales, V.; Vogiatzis, K. D.; Planas, N.; Clouston, L. J.; Bill, E.; Gagliardi, L.; Lu, C. C., *J. Am. Chem. Soc.* **2015,** 137, (14), 4638-4641.

[3] Somerville, R. J.; Hale, L. V. A.; Gómez-Bengoa, E.; Burés, J.; Martin, R., *J. Am. Chem. Soc.* **2018,** 140, (28), 8771-8780.

[4] Bizzarri, C.; Spuling, E.; Knoll, D. M.; Volz, D.; Bräse, S., *Coord. Chem. Rev.* **2017**.

[5] Pedersen, K. S.; Bendix, J.; Clérac, R., *ChemComm* **2014,** 50, (34), 4396-4415.

[6] Ferreira, K. N.; Iverson, T. M.; Maghlaoui, K.; Barber, J.; Iwata, S., *Science* **2004,** 303, (5665), 1831.

[7] Thompson, L. K.; Dawe, L. N., *Coord. Chem. Rev.* **2015,** 289-290, 13-31.

[8] Duros, V.; Sartzi, H.; Teat, S. J.; Sanakis, Y.; Roubeau, O.; Perlepes, S. P., *Inorg. Chem. Commun.* **2014,** 50, 117-121.

[9] Kopylovich, M. N.; Lasri, J.; Guedes da Silva, M. F. C.; Pombeiro, A. J. L., *Dalton Trans.* **2009**, (16), 3074-3084.

[10] Kopylovich, M. N.; Kirillov, A. M.; Tronova, E. A.; Haukka, M.; Kukushkin, V. Y.; Pombeiro, A. J. L., *Eur. J. Inorg. Chem.* **2010,** , (16), 2425-2432.

[11] Kajiwara, T.; Kamiyama, A.; Ito, T., *ChemComm* **2002**, (12), 1256-1257.

[12] Glaser, T.; Theil, H.; Liratzis, I.; Weyhermüller, T.; Bill, E., *Inorg. Chem.* **2006,** 45, (13), 4889-4891.

[13] Leitch, A. A.; Korobkov, I.; Assoud, A.; Brusso, J. L., *ChemComm* **2014,** 50, (38), 4934-4936.

[14] Yousaf, M.; Yutronkie, N. J.; Castañeda, R.; Klein, J. A.; Brusso, J., *New J Chem* **2017,** 41, (20), 12218-12224.

[15] Casanova, D.; Llunell, M.; Alemany, P.; Alvarez, S., *Chem.: Eur. J.* **2005,** 11, (5), 1479-1494.

[16] Macrae, C. F.; Bruno, I. J.; Chisholm, J. A.; Edgington, P. R.; McCabe, P.; Pidcock, E.; Rodriguez-Monge, L.; Taylor, R.; van de Streek, J.; Wood, P. A., *J. Appl. Crystallogr.* **2008,** 41, (2), 466-470.

[17] Markosyan, A. S.; Gaidukova, I. Y.; Ruchkin, A. V.; Anokhin, A. O.; Irkhin, V. Y.; Ryazanov, M. V.; Kuz'mina, N. P.; Nikiforov, V. N., *Physica B* **2014,** 432, 53-57.

[18] Machura, B.; Palion, J.; Mroziński, J.; Kalińska, B.; Amini, M.; Najafpour, M. M.; Kruszynski, R., *Polyhedron* **2013,** 53, 132-143.

[19] Wu, J.-Z.; Bouwman, E.; Mills, A. M.; Spek, A. L.; Reedijk, J., *Inorganica Chim. Acta* **2004,** 357, (9), 2694-2702.

[20] Chilton, N. F.; Anderson, R. P.; Turner, L. D.; Soncini, A.; Murray, K. S., *J. Comput. Chem.* **2013,** 34, (13), 1164-1175.

[21] Colmer, H. E.; Margarit, C. G.; Smith, J. M.; Jackson, T. A.; Telser, J., *Eur. J. Inorg. Chem.* **2015,** 2016, (15-16), 2413-2423.

[22] Buschmann, W. E.; Liable-Sands, L.; Rheingold, A. L.; Miller, J. S., *Inorganica Chim. Acta* **1999,** 284, (2), 175-179.

[23] Blake, A. B.; Figgis, B. N.; Reynolds, P. A.; Engelhardt, L. M.; Moubaraki, B.; Murray, K. S., *Dalton Trans.* **1994**, (7), 1121-1123.

[24] Hansen, A. P.; Goff, H. M., *Inorg. Chem.* **1984,** 23, (26), 4519-4525.

[25] Landrum, J. T.; Hatano, K.; Scheidt, W. R.; Reed, C. A., *J. Am. Chem. Soc.* **1980,** 102, (22), 6729-6735.

[26] Basu, P.; Chakravorty, A., *Inorg. Chem.* **1992,** 31, (24), 4980-4986.

[27] Ganguly, S.; Karmakar, S.; Chakravorty, A., *Inorg. Chem.* **1997,** 36, (1), 116-118.

[28] Forshaw, A. P.; Smith, J. M.; Ozarowski, A.; Krzystek, J.; Smirnov, D.; Zvyagin, S. A.; Harris, T. D.; Karunadasa, H. I.; Zadrozny, J. M.; Schnegg, A.; Holldack, K.; Jackson, T. A.; Alamiri, A.; Barnes, D. M.; Telser, J., *Inorg. Chem.* **2013,** 52, (1), 144-159.

[29] Colmer Hannah, E.; Margarit Charles, G.; Smith Jeremy, M.; Jackson Timothy, A.; Telser, J., *Eur. J. Inorg. Chem.* **2015,** 2016, (15-16), 2413-2423.

[30] Kajiwara, T.; Ito, T., *Dalton Trans.* **1998**, (20), 3351-3352.

[31] Kamiyama, A.; Noguchi, T.; Kajiwara, T.; Ito, T., *Inorg. Chem.* **2002,** 41, (3), 507-512.

[32] Kajiwara, T.; Sensui, R.; Noguchi, T.; Kamiyama, A.; Ito, T., *Inorganica Chim. Acta* **2002,** 337, 299-307.

[33] F., W. R.; A., K., *Z. Anorg. Allg. Chem.* **1921,** 120, (1), 209-231.

[34] Caputo, R.; Willett, R. D.; Morosin, B., *J. Chem. Phys* **1978,** 69, (11), 4976-4983.

[35] Felloni, M.; Hubberstey, P.; Wilson, C.; Schroder, M., *CrystEngComm* **2004,** 6, (19), 87-95.

[36] Blachnik, R.; Eickmeier, H.; Gather, M.; Reuter, H., *Z. Kristallogr. - New Cryst. Struct.* **2000,** 215, (1), 93-94.

[37] Brassy, C.; Robert, R.; Bachet, B.; Chevalier, R., *Acta Crystallogr. B* **1976,** 32, (5), 1371-1376.

[38] Bruker *APEX3, SAINT, SADABS and TWINABS*, Bruker Analytical X-ray Instruments Inc.: Madison, WI, 2016.

[39] Sheldrick, G., *Acta Cryst. A* **2015,** 71, (1), 3-8.

[40] Sheldrick, G., *Acta Cryst. C* **2015,** 71, (1), 3-8.

[41] Spek, A., *Acta Cryst. C* **2015,** 71, (1), 9-18.

Chapter 4

Controlling the Nuclearity and Topology of Cobalt Complexes Through Hydration

Authorship disclosure: A version of this chapter was published in *Journal of Material Chemistry C* as "Controlling the nuclearity and topology of cobalt complexes through hydration at the ppm level" R. Castañeda, M. Mathieu Rouzières, R. Clérac, J. L. Brusso, *J. Mater. Chem. C*. The synthesis of all compounds was performed by Luis Raúl Castañeda Perea. The single crystal structures presented in this chapter were collected and refined by Luis Raúl Castañeda Perea. The collection of the magnetic data and interpretation was done by Mathieu Rouzières, and professor Rodolphe Clérac.

4.1 Introduction

Complexes comprised of transition metal ions coordinated to bidentate organic ligands such as acetylacetonate (**4.1a**; acac; Chart 4.1) and 1,3-diketoiminate (**4.2a**; nacnac; Chart 4.1), or tridentate ligands like terpyridine (**4.3a**; terpy; Chart 4.1) have been extensively studied for a number of applications including, but not limited to, the reduction of carbon dioxide to oxalate,[1] water splitting,[2] coupling reactions,[3, 4] magnetic materials,[5, 6] and molecular switches.[7] Although much less studied, *N*-imidoylamidine (ImAm) ligands may be considered as triaza analogues of acac/nacnac, representing excellent candidates for the development of coordination complexes. Furthermore, resulting from the presence of the central nitrogen atom within the triaza moiety, sagacious selection of the β-substituents facilitates the development of two distinct coordination environments within a single rigid framework.

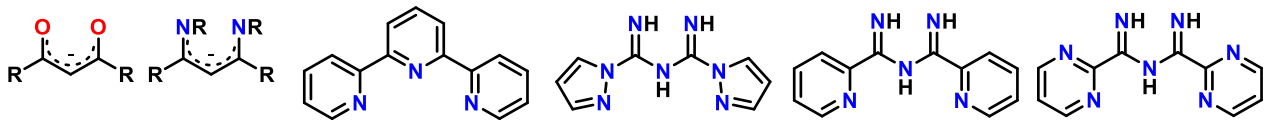

Chart 4.1. Structure of acetylacetonate (acac), 1,3-diketoiminate (nacnac) and *N*-imidoylamidine (ImAm) ligands including Pz_2ImAm, Py_2ImAm and Pm_2ImAm.

Interestingly, while *N*-imidoylamidine based ligands possessing both a bidentate and tridentate coordination site hold great appeal, only a few examples can be found in literature.[8] This is likely due to the generation of these ligands, which until recently were only prepared in one pot synthetic procedures through metal-assisted transformations. For example, the first ImAm-based complex to be reported was prepared through thermal decomposition of triazine in the presence of copper(II), resulting in the formation of a square planar copper complex in which unsubstituted ImAm is coordinated in a bidentate fashion.[9] Two years later, Boča *et al.* synthesized a similar system via nucleophilic addition of methanol to dicyanamidinate, resulting in a methoxy substituted ImAm ligand.[10] These results inspired the synthesis of a trinuclear copper complex prepared under similar conditions with the addition of pyrazole. This reaction afforded *N*-1-pyrazolylimidoyl-1-pyrazolylamidine (**4.4a**; Pz_2ImAm; Chart 4.1), in which two Pz_2ImAm ligands coordinate in a bidentate fashion to a central Cu^{II} ion with two additional Cu^{II} metal ions bound to the tridentate pocket of each Pz_2ImAm.[11] Subsequent work employing the aforementioned trinuclear moiety as the starting material and reacting it with EDTA enabled isolation of **$[Cu^{II}(Pz_2ImAm)_2]$** (**1.5b**) and therefore facilitated the development of hetero-trinuclear complexes **$[M_2Cu^{II}(Pz_2ImAm)_2][ClO_4]_4$** (where M = Mn, Co or Ni).[12] In these systems, Pz_2ImAm acts as a ferromagnetic linker between metal ion sites.[11, 12] Recently, Starikova[13] conducted a computational study to predict the magnetic properties of trinuclear heterometallic complexes of the general formula **$[M^{II}_2M^{II}(Pz_2ImAm)_2terpy_2]$**, in which the central M^{II} ion coordinates to two Pz_2ImAm in either square planar or tetrahedral geometry. Using various first row transition metal ions (M^{II}), many of these systems were predicted to exhibit two-step spin-crossover phenomenon.[13]

Similar ligand frameworks incorporating pyridyl (**4.5a**; *N*-2-pyridylimidoyl-2-pyridylamidine; Py_2ImAm) or pyrimidyl (**4.6a**; *N*-2-pyrimidylimidoyl-2-pyrimidylamidine; Pm_2ImAm) moieties at the *β*-position have also been reported;[4, 14-17] however, here again the ImAm ligands were prepared through metal-assisted transformations using a metal salt and a pyridyl/pyrimidyl synthon. For example, a copper coordination polymer or dimer can be isolated following decomposition of either tris(2-pyridyl)triazine[14] or tris(2-pyrimidyl)triazine,[15] respectively, in the presence of copper(II) salts. Similar to the Pz_2ImAm complexes, the ligand acts to ferromagnetically couple the adjoining Cu^{II} ions. Py_2ImAm complexes have also been reported through *in situ* reactions of 2-cyanidopyridine and butan-2-one oxime with $PdCl_2$ to make

a palladium (II) square planar complex,[4] or pyridine-2-amidoxime with MnF_2 resulting in a manganese (III) octahedral complex.[17]

While these studies demonstrate the potential of ImAm ligands, a significant drawback lies in their synthesis, which relies on relatively low yielding *in situ* reactions.[8] Recently, our group developed the synthesis of both Py_2ImAm[18] and Pm_2ImAm[19] in large scale without metal ion assistance, thereby enabling us to tailor the reaction conditions in order to selectively bind to the bidentate and/or tridentate coordination sites. In that regard, in the second chapter it is established the synthetic methodology to control the topology with first row transition metal ions (e.g. Mn, Fe, Co) affording mononuclear, dinuclear and tetranuclear complexes.[20, 21] These studies demonstrate that the key factor in controlling coordination site preference (i.e. bidentate *vs*. tridentate) is the presence (or absence) of a weak acid. Having resolved the necessary conditions to selectively coordinate the specific sites in ImAm-based ligands in the second chapter, and determined the methodology to isolate tetranuclear **$[M_4(Pm_2ImAm)_3Cl_x]$** complexes (where x = 6 or 9) in the third chapter, the versatility of this ligand framework was probed in the development of polynuclear complexes possessing square planar geometry at the central metal ion. To that end, presented herein are the synthesis, structural analysis and magnetic characterization of the trinuclear and hexanuclear complexes, **$[Co^{II}_3(Pm_2ImAm)_2Cl_4]$** (**4.1b**) and **$[Co^{II}_6(\mu\text{-}Cl)_2(Pm_2ImAm)_4Cl_8]$** (**4.2b**), respectively. To help elucidate the electronic structure of the polynuclear complexes, the structural and magnetic properties of the mononuclear species, **$[Co^{II}(Py_2ImAm)_2]$** (**4.3b**), is also reported. Similar to the third chapter the results reveal a unique combination of spin states within the polynuclear complexes, namely low-spin (LS) Co^{II} central ions and high-spin (HS) Co^{II} ions at the periphery, where the nuclearity and topology are determined by precise control at the ppm level (e.g. 300 ppm *vs*. 10000 ppm) of hydration.

4.2 Synthesis and Crystallographic Description of the Central Mononuclear Complex $[Co^{II}(Py_2ImAm)_2]$

As discussed in the second chapter, the coordination environment of first row transition metals in either a bidentate or tridentate fashion with ImAm ligands can be controlled by tailoring the reaction conditions.[20] Following a similar procedure, selective bidentate coordination was achieved by employing basic reaction media. The key difference here is the use of anaerobic conditions, which led to the isolation of **$[Co^{II}(Py_2ImAm)_2]$**, as opposed to its octahedrally coordinated analog **$[Co^{III}(Py_2ImAm)_3]$** presented in the second chapter. More specifically, **$[Co^{II}(Py_2ImAm)_2]$** can be prepared on a multigram scale by combining a solution of Py_2ImAm and triethylamine (Et_3N) in acetonitrile (MeCN) with a dimethylformamide (DMF) solution of $Co(acac)_2$ under nitrogen atmosphere (Scheme 4.1). After leaving the resulting solution to stand for three days, orange block-like crystals suitable for X-ray analysis were obtained confirming the identity of **$[Co^{II}(Py_2ImAm)_2]$**. In this complex, which crystallizes in the monoclinic space group *$P2_1/n$*, the cobalt ion is coordinated to two Py_2ImAm ligands in a bidentate fashion leading to a nearly ideal square planar configuration (Figure 4.1), a geometry and ligand field strength commonly associated with a low spin configuration.[22, 23] Deprotonation of the *N*-imidoylamidine ligands in **$[Co^{II}(Py_2ImAm)_2]$** suggest an oxidation state of +2 for the cobalt ion, which is further supported by the magnetic analysis (*vide infra*). Within the supramolecular structure, the molecules arrange into a herringbone fashion (Figure 4.1) leading to two π-π interactions (3.6389(3) and 3.7593(3) Å) between the pyridyl rings of the ligand framework on neighbouring complexes and a Co-Co distance of 7.738(1) Å.

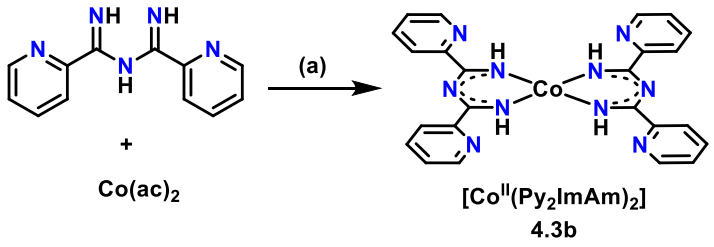

Scheme 4.1. Synthesis of **$[Co^{II}(Py_2ImAm)_2]$**. Conditions: (a) MeCN/DMF, triethylamine as base and inert atmosphere.

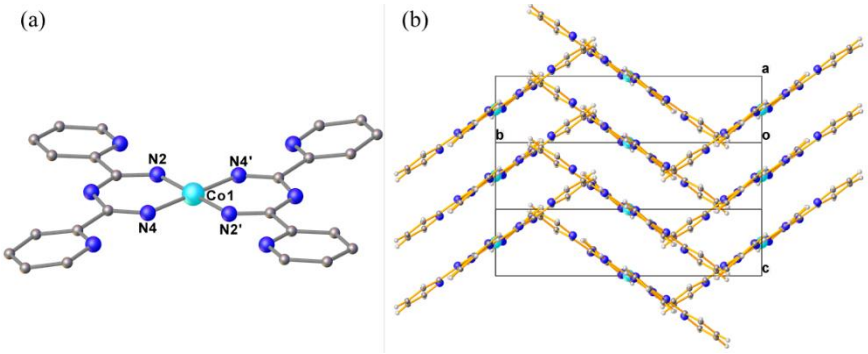

Figure 4.1. (a) Structural diagram of **[Co^{II}(Py$_2$ImAm)$_2$]**. (b) Crystal packing of **[Co^{II}(Py$_2$ImAm)$_2$]** viewed along the 201 plane.

4.3 Synthesis of Trinuclear and Hexanuclear Complexes

Having isolated the mononuclear square planar cobalt complex, the next step was naturally to explore the possibility to synthesize polynuclear systems taking advantage of both coordination sites available within these *N*-imidoylamidine ligand frameworks. Previously, we demonstrated that the employment of metal salts containing slightly acidic counter ions such as pyridinium was an effective method in the isolation of tetranuclear complexes with *N*-imidoylamidines.[21] In the same vein, both **[Co$^{II}_3$(Pm$_2$ImAm)$_2$Cl$_4$]** and **[Co$^{II}_6$(μ-Cl)$_2$(Pm$_2$ImAm)$_4$Cl$_8$]** can be prepared upon adding a methanolic solution of *bis*(pyridinium) tetrachlorocobaltate(II) (**[PyH]$_2$[Co^{II}Cl$_4$]**) to a stirring solution of Pm$_2$ImAm in DCM under inert conditions (Scheme 4.2). The key difference between isolation of the trinuclear *vs*. hexanuclear cobalt complexes is in the degree of hydration of the methanol. In other words, the water content of the methanol leads to crystallization of complexes with different nuclearity. For example, when the water content is 10000 ppm (99% MeOH) the trinuclear complex is formed, whereas the hexanuclear complex is isolated when 99.97% (300 ppm) MeOH is employed. Interestingly, when the water content in the solvent is greater than 10000 ppm, nothing is recovered from the reaction mixture – i.e. neither complex is isolated nor any other coordination complex. In either case, leaving the reaction mixture to stand for two days affords red plate-like crystals of **[Co$^{II}_3$(Pm$_2$ImAm)$_2$Cl$_4$]·5H$_2$O** or block-like crystals of **[Co$^{II}_6$(μ-Cl)$_2$(Pm$_2$ImAm)$_4$Cl$_8$]·2MeOH·2DCM** suitable for single crystal X-ray diffraction (SCXRD). For the reported compounds, a single crystalline phase of the as-synthesized products were confirmed through SCXRD and Powder X-ray diffraction (See Appendix E; Figures E.1-E.3).

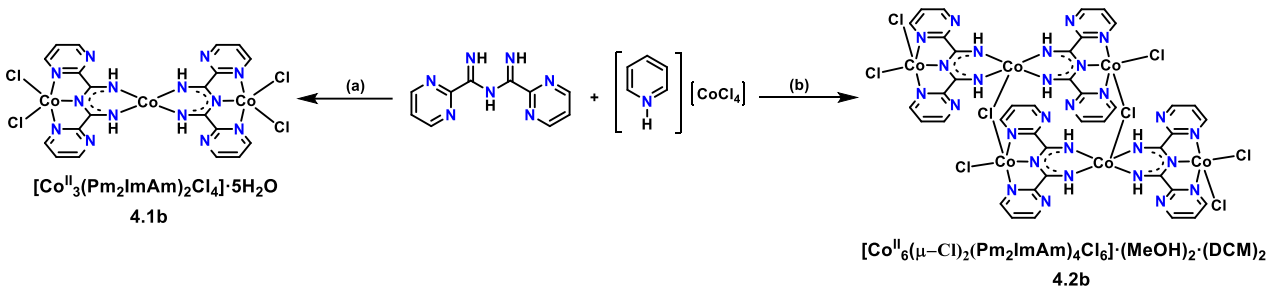

Scheme 4.2. Synthesis of complexes **[Co^{II}$_3$(Pm$_2$ImAm)$_2$Cl$_4$]·5H$_2$O** and **[Co^{II}$_6$(μ-Cl)$_2$(Pm$_2$ImAm)$_4$Cl$_6$]·2MeOH·2DCM** employing the Pm$_2$ImAm ligand. Conditions: (a) MeOH(99%)/DCM; (b) MeOH(99.97%)/DCM.

4.4 Structural Analysis of [Co^{II}$_3$(Pm$_2$ImAm)$_2$Cl$_4$]·5H$_2$O

Crystals of **[Co^{II}$_3$(Pm$_2$ImAm)$_2$Cl$_4$]·5H$_2$O**, which belong to the triclinic *P*-1 space group, contain two crystallographically independent molecules in the asymmetric unit with a point of inversion located at the central cobalt ion of each molecule. Nonetheless, these crystallographically independent complexes have essentially the same geometry and metal to ligand bond distances (Figure 4.2, and Table 4.2). In **[Co^{II}$_3$(Pm$_2$ImAm)$_2$Cl$_4$]·5H$_2$O**, each Pm$_2$ImAm ligand is anionic and coordinates to two Co ions resulting in two distinct Co moieties – one coordinated in a bidentate fashion, the other in the tridentate pocket of the ligand (Figure 4.2). The central Co ions (Co1 and Co3), are bound to two anionic Pm$_2$ImAm ligands in a bidentate fashion, adopt a nearly ideal square planar environment that is very similar to that of the mononuclear complex **[Co^{II}(Py$_2$ImAm)$_2$]** (as highlighted in the overlay of the two structures in Figure 4.2c). Comparing the Co–N distances of the central metal in **[Co^{II}$_3$(Pm$_2$ImAm)$_2$Cl$_4$]** to those of **[Co^{II}(Py$_2$ImAm)$_2$]** reveal a nominal elongation of these bonds upon development of the polynuclear complex (1.847(1)-1.856(1) Å in **[Co^{II}(Py$_2$ImAm)$_2$]** to 1.86509(13)-1.88734(11) Å in **[Co^{II}$_3$(Pm$_2$ImAm)$_2$Cl$_4$]**). This slight elongation suggests the metal ion remains in the same oxidation (i.e. +2) and spin (*vide infra*) states for both complexes, and the Co–N distances of both complexes are in the expected range for low spin Co(II) ions.[23-25] The outer cobalt ions (Co2 and Co4) are pentacoordinate with the metal ion residing within the plane of the tridentate Pm$_2$ImAm ligand. The remaining metal coordination environment is filled by two Cl anions above and below the plane of the ligand framework. Analysis of the coordination geometry using SHAPE[26] suggests the coordination environment about the peripheryl Co ions is in between square pyramidal and

trigonal bipyramidal (Table 4.2 and Figure 4.3). Interestingly, the coordination environment of the outer cobalt ions is very similar to that observed in the tridentate mononuclear complex **[Co^{II}(Py$_2$ImAm)Cl$_2$]** reported in chapter 2.[20] Based on the above mentioned similarities, along with charge balance, this would suggest an oxidation state of +2 for these cobalt ions. A review of related cobalt(II) complexes in literature that possess similar geometries and coordination spheres as Co2 and Co4 (i.e. one terpy-like ligand and two chloride ions) suggest these metal centres adopt high spin S = 3/2 configurations based on structural arguments.[6, 27, 28]

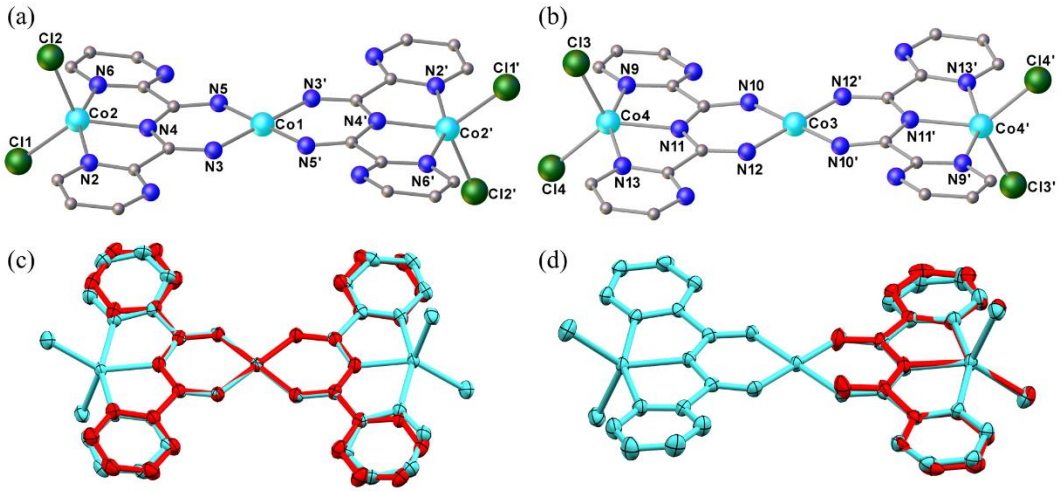

Figure 4.2. (a-b) Structural diagram for both crystallographically independent molecules in **[Co$^{II}_3$(Pm$_2$ImAm)$_2$Cl$_4$]**. (c) Structural overlay of mononuclear complex **[Co^{II}(Py$_2$ImAm)$_2$]** (red) with trinuclear complex **[Co$^{II}_3$(Pm$_2$ImAm)$_2$Cl$_4$]** (blue). (d) Structural overlay of **[Co^{II}(Py$_2$ImAm)Cl$_2$]** (red) with **[Co$^{II}_3$(Pm$_2$ImAm)$_2$Cl$_4$]** (blue). Hydrogen atoms have been omitted for clarity.

Table 4.1. Relevant cobalt bond distances in **4.1b** at 200 K.

Molecule A			**Molecule B**		
Connectivity	Type	Distance (Å)	Connectivity	Type	Distance (Å)
N5 to Co1	Square planar	1.87911(13)	N10 to Co3	Square planar	1.86476(13)
N3 to Co1	Square planar	1.87931(11)	N12 to Co3	Square planar	1.88707(11)
N4 to Co2	Terpy central N	2.02538(14)	N11 to Co4	Terpy central N	2.03279(14)
N6 to Co2	Terpy	2.14924(15)	N13 to Co4	Terpy	2.14839(15)
N2 to Co2	Terpy	2.14610(12)	N9 to Co4	Terpy	2.14686(12)
Cl1 to Co2	Chloride	2.28003(12)	Cl3 to Co4	Chloride	2.28273(12)
Cl2 to Co2	Chloride	2.27888(13)	Cl4 to Co4	Chloride	2.27468(15)

*There are two crystallographic independent molecules

Table 4.2. Results from shape analysis and *tau* parameters for the pentacoordinate cobalt atoms in **[Co^{II}_3(Pm2ImAm)2Cl4]**.

Molecule	Metal Centre	PP-5	vOC-5	TBPY-5	SPY-5	JTBPY-5	τ
Molecule A	Co2	31.316	5.310	2.487	2.950	6.037	0.36
Molecule B	Co4	31.026	5.789	2.425	3.257	6.006	0.40

PP-5: D_{5h}, Pentagon; vOC-5: C_{4v}, Vacant octahedron; TBPY-5: D_{3h}, Trigonal bipyramid; SPY-5: C_{4v}, Spherical square pyramid; JPPY-6: C_{5v}, Johnson trigonal bipyramid J12

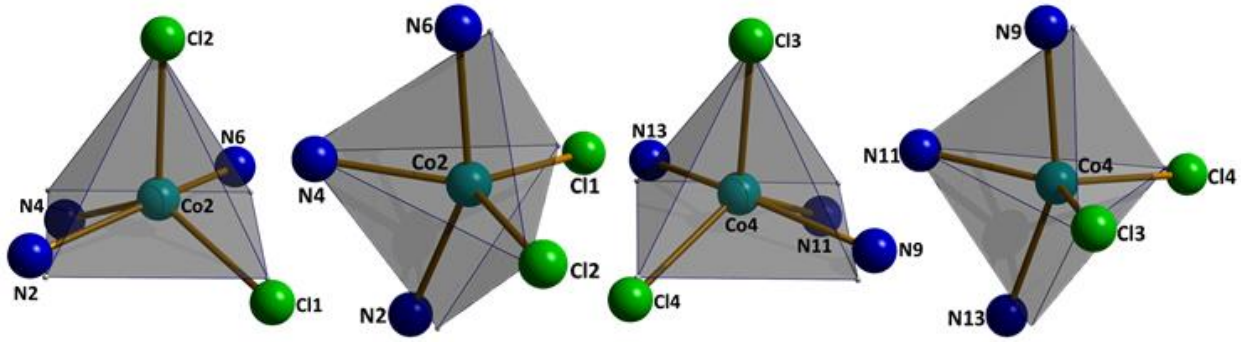

Figure 4.3. Deviation from ideal square pyramidal or trigonal bipyramidal within each molecule in **4.1b**. Cobalt atoms are depicted light blue and located in the centre of an ideal square pyramid or trigonal bipyramid.

4.5 Crystal Packing Description of [Co^{II}_3(Pm2ImAm)2Cl4]·5H2O

Crystal packing of **[Co^{II}_3(Pm2ImAm)2Cl4]·5H2O** is comprised of columnar stacks of alternating complexes that are twisted by 85° with respect to the neighbouring molecules above and below (Figure 4.4a). This structural feature likely results from the peripheral cobalt dichloride moiety, which is bulky enough to align the square planar portion of the complexes in a staggered fashion to one other. As a result, a Co-Co distance of 3.6268(3) Å is found between the central metal ions (Co1 and Co3, gray dashed line in Figure 4.4a), which is significantly shorter than the intramolecular Co-Co distances (i.e. Co1-Co2 = 5.2932(4) Å; Co3-Co4 = 5.2981(4) Å). This proximity between neighbouring molecules within the stacked array also leads to short Co-N contacts (3.2523(2) - 3.2582(2) Å) and other relatively close Co-Co interactions (5.6865(3), 5.7287(4) Å). In addition to playing a pivotal role in the synthesis of the tri *vs*. hexanuclear complex, water also plays an important role in the formation of the extended stacks as each water molecule is connected to three different trinuclear molecules by a set of intra-stack hydrogen bonds (Figure 4.4b and Table B.12). Within the columnar packing arrangement of

[Co^{II}_3(Pm_2ImAm)$_2Cl_4$], extended solvent channels are observed (Figure 4.5), with the total volume of these channels being 17.5% of unit cell volume using a probe radius of 1.2 Å in Mercury.[29] Solvent molecules located in these channels lack of intermolecular interactions, and therefore they were *squeezed*.[30] To asses the amount of solvent in these channels TGA was used, and it shows a 6% weight loss below 100 °C followed by a plateau up to 350 °C (Figure 4.5c). Given the molecular weight of **[Co^{II}_3(Pm_2ImAm)$_2Cl_4$]·$5H_2O$** is 865.15 g/mol and five water molecules accounts for 90.08 g/mol, a loss of all the water molecules should lead to 10%. Since only 6% weight loss is observed, this corresponds to the loss of three water molecules, which is consistent with the SCXRD as two of the five water molecules are bound to the **[Co^{II}_3(Pm_2ImAm)$_2Cl_4$]** framework through hydrogen bonds. As such, we would only expect to see a weight loss consistent with three water molecules below 100 °C. Although solvent voids exist between the columnar packing arrangement of **[Co^{II}_3(Pm_2ImAm)$_2Cl_4$]**, a number of inter-stack interactions are present, primarily composed of weak C-H···Cl hydrogen bonds (See Appendix B; Table B.12). Compared to intra-stack, the inter-stack interactions are much more limited, leading to Co-Co distances between columns that are much longer (e.g. ≥ 7.0704(4) Å; Tables B.13-B.14).

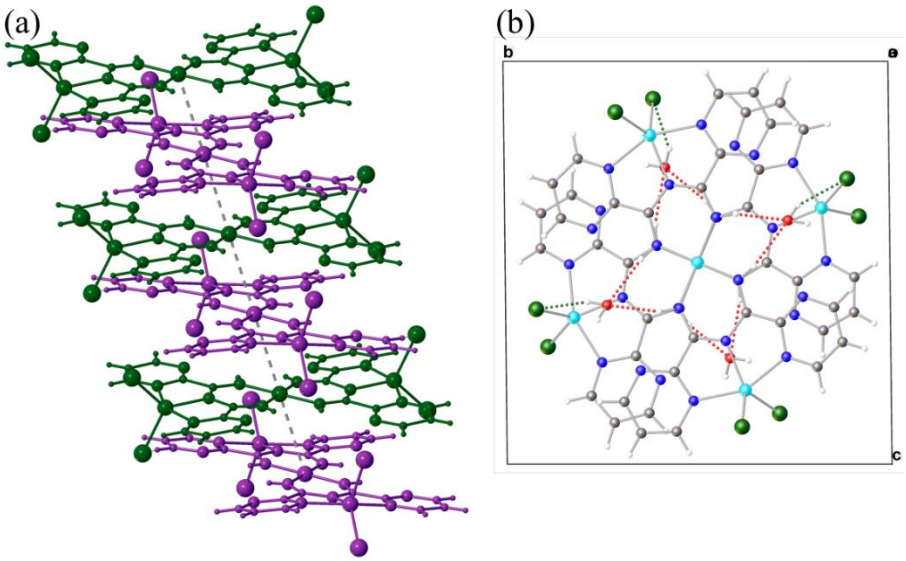

Figure 4.4. (a) View of a single stack in **4.1b** with independent crystallographic molecules in different colour. A gray dashed line was drawn to indicate short Co-Co distances. (b) Top view of

a single stack along the (100) plane in **4.1b**. N-H···O hydrogen bonds are denoted as red dashed lines, and O-H···Cl as green dashed lines.

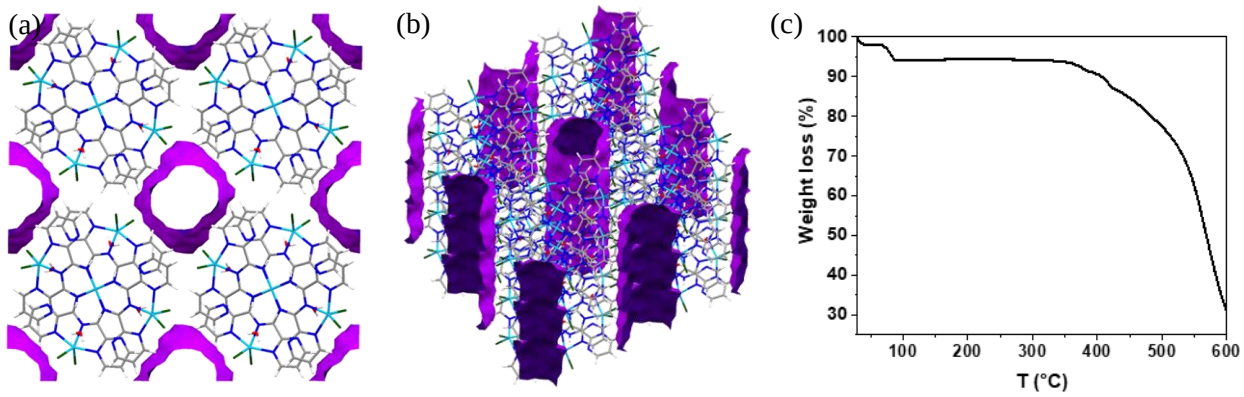

Figure 4.5. (a) Top view and (b) side view of solvent channels in **4.1b**. (c) TGA of **4.1b** demonstrating a weight loss corresponding to three water molecules below 100 °C.

4.6 Structural Analysis of $[Co^{II}_6(\mu\text{-}Cl)_2(Pm_2ImAm)_4Cl_8]\cdot 2MeOH\cdot 2DCM$

Perhaps unsurprisingly, many similarities exist between the molecular structure of **$[Co^{II}_6(\mu\text{-}Cl)_2(Pm_2ImAm)_4Cl_8]\cdot 2MeOH\cdot 2DCM$** and **$[Co^{II}_3(Pm_2ImAm)_2Cl_4]\cdot 5H_2O$**. The former, which crystallizes in the monoclinic *P2₁/c* space group, may be considered as two linear trinuclear moieties similar to **$[Co^{II}_3(Pm_2ImAm)_2Cl_4]$** that are linked together through two bridging chloride ions (Figure 4.6). This leads to three unique cobalt centres and is consistent with the asymmetric unit of **$[Co^{II}_6(\mu\text{-}Cl)_2(Pm_2ImAm)_4Cl_8]\cdot 2MeOH\cdot 2DCM$**, which is located about a point of inversion. Within the asymmetric unit, the central Co ion (Co1) is pentacoordinate, bound to two anionic Pm_2ImAm ligands in a bidentate fashion with a bridging chloride ion completing the coordination environment. As revealed by SHAPE[26] analysis, the geometry of this central cobalt ion is best described as nearly ideal square pyramidal (Table 4.3 and Figure 4.7), with a longer Co-Cl bond (2.628(3) Å) when compared to the other Co-Cl bonds (2.286(2)- 2.298(3) Å) within this complex. The change in geometry from square planar to square pyramidal results in elongation of the Co-N distances in **$[Co^{II}_6(\mu\text{-}Cl)_2(Pm_2ImAm)_4Cl_8]\cdot 2MeOH\cdot 2DCM$** (1.888(7)-1.918(7) Å) compared to **$[Co^{II}_3(Pm_2ImAm)_2Cl_4]\cdot 5H_2O$** (1.86509(13)-1.88734(11) Å). Although the polynuclear complexes are rather similar, the differences between them can been seen in the overlay shown in Figure 4.6. Interestingly, the geometry of all three unique cobalt ions in **$[Co^{II}_6(\mu\text{-}$**

Cl)$_2$(Pm$_2$ImAm)$_4$Cl$_8$]·2MeOH·2DCM is closer to square pyramidal than trigonal bipyramidal as indicated by the τ parameter[31] (i.e. 0.01, 0.09 and 0.14 for Co1, Co2 and Co3, respectively). It is worth mentioning that SHAPE[26] analysis also reveal these three cobalt centres as being closer to square pyramidal than trigonal bipyramidal (Figure 4.7). The interplanar distance between the ligands with bridging groups within the hexanuclear complex is very short (3.189(8) Å), resulting in π-π interactions between the pyrimidyl rings of the Pm$_2$ImAm ligand coordinated to Co3.

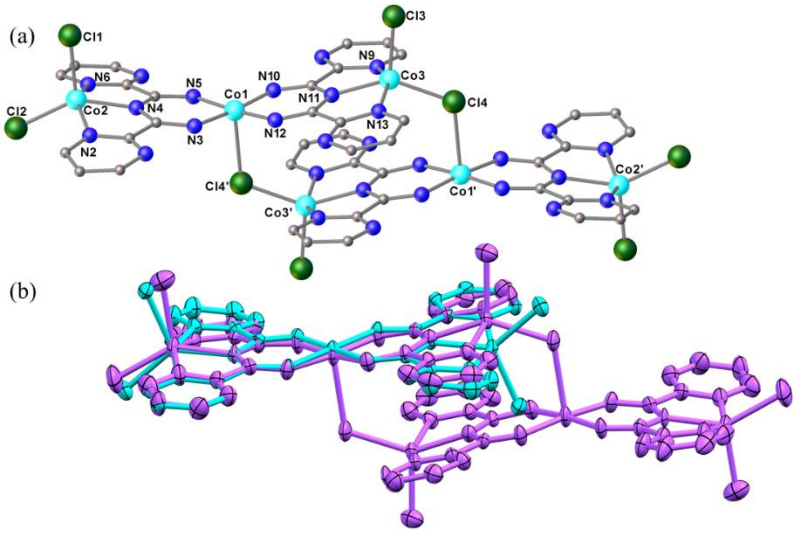

Figure 4.6. (a) Structural diagram of **[Co$^{II}_6$(*μ*-Cl)$_2$(Pm$_2$ImAm)$_4$Cl$_8$]·2MeOH·2DCM**. (b) Structural overlay of trinuclear complex **[Co$^{II}_3$(Pm$_2$ImAm)$_2$Cl$_4$]** (blue) with hexanuclear complex **[Co$^{II}_6$(*μ*-Cl)$_2$(Pm$_2$ImAm)$_4$Cl$_8$]** (violet). Hydrogen atoms have been omitted for clarity.

Table 4.3. Results from shape analysis and *tau* parameters for the pentacoordinate cobalt atoms in **[Co$^{II}_6$(*μ*-Cl)$_2$(Pm$_2$ImAm)$_4$Cl$_8$]**.

Metal Centre	PP-5	vOC-5	TBPY-5	SPY-5	JTBPY-5	τ
Co1	34.254	2.195	6.235	1.076	9.774	0.01
Co2	32.738	3.720	4.482	1.375	8.197	0.09
Co3	31.124	3.752	4.127	1.647	7.584	0.14

PP-5: D_{5h}, Pentagon; vOC-5: C_{4v}, Vacant octahedron; TBPY-5: D_{3h}, Trigonal bipyramid; SPY-5: C_{4v}, Spherical square pyramid; JPPY-6: C_{5v}, Johnson trigonal bipyramid J12

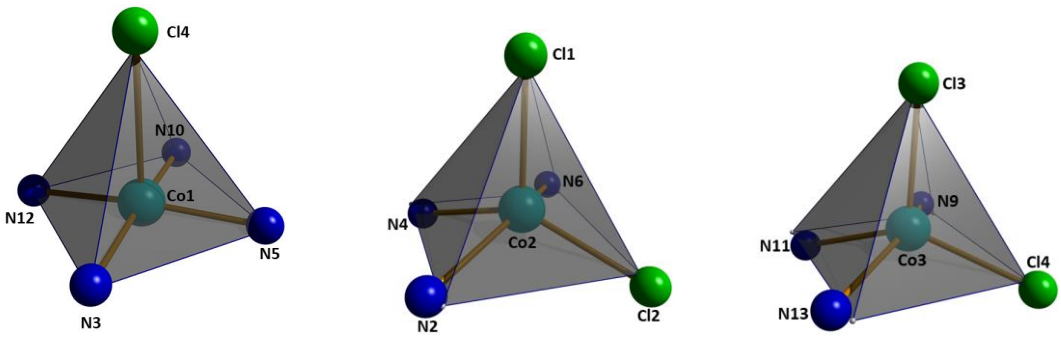

Figure 4.7. Deviation from ideal square pyramidal geometry in **4.2b** at 200 K. Cobalt atoms are depicted light blue and located in the centre of an ideal square pyramid.

4.7 Crystal Packing Description of $[Co^{II}_6(\mu\text{-}Cl)_2(Pm_2ImAm)_4Cl_8]\cdot 2MeOH\cdot 2DCM$

Crystal packing of **$[Co^{II}_6(\mu\text{-}Cl)_2(Pm_2ImAm)_4Cl_8]\cdot 2MeOH\cdot 2DCM$** is composed of a brick-like array of hexanuclear complexes (Figure 4.8), that are connected by weak C-H···Cl hydrogen bonds (See Appendix B; Table B.12). Within the supramolecular structure, two crystallographically independent solvent molecules were refined (i.e. DCM and MeOH). While dichloromethane is disordered and occupies a solvent void, methanol molecules act as a hydrogen bond acceptor from the imino hydrogen atoms of one complex and a hydrogen bond donor to a chloride ion in a neighbouring molecule in the plane below. Here, MeOH plays a similar role to water in **$[Co^{II}_3(Pm_2ImAm)_2Cl_4]\cdot 5H_2O$**, although in this case it acts as a hydrogen donor to only one complex instead two. Dichloromethane has a Cl-Co contact with Co1, which is equal to 3.314(7) Å, and shorter than the sum of van der Walls radii of cobalt and chlorine.[32, 33] The shortest Co-Co distance in **$[Co^{II}_6(\mu\text{-}Cl)_2(Pm_2ImAm)_4Cl_8]\cdot 2MeOH\cdot 2DCM$** is 4.1544(17) Å (Co1-Co3), which is longer than that found in **$[Co^{II}_3(Pm_2ImAm)_2Cl_4]\cdot 5H_2O$** (3.6268(3) Å). This is to be expected due to the chloride bridging ions separating the planar trinuclear fragments in **$[Co^{II}_6(\mu\text{-}Cl)_2(Pm_2ImAm)_4Cl_8]$**, which are not present in **$[Co^{II}_3(Pm_2ImAm)_2Cl_4]$** allowing for close association between the central Co^{II} ions between neighbouring molecules. The distance between the central (Co1) and the outer (Co2 and Co3) cobalt ions are the essentially the same (5.2969(17) and 5.2881(16) Å, respectively), and are comparable to the values found in **$[Co^{II}_3(Pm_2ImAm)_2Cl_4]\cdot 5H_2O$**. As well, a number of close intermolecular Co-Co interactions are present in **$[Co^{II}_6(\mu\text{-}Cl)_2(Pm_2ImAm)_4Cl_8]\cdot 2MeOH\cdot 2DCM$**, the shortest being 6.628(2) Å. A comprehensive list of Co-Co distances can be found in Appendix B (Tables B.15-B.16).

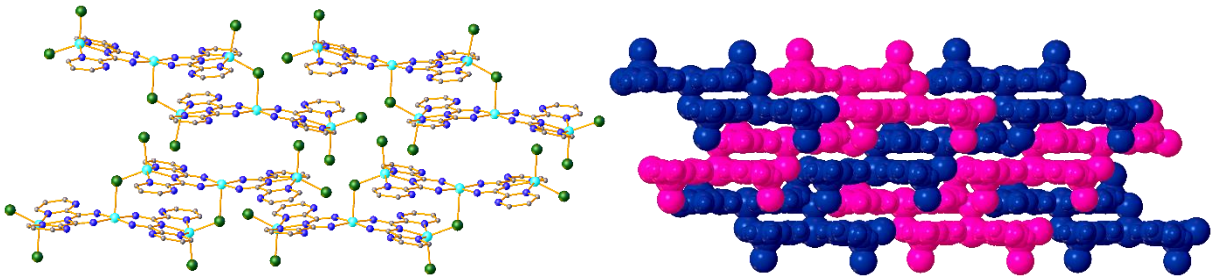

Figure 4.8. Two views of the brick-like packing of **4.2b** at 200 K. In the right figure individual molecules are differentiated by colour coding in blue and pink.

4.8 Magnetochemistry of the Central Mononuclear Complex [$Co^{II}(Py_2ImAm)_2$]

To investigate the magnetic behaviour of both **[$Co^{II}_3(Pm_2ImAm)_2Cl_4$]·$5H_2O$** and **[$Co^{II}_6(\mu$-$Cl)_2(Pm_2ImAm)_4Cl_6$]·2MeOH·2DCM**, variable-temperature magnetic susceptibility data was collected on polycrystalline samples. For comparative purposes, magnetic susceptibility studies were also performed on **[$Co^{II}(Py_2ImAm)_2$]**, revealing a χT product of 0.48 cm^3 K mol^{-1} at room temperature (Figure 4.9). This value is larger than what is expected for low spin Co^{II} from the spin-only formalism (C = 0.375 cm^3 K mol^{-1}; assuming g = 2) indicating a g value around 2.26(5). Upon lowering the temperature, the χT product remains relatively constant until 10 K, where a decrease in the χT product is observed until it reaches 0.43 cm^3 K mol^{-1} at 1.9 K. This decrease at low temperature is likely due to very weak antiferromagnetic intermolecular interactions between spin-carriers estimated at -0.13 K from a Curie-Weiss fit ($\theta = 2zJS(S+1)/3k_B$ = -0.26 K, z = 4). The field dependence of the magnetization is also in good agreement with a low spin S = ½ configuration of the Co^{II} centre (Figure 4.9), as confirmed via fitting to the S = ½ Brillouin function, which affords a consistent g-factor of 2.16(5).

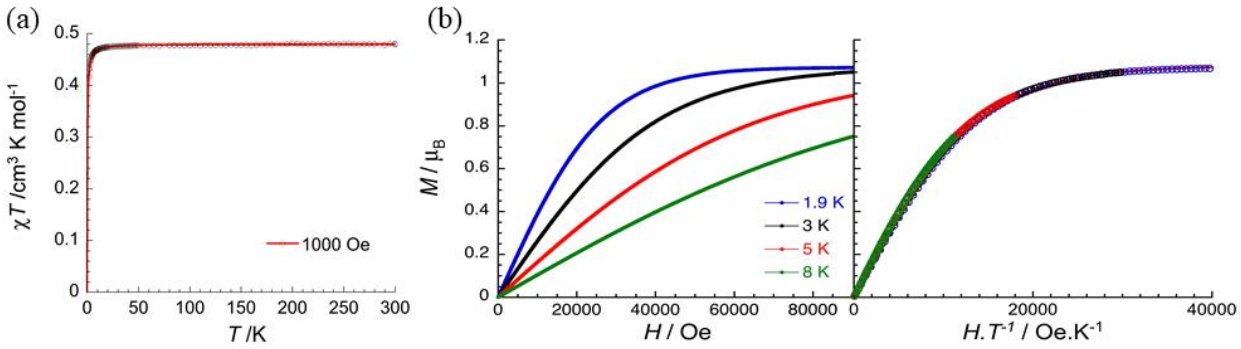

Figure 4.9. (a) Temperature dependence of the dc magnetic susceptibility ($\chi = M/H$ per mole of complex) plotted as χT vs T for **[Co^{II}(Py$_2$ImAm)$_2$]**, collected under an applied field of 1000 Oe. The solid red line corresponds to the best fit to a Curie-Weiss law for an S = 1/2 spin (g = 2.26(5), χ = -0.26(2) K). (b) Field (H) dependence of the magnetization (M) plotted as M vs H (left) and M vs H/T (right) for **[Co^{II}(Py$_2$ImAm)$_2$]** at the indicated temperatures (T). The solid line on the M vs H/T data is the best fit to the S = 1/2 Brillouin function with g = 2.16(5).

4.9 Magnetochemistry of [Co$^{II}_3$(Pm$_2$ImAm)$_2$Cl$_4$]·5H$_2$O

Given the above information, the variable temperature magnetic susceptibility of the polynuclear complexes were analyzed (Figure 4.10). For **[Co$^{II}_3$(Pm$_2$ImAm)$_2$Cl$_4$]·5H$_2$O**, the χT product at room temperature is around 5.2 cm^3 K mol^{-1}, which corresponds well to one S = ½ Co^{II} unit similar to **[Co^{II}(Py$_2$ImAm)$_2$]** (*cf.* 0.48 cm^3 K mol^{-1}) and two high spin S = 3/2 Co^{II} centres with C = 2.36 cm^3 K mol^{-1}, thus $g \approx 2.24(5)$.[34] Magnetic coupling between the central (low spin Co^{II}) and peripheral (high spin Co^{II}) metal ion spins appears to be antiferromagnetic, with a decrease of the χT product down 4.4 cm^3 K mol^{-1} at about 56 K (Figure 4.10 inset). It should be noted that the intrinsic spin-orbit coupling of high spin octahedral Co(II) metal ions[34] could also explain in part the χT decrease in this temperature range. As a result of the intramolecular antiferromagnetic coupling, the χT increase at lower temperatures is likely due to the non-compensation of the spin and stabilization of an S_T = 5/2 ground state. However, this simple description is not supported by the χT product of 15.4 cm^3 K mol^{-1} that is reached at 1.85 K, which is neither compatible with an S_T = 5/2 (C = 4.375 cm^3 K mol^{-1}) nor an S_T = 7/2 (C = 7.875 cm^3 K mol^{-1}) ground state expected for intra-complex antiferromagnetic or ferromagnetic interactions, respectively. Therefore, the presence of intermolecular magnetic interactions which align the

macro-spin, S_T, of the trinuclear complexes is necessary to explain the magnetic data below 50 K. With very close Co-Co interactions between neighbouring molecules (3.6268(3) Å), along with a number of intra-stack and inter-stack Co-Co interactions (See Appendix B; Table B.13-B.14), it is difficult to assign specific interactions that dominate the magnetic exchange. Nevertheless, it is important to note that the inter-complex interactions could be antiferromagnetic between the different types of Co spins (i.e. central and peripheral metal ion exchange interactions) or ferromagnetic between similar ones; however, the nature of the supramolecular packing and degree of intermolecular interactions, mitigates the effectiveness of extracting exchange couplings based on a particular fit function. Nonetheless, the *M vs. H* data have been measured between 1.85 and 8 K and, even at 7 T, the magnetization does not saturate, reaching a value of 3.5 μ_B supporting an $S_T = 5/2$ ground state rather than $S_T = 7/2$ (Figure 4.11). Furthermore, it is worth noting that the *S*-shaped curve observed around 1.5 T further suggests the presence of weak antiferromagnetic interactions between complexes. In addition, ac susceptibility measurements were also performed on **[Co$^{II}_3$(Pm$_2$ImAm)$_2$Cl$_4$]·5H$_2$O**, however, even under an applied static field up to 1 T, an out-of-phase ac susceptibility signal was not detected above 1.8 K between 0.1 and 10000 Hz.

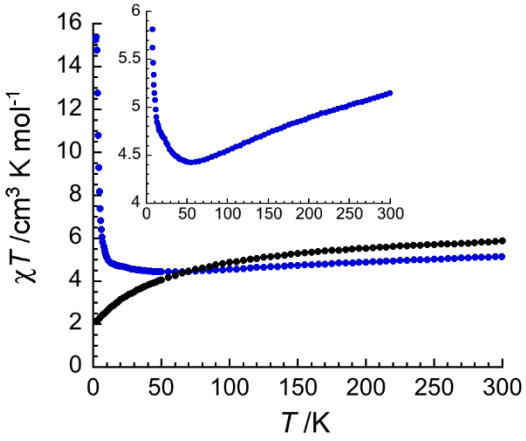

Figure 4.10. Temperature dependence of the χT product at 0.1 T (where χ is defined as the magnetic susceptibility equal to M/H per mole of |Co$^{II}_3$(Pm$_2$ImAm)$_2$Cl$_4$| unit) for **[Co$^{II}_3$(Pm$_2$ImAm)$_2$Cl$_4$]·5H$_2$O** (in blue) and **[Co$^{II}_6$(μ-Cl)$_2$(Pm$_2$ImAm)$_4$Cl$_6$]·2MeOH·2DCM** (in black).

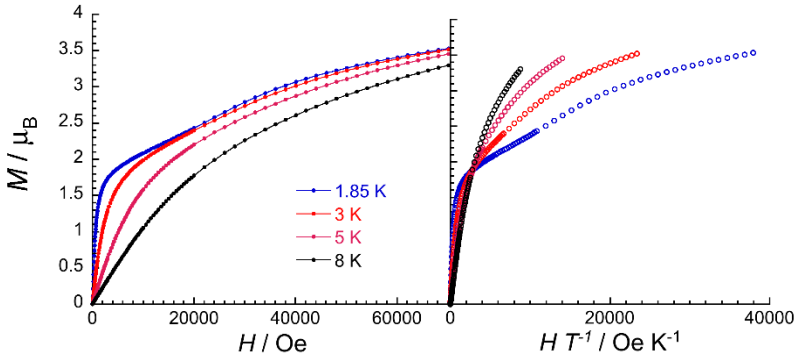

Figure 4.11. Field (*H*) dependence of the magnetization (*M* normalized per |$Co^{II}_3(Pm_2ImAm)_2Cl_4$| unit) plotted as *M* vs *H* (left) and *M* vs *H*/*T* (right) for **$[Co^{II}_3(Pm_2ImAm)_2Cl_4]\cdot 5H_2O$** at the indicated temperatures (*T*).

4.10 Magnetochemistry of $[Co^{II}_6(\mu\text{-}Cl)_2(Pm_2ImAm)_4Cl_6]\cdot 2MeOH\cdot 2DCM$

In the case of **$[Co^{II}_6(\mu\text{-}Cl)_2(Pm_2ImAm)_4Cl_6]\cdot 2MeOH\cdot 2DCM$**, the χT product at 300 K is approximately 5.8 $cm^3\,K\,mol^{-1}$ (per |$Co^{II}_3(Pm_2ImAm)_2Cl_4$| unit) which corresponds to one $S = ½$ Co^{II} moiety similar to **$[Co^{II}(Py_2ImAm)_2]$** (*cf.* 0.48 $cm^3\,K\,mol^{-1}$) and two high spin $S = 3/2$ Co^{II} centres with $C = 2.66$ $cm^3\,K\,mol^{-1}$ and therefore a *g*-value of 2.38(5) (Figure 4.10).[34] Similar to **$[Co^{II}_3(Pm_2ImAm)_2Cl_4]\cdot 5H_2O$**, coupling between the two types of metal ions (i.e. the central low spin Co^{II} and peripheral high spin Co^{II}) appears to be antiferromagnetic, with a decrease of the χT product down 2.1 $cm^3\,K\,mol^{-1}$ at 1.85 K and 0.1 T for **$[Co^{II}_6(\mu\text{-}Cl)_2(Pm_2ImAm)_4Cl_6]\cdot 2MeOH\cdot 2DCM$**. As in **$[Co^{II}_3(Pm_2ImAm)_2Cl_4]\cdot 5H_2O$** (*vide supra*), the presence of a significant spin-orbit coupling could also explain in part the χT decrease. Nevertheless, this simple description is not supported by the χT product of 2.1 $cm^3\,K\,mol^{-1}$ that is reached at 1.85 K. This value is not compatible with one $S_T = 5/2$ units ($C = 4.375$ $cm^3\,K\,mol^{-1}$) expected for intra-complex antiferromagnetic interactions. Therefore, the presence of magnetic interactions through the chlorine bridge or/and the presence of effective $S = 1/2$ spins at low temperature on the peripherical Co sites, might explain the reduced dc-susceptibility. The *M vs. H* data have also been measured between 1.85 and 8 K (Figure 4.12). At 7 T, the magnetization does not saturate reaching a value of 3.2 μ_B, which is close to what was found for **$[Co^{II}_3(Pm_2ImAm)_2Cl_4]\cdot 5H_2O$** (Figure 4.11).

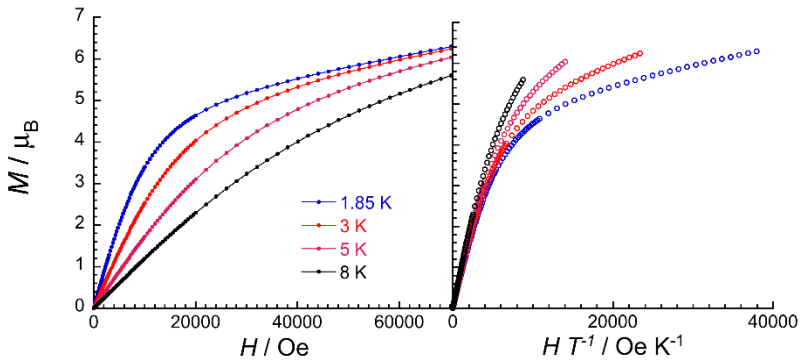

Figure 4.12. Field (*H*) dependence of the magnetization (*M*, normalized per [Co^{II}_6(μ-Cl)$_2$(Pm_2ImAm)$_4Cl_6$] unit) plotted as *M* vs *H* (left) and *M* vs *H*/*T* (right) for **[Co^{II}_6(μ-Cl)$_2$(Pm_2ImAm)$_4Cl_8$]·2MeOH·2DCM** at the indicated temperatures (*T*).

In contrast to **[Co^{II}_3(Pm_2ImAm)$_2Cl_4$]·5H_2O**, an out-of-phase signal was observed for **[Co^{II}_6(μ-Cl)$_2$(Pm_2ImAm)$_4Cl_6$]·2MeOH·2DCM** when ac susceptibility measurements were performed under an applied dc field at 1.9 K (See Appendix E; Figure E.4). Although no ac signal was detected under zero dc field, upon application of increasingly higher fields a clear relaxation mode begins to appear. This behavior is commonly observed in cases where the magnetic relaxation is influenced by quantum tunneling of the magnetization (QTM).[35, 36] Subsequently, ac measurements were performed under an optimal static dc field of 0.1 T, which revealed a frequency and temperature dependent relaxation mode, indicating unambiguously slow dynamics of the magnetization of **[Co^{II}_6(μ-Cl)$_2$(Pm_2ImAm)$_4Cl_6$]·2MeOH·2DCM** (Figure 4.13) and thus its Single-Molecule Magnet (SMM) properties.

The analysis of the field and temperature dependence of the relaxation time (τ; Figure 4.14) should start by calculating the uncertainty on the obtained values. Based on the illuminating work of N. Chilton and D. Reta,[37] the error bars on the relaxation time can be estimated easily from the generalized Debye fits of the experimental data (Figure 4.13 and Figure E.5) and the obtained α parameter (See Appendix E; Figures E.5 and E.6), which quantify the broadness of the relaxation time distribution. As shown in Figure 4.14, the obtained uncertainties are large and thus the following analysis of the relaxation must be taken with caution and certainly as a qualitative description.

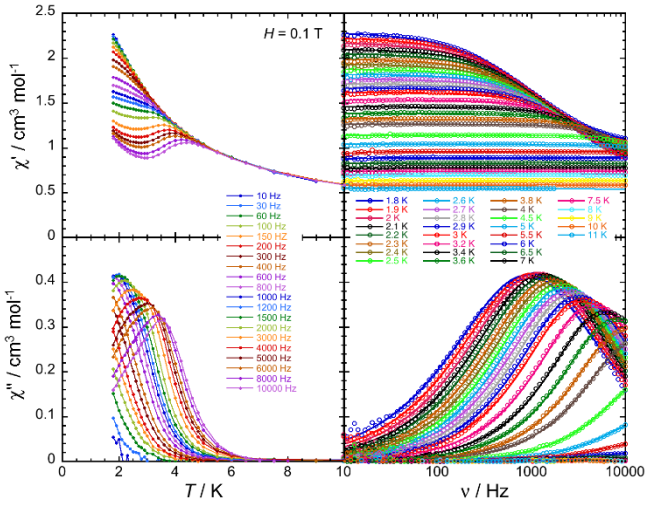

Figure 4.13. Temperature (left) and ac frequency (right) dependences of the real (χ', top) and imaginary (χ'', bottom) parts of the ac susceptibility, between 1.85 and 10 K and between 10 and 10000 Hz, for **[Co$^{II}_6$(μ-Cl)$_2$(Pm$_2$ImAm)$_4$Cl$_6$]·2MeOH·2DCM** in a 0.1-T dc field. Solid lines are visual guides on the left plots while they show the generalized Debye fit of the ac data on the right.

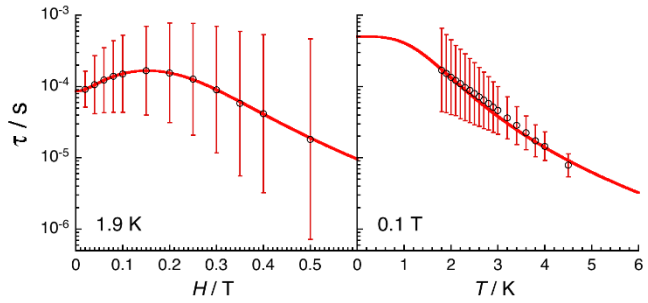

Figure 4.14. Dc-field (left) and temperature (right) dependences of the relaxation time for **[Co$^{II}_6$(μ-Cl)$_2$(Pm$_2$ImAm)$_4$Cl$_6$]·2MeOH·2DCM** estimated from the generalized Debye fits of the ac susceptibility data shown in Figures E.5 and 4.12 collected at 1.9 K and under an 0.1-T applied field, respectively. The error bars on the relaxation time have been calculated from the α parameters of the generalized Debye fit (See Appendix E; Figures E.5 and E.6) and the log-normal distribution as described in reference [35]. The solid red lines are the best fit discussed in the text.

To explain paramagnetic relaxations,[38] four main mechanisms are usually involved, which include Raman,[39] direct,[38] thermally activated (Arrhenius)[39] and QTM[40, 41] relaxation processes, as summarized in the following equation:[40]

Equation 4.1 $$\tau^{-1} = \tau_{Raman}^{-1} + \tau_{Direct}^{-1} + \tau_{Arrhenius}^{-1} + \tau_{QTM}^{-1}$$

Equation 4.2 $$\tau^{-1} = C\frac{1+C_1H^2}{1+C_2H^2}T^n + ATH^4 + \tau_0^{-1}\exp\left(-\frac{\Delta}{k_BT}\right) + \frac{B_1}{1+B_2H^2}$$

As shown by Equations 4.1 and 4.2, each relaxation has its own characteristic temperature (*T*) and dc-field (*H*) dependence. Considering the field dependence of the relaxation time (left part of Figure 4.14), it should be noted first that the τ increase below 0.15 T agrees with only QTM or Raman (with $C_2 > C_1$) processes, while at higher fields, the H^4 variation strongly suggest a direct relaxation mechanism. Therefore, the τ *vs. H* data have been fit by two simple models including i) Raman & Direct and ii) QTM & Direct processes but only when the three mechanisms are considered the field and temperature dependence of the relaxation time can be satisfactory fitted (Figure 4.14; with A = 4(1) 10^5 $K^{-1}T^{-4}s^{-1}$, B_1 = 6920(200) s^{-1}, B_2 = 260(30) T^{-2}, C = 433(50) $K^{-3.7}s^{-1}$, C_1 = C_2 set to 0 and n = 3.7(5)). It is worth mentioning that different models including an Arrhenius relaxation did not improve significantly the fitting agreement. As mentioned above, even if this analysis should be taken with a great caution, it suggests that QTM, Raman and direct processes are responsible for the observed SMM properties in **[Co^{II}_6(μ-$Cl)_2$($Pm_2ImAm)_4Cl_6$]·2MeOH·2DCM**.

4.11 Conclusions

By tapping into the rich ligating affinity of *N*-imidoylamidine ligands, we have prepared a family of cobalt complexes in which both nuclearity and topology may be controlled. This was achieved through judicious choice of the cobalt salt employed and meticulous control of the solvent conditions, thereby enabling selective isolation of mono-, tri- and hexanuclear cobalt complexes. In the case of the latter two materials, where coordination occurs in both the bidentate and tridentate sites within the *N*-imidoylamidine ligands, the nuclearity is determined through careful control of the hydration at the ppm level (e.g. 10000 *vs*. 300 ppm). The spin states of the cobalt ions in these complexes were elucidated by magnetic susceptibility measurements, which reveal a unique combination of low and high spin states for the Co^{II} ions within the |Co^{II}_3|

aggregates. This study demonstrates the versatility of this ligand framework, affording an ideal platform in the development of polynuclear complexes. Furthermore, this design strategy provides an avenue towards achieving tailor-made polynuclear homo and heterometallic complexes, and enables the exploration of polynuclear species with differing spin states.

4.12 Experimental Section

General Procedures. All solvents and reagents were reagent grade and used without further purification. *Bis*(pyridinium) tetrachlorocobaltate(II) (**[PyH]$_2$[CoCl$_4$]**), *N*-2-pyridylimidoyl-2-pyridylamidine (**Py$_2$ImAm**), and *N*-2-pyrimid ylimidoyl-2-pyrimidylamidine (**Pm$_2$ImAm**) were synthesized according to the literature procedure reported earlier by us.[19, 20] IR spectra were recorded on an Agilent Technologies Cary 630 FT-IR spectrometer. A single crystalline phase was confirmed by comparison of powder XRD patterns with those calculated from the single crystal data (See Appendix E; Figures E.1-E.3).

Synthesis of [Co^{II}(Py$_2$ImAm)$_2$]. A degassed solution of cobalt(II) acetate tetrahydrate (0.3969 g, 1.59 mmol) in 8 mL dry DMF was added via syringe to a degassed solution of **Py$_2$ImAm** (0.7111 g, 3.15 mmol) in 60 mL anhydrous acetonitrile (CH_3CN) and 10 mL triethyl amine (Et_3N) under continuous stirring. After stirring for 5 min, the resulting orange solution was left to stand at RT. After three days, orange block-like crystals were collected and rinsed with methanol and hexanes. Yield: 0.6197 g (1.22 mmol, 76.6%). IR (cm^{-1}): 3252 (m), 3051 (w), 1592 (m), 1575 (m), 1523 (m), 1498 (w), 1470 (m), 1441 (s), 1420 (m), 1272 (m), 1241 (w), 1065 (m), 998 (m), 947 (w), 845 (s), 812 (m), 755 (m), 738 (s), 717 (s).

Synthesis of [Co$^{II}_3$(Pm$_2$ImAm)$_2$Cl$_4$]·5H$_2$O. A degassed solution of **[PyH]$_2$[CoCl$_4$]** (0.4364 g, 1.21 mmol) in 17 mL of 99% methanol was added via syringe to a degassed solution of **Pm$_2$ImAm** (0.1836 g, 0.81 mmol) in 17 mL of anhydrous DCM under continuous stirring. After stirring for 5 min, the resulting deep red-black solution was left to stand at room temperature. After two days, red plate-like crystals were filtered, rinsed with 4 mL of a 1:1 mixture of methanol and DCM, then left to dry in air. Yield: 0.1473 g (0.17 mmol, 42.3%). IR (cm^{-1}): 3542 (m), 3467 (m), 3218 (s), 3069 (m), 1609 (m), 1579 (m), 1557 (s), 1542(m), 1489 (s), 1439 (w), 1407 (s), 1395 (s), 1321 (m), 1287 (m), 1273 (m), 1195 (w), 1099 (m), 1056 (m), 1015 (m), 1005 (m), 905 (s), 830

(s), 735 (w), 713 (s). Anal. Calcd for $C_{20}H_{24}Cl_4Co_3N_{14}O_4$: C, 28.49; H, 2.87; N, 23.26. Found: C, 28.74; H, 2.95; N, 23.09.

Synthesis of $[Co^{II}_6(\mu\text{-}Cl)_2(Pm_2ImAm)_4Cl_6]\cdot 2MeOH\cdot 2DCM$. A degassed solution of **$[PyH]_2[CoCl_4]$** (0.5671 g, 1.57 mmol) in 20 mL of 99.97% methanol was added via syringe to a degassed solution of **Pm_2ImAm** (0.2363 g, 1.04 mmol) in 20 mL of anhydrous DCM. After stirring for 5 minutes, the resulting deep red-black solution was left to stand at room temperature. After two days, block-like black crystals were filtered, rinsed with 0.5 mL of a 1:1 mixture of anhydrous methanol and anhydrous DCM, then dried in air. Yield: 0.0929 g (0.22 mmol, 20.1%). IR (cm^{-1}): 3423 (m), 3268 (w), 3220 (m), 3059 (w), 1605 (w), 1554 (s), 1474 (s), 1439 (w), 1394 (s), 1308 (w), 1272 (m), 1231 (w), 1190 (w), 1093 (m), 1053 (m), 1016 (w), 1003 (m), 865 (m), 831 (s), 739 (w), 708 (s).

X-ray crystallography. Data collection for single crystals of **$[Co^{II}(Py_2ImAm)_2]$**, **$[Co^{II}_3(Pm_2ImAm)_2Cl_4]\cdot 5H_2O$** and **$[Co^{II}_6(\mu\text{-}Cl)_2(Pm_2ImAm)_4Cl_6]\cdot 2MeOH\cdot 2DCM$** (See Appendix B; Table B.10) were obtained on a Bruker KAPPA APEX-II CCD diffractometer (graphite monochromated Mo K_α radiation, $\lambda = 0.71073$ Å, ω-scans with a 0.5° step in ω) at 200 K. Absorption corrections were applied by using the semi-empirical method of the SADABS program[42] for all samples. The structures were solved using SHELXT[43] and refined by full-matrix least-squares methods on F^2 with SHELXL-2015[44] in anisotropic approximation for all non-hydrogen atoms. The hydrogen atoms on pyridine or pyrimidine were constrained to ride on their parent atoms with C-H = 0.95 Å and $U_{iso} = 1.2U_{eq}(C)$, while imino N-H hydrogen atoms were refined isotropically. SADI restrain was used to associate the imino N-H distances with a 0.02 standard deviation in the three complexes. Some electron density contribution was removed using *Squeeze* protocol in the crystal structure of **$[Co^{II}_3(Pm_2ImAm)_2Cl_4]\cdot 5H_2O$**,[30] and the electrons removed during squeezing were assumed to be water molecules. Powder X-ray diffraction (PXRD) was performed on a Rigaku Ultima IV diffractometer, with Cu K_α monochromatic radiation (λ = 1.54056 Å) and θ–2θ geometry. The simulated PXRD pattern was calculated using Mercury[29] and was compared to the experimental PXRD of the bulk sample.

Magnetic Measurements. To prevent solvent loss in the sample of **[Co^{II}_6(μ-Cl)$_2$(Pm_2ImAm)$_4Cl_8$]** the crystals of this complex were filtered immediately prior to the measurements, and the molecular weight was taken from the cif file. On the other hand, **[Co^{II}(Py_2ImAm)$_2$]** and **[Co^{II}_3(Pm_2ImAm)$_2Cl_4$]** retain their crystallinity outside the mother liquor and they were measured as dry solids. The crystal lattice of **[Co^{II}(Py_2ImAm)$_2$]** does not contain solvent and the molecular weight was taken from the cif file. In the case of **[Co^{II}_3(Pm_2ImAm)$_2Cl_4$]** it has porous channels. The final molecular weight of **[Co^{II}_3(Pm_2ImAm)$_2Cl_4$]** was corroborated by elemental analysis and TGA. Magnetic susceptibility measurements were performed on a Quantum Design SQUID MPMS-XL magnetometer and PPMS-II susceptometer housed at the Centre de Recherche Paul Pascal at temperatures between 1.8 and 400 K and *dc* magnetic fields ranging from -9 to +9 T. *Ac* magnetic susceptibility measurements were performed in an oscillating *ac* field of 1 to 6 Oe with frequencies between 1 and 10000 Hz and various *dc* fields (including zero). The measurements were carried out on polycrystalline samples (16.16, 48.61 and 39.32 mg for **[Co^{II}(Py_2ImAm)$_2$]**, **[Co^{II}_3(Pm_2ImAm)$_2Cl_4$]**, and **[Co^{II}_6(μ-Cl)$_2$(Pm_2ImAm)$_4Cl_8$]**) suspended in mineral oil (typically 10-20 mg) and introduced in a sealed polyethylene bag (3 $\times$ 0.5 $\times$ 0.02 cm; typically 24-32 mg). Prior to the experiments, the field-dependent magnetization was measured at 100 K on each sample in order to detect the presence of any bulk ferromagnetic impurities. In fact, paramagnetic or diamagnetic materials should exhibit a perfectly linear dependence of the magnetization that extrapolates to zero at zero *dc* field; the samples appeared to be free of any ferromagnetic impurities. The magnetic susceptibilities were corrected for the sample holder, the oil and the intrinsic diamagnetic contributions.

4.13 References

[1] Pokharel, U. R.; Fronczek, F. R.; Maverick, A. W., *Nat. Commun.* **2014,** 5, 5883.

[2] Kaeffer, N.; Chavarot-Kerlidou, M.; Artero, V., *Acc. Chem. Res.* **2015,** 48, (5), 1286-1295.

[3] Boit, T. B.; Weires, N. A.; Kim, J.; Garg, N. K., *ACS Catal.* **2018,** 8, (2), 1003-1008.

[4] Kopylovich, M. N.; Lasri, J.; Guedes da Silva, M. F. C.; Pombeiro, A. J. L., *Dalton Trans.* **2009**, (16), 3074-3084.

[5] Jurca, T.; Farghal, A.; Lin, P.-H.; Korobkov, I.; Murugesu, M.; Richeson, D. S., *J. Am. Chem. Soc.* **2011,** 133, (40), 15814-15817.

[6] Habib, F.; Luca, O. R.; Vieru, V.; Shiddiq, M.; Korobkov, I.; Gorelsky, S. I.; Takase, M. K.; Chibotaru, L. F.; Hill, S.; Crabtree, R. H.; Murugesu, M., *Angew. Chem. Int. Ed.* **2013,** 52, (43), 11290-11293.

[7] Harris, J. D.; Moran, M. J.; Aprahamian, I., *Proc. Natl. Acad. Sci. U.S.A.* **2018,** 115, (38), 9414-9422.

[8] Kopylovich, M. N.; Pombeiro, A. J. L., *Coord. Chem. Rev.* **2011,** 255, (1), 339-355.

[9] Turnbull, M. M.; Wei, M. Y.; Willett, R. D., *J. Coord. Chem.* **1995,** 35, (1-2), 11-17.

[10] Boča, R.; Hvastijová, M.; Kožíšek, J.; Valko, M., *Inorg. Chem.* **1996,** 35, (16), 4794-4797.

[11] Tong, M.-L.; Wu, Y.-M.; Tong, Y.-X.; Chen, X.-M.; Chang, H.-C.; Kitagawa, S., *Eur. J. Inorg. Chem.* **2003,** , (13), 2385-2388.

[12] Igashira-Kamiyama, A.; Kajiwara, T.; Konno, T.; Ito, T., *Inorg. Chem.* **2006,** 45, (16), 6460-6466.

[13] Starikova, A. A., *Chem. Pap.* **2018,** 72, (4), 821-828.

[14] Kajiwara, T.; Kamiyama, A.; Ito, T., *ChemComm* **2002**, (12), 1256-1257.

[15] Glaser, T.; Theil, H.; Liratzis, I.; Weyhermüller, T.; Bill, E., *Inorg. Chem.* **2006,** 45, (13), 4889-4891.

[16] Kopylovich, M. N.; Kirillov, A. M.; Tronova, E. A.; Haukka, M.; Kukushkin, V. Y.; Pombeiro, A. J. L., *Eur. J. Inorg. Chem.* **2010,** , (16), 2425-2432.

[17] Duros, V.; Sartzi, H.; Teat, S. J.; Sanakis, Y.; Roubeau, O.; Perlepes, S. P., *Inorg. Chem. Commun.* **2014,** 50, 117-121.

[18] Leitch, A. A.; Korobkov, I.; Assoud, A.; Brusso, J. L., *ChemComm* **2014,** 50, (38), 4934-4936.

[19] Yousaf, M.; Yutronkie, N. J.; Castañeda, R.; Klein, J. A.; Brusso, J., *New J Chem* **2017,** 41, (20), 12218-12224.

[20] Castañeda, R.; Hollingshead, A.; Gabidullin, B.; Brusso, J. L., *Cryst. Growth Des.* **2017,** 17, (12), 6572-6578.

[21] Castañeda, R.; Harriman, K. L. M.; Wong, J. W. L.; Gabidullin, B.; Murugesu, M.; Brusso, J. L., *Eur. J. Inorg. Chem.* **2019,** , (7), 963-972.

[22] Jenkins, D. M.; Di Bilio, A. J.; Allen, M. J.; Betley, T. A.; Peters, J. C., *J. Am. Chem. Soc.* **2002,** 124, (51), 15336-15350.

[23] Marshak, M. P.; Chambers, M. B.; Nocera, D. G., *Inorg. Chem.* **2012,** 51, (20), 11190-11197.

[24] Leconte, N.; Baptiste, B.; Philouze, C.; Thomas, F., *Dalton Trans.* **2018,** 47, (33), 11303-11307.

[25] Whyte, A. M.; Shuku, Y.; Nichol, G. S.; Matsushita, M. M.; Awaga, K.; Robertson, N., *J. Mater. Chem.* **2012,** 22, (34), 17967-17975.

[26] Casanova, D.; Llunell, M.; Alemany, P.; Alvarez, S., *Chem.: Eur. J.* **2005,** 11, (5), 1479-1494.

[27] Świtlicka, A.; Machura, B.; Penkala, M.; Bieńko, A.; Bieńko, D. C.; Titiš, J.; Rajnák, C.; Boča, R.; Ozarowski, A.; Ozerov, M., *Inorg. Chem.* **2018,** 57, (20), 12740-12755.

[28] Higgins, R. F.; Livesay, B. N.; Ozumerzifon, T. J.; Joyce, J. P.; Rappé, A. K.; Shores, M. P., *Polyhedron* **2018,** 143, 193-200.

[29] Macrae, C. F.; Bruno, I. J.; Chisholm, J. A.; Edgington, P. R.; McCabe, P.; Pidcock, E.; Rodriguez-Monge, L.; Taylor, R.; van de Streek, J.; Wood, P. A., *J. Appl. Crystallogr.* **2008,** 41, (2), 466-470.

[30] Spek, A., *Acta Cryst. C* **2015,** 71, (1), 9-18.

[31] Addison, A. W.; Rao, T. N.; Reedijk, J.; van Rijn, J.; Verschoor, G. C., *Dalton Trans.* **1984**, (7), 1349-1356.

[32] Bondi, A., *J. Phys. Chem.* **1964,** 68, (3), 441-451.

[33] Batsanov, S. S., *Inorg. Mater.* **2001,** 37, (9), 871-885.

[34] Carlin, R. L., *Magnetochemistry*. ed.; Springer-Verlag: 1986; p 328 pp.

[35] Gatteschi, D.; Villain, D. G. R. S. J.; Sessoli, R.; Villain, J.; Knovel, *Molecular Nanomagnets*. ed.; OUP Oxford: 2006.

[36] Lecren, L.; Wernsdorfer, W.; Li, Y.-G.; Roubeau, O.; Miyasaka, H.; Clérac, R., *J. Am. Chem. Soc.* **2005,** 127, (32), 11311-11317.

[37] Reta, D.; Chilton, N. F., *Phys. Chem. Chem. Phys.* **2019,** 21, (42), 23567-23575.

[38] Shrivastava, K. N., *Phys. Stat. Sol. A* **1983,** 117, (2), 437-458.

[39] Van Vleck, J. H., *Phys. Rev.* **1940,** 57, (5), 426-447.

[40] Abragam, A.; Bleaney, B., *Electron Paramagnetic Resonance of Transition Ions*. ed.; OUP Oxford: 2012.

[41] Ding, M.; Hickey, A. K.; Pink, M.; Telser, J.; Tierney, D. L.; Amoza, M.; Rouzières, M.; Ozumerzifon, T. J.; Hoffert, W. A.; Shores, M. P.; Ruiz, E.; Clérac, R.; Smith, J. M., *Chem.: Eur. J.* **2019,** 25, (45), 10625-10632.

[42] Bruker *APEX3, SAINT, SADABS and TWINABS*, Bruker Analytical X-ray Instruments Inc.: Madison, WI, 2016.

[43] Sheldrick, G., *Acta Cryst. A* **2015,** 71, (1), 3-8.

[44] Sheldrick, G., *Acta Cryst. C* **2015,** 71, (1), 3-8.

Chapter 5

One-Pot Synthesis of Heterometallic Copper-Manganese Complexes with Polyfunctional Imidoyl Amidine Ligands

Authorship disclosure: The research presented in this chapter has not yet been published, but we are in the process of preparing a manuscript. The synthesis of all compounds was done by Luis Raúl Castañeda Perea. The single crystal structures were collected and refined by Luis Raúl Castañeda Perea. The EPR data was collected and interpreted by Luis Raúl Castañeda Perea. The magnetic data was collected by Professor Rodolphe Clérac.

5.1 Introduction

Copper and manganese are two metals frequently found in different metalloenzymes such as photosystem II,[1] ribonucleotide reductase,[2] amine oxidase,[3] and galactose oxidase.[4] Organic ligands can sometimes play a similar role to enzymes and, as a result, copper or manganese complexes have been proposed for various applications including, but not limited to, water splitting,[5] MRI contrast agents,[6] magnetic materials,[7] and solar cells dyes.[8] In general, the synthesis of homometallic complexes typically involves a one-pot process of combining a solution of the ligand with a solution of the metal salt, resulting in the formation of a crystalline complex. On the other hand, the synthesis of heterometallic complexes normally follows a stepwise approach with the preparation of a mononuclear complex followed by subsequent coordination to a second metal ion to a secondary binding site in the ligand framework. As such, these ligands require multiple coordination sites or bridging groups (e.g. CN^-, or N_3^-) in order to make the heterometallic complexes. To that end, our group recently synthesized *N*-2-pyridylimidoyl-2-pyridylamidine (**5.1a**; Py_2ImAm; Chart 5.1) and *N*-2-pyrimidylimidoyl-2-pyrimidylamidine (**5.2a**; Pm_2ImAm; Chart 5.1), [9, 10] which represent two ligands possessing distinct coordination sites (i.e. bidentate and tridentate). In addition to having two coordination pockets, it has also been demonstrated that selective coordination to Py_2ImAm and Pm_2ImAm in either a tridentate or bidentate fashion can be achieved through the use of acidic or neutral conditions, respectively.[11] These interesting features make Py_2ImAm and Pm_2ImAm attractive building blocks for the preparation of heterometallic complexes.

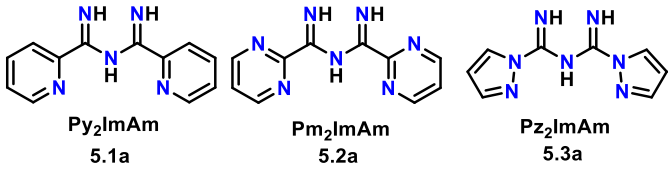

Chart 5.1. Structure of the imidoyl amidine ligands Py_2ImAm, Pm_2ImAm and Pz_2ImAm.

Prior to our investigation into imidoyl amidine ligands, their synthesis had not yet been extensively explored, despite the potential of these ligand frameworks. To that end, complexes employing Py_2ImAm and Pm_2ImAm as well as similar ligands such as *N*-1-pyrazolylimidoyl-1-pyrazolylamidine (**5.3a**; Pz_2ImAm; Chart 5.1) had been isolated via a metal assisted transformation with a metal salt, and a pyridyl, pyrimidyl, or pyrazolyl synthon.[12-15] An interesting example of such a synthesis is the copper catalyzed nucleophilic addition of pyrazole to dycianamidate, that results in the formation of a linear trinuclear complex with Pz_2ImAm (**$[Cu^{II}_3(Pz_2ImAm)_2(Pz)_2(4ClO_4)]$**),[14] in which two Pz_2ImAm ligands coordinate in a bidentate fashion to a central Cu^{II} ion with two additional Cu^{II} metal ions bound to the tridentate pocket of each Pz_2ImAm. Subsequent work employing the aforementioned trinuclear moiety as the starting material and reacting it with EDTA enabled isolation of **$[Cu^{II}(Pz_2ImAm)_2]$**.[14] Finally after three steps the development of hetero-trinuclear complexes **$[M_2Cu^{II}(Pz_2ImAm)_2][ClO_4]_4$** (where M = Mn, Co or Ni) was possible by coordinating **$[Cu^{II}(Pz_2ImAm)_2]$** to a second metal ion. To the best of our knowledge, without employing a copper salt, Pz_2ImAm as a free molecule had yet to be prepared. Nevertheless, Pz_2ImAm can be isolated from **$[Cu^{II}_3(Pz_2ImAm)_2(Pz)_2(4ClO_4)]$**, by precipitating the copper ions with $(NH_4)_2S$.[15] With Pz_2ImAm in hand, it is possible to isolate the mononuclear complex **$[Cu^{II}(Pz_2ImAm)_2]$**, and then use this mononuclear complex to build hetero-trinuclear complexes **$[M_2Cu^{II}(Pz_2ImAm)_2(pdm)_2][NO_3]_4$** (where M = Co or Ni and **pdm** = 2,6-pyridinedimethanol).[15] Other examples involving the formation of Py_2ImAm and Pm_2ImAm in copper complexes include the decomposition of either tris(2-pyridyl)triazine[12] or tris(2-pyrimidyl)triazine,[16] respectively, in the presence of copper (II) salts. Interestingly, in the three imidoyl amidine ligands mentioned thus far, the ligand acts to ferromagnetically couple the adjoining Cu^{II} ions. Other metals, such as nickel and palladium, are also able to catalyze the formation imidoyl amidine complexes, in this case with a nitrile and an oxime as starting materials.[17-20]

Chapter 3 and 4 of this thesis reports the synthesis and characterization of homometallic complexes employing Pm_2ImAm ligands coordinated to manganese, iron or cobalt.[21] In these complexes the main factors that direct metal coordination are: (i) the source of acidic counter ion, (ii) the solvent choice, and (iii) the water content. These three factors can be adjusted to slowly crystallize the polynuclear complexes thereby providing the metal ion enough time to coordinate to both sides of Pm_2ImAm. In this chapter, we took the opportunity to synthesize heterometallic complexes with Pm_2ImAm. Like the homometallic complexes with manganese, iron or cobalt, we chose to develop a one pot synthesis for these heterometallic complexes. A one pot synthesis has great potential as a means to afford higher yields and can be considered greener in terms of using less solvents and resources. The metal ions chosen for this study were copper(II) to be coordinated in the bidentate pocket of Pm_2ImAm in a square planar fashion, and manganese(II) chloride was used to coordinate the terpy-like pocket of Pm_2ImAm. These results show the formation of two different frameworks, a linear trinuclear complex with the formula **$[Mn^{II}_2Cu^{II}(Pm_2ImAm)_2Cl_4]\cdot 2H_2O$** (**5.1b**) and a hexanuclear complex with the formula **$[Mn^{II}_4Cu^{II}_2(\mu\text{-}Cl)_2(Pm_2ImAm)_4Cl_6]\cdot 2MeOH\cdot 2DCM$** (**5.2b**). Interestingly the frameworks of both polynuclear complexes are analogous to those observed with cobalt in chapter 4. Aditionally, a new mononuclear complex **$[Cu^{II}(Py_2ImAm)_2]$** (**5.3b**) was isolated, characterized by X-ray single crystal diffraction, and used as a structural comparison point to **5.1b** and **5.2b**. The magnetochemistry of **5.3b** was also studied, as a first step towards towards future magnetic studies on the heterometallic complexes **5.1b** and **5.2b**.

5.2 Synthesis and Crystallographic Description of the Central Mononuclear Complex $[Cu^{II}(Py_2ImAm)_2]$

In chapter 2 it was shown that the use of a weak base such as triethylamine led to selective coordination in the bidentate pocket of Py_2ImAm with first row transition metal ions. Following that strategy, **$[Cu^{II}(Py_2ImAm)_2]$** was synthesized in 72.4% yield by layering an isopropanol solution of $CuCl_2$ on top of a dichloromethane solution of Py_2ImAm (Scheme 5.1). A near ideal square planar configuration (Figure 5.1a) was observed for this complex with an average N-Cu distance equal to 1.934(2) Å, which is in good correlation to similar copper(II) ImAm complexes.[12, 14, 22, 23] It worth mentioning a chloroform adduct of this complex was previously reported via a two step metal assisted transformation;[12] however, this complex is not reproduced

by starting with Py_2ImAm as a ligand. Nevertheless, the absence of chloroform in the crystal lattice of **[$Cu^{II}(Py_2ImAm)_2$]** is advantageous since solvent loss is no longer an issue. **[$Cu^{II}(Py_2ImAm)_2$]** grows as thin red plate crystals (Figure 5.2a) and crystalizes in the monoclinic space group *C*2/*c*, with the complex molecule siting in a general position. Interestingly, four coordinate copper(II) complexes with nitrogen ligands are typically blue,[24, 25] and unfrequently red as seen with **[$Cu^{II}(Py_2ImAm)_2$]**. Within the crystal lattice, **[$Cu^{II}(Py_2ImAm)_2$]** forms discrete hydrogen bonded dimers connected through the N4-H4···N5 hydrogen bond (Figure 5.1b), which pack in a herringbone arrangement (Figure 5.1c). Other crystal lattice interactions include weak π-π interactions and a N2-Cu1 close contact (3.125(2) Å).

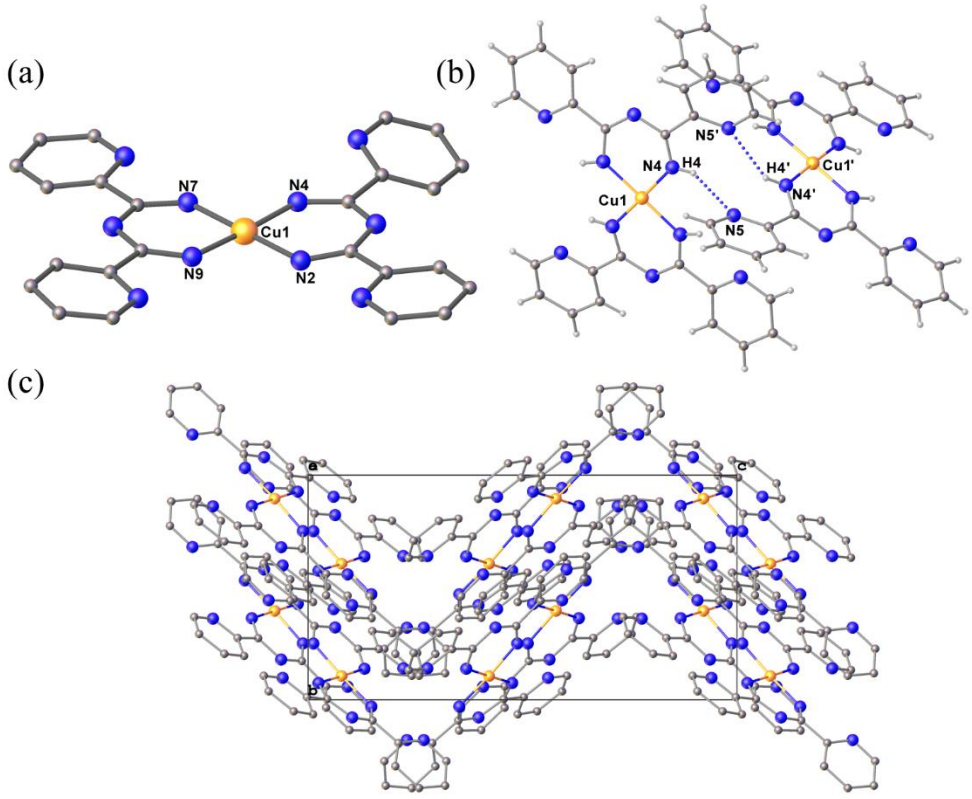

Figure 5.1. (a) Structural diagram of **[$Cu^{II}(Py_2ImAm)_2$]**. (b) Hydrogen bond dimer of **[$Cu^{II}(Py_2ImAm)_2$]**. (c) Crystal packing of **[$Cu^{II}(Py_2ImAm)_2$]** viewed along the 100 plane.

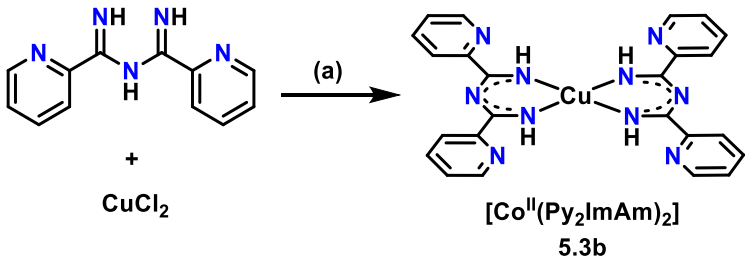

Scheme 5.1. Synthesis of **[Cu^{II}(Py$_2$ImAm)$_2$]**. Conditions: (a) DCM/iPrOH, triethylamine as base. Reaction was carried out under air atmosphere.

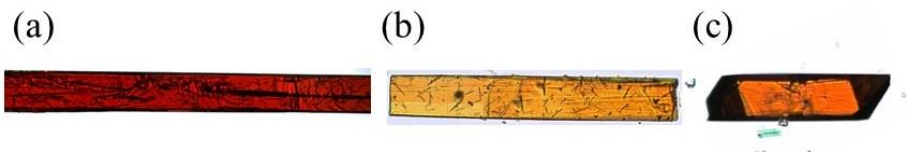

Figure 5.2. Crystal photo of: (a) **[Cu^{II}(Py$_2$ImAm)$_2$]**, (b) **[Mn$^{II}_2$Cu^{II}(Pm$_2$ImAm)$_2$Cl$_4$]·2H$_2$O**, (c) **[Mn$^{II}_4$Cu$^{II}_2$(μ-Cl)$_2$(Pm$_2$ImAm)$_4$Cl$_6$]·2MeOH·2DCM**.

5.3 Synthesis of Heterometallic Copper-Manganese Complexes

In order to successfully isolate heterometallic complexes via a one-pot synthesis, it is necessary to control the coordination of each metal ion into a specific coordination site in Pm$_2$ImAm. In part this can be done by adding the metal ions in a specific order. First, the synthesis begins with ligand substitution of **[Cu^{II}(acac)$_2$]** for Pm$_2$ImAm. This substitution is accomplished by mixing a chloroform or a dichloromethane (DCM) solution of **[Cu^{II}(acac)$_2$]** with a DCM solution of Pm$_2$ImAm (Scheme 5.2). An immediate colour change is observed from the blue solution of **[Cu^{II}(acac)$_2$]** to red, which is the colour of **[Cu^{II}(Pm$_2$ImAm)$_2$]** (Figure 5.3). After the initial coordination of Cu(II), the tridentate pocket can then be occupied by layering a methanolic solution of $MnCl_2$ on top of the red solution containing **[Cu^{II}(Pm$_2$ImAm)$_2$]**. Similar to the preparation of the cobalt complexes described in chapter 4, depending on the water content in the methanol used,[‡] two different complexes can be obtained. Using 99% methanol affords a linear trinuclear complex with the formula **[Mn$^{II}_2$Cu^{II}(Pm$_2$ImAm)$_2$Cl$_4$]·2H$_2$O** (Scheme 5.2), while using methanol with a much lower water content (99.97%) leads to a hexanuclear complex

[‡] The water content in the methanol was quantified by the Karl Fischer method.[34]

(**[$Mn^{II}_4Cu^{II}_2$(μ-Cl)$_2$(Pm$_2$ImAm)$_4$Cl$_6$]·2MeOH·2DCM**), which can be considered a dimer of the trinuclear complex formed through bridging of the chloride ions. It is noteworthy that prolonged exposure of crystals of **[$Mn^{II}_2Cu^{II}$(Pm$_2$ImAm)$_2$Cl$_4$]·2H$_2$O** to methanolic solutions at room temperature, the complex begins to dimerize forming **[$Mn^{II}_4Cu^{II}_2$(μ-Cl)$_2$(Pm$_2$ImAm)$_4$Cl$_6$]·2MeOH·2DCM**, regardless of the of the water content in the methanol employed. This behaviour was not observed for the analogous cobalt complexes and can be prevented by isolating crystals of **[$Mn^{II}_2Cu^{II}$(Pm$_2$ImAm)$_2$Cl$_4$]·2H$_2$O** after three hours. Pale orange plate crystals of **[$Mn^{II}_2Cu^{II}$(Pm$_2$ImAm)$_2$Cl$_4$]·2H$_2$O** (Figure 5.2b) can be filtered out, rinsed with isopropanol, and they are stable under ambient conditions. On the other hand orange block crystals of **[$Mn^{II}_4Cu^{II}_2$(μ-Cl)$_2$(Pm$_2$ImAm)$_4$Cl$_6$]·2MeOH·2DCM** (Figure 5.2c) were keept under a MeOH/DCM solvent mixture because they lose crystallinity over time due solvent loss.

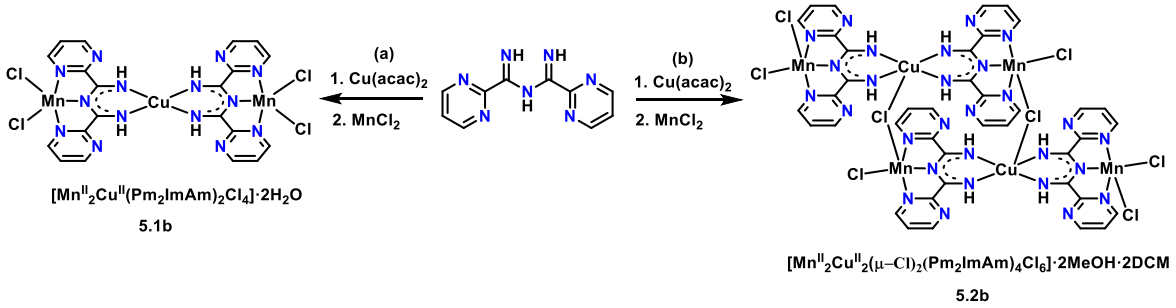

Scheme 5.2. Synthesis of complexes **[$Mn^{II}_2Cu^{II}$(Pm$_2$ImAm)$_2$Cl$_4$]·2H$_2$O** and **[$Mn^{II}_4Cu^{II}_2$(μ-Cl)$_2$(Pm$_2$ImAm)$_4$Cl$_6$]·2MeOH·2DCM**. Conditions: (a) 1. chloroform/chloroform and 2. methanol (99%); (b) 1. dichloromethane/dichloromethane and 2. methanol (99.97%).

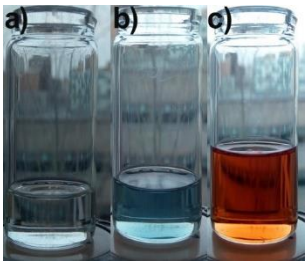

Figure 5.3. Colours observed in the solution of: (a) Pm$_2$ImAm, (b) **[Cu^{II}(acac)$_2$]**, (c) **[Cu^{II}(Pm$_2$ImAm)$_2$]** made after mixing vial a and b.

5.4 Structural Analysis of $[Mn^{II}_2Cu^{II}(Pm_2ImAm)_2Cl_4]\cdot 2H_2O$

Crystals of **$[Mn^{II}_2Cu^{II}(Pm_2ImAm)_2Cl_4]\cdot 2H_2O$**, which belong to the triclinic *P*-1 space group, contain two crystallographically independent molecules in the asymmetric unit with a point of inversion located at the central copper ion of each molecule. Nonetheless, these crystallographically independent trinuclear molecules have essentially the same geometry and metal to ligand bond distances (Figure 5.4 and Table 5.1). The Cu(II) ion is located in the centre of the complex, is bound to two anionic Pm_2ImAm ligands in a bidentate fashion, and adopts a nearly ideal square planar geometry very similar to that of the mononuclear complex **$[Cu^{II}(Py_2ImAm)_2]$** as highlighted in the overlay of the two structures in Figure 5.4c. Comparing the N-Cu distances of the central metal in **$[Mn^{II}_2Cu^{II}(Pm_2ImAm)_2Cl_4]\cdot 2H_2O$** to those of **$[Cu^{II}(Py_2ImAm)_2]$** reveals a nominal elongation of these bonds upon development of the polynuclear complex (cf., 1.927(2) -1.939(2) Å in **$[Cu^{II}(Py_2ImAm)_2]$** to 1.943(3) -1.974(3) Å in **$[Mn^{II}_2Cu^{II}(Pm_2ImAm)_2Cl_4]\cdot 2H_2O$**). This slight elongation suggests the central metal ion remains in the same oxidation state for both complexes (i.e. +2). On the other hand, the manganese ions (Mn1 and Mn2) are coordinated at both ends of the trinuclear complex, with a pentacoordinate environment and the metal ion residing within the plane of the tridentate Pm_2ImAm ligand (Figure 5.4). The remaining manganese coordination environment is filled by two Cl anions above and below the plane of the ligand framework. Analysis of the coordination geometry using SHAPE[26] suggests the coordination environment about the peripheryl Mn ions is best described as intermediate between square pyramidal and trigonal bipyramidal (Table 5.2 and Figure 5.5). Interestingly, the coordination environment of the outer manganese ions is very similar to that observed in the tridentate mononuclear complex **$[Mn^{II}(Py_2ImAm)Cl_2]$** discussed in chapter 2, as can be seen in the overlay of both structures (Figure 5.4d). Based on the above-mentioned similarities, along with charge balance, this would suggest an oxidation state of +2 for these manganese ions.

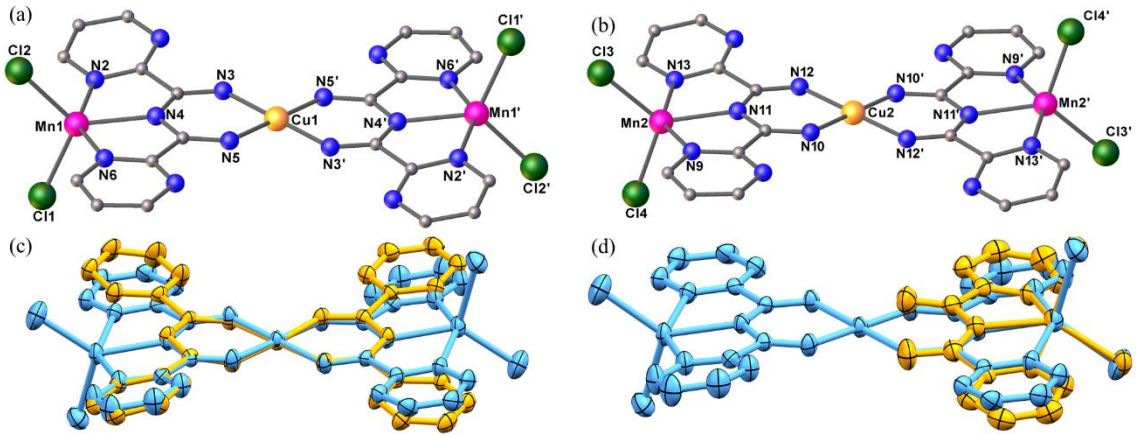

Figure 5.4. (a-b) Structural diagram for both crystallographically independent molecules in **5.1b**. (c) Structural overlay of mononuclear complex **[Cu^{II}(Py$_2$ImAm)$_2$]** (orange) with trinuclear complex **5.1b** (blue). (d) Structural overlay of **[Mn^{II}(Py$_2$ImAm)Cl$_2$]** (orange) with **5.1b** (blue). Hydrogen atoms have been omitted for clarity.

Table 5.1. List of nitrogen to copper distances in the complexes presented in this chapter

[Cu^{II}(Py$_2$ImAm)$_2$]		**[Mn$^{II}_2$Cu^{II}(Pm$_2$ImAm)$_2$Cl$_4$]·2H$_2$O**		**[Mn$^{II}_4$Cu$^{II}_2$(μ-Cl)$_2$(Pm$_2$ImAm)$_4$Cl$_8$] ·2MeOH·2DCM**	
Bond	Length (Å)	Bond	Length (Å)	Bond	Length (Å)
N2-Cu1	1.939(2)	N3-Cu1	1.943(3)	N3-Cu1	1.959(3)
N4-Cu1	1.934(2)	N5-Cu1	1.974(3)	N5-Cu1	1.958(3)
N7-Cu1	1.935(2)	N10-Cu2	1.958(3)	N10-Cu1	1.967(3)
N9-Cu1	1.927(2)	N12-Cu2	1.952(3)	N12-Cu1	1.955(3)

Table 5.2. Results from shape analysis and *tau* parameters for the pentacoordinate metals in **[Mn$^{II}_2$Cu^{II}(Pm$_2$ImAm)$_2$Cl$_4$]·2H$_2$O** and **[Mn$^{II}_4$Cu$^{II}_2$(μ-Cl)$_2$(Pm$_2$ImAm)$_4$Cl$_6$]·2MeOH·2DCM**

Complex	**Metal Centre**	**PP-5**	**vOC-5**	**TBPY-5**	**SPY-5**	**JTBPY-5**	**τ**
[Mn$^{II}_2$Cu^{II}(Pm$_2$ImAm)$_2$Cl$_4$]	**Mn1**	29.85	6.66	3.27	3.67	7.26	0.30
[Mn$^{II}_2$Cu^{II}(Pm$_2$ImAm)$_2$Cl$_4$]	**Mn2**	30.24	5.93	3.27	3.24	7.09	0.25
[Mn$^{II}_4$Cu$^{II}_2$(μ-Cl)$_2$(Pm$_2$ImAm)$_4$Cl$_8$]	**Mn1**	32.15	4.23	5.41	1.77	9.25	0.03
[Mn$^{II}_4$Cu$^{II}_2$(μ-Cl)$_2$(Pm$_2$ImAm)$_4$Cl$_8$]	**Mn2**	32.48	4.01	5.52	1.70	9.33	0.05
[Mn$^{II}_4$Cu$^{II}_2$(μ-Cl)$_2$(Pm$_2$ImAm)$_4$Cl$_8$]	**Cu1**	29.49	4.53	7.46	2.57	11.71	0

PP-5: D_{5h}, Pentagon; vOC-5: C_{4v}, Vacant octahedron; TBPY-5: D_{3h}, Trigonal bipyramid; SPY-5: C_{4v}, Spherical square pyramid; JPPY-6: C_{5v}, Johnson trigonal bipyramid J12

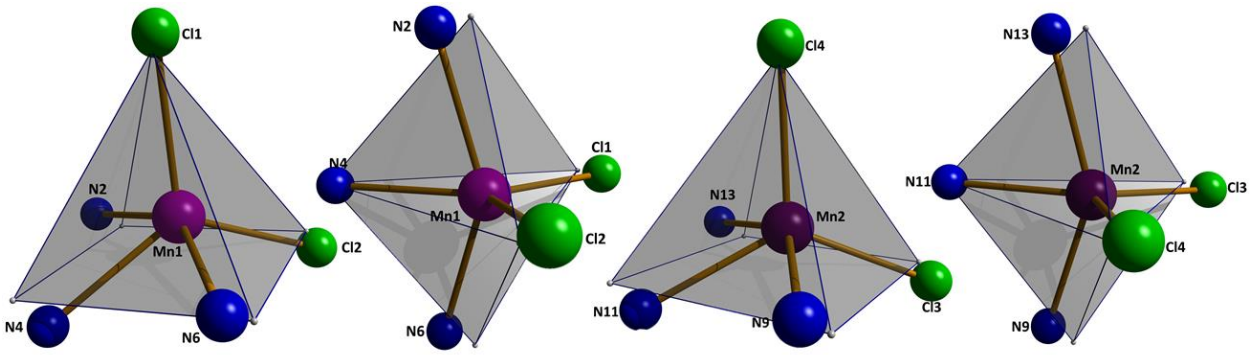

Figure 5.5. Deviation from ideal square pyramidal or trigonal bipyramidal within each molecule in **5.1b**. Manganese atoms are depicted magenta and located in the centre of an ideal square pyramid or trigonal bipyramid.

5.5 Crystal Packing of $[Mn^{II}_2Cu^{II}(Pm_2ImAm)_2Cl_4]\cdot 2H_2O$

In chapter 4, the crystal packing of $\mathbf{[Co^{II}_3(Pm_2ImAm)_2Cl_4]\cdot 5H_2O}$ was discussed, which is equivalent to $\mathbf{[Mn^{II}_2Cu^{II}(Pm_2ImAm)_2Cl_4]\cdot 2H_2O}$, as these complexes are isomorphic. The crystal packing of $\mathbf{[Mn^{II}_2Cu^{II}(Pm_2ImAm)_2Cl_4]\cdot 2H_2O}$ is comprised of columnar stacks of alternating complexes that are twisted by 87.5° with respect to the neighbouring molecules above and below (Figure 5.6). This structural feature likely results from the peripheral manganese dichloride moiety, which is bulky enough to align the planar portion of the complexes in a staggered fashion with respect to one another (Figure 5.6). This results in close Cu-Cu distances of 3.665(3) Å between the central copper ions (Cu1 and Cu2), which is significantly shorter than the intramolecular Cu-Mn distances (i.e. Cu1-Mn1 = 5.566(4) Å; Cu2-Mn2 = 5.525(4) Å). This proximity between neighbouring molecules within the stacked array also leads to short Cu-N contacts (3.210(4) - 3.234(4) Å) and other relatively close Cu-Mn distances (5.915(4) Å and 5.968(4) Å). In addition to playing a pivotal role in the synthesis of the tri *vs*. hexanuclear complex, water also plays an important role in the formation of the extended stacks as each water molecule is connected to three different trinuclear molecules by a set of intra-stack hydrogen bonds (Figure 5.6b and Table A.18). Within the columnar packing arrangement of $\mathbf{[Mn^{II}_2Cu^{II}(Pm_2ImAm)_2Cl_4]\cdot 2H_2O}$, extended solvent channels are observed (Figure 5.7), with the total volume of these channels being 18.4% of unit cell volume using a probe radius of 1.2 Å in Mercury.[27] Although solvent voids exist between the columnar packing arrangement of $\mathbf{[Mn^{II}_2Cu^{II}(Pm_2ImAm)_2Cl_4]\cdot 2H_2O}$, a number of

inter-stack interactions are present, primarily composed of weak C-H···Cl hydrogen bonds (Table B.18). Compared to intra-stack, the inter-stack interactions are much more limited, leading to Mn-Mn distances between columns that are much longer (e.g. ≥ 7.283(4) Å).

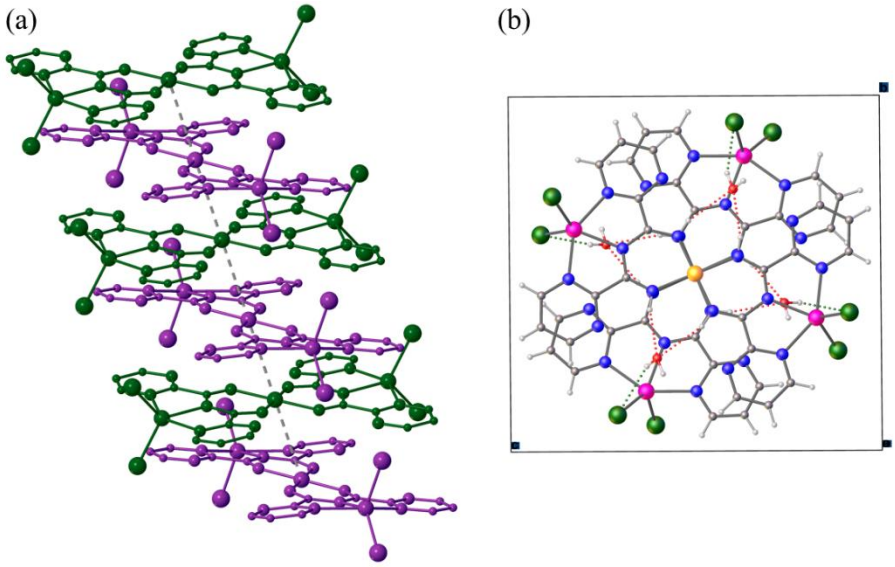

Figure 5.6. (a) View of a single stack in **5.1b** with independent crystallographic molecules in different colour. A gray dashed line was drawn to indicate short Cu-Cu distances. (b) Top view of a single stack along the (100) plane in **5.1b**. N-H···O hydrogen bonds are denoted as red dashed lines, and O-H···Cl as green dashed lines.

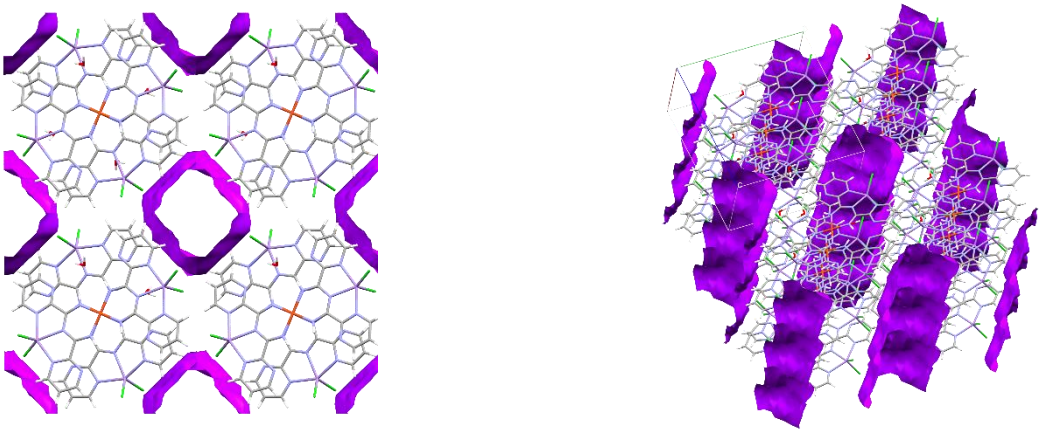

Figure 5.7. Top view (left) and side view (right) of solvent channels in **5.1b**.

5.6 Structural Analysis of $[Mn^{II}_4Cu^{II}_2(\mu\text{-}Cl)_2(Pm_2ImAm)_4Cl_6]\cdot 2MeOH\cdot 2DCM$

Perhaps unsurprisingly, many similarities also exist between the molecular structure of **$[Mn^{II}_4Cu^{II}_2(\mu\text{-}Cl)_2(Pm_2ImAm)_4Cl_6]\cdot 2MeOH\cdot 2DCM$** and **$[Mn^{II}_2Cu^{II}(Pm_2ImAm)_2Cl_4]\cdot 2H_2O$**. The former may be considered as two linear trinuclear moieties similar to **$[Mn^{II}_2Cu^{II}(Pm_2ImAm)_2Cl_4]$** that are linked together through two bridging chloride ions (Figure 5.8). Both complexes crystallize in the triclinic *P*-1 space group. The asymmetric unit of **$[Mn^{II}_4Cu^{II}_2(\mu\text{-}Cl)_2(Pm_2ImAm)_4Cl_6]\cdot 2MeOH\cdot 2DCM$** contains a single copper ion and two manganese ions as the complex is located about a point of inversion. Within the asymmetric unit, the copper ion (Cu1) is bound to two anionic Pm_2ImAm ligands in a bidentate fashion with a bridging chloride ion completing the coordination environment. As revealed by SHAPE[26] analysis, the geometry of Cu1 is best described as elongated square pyramidal (Table 5.2 and Figure 5.9). The bridging Cu-Cl distance is equal to 3.038(2) Å, and this distance is longer than a non-bridging Cu-Cl bond (<2.7 Å).[28] However, the Cu-Cl distance (3.038(2) Å) is shorter than the sum of van der Waals radii for copper and chlorine (3.15 Å).[29] On the other hand, when chloride is bridging a copper ion, there are at least 13 other complexes in the CCDC database with a distance longer than 3 Å.[30-32] Additionally, there is no change in the Cu-N distances of **$[Mn^{II}_4Cu^{II}_2(\mu\text{-}Cl)_2(Pm_2ImAm)_4Cl_6]\cdot 2MeOH\cdot 2DCM$** (1.955(3)-1.967(3) Å) compare to **$[Mn^{II}_2Cu^{II}(Pm_2ImAm)_2Cl_4]\cdot 2H_2O$** (1.943(3)-1.974(3) Å), suggesting the bridging chloride ions have little to no effect on the other coordination bonds (e.g. N-Cu). Base on all the information, the bridging Cu-Cl could be just an electrostatic interaction rather than a coordination bond. Manganese ions in **$[Mn^{II}_4Cu^{II}_2(\mu\text{-}Cl)_2(Pm_2ImAm)_4Cl_6]\cdot 2MeOH\cdot 2DCM$** (Mn1 and Mn2) have minimal deviatiations of the N-Mn and Cl-Mn distances when compare to those in **$[Mn^{II}_2Cu^{II}(Pm_2ImAm)_2Cl_4]\cdot 2H_2O$** (Table 5.3). Despite the small deviation in the N-Mn and Cl-Mn distances, the geometry is different to **$[Mn^{II}_2Cu^{II}(Pm_2ImAm)_2Cl_4]\cdot 2H_2O$**, with the manganese ions in **$[Mn^{II}_4Cu^{II}_2(\mu\text{-}Cl)_2(Pm_2ImAm)_4Cl_6]\cdot 2MeOH\cdot 2DCM$** being closer to square pyramidal than trigonal bypiramidal (Figure 5.9, and Table 5.2).

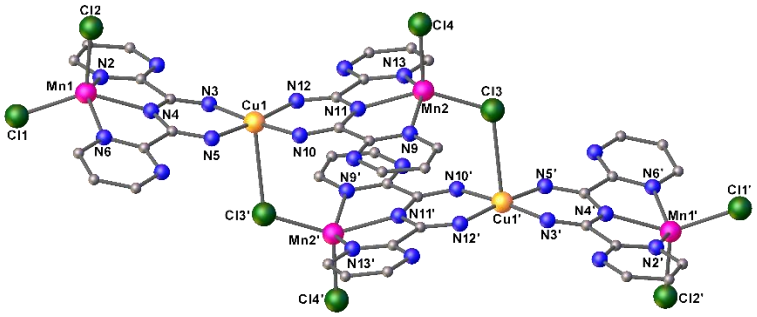

Figure 5.8. Structural diagram of **[$Mn^{II}_4Cu^{II}_2$(μ-Cl)$_2$(Pm$_2$ImAm)$_4$Cl$_6$]·2MeOH·2DCM**. Hydrogen atoms had been omitted for clarity.

Table 5.3. List of manganese distances in both heterometallic complexes

	[$Mn^{II}_2Cu^{II}$(Pm$_2$ImAm)$_2$Cl$_4$]·2H$_2$O	**[$Mn^{II}_4Cu^{II}_2$(μ-Cl)$_2$(Pm$_2$ImAm)$_4$Cl$_8$] ·2CH$_3$OH·2CH$_2$Cl$_2$**
Bond	Lenght (Å)	Lenght (Å)
N2-Mn1	2.250(4)	2.250(3)
N4-Mn1	2.217(3)	2.191(3)
N6-Mn1	2.245(3)	2.234(3)
Cl1-Mn1	2.367(2)	2.348(2)
Cl2-Mn1	2.357(2)	2.351(2)
N9-Mn2	2.258(3)	2.234(3)
N11-Mn2	2.208(3)	2.187(3)
N13-Mn2	2.259(3)	2.235(3)
Cl3-Mn2	2.347(2)	2.337(2)
Cl4-Mn2	2.365(2)	2.370(2)

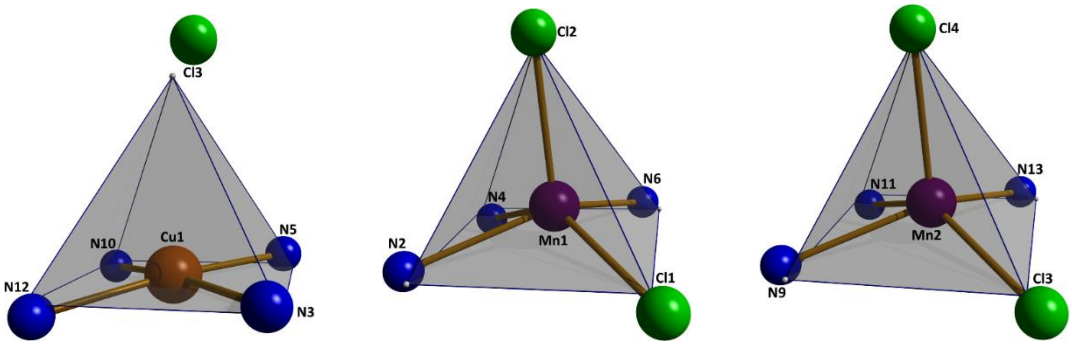

Figure 5.9. Deviation from ideal square pyramidal geometry in **[$Mn^{II}_4Cu^{II}_2$(μ-Cl)$_2$(Pm$_2$ImAm)$_4$Cl$_8$]·2MeOH·2DCM**. Copper atoms are depicted orange, and manganese atoms as magenta. Metal ions are located in the centre of an ideal square pyramid.

5.7 Crystal Packing of $[Mn^{II}_4Cu^{II}_2(\mu\text{-}Cl)_2(Pm_2ImAm)_4Cl_6]\cdot 2MeOH\cdot 2DCM$

Even though there are many similarities between the crystal packing of **$[Mn^{II}_4Cu^{II}_2(\mu\text{-}Cl)_2(Pm_2ImAm)_4Cl_6]\cdot 2MeOH\cdot 2DCM$** and the cobalt analogue presented in chapter 2 (**$[Co^{II}_6(\mu\text{-}Cl)_2(Pm_2ImAm)_4Cl_8]\cdot 2MeOH\cdot 2DCM$**), these structures are not isomorphic. Crystal packing of **$[Mn^{II}_4Cu^{II}_2(\mu\text{-}Cl)_2(Pm_2ImAm)_4Cl_6]\cdot 2MeOH\cdot 2DCM$** is composed of a brick-like array of hexanuclear complexes (Figure 5.10), that are connected by weak C-H···Cl hydrogen bonds (See Appendix B; Table B.18). Within the supramolecular structure, two crystallographically independent solvent molecules were refined (i.e. DCM and methanol (MeOH)). While DCM is disordered and occupies a solvent void, MeOH acts as a hydrogen bond acceptor from the imino hydrogen atoms of one complex and a hydrogen bond donor to a chloride ion in a neighbouring molecule in the plane below. Here, MeOH plays a similar role to water in **$[Mn^{II}_2Cu^{II}(Pm_2ImAm)_2Cl_4]\cdot 2H_2O$**, although in this case it acts as a hydrogen bond donor to only one complex instead two. A short interplanar distance of 3.350(3) Å between the pyrimidyl rings of the Pm_2ImAm ligand coordinated to Mn2 was observed, suggesting π-π interactions between these pyrimidyl rings. While there are shorter intramolecular Cu-Mn distances in **$[Mn^{II}_4Cu^{II}_2(\mu\text{-}Cl)_2(Pm_2ImAm)_4Cl_6]\cdot 2MeOH\cdot 2DCM$** (Table 5.4) compared to **$[Mn^{II}_2Cu^{II}(Pm_2ImAm)_2Cl_4]\cdot 2H_2O$** (Table 5.4), the hexanuclear complex lacks of inter and intramolecular Cu-Cu contacts, with the shortest being equal to 8.3814(8) Å. This is to be expected due to the chloride bridging ions separating the planar trinuclear fragments in **$[Mn^{II}_4Cu^{II}_2(\mu\text{-}Cl)_2(Pm_2ImAm)_4Cl_6]\cdot 2MeOH\cdot 2DCM$**, which are not present in **$[Mn^{II}_2Cu^{II}(Pm_2ImAm)_2Cl_4]\cdot 2H_2O$** allowing for close association between the Cu^{II} ions between neighbouring molecules. A brick-like array of the complex molecules results in short intermolecular Cu1-Mn1 distances (5.857(1) Å), and intermolecular homometallic Mn-Mn distances (6.152(1) Å and 7.085(1) Å), that could be a potential source of intermolecular interactions.

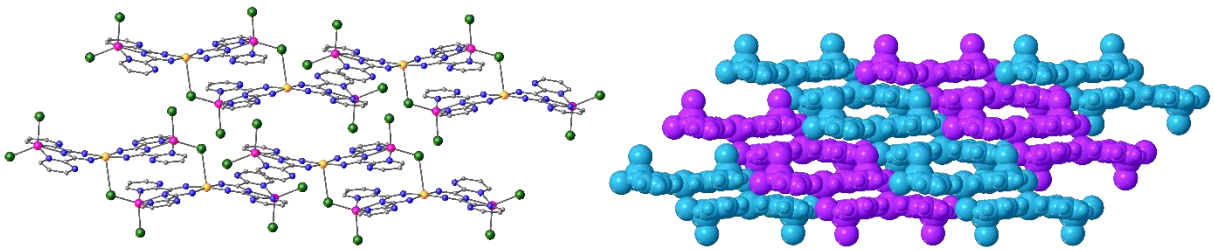

Figure 5.10. Two views of the brick-like packing of **5.2b** at 200 K. Manganese atoms are depicted as magenta and copper atoms are depicted as orange. In the left figure individual molecules are differentiated by colour coding in blue and violet. Solvent molecules and hydrogen bonds had been omitted for clarity.

Table 5.4. List of relevant copper to manganese distances

$[Mn^{II}_2Cu^{II}(Pm_2ImAm)_2Cl_4]\cdot 2H_2O$			**$[Mn^{II}_4Cu^{II}_2(\mu\text{-}Cl)_2(Pm_2ImAm)_4Cl_8]\cdot 2MeOH\cdot 2DCM$**		
Atoms	Type	Distance (Å)	Atoms	Type	Distance (Å)
Cu1-Mn1	Intra	5.566(4)	Cu1-Mn2	Intra	4.5081(7)
Cu1-Mn2	Inter	5.915(4)	Cu1-Mn1	Intra	5.5122(7)
Cu1-Mn2	Intra	7.276(4)	Cu1-Mn2	Intra	5.5152(6)
Cu2-Mn2	Inter	5.525(4)	Cu1-Mn1	Inter	5.8568(8)
Cu2-Mn1	Intra	5.968(4)	Cu1-Mn2	Inter	7.3259(7)
Cu2-Mn1	Intra	7.295(5)			

5.8 Magnetochemistry of the Central Mononuclear Complex $[Cu^{II}(Py_2ImAm)_2]$

To investigate the magnetic behaviour of **$[Cu^{II}(Py_2ImAm)_2]$**, variable-temperature magnetic susceptibility data was collected on a polycrystalline sample, revealing a χT product of 0.42 cm^3 K mol^{-1} at room temperature (Figure 5.11). This value is close to what is expected for Cu^{II} from the spin-only formalism (C = 0.375 cm^3 K mol^{-1}; assuming g = 2) indicating a g-value around 2.12(5). Upon lowering the temperature, the χT product remains relatively constant until 15 K, where a decrease in the χT product is observed until it reaches 0.29 cm^3 K mol^{-1} at 1.9 K. This decrease at low temperature is likely due to very weak antiferromagnetic intermolecular interactions between spin-carriers estimated at -0.69 K from a Curie-Weiss fit ($\theta = 2zJS(S+1)/3k_B$ = -1.38 K, z = 4). The field dependence of the magnetization is also in good agreement with an S = ½ configuration of the Cu^{II} centre (Figure 5.11), as confirmed via fitting to the S = ½ Brillouin function, which affords a consistent g-factor of 2.11(5). This g-factor is also in good correlation with the value of 2.10 observed from EPR at RT (Figure 5.12).

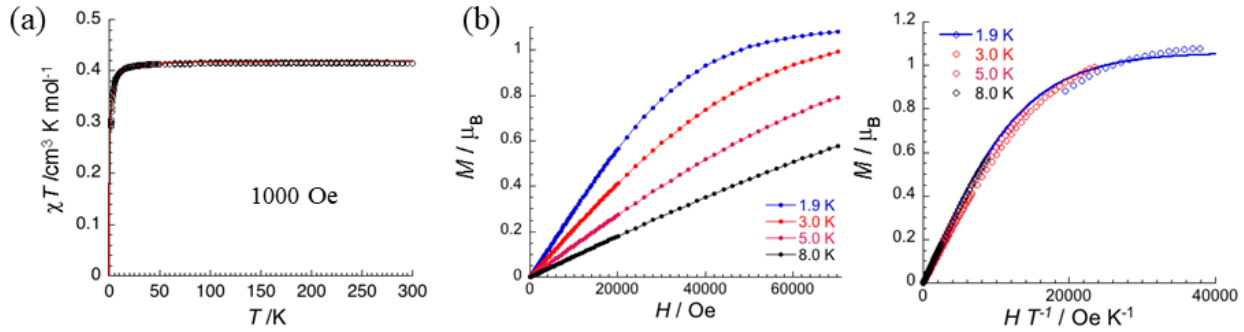

Figure 5.11. (a) Temperature dependence of the dc magnetic susceptibility ($\chi = M/H$ per mole of complex) plotted as χT vs T for **[Cu^{II}(Py$_2$ImAm)$_2$]**, collected under an applied field of 1000 Oe. The solid red line corresponds to the best fit to a Curie-Weiss law for an S = 1/2 spin (g = 2.12(5), χ = -1.38(2) K). (b) Field (H) dependence of the magnetization (M) plotted as M vs H (left) and M vs H/T (right) for **[Cu^{II}(Py$_2$ImAm)$_2$]** at the indicated temperatures (T). The solid line on the M vs H/T data is the best fit to the S = 1/2 Brillouin function with g = 2.11(5).

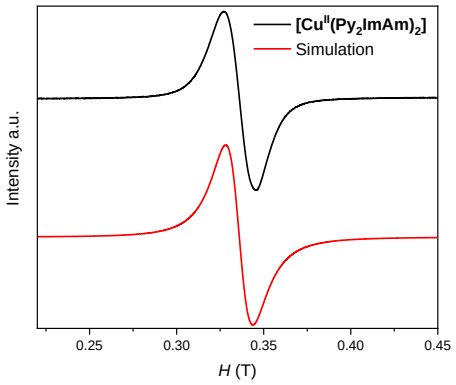

Figure 5.12. EPR spectrum of **[Cu^{II}(Py$_2$ImAm)$_2$]** at RT. EPR was collected in a crystalline sample.

5.9 Conclusions

Heterometallic complexes have been successfully synthesized for first time with Pm$_2$ImAm. The one pot synthesis of heterometallic complexes presented here has significant potential to improve both the yield and scale of the preparation of these complexes, especially when compared to a multi-step synthesis. These finding may aid in the development of the complexes presented here as well as others with varying metal ions, and afford materials relevant to a number of

applications. The imino groups within Pm_2ImAm act as hydrogen bond donors in the complexes reported here, which induces similar crystal packing motifs to comparable molecular frameworks. For example, **$[Co^{II}_3(Pm_2ImAm)_2Cl_4]\cdot 5H_2O$** and **$[Mn^{II}_2Cu^{II}(Pm_2ImAm)_2Cl_4]\cdot 2H_2O$** are isomorphic, and **$[Co^{II}_6(\mu\text{-}Cl)_2(Pm_2ImAm)_4Cl_8]\cdot 2MeOH\cdot 2DCM$** and **$[Mn^{II}_4Cu^{II}_2(\mu\text{-}Cl)_2(Pm_2ImAm)_4Cl_6]\cdot 2MeOH\cdot 2DCM$** have similar crystal packing and hydrogen bonding interactions. We anticipate these heterometallic complexes will afford intriguing magnetic properties and are awaiting results regarding testing of their magnetochemistry, as well as their introduction as MRI contrast agents. These experiments are underway in collaboration by our collogues at the University of Ottawa and abroad.

5.10 Experimental Section

General Procedures. Chloroform, isopropanol, and triethyl amine were reagent grade and used without further purification. Anhydrous dichloromethane (DCM) was obtained from a dry solvent system. Methanol was distilled over sodium and the water content on the methanol was quantified by the Karl Fischer method.[33] The 99% methanol was prepared from the dry methanol and a known amount of water was added to it. *N*-2-pyridylimidoyl-2-pyridylamidine (Py_2ImAm), and *N*-2-pyrimidylimidoyl-2-pyrimidylamidine (Pm_2ImAm) were synthesized according to the literature procedures reported earlier by us.[9, 10] IR spectra were recorded on an Agilent Technologies Cary 630 FT-IR spectrometer. Solid state EPR was collected at RT in a Bruker EMXmicro EPR and a frequency of 9.86 GHz. A single crystalline phase was confirmed by comparison of powder XRD patterns with those calculated from the single crystal data (See Appendix F; Figure F.1-F.3).

Synthesis of $[Cu^{II}(Py_2ImAm)_2]$. A solution of copper(II) chloride dihydrate (0.0560 g, 0.328 mmol) in 6 mL of isopropanol was added to a solution of Py_2ImAm (0.1495 g, 0.663 mmol) in 16.2 mL of DCM and 1.8 mL of triethylamine. Small red plate crystals were filtered after a week and rinsed with 5 mL of methanol. Yield: 0.1047 g (0.204 mmol, 62.2%). IR (cm^{-1}): 3278 (w), 3256 (m), 3242 (m), 3053 (w), 1597 (w), 1576 (m), 1549 (m), 1507 (m), 1474 (s), 1444 (s), 1419 (s), 1290 (m), 1265 (m), 1242 (m), 1217 (m), 1137 (w), 1055 (s), 998 (s), 898 (w), 876 (w), 855 (w), 817 (s), 743 (s), 702 (s).

Synthesis of $[Mn^{II}_2Cu^{II}(Pm_2ImAm)_2Cl_4]\cdot 2H_2O$. A solution of copper(II) acetylacetonate (0.2338 g, 0.893 mmol) in 20 mL of chloroform was added to a solution of Pm_2ImAm (0.4010 g, 1.76 mmol) in 20 mL of chloroform. A deep red solution formed. In a separate flask $MnCl_2\cdot 4H_2O$ (1.0214 g, 5.16 mmol) was dissolved using 20 mL of 99% methanol. After ten minutes of the formation of the red chloroform solution, the methanol solution was layered on top of the chloroform solution. After three hours pale pink-orange crystals were filtered out and rinsed with 10 mL of isopropanol. Yield: 0.5120 g (72.4%, 0.637 mmol). IR: 3569 (m), 3484 (m), 3245 (s), 3075 (m), 1611 (s), 1572 (s), 1560 (s), 1546 (s), 1477 (s), 1439 (w), 1408 (s), 1392 (s), 1293 (m), 1264 (m), 1232 (m), 1195 (m), 1109 (w), 1093 (w), 1052 (m), 1017 (s), 887 (s), 835 (s), 754 (w), 703 (s), 686 (m). Prior to elemental analysis the solvent from the porous channels was removed in vacuo at 60 °C. Anal. Calcd for $C_{20}H_{20}Cl_4CuMn_2N_{14}O_2$: C, 29.89; H, 2.51; N, 24.40. Found: C, 30.31; H, 2.18; N, 24.43.

Synthesis of $[Mn^{II}_4Cu^{II}_2(\mu\text{-}Cl)_2(Pm_2ImAm)_4Cl_8]\cdot 2MeOH\cdot 2DCM$. A degassed solution of copper(II) acetylacetonate(0.1321 g, 0.507 mmol) in 20 mL of anhydrous DCM was added via syringe to a degassed solution of Pm_2ImAm (0.2273 g, 1.00 mmol) in 20 mL of anhydrous DCM. A deep red solution formed. In a separate flask $MnCl_2$ (0.1300 g, 1.033 mmol) was dissolved using 20 mL of 99.97% methanol. The methanol solution was then transferred via syringe on top of the red DCM solution. After one day an orange crystalline precipitate appear, and the mother liquor of the precipitate was removed by carefully decanting the solvent above the crystals and replacing it with 30 mL of a fresh 1:1 mixture of DCM and methanol. One-week later block orange crystals were filtered out. Yield: 0.1860 g (0.105 mmol, 42.0%). IR (cm^{-1}): 3448 (m), 3262 (w), 3221 (m), 1615 (s), 1572 (m), 1547 (s), 1474 (s), 1406 (m), 1390 (s), 1288 (m), 1261 (m), 1230 (w), 1194 (m), 1088 (m), 1050 (m), 1030 (m), 1013 (m), 908 (m), 844 (m), 826 (s), 734 (m), 702 (s), 678 (s).

X-ray crystallography. Data collection for single crystals of **$[Cu^{II}(Py_2ImAm)_2]$**, **$[Mn^{II}_2Cu^{II}(Pm_2ImAm)_2Cl_4]\cdot 2H_2O$** and **$[Mn^{II}_4Cu^{II}_2(\mu\text{-}Cl)_2(Pm_2ImAm)_4Cl_8]\cdot 2MeOH\cdot 2DCM$** (See Appendix B; Table B.17) were obtained on a Bruker KAPPA APEX-II CCD diffractometer (graphite monochromated Mo K_α radiation, $\lambda = 0.71073$ Å, ω-scans with a 0.5° step in ω) at 210 K, 295 K, and 200 K respectively. For all samples the data integration was done using Apex3 and the absorption corrections were applied by using the semi-empirical method of the SADABS program.[34] The structures were solved using SHELXT[35] and refined by full-matrix least-squares

methods on F^2 with SHELXL-2015[36] in anisotropic approximation for all non-hydrogen atoms. The hydrogen atoms on the aromatic rings were constrained to ride on their parent atoms with C-H = 0.95 Å and $U_{iso} = 1.2U_{eq}(C)$, while imino N-H hydrogen atoms were refined isotropically. SADI restrain was used to associate the imino N-H distances with a 0.02 standard deviation in the four complexes. The single crystal used to collect **$[Mn^{II}_2Cu^{II}(Pm_2ImAm)_2Cl_4]\cdot 2H_2O$** was a non-merohedral twin, after integrating the data in Apex3[34] a HKL 5 file was generated using Platon.[37] Powder X-ray diffraction (PXRD) was performed on a Rigaku Ultima IV diffractometer, with Cu K_α monochromatic radiation (λ = 1.54056 Å) and θ–2θ geometry. The simulated PXRD pattern was calculated using Mercury[27] and was compared to the experimental PXRD of the bulk sample.

5.11 References

[1] Zavafer, A.; Koinuma, W.; Chow, W. S.; Cheah, M. H.; Mino, H., *Sci. Rep.* **2017,** 7, (1), 7604.

[2] Högbom, M.; Andersson, M. E.; Nordlund, P., *J. Biol. Inorg. Chem.* **2001,** 6, (3), 315-323.

[3] Chang, C. M.; Klema, V. J.; Johnson, B. J.; Mure, M.; Klinman, J. P.; Wilmot, C. M., *Biochemistry* **2010,** 49, (11), 2540-2550.

[4] Wang, Y.; Stack, T. D. P., *J. Am. Chem. Soc.* **1996,** 118, (51), 13097-13098.

[5] Nestke, S.; Ronge, E.; Siewert, I., *Dalton Trans.* **2018,** 47, (31), 10737-10741.

[6] Gale, E. M.; Jones, C. M.; Ramsay, I.; Farrar, C. T.; Caravan, P., *J. Am. Chem. Soc.* **2016,** 138, (49), 15861-15864.

[7] Pedersen, K. S.; Bendix, J.; Clérac, R., *ChemComm* **2014,** 50, (34), 4396-4415.

[8] Housecroft, C. E.; Constable, E. C., *Chem. Soc. Rev.* **2015,** 44, (23), 8386-8398.

[9] Leitch, A. A.; Korobkov, I.; Assoud, A.; Brusso, J. L., *ChemComm* **2014,** 50, (38), 4934-4936.

[10] Yousaf, M.; Yutronkie, N. J.; Castañeda, R.; Klein, J. A.; Brusso, J., *New J Chem* **2017,** 41, (20), 12218-12224.

[11] Castañeda, R.; Hollingshead, A.; Gabidullin, B.; Brusso, J. L., *Cryst. Growth Des.* **2017,** 17, (12), 6572-6578.

[12] Kajiwara, T.; Kamiyama, A.; Ito, T., *ChemComm* **2002**, (12), 1256-1257.

[13] Igashira-Kamiyama, A.; Kajiwara, T.; Konno, T.; Ito, T., *Inorg. Chem.* **2006,** 45, (16), 6460-6466.

[14] Tong, M.-L.; Wu, Y.-M.; Tong, Y.-X.; Chen, X.-M.; Chang, H.-C.; Kitagawa, S., *Eur. J. Inorg. Chem.* **2003,** , (13), 2385-2388.

[15] Zheng, L.-L.; Zhang, W.-X.; Qin, L.-J.; Leng, J.-D.; Lu, J.-X.; Tong, M.-L., *Inorg. Chem.* **2007,** 46, (23), 9548-9557.

[16] Glaser, T.; Theil, H.; Liratzis, I.; Weyhermüller, T.; Bill, E., *Inorg. Chem.* **2006,** 45, (13), 4889-4891.

[17] Kopylovich, M. N.; Tronova, E. A.; Haukka, M.; Kirillov, A. M.; Kukushkin, V. Y.; Fraústo da Silva, J. J. R.; Pombeiro, A. J. L., *Eur. J. Inorg. Chem.* **2007,** 2007, (29), 4621-4627.

[18] Kopylovich, M. N.; Lasri, J.; Guedes da Silva, M. F. C.; Pombeiro, A. J. L., *Dalton Trans.* **2009**, (16), 3074-3084.

[19] Kopylovich, M. N.; Haukka, M.; Kirillov, A. M.; Kukushkin, V. Y.; Pombeiro, A. J. L., *Chem.: Eur. J.* **2007,** 13, (3), 786-791.

[20] Kopylovich, M. N.; Kirillov, A. M.; Tronova, E. A.; Haukka, M.; Kukushkin, V. Y.; Pombeiro, A. J. L., *Eur. J. Inorg. Chem.* **2010,** , (16), 2425-2432.

[21] Castañeda, R.; Harriman, K. L. M.; Wong, J. W. L.; Gabidullin, B.; Murugesu, M.; Brusso, J. L., *Eur. J. Inorg. Chem.* **2019,** , (7), 963-972.

[22] Boča, R.; Hvastijová, M.; Kožíšek, J.; Valko, M., *Inorg. Chem.* **1996,** 35, (16), 4794-4797.

[23] Nesterova, V. O.; Kopylovich, N. M.; Nesterov, S. D., *Inorganics* **2019,** 7, (7).

[24] Kahn, O., *Molecular Magnetism*. ed.; VCH: 1993.

[25] Van Vleck, J. H., *The theory of electric and magnetic susceptibilities*. ed.; Clarendon Press: Oxford, 1932.

[26] Casanova, D.; Llunell, M.; Alemany, P.; Alvarez, S., *Chem.: Eur. J.* **2005,** 11, (5), 1479-1494.

[27] Macrae, C. F.; Bruno, I. J.; Chisholm, J. A.; Edgington, P. R.; McCabe, P.; Pidcock, E.; Rodriguez-Monge, L.; Taylor, R.; van de Streek, J.; Wood, P. A., *J. Appl. Crystallogr.* **2008,** 41, (2), 466-470.

[28] Wohlert, S.; Wriedt, M.; Jess, I.; Nather, C., *Acta Cryst. E.* **2011,** 67, (6), m695.

[29] Bondi, A., *J. Phys. Chem.* **1964,** 68, (3), 441-451.

[30] Groom, C. R.; Bruno, I. J.; Lightfoot, M. P.; Ward, S. C., *Acta Cryst. B* **2016,** 72, (2), 171-179.

[31] Chiari, B.; Cinti, A.; Piovesana, O.; Zanazzi, P. F., *Inorg. Chem.* **1995,** 34, (10), 2652-2657.

[32] Beznischenko, A. O.; Makhankova, V. G.; Kokozay, V. N.; Dyakonenko, V. V.; Zubatyuk, R. I.; Shishkin, O. V.; Jezierska, J., *Inorganica Chim. Acta* **2009,** 362, (4), 1307-1314.

[33] Fischer, K., *Angew. Chem.* **1935,** 48, (26), 394-396.

[34] Bruker *APEX3, SAINT, SADABS and TWINABS*, Bruker Analytical X-ray Instruments Inc.: Madison, WI, 2016.

[35] Sheldrick, G., *Acta Cryst. A* **2015,** 71, (1), 3-8.

[36] Sheldrick, G., *Acta Cryst. C* **2015,** 71, (1), 3-8.

[37] Spek, A., *Acta Cryst. D* **2009,** 65, (2), 148-155.

Chapter 6

Conclusion

6.1 Summary and Conclusions

The formation of mononuclear, homometallic and heterometallic polynuclear complexes employing the imidoyl amidine ligands *N*-2-pyridylimidoyl-2-pyridylamidine (Py_2ImAm) or *N*-2-pyrimidylimidoyl-2-pyrimidylamidine (Pm_2ImAm) with first row transition metals was achieved during the course of this thesis. Prior to this study, only four examples of coordination complexes using these ligand frameworks had had been reported, with the ligand prepared via metal assisted transformations.[1-4] Having Py_2ImAm and Pm_2ImAm in hand enabled us to study the chemistry of these ligands and explore how to selectively coordinate to first row transition metal ions in a discrete coordination fashion (e.g. bidentate or tridentate mononuclear complexes), or through coordination into both sites to afford polynuclear complexes. Interestingly, one of the main factors that direct the coordination of these ligands is the presence or absence of a weak acid. While a weak acid directs the metal ion to terpy-like coordination, neutral or basic conditions direct the metal ion to coordinate in a bidentate fashion. This may be related to the fact these ligands possess labile imino hydrogens atoms, and display imino-amino tautomerism that could help during the deprotonation of these ligands. In the presence of a metal, both Py_2ImAm and Pm_2ImAm can be easily deprotonated by a weak base such as triethylamine. In the solid state, these imino hydrogen atoms are frequently an important aspect in the crystal packing, as they act as hydrogen bond donors and tend to result in the formation of isomorphic structures with different metal ions. Since this seminal work, other research groups have begun to explore the chemistry of Py_2ImAm, with the recently reported complex **[Ni(PyImAm)$_2$]** carrying out the electrochemical reduction of CO_2 into CO.[5] This demonstrates the potential of Py_2ImAm as a non-innocent ligand capable of being reduced; however, also shows the ligand was unstable under those conditions – e.g. reaction with CO_2 produces the carboxylic acid ligand derivatives.

In general, the formation of mononuclear and polynuclear complexes with Py_2ImAm and Pm_2ImAm was studied, and it was observed that mononuclear complexes are favored by attempting a fast crystallization, while polynuclear complexes are favored under conditions that retard the formation of the polynuclear complexes. Examples of conditions that slow down the

crystallization include the use of a very weak acidic counter ion such as diaminopyridinium, or the use of a small amount of a highly polar solvent such as dimethylsulfoxide. Slow crystallization affords more time for the metal ions to coordinate in both sides of the ligand framework. Ligands with multiple coordination sites have the opportunity to coordinate the same metal in different electronic configurations. In that regard, two main complexes had been studied during the course of this thesis, low and high spin state complexes. Low spin mononuclear complexes were the result of coordinating Mn^{III}, Fe^{III}, Co^{II}, Co^{III} to the bidentate pocket of the anionic ligands Py_2ImAm and Pm_2ImAm. On the other hand coordinating the metal chloride salts $MnCl_2$, $FeCl_3$ and $CoCl_2$ to the tridentate pocket of the neutral ligands Py_2ImAm and Pm_2ImAm resulted in high spin mononuclear complexes. The results obtained from these mononuclear complexes aided in the understanding of the magnetochemistry of polynuclear complexes **$[Mn^{III}Mn^{II}_3(Pm_2ImAm)_3Cl_6]$**, **$[Fe^{III}_4(Pm_2ImAm)_3Cl_9]$**, **$[Co^{II}_3(Pm_2ImAm)_2Cl_4]$** and **$[Co^{II}_6(\mu\text{-}Cl)_2(Pm_2ImAm)_4Cl_8]$** in more detail. These results revealed the polynuclear complexes possess the same metal ions in low and high spin configurations, depending on the coordination environment. Mixed low and high spin complexes are not very common, and in the case of manganese this is the first example of a complex with both low and high spin manganese ions. Overall, these imidoyl amidine ligands have great potential to build several metallic complex architectures.

6.2 Future Works

The strategy used to build copper-manganese heterometallic complexes in chapter five, can serve as a template to obtain heterometallic complexes with different metal ions; as, for example, combinations of nickel-manganese, cobalt-manganese, and iron-manganese can be attempted by employing the same procedure. The magnetochemistry of **$[Mn^{II}_2Cu^{II}(Pm_2ImAm)_2Cl_4]\cdot 2H_2O$** and **$[Mn^{II}_4Cu^{II}_2(\mu\text{-}Cl)_2(Pm_2ImAm)_4Cl_6]\cdot 2MeOH\cdot 2DCM$** is currently underway by our colleagues at the Centre de Recherche Paul Pascal. As well, lanthanides in general are a very interesting topic, although imidoyl amidine complexes with lanthanides have yet to be reported. Our group is currently exploring the chemistry of Py_2ImAm and Pm_2ImAm with various lanthanides, as luminescent materials and single molecule magnets.

Interestingly, all the complexes described here with a metal ion coordianted in a tridentate fashion are water soluble, and for that reason they are suitable to be tested in applications such as

water splitting and MRI contrast agents. In collaboration with the Shuhendler group at University of Ottawa, we are currently exploring the potential of these systems as MRI contrast agents. These complexes bring many opportunities never explored before in MRI contrast agents, such as studying polynuclear complexes and heterometallic complexes.

6.3 References

[1] Kajiwara, T.; Kamiyama, A.; Ito, T., *ChemComm* **2002**, (12), 1256-1257.

[2] Igashira-Kamiyama, A.; Kajiwara, T.; Konno, T.; Ito, T., *Inorg. Chem.* **2006,** 45, (16), 6460-6466.

[3] Tong, M.-L.; Wu, Y.-M.; Tong, Y.-X.; Chen, X.-M.; Chang, H.-C.; Kitagawa, S., *Eur. J. Inorg. Chem.* **2003,** , (13), 2385-2388.

[4] Zheng, L.-L.; Zhang, W.-X.; Qin, L.-J.; Leng, J.-D.; Lu, J.-X.; Tong, M.-L., *Inorg. Chem.* **2007,** 46, (23), 9548-9557.

[5] Bohu, T.; Santelli, C. M.; Akob, D. M.; Neu, T. R.; Ciobota, V.; Rösch, P.; Popp, J.; Nietzsche, S.; Küsel, K., *Front. Microbiol.* **2015,** 6, 734.

Appendix A: Molecular Magnetism

Nowadays, data centers around the world use hard drives to store the vast majority of the data used on the internet. One of the main limitations of hard drives is the density of information that can be saved within them. To store information, hard drives are built using inorganic oxide materials that have magnetic domains composed of thousands of metal ions. Molecular magnetic materials are very interesting because they can decrease these domains down to the molecular level. In this context, it is not surprising that a number of research groups are currently studying the magnetochemistry of metallic complexes to increase the storage capacity of hard drives, and by doing so reducing the cost of data storage. This appendix has the purpose to clarify the main factors and variables in the characterization of metallic complexes by magnetometry.

The principles of molecular magnetism have been studied in more detail and can be found in the early works of Olivier Kahn and John Hasbrouck Van Vleck.[1, 2] Magnetic materials in general can be classified as diamagnetic or paramagnetic. Diamagnetism is present in all matter and originates from the interaction of paired electrons with an applied magnetic field (*H*) which results in an induced magnetic field with opposite direction to the applied field. Therefore, the value of the diamagnetic contribution is always negative and on the order of 10^{-6} cm^3mol^{-1}. Paramagnetism, on the other hand, is experienced by materials with unpaired electrons, which lead to an attraction to the applied magnetic field.

In diamagnetic or paramagnetic materials, the response to an applied magnetic field is known as its magnetization (*M*, Equation A.1). The relation between *M* and *H* is the magnetic susceptibility (χ).

Equation A.1

$$\chi = \frac{M}{H}$$

By convention χ is normally given as the molar magnetic susceptibility (χT). The Curie law describes the change in χT at different spins (Equation A.2) and can be applied to non-interacting magnetic ions.

Equation A.2

$$\chi\mathrm{T} = \frac{Ng^2\mu_B^2 S(S+1)}{3k\mathrm{T}}$$

In this equation *N* is the Avogadro's number, *g* is the Landé *g* factor or the spectroscopic splitting factor, μ_B is the Bohr magneton, *k* is the Boltzmann constant, T is the temperature and *S* the spin of the magnetic ion. At RT therefore it is possible to use the Equation A.2 to calculate the χT of a mononuclear complex using the *g* value of a free electron (2.00), this calculation is sometimes referred as the "*spin only formalism*". Although metals do not have the *g* value of a free electron, the *g* values of first row transition metals from manganese to copper are generally close to 2.00 and the spin only formalism is very useful to quickly identify the electron configuration in these complexes. For the convenience of the reader the spin only χT values for the spins discussed in this thesis can be found in Table A.1.

Table A.1. Expected χT values according the spin only formalism for ions with different spins.

Spin (*S*)	½	**1**	**3/2**	**2**	**5/2**
χT (cm^3Kmol^{-1})	0.375	1	1.875	3	4.375
Names	Doublet	Triplet	Quartet	Quintet	Sextet
Examples	Cu^{II}, Co^{II} (L.S.), Fe^{III} (L.S.)	Ni^{II} (H.S.), Mn^{III} (L.S.)	Co^{II} (H.S.), Mn^{IV}	Mn^{III} (H.S.), Fe^{II} (H.S.)	Mn^{II} (H.S.), Fe^{III} (H.S.)

Polynuclear complexes in general can have magnetic interactions between the different metal ions. The main pathways of magnetic interactions are superexchange and direct exchange. In the case of superexchange the magnetic interactions occur through a diamagnetic bridging ligand. This exchange is the most common in molecular complexes. On the other hand, direct exchange involves magnetic coupling as a consequence of the direct overlap of magnetic orbitals. Direct exchange represents the strongest magnetic exchange pathway, although in the case of first row transition metals from manganese to copper requires metals that are close to each other (< 4 Å). Magnetic interactions can also be categorized as ferromagnetic (↑↑↑↑) or antiferromagnetic (↑↓↑↓) when the alignment of magnetic moments is in the same, or opposite direction, respectively.

Frequently, polynuclear complexes lack of meaningful interactions at RT, and in such a case it is possible to use Equation A.2 or Table A.1 to predict the expected χT value at RT. A very practical way to visualize magnetic interactions is the plot χT *vs.* T, and this plot is used by convention when presenting magnetic data. Depending on the type of interaction, a decrease of temperature results in a curve appearing at low temperature (Figure A.1). If the interaction of the spins is ferromagnetic, the magnetic moment of the spins is aligned in the same direction (↑↑), and

thus, an increase of the χT value is observed ($J > 0$). However, if the interaction is antiferromagnetic the spins are aligned in opposite direction (↑↓) and a decrease of the χT is observed in the plot ($J < 0$).

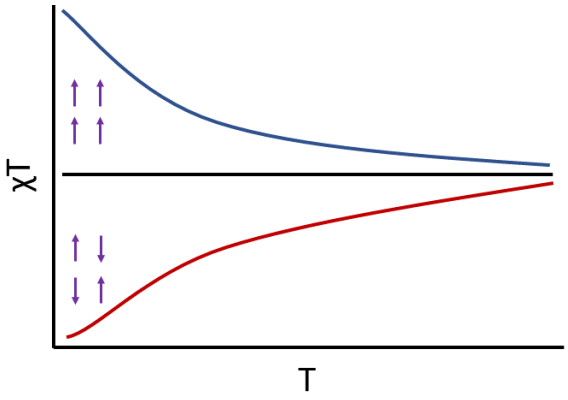

Figure A.1. Illustration of ferromagnetic (top, blue line) and antiferromagnetic (bottom, red line) interactions in a χT *vs.* T plot.

By allowing the identification of the spin configuration of metal ions, magnetochemistry provides very valuable information about the metal ions, and this information can be used in other chemistry fields, as for example catalysis. Single Molecule Magnets (SMM) belong to a new class of magnetic materials in which the magnetic like behavior arises from the intrinsic large spin ground state and uniaxial magnetic anisotropy. More detailed information about SMMs can be found in the review of Pedersen *et al.*[3]

Appendix B: Crystallographic Tables

Table B.1. Unit cell parameters measured for the **[$Fe^{III}(Py_2ImAm)_3$]** complexes grown using different solvents to dissolve the ligand.

Solvent	Acetonitrile	Dichloromethane	Chloroform	Dichloroethane	Chlorobenzene
Crystal system	P	C	C	P	P
Lattice type	hexagonal	monoclinic	monoclinic	monoclinic	monoclinic
a (Å)	14.794(5)	20.3666(8)	20.83(7)	12.400(16)	15.130(12)
b (Å)	14.794(5)	17.2928(7)	17.74(6)	17.107(24)	15.955(13)
c (Å)	28.457	11.4834(4)	11.71(4)	16.108(22)	16.558(13)
	90	90	90	90	90
β (°)	90	111.733(2)	111.68(4)	95.510(29)	95.3387(10)
	120	90	90	90	90
Volume ($Å^3$)		3756.9(3)	4020(40)	3401(14)	3980(9.6)

Table B.2. Experimental crystallographic details for **1.3a** and the octahedral isomorphic structures with MeCN.

Abbreviation	**1.3a**	**2.1b·MeCN**	**2.2b·MeCN**	**2.3b·MeCN**
Empirical formula	$C_{12}H_{11}N_5$	$C_{36}H_{30}MnN_{15}$	$C_{38}H_{33}FeN_{16}$	$C_{38}H_{33}CoN_{16}$
Formula weight	225.26	727.70	769.73	772.74
Temperature (K)	200	200	200	210
Crystal system	Monoclinic	hexagonal	hexagonal	hexagonal
Space group	$P2_1/c$	*R*-3	*R*-3	*R*-3
a (Å)	11.2479(11)	14.8272(4)	14.794(5)	14.827(3)
b (Å)	15.8874(15)	14.8272(4)	14.794(5)	14.827(3)
c (Å)	12.7429(11)	28.0739(7)	28.457(10)	28.357(6)
α	90	90	90	90
β	98.132(7)	90	90	90
γ°	90	120	120	120
Volume ($Å^3$)	2254.3(4)	5345.1(3)	5394(4)	5399(2)
Z	8	6	6	6
ρ_{calc} (g/cm^3)	1.327	1.356	1.422	1.426
μ (mm^{-1})	0.086	0.421	0.474	0.531
F(000)	944	2256.0	2394.0	2400
2Θ range for data collection (°)	3.65 to 57.99	3.48 to 56.64	3.48 to 57.97	3.482 to 55.49
Reflections collected	32489	11087	19031	29109
Independent reflections	5926	2970	3062	2789
Data/restraints/parameters	5926/1/327	2970/0/163	3062/0/185	2789/0/185
Goof on F^2	1.045	1.049	1.054	0.994
R_1 [I>=2σ (I)]	0.0552	0.0432	0.0508	0.0449
wR_2 [I>=2σ (I)]	0.1562	0.1085	0.1175	0.1088
wR_2 all reflections	0.1736	0.1191	0.1252	0.1144
H atom treatment	Mixed	Mixed	Mixed	Mixed

Table B.3. Experimental crystallographic details for isomorphic structures with DCM.

Abbreviation	**2.1b·DCM**	**2.2b·DCM**	**2.3b·DCM**
Empirical formula	$C_{37}H_{32}Cl_2MnN_{15}$	$C_{37}H_{32}Cl_2FeN_{15}$	$C_{37}H_{32}Cl_2CoN_{15}$
Formula weight	812.61	813.52	816.60
Temperature (K)	200	200	200.0
Crystal system	Monoclinic	Monoclinic	Monoclinic
Space group	*C2/c*	*C2/c*	*C2/c*
a (Å)	20.3666(8)	20.4049(5)	20.242(2)
b (Å)	17.2928(7)	17.1474(4)	17.3783(19)
c (Å)	11.4834(4)	11.5359(3)	11.3976(12)
β	111.733(2)	112.2950(10)	110.899(2)
Volume (Å^3)	3756.9(3)	3734.56(16)	3745.6(7)
Z	4	4	4
ρ_{calc} (g/cm^3)	1.437	1.447	1.448
μ (mm^{-1})	0.545	0.598	0.652
F(000)	1672.0	1676.0	1680.0
2Θ range for data collection/°	3.19 to 57	3.208 to 56.624	4.308 to 61.066
Reflections collected	18160	33721	60945
Independent reflections	4648	4650	5669
Data/restraints/parameters	4648/24/229	4650/0/262	5669/0/259
Goof on F^2	1.101	1.041	1.067
R_1 [I>=2σ (I)]	0.0642	0.0434	0.0431
wR_2 [I>=2σ (I)]	0.1709	0.1154	0.1132
wR_2 all reflections	0.1837	0.1262	0.1253
H atom treatment	Mixed	Mixed	Mixed

Table B.4. Experimental crystallographic details for the tridentate complexes with Py_2ImAm.

Abbreviation	**2.4b**	**2.5b**	**2.6b**
Empirical formula	$C_{12}H_{10}Cl_2MnN_5$	$C_{12}H_{11}Cl_3FeN_5$	$C_{12}H_{11}Cl_2CoN_5$
Formula weight	350.09	387.46	355.09
Temperature (K)	200	200	200
Crystal system	monoclinic	monoclinic	monoclinic
Space group	*P2$_1$/n*	*C2/c*	*P2$_1$/n*
a (Å)	8.9312(3)	15.3362(9)	8.6835(6)
b (Å)	14.6237(4)	9.4902(5)	14.6441(11)
c (Å)	10.7801(3)	10.4548(6)	10.7488(7)
β	95.806(2)	96.216(4)	95.073(4)
Volume (Å^3)	1400.7(1)	1512.68(15)	1361.5(2)
Z	4	4	4
ρ_{calc} (g/cm^3)	1.660	1.701	1.732
μ (mm^{-1})	1.319	1.525	1.648
F(000)	704.0	780.0	716.0
2Θ range for data collection/°	5.364 to 56.988	5.056 to 51.51	4.712 to 51.992
Reflections collected	13356	5371	9905
Independent reflections	3497	1429	2633
Data/restraints/parameters	3497/188/187	1429/0/97	2633/3/193
Goof on F^2	1.099	1.077	0.945
R_1 [I>=2σ (I)]	0.0559	0.0642	0.0677
wR_2 [I>=2σ (I)]	0.1434	0.1621	0.1160
wR_2 all reflections	0.1560	0.1937	0.1380
H atom treatment	Mixed	Mixed	Mixed

Table B.5. List of hydrogen bonds in the structures presented in the second chapter.

D-H···*A*	Type	*D*-H	H···*A*	*D*···*A*	<(DHA)
Py_2ImAm					
N7-H7A···N6	Intra	0.96(2)	2.25(2)	2.704(2)	108.4(15)
N7-H7A···N5	Inter	0.96(2)	2.40(2)	3.140(2)	133.6(16)
N4-H4A···N6	Inter	0.86(2)	2.51(2)	3.204(2)	138(2)
N4-H4A···N5	Intra	0.86(2)	2.29(2)	2.729(2)	111.4(2)
N2-H2···N1	Intra	0.91(2)	2.28(2)	2.787(2)	115.0(2)
N9-H9A···N10	Intra	0.90(2)	2.21(2)	2.724(2)	115.4(2)
N4-H4B···N2	Intra	0.948(2)	1.93(3)	2.640(2)	130(3)
N7-H7B···N9	Intra	0.87(3)	1.93(3)	2.599(3)	133(2)
$[Mn^{III}(Py_2ImAm)_3]\cdot MeCN$					
N2-H2···N1	Intra	0.82(2)	2.29(3)	2.741(2)	115(3)
N4-H4···N5	Intra	0.86(2)	2.23(3)	2.689(3)	114(2)
$[Fe^{III}(Py_2ImAm)_3]\cdot MeCN$					
N2-H2···N1	Intra	0.85(2)	2.20(3)	2.690(3)	117(3)
N4-H4···N5	Intra	0.83(2)	2.22(3)	2.734(3)	120(3)
$[Mn^{III}(Py_2ImAm)_3]\cdot DCM$					
N2-H2A···N1	Intra	0.83(3)	2.24(3)	2.695(3)	115(3)
N4-H4A···N5	Intra	0.84(3)	2.21(3)	2.682(3)	116(3)
N7-H7···N6	Intra	0.84(3)	2.30(3)	2.747(4)	114(3)
C19-H19B···N3^{ii}	Inter	0.99	2.48	3.334(3)	145
$[Fe^{III}(Py_2ImAm)_3]\cdot DCM$					
N2-H2A···N1	Intra	0.80(3)	2.23(3)	2.697(3)	117.2(2)
N4-H4A···N5	Intra	0.81(3)	2.22(2)	2.671(3)	115.9(2)
N7-H7···N6	Intra	0.85(3)	2.29(3)	2.748(3)	114(2)
C19-H19B···N3^{ii}	Inter	0.99	2.47	3.321(2)	144
$[Co^{III}(Py_2ImAm)_3]\cdot DCM$					
N2-H2A···N1	Intra	0.84(2)	2.24(2)	2.691(2)	113.7(2)
N4-H4A···N5	Intra	0.83(3)	2.21(2)	2.679(2)	116(2)
N7-H7···N6	Intra	0.91(2)	2.27(2)	2.742(2)	111.8(2)
C19-H19B···N3^{ii}	Inter	0.99	2.47	3.3223(3)	144.7
$[Fe^{III}(Py_2ImAm)Cl_3]$					
N3-H3A···Cl2^{iii}	Inter	0.83(5)	2.81(5)	3.475(5)	139(4)
N3-H3B···Cl1^{iv}	Inter	0.83(9)	2.63(5)	3.391(4)	153(7)
C3-H3···Cl1^{v}	Inter	0.95	2.74	3.570(6)	146
C1-H1···Cl1^{vi}	Inter	0.95	2.88	3.652(5)	139
C4-H4···Cl1^{iv}	Inter	0.95	2.74	3.591(5)	150
$[Mn^{II}(Py_2ImAm)Cl_2]$					
N2-H2A···N4	Intra	0.99(2)	1.91(3)	2.597(4)	124(3)
N2-H2B···Cl2^{vii}	Inter	0.84(3)	2.59(3)	3.332(3)	147(3)
N4-H4B···Cl1^{viii}	Inter	0.81(3)	2.82(4)	3.487(3)	141(4)
C2-H2···Cl1^{ix}	Inter	0.95	2.81	3.760(3)	177
C11-H11···Cl1^{x}	Inter	0.95	2.67	3.586(3)	162
$[Co^{II}(Py_2ImAm)Cl_2]$					
N2-H2B···N4	Intra	0.90(4)	1.82(3)	2.604(8)	145(6)
N2-H2A···Cl2^{xi}	Inter	0.88(4)	2.53(6)	3.244(6)	145(6)
C3-H3···Cl2^{xii}	Inter	0.95	2.83	3.676(7)	149
C11-H11···Cl1^{ix}	Inter	0.95	2.69	3.550(7)	152

Symmetry codes: ^{i} y -1/3, 1/3 -x +y, 4/3 -z; ^{ii} 1 -x, ½ +y, ½ -z; ^{iii} x, y +1,z; ^{iv}1 -x, y -1, 1 -z; ^{v} ½ -x, ½ -y, ½ +z; ^{vi} 1 -x, y, ½ +z; ^{vii} x +½, -y +½, z –½; ^{viii} 1 -x, 1 -y, 1 -z; ^{ix} ½ -x, y -½, 3/2 -z; ^{x} ½ -x, y +½, 3/2 -z; ^{xi} x +½, 3/2 -y, z -½, ^{xii} 3/2 -x, y +½, 3/2 -x.

Table B.6. Experimental crystallographic details for the complexes discussed in the third chapter.

Abbreviation	**3.1b**	**3.2b**	**3.3b**	**3.4b**
Empirical formula	$C_{20}H_{18}Cl_4Mn_2N_{14}$	$C_{10}H_9Cl_3FeN_7$	$C_{30}H_{24}Cl_6Mn_4N_{21}$	$C_{32}H_{26}Cl_{15}Fe_4N_{21}$
Formula weight	706.16	389.44	1111.16	1459.89
Temperature (K)	210.0	239	200	200
Crystal System	Triclinic	Monoclinic	Monoclinic	Monoclinic
Space group	*P-1*	*P2/c*	*C2/c*	*C2/c*
a (Å)	7.941(2)	8.491(3)	13.3141(4)	14.9895(14)
b (Å)	9.062(3)	9.744(3)	28.151(1)	24.937(2)
c (Å)	9.883(3)	9.878(4)	14.3881(5)	21.250(3)
α	77.381(5)	90	90	90
β (°)	75.049(5)	115.377(4)	109.326(2)	107.723(4)
γ	80.186(6)	90	90	90
Volume ($Å^3$)	665.6(3)	738.5(4)	5088.9(3)	7566.2(14)
Z	2	2	4	4
ρ_{calc} (g/mL)	1.762	1.751	1.450	1.282
μ (mm^{-1})	1.392	1.566	1.330	1.318
F(000)	354.0	390	2212	2896
data collection range (°)	4.34 to 49.91	5.31 to 53.99	2.894 to 53.99	3.266 to 57.99
Reflections collected	2308	4730	31509	63020
Independent reflections	2308	1602	5512	9576
Goof on F^2	1.084	1.059	1.019	1.037
R_1 [I>=2σ (I)]	0.0611	0.0320	0.0686	0.0540
wR_2 all reflections	0.1325	0.0842	0.2072	0.1765
H atom treatment	Mixed	Mixed	Mixed	Mixed

Table B.7. List of hydrogen bonds in the structures presented in the third chapter.

D-H···*A*	Type	*D*-H	H···*A*	*D*···*A*	<(DHA)
[$Mn_2(\mu\text{-}Cl)_2(Pm_2ImAm)_2Cl_2$]					
N3-H3A···N5	Intra	0.88(6)	1.89(7)	2.619(12)	139(4)
N3-H3B···N1	Intra	0.85(6)	2.38(6)	2.724(11)	105(4)
N3-H3B···Cl2^{i}	Inter	0.85(6)	2.56(5)	3.174(8)	129(4)
N5-H5···N7	Intra	0.87(7)	2.42(6)	2.809(11)	108(4)
C2-H2···Cl2^{ii}	Inter	0.94	2.82	3.567(9)	137
[$Mn^{III}Mn^{II}_3(Pm_2ImAm)_3Cl_6$]					
N3-H3···N1	Intra	0.80(4)	2.37(5)	2.740(6)	110(4)
N5-H5···N7	Intra	0.81(5)	2.29(5)	2.735(6)	116(4)
N8-H8···N11	Intra	0.81(5)	2.29(5)	2.710(6)	113(4)
N3-H3···Cl2^{ii}	Inter	0.80(4)	2.69(4)	3.351(4)	141(4)
N8-H8···Cl2^{iii}	Inter	0.81(5)	2.76(5)	3.512(4)	154(5)
C1-H1···Cl3^{iv}	Inter	0.95	2.72	3.562(6)	148
C2-H2···Cl4^{v}	Inter	0.95	2.68	3.626(6)	173
C3-H3A···N11^{vi}	Inter	0.95	2.44	3.386(7)	173
C8-H8A···Cl2^{vii}	Inter	0.95	2.74	3.526(6)	141
C10-H10···Cl1^{viii}	Inter	0.95	2.74	3.616(6)	153
C14-H14···Cl1^{ix}	Inter	0.95	2.74	3.451(6)	132
[$Fe^{III}(Pm_2ImAm)Cl_3$]					
N3-H3A···N1	Intra	0.81(3)	2.48(3)	2.803(4)	105(2)
N3-H3A···Cl1^{vii}	Inter	0.81(3)	2.59(3)	3.325(3)	152(3)
N3-H3B···N3^{x}	Intra	0.81(4)	2.09(5)	2.678(4)	129(4)
C3-H3···Cl1^{xi}	Inter	0.88	2.47	3.217(16)	144
[$Fe^{III}_4(Pm_2ImAm)_3Cl_9$]					
N11-H11···N17	Intra	0.81(3)	2.40(4)	2.812(4)	113(3)
N14-H14···N29	Intra	0.77(3)	2.39(4)	2.760(5)	111(3)
N15-H15···N24	Intra	0.79(3)	2.44(4)	2.774(4)	107(3)
C39-H39···Cl4^{xii}	Inter	0.95	2.80	3.678(6)	155
C39-H39···Cl5^{xii}	Inter	0.95	2.72	3.420(5)	131
C50A-H50A···Cl3^{xiii}	Inter	1.00	2.38	3.368(17)	168

Symmetry codes: ^{i} -x, 1 -y, 2 -z; ^{ii} -x, 1 -y, 1 -z; ^{iii} ½ -x, ½ -y, 1 -z; ^{iv} ½ +x, ½ -y, ½ +z; ^{v} -½ +x, -½ +y, z; ^{vi} -½ +x, ½ -y, -½+z; ^{vii} 1 -x, y, ½ -z; ^{viii} 3/2 -x, ½ -y, 1 -z; ^{ix} x +½, -y +½, z –½; ^{viii} 3/2 -x, 3/2 -y, 1 -z; ^{ix} -½ +x, 3/2 -y, -½ +z; ^{x} x, 1 -y, ½ -z; ^{xi} x, -y, ½ +z; ^{xii} ½ -x, -½ +y, ½ -z; ^{xiii} -x , y, ½ -z.

Table B.8. Metal bond distances in tetranuclear complexes **$[Mn^{III}Mn^{II}_3(Pm_2ImAm)_3Cl_6]$** and **$[Fe^{III}_4(Pm_2ImAm)_3Cl_9]$**.

$[Mn^{III}Mn^{II}_3(Pm_2ImAm)_3Cl_6]$		**$[Fe^{III}_4(Pm_2ImAm)_3Cl_9]$**	
Atoms	Distance (Å)	Atoms	Distance (Å)
N3-Mn1	1.955(4)	N3-Fe1	1.94236(18)
N5-Mn1	1.969(5)	N5-Fe1	1.91924(12)
N8-Mn1	1.952(4)	N10-Fe1	1.93266(12)
N2-Mn2	2.261(4)	N2-Fe2	2.15060(14)
N4-Mn2	2.195(4)	N4-Fe2	2.10239(14)
N6-Mn2	2.246(4)	N6-Fe2	2.14580(19)
Cl1-Mn2	2.342(2)	Cl1-Fe2	2.3984(2)
Cl2-Mn2	2.3593(2)	Cl2-Fe2	2.22897(15)
N10-Mn3	2.294(5)	Cl3-Fe2	2.3504(2)
N9-Mn3	2.260(6)	N9-Fe3	2.15592(16)
Cl3-Mn3	2.382(2)	N11-Fe3	2.09769(19)
Cl4-Mn3	2.326(5)	Cl4-Fe3	2.3440(2)
		Cl5-Fe3	2.2571(2)

Table B.9. Metal bond distances in **$[Mn_2(\mu\text{-}Cl)_2(Pm_2ImAm)_2Cl_2]$**. Symmetry related atoms had been labeled with the primer symbol.

$[Mn_2(\mu\text{-}Cl)_2(Pm_2ImAm)_2Cl_2]$	
Atoms	Distance (Å)
N2-Mn1	2.2907(5)
N4-Mn1	2.1959(6)
N6-Mn1	2.2643(4)
Cl1-Mn1	2.4386(6)
Cl1'-Mn1	2.6680(5)
Cl2-Mn1	2.4569(5)

Table B.10. Experimental crystallographic details for the complexes discussed in the fourth chapter.

Abbreviation	**4.3b**	**4.1b**	**4.2b**
Empirical formula	$C_{24}H_{20}CoN_{10}$	$C_{40}H_{40}Cl_8Co_6N_{28}O_4$	$C_{44}H_{44}Cl_{12}Co_6N_{28}O_2$
Formula weight	507.43	1614.18	1776.05
Temperature (K)	200	200	200
Crystal System	Monoclinic	Triclinic	Monoclinic
Space group	$P2_1/n$	P-1	$P2_1/c$
a (Å)	7.7384(9)	7.2535(6)	16.7152(9)
b (Å)	16.591(2)	14.6590(12)	13.0215(6)
c (Å)	8.8849(12)	15.4268(12)	16.2157(11)
α (°)	90	90.5430(10)	90
β (°)	100.599(6)	97.457(2)	114.262(7)
γ (°)	90	90.4780(10)	90
Volume (Å^3)	1121.3(2)	1626.3(2)	3217.7(4)
Z	2	1	2
ρ_{calc} (g/mL)	1.503	1.648	1.833
μ (mm^{-1})	0.802	1.885	2.072
F(000)	522	806	1772.0
data collection range (°)	4.91 to 66.092	5.326 to 55.994	4.114 to 56.998
Reflections collected	31138	31758	52197
Independent reflections	4080	7821	8022
Goof on F^2	1.056	1.027	1.074
R_1 [$I \geq 2\sigma(I)$]	0.0324	0.0363	0.1018
wR_2 all reflections	0.0902	0.0873	0.2465
H atom treatment	Mixed	Mixed	Mixed

Table B.11. List of relevant metal bond angles for the complexes presented in the fourth chapter.

4.3b		**4.1b**		**4.2b**	
Bond	Angle (°)	Bond	Angle (°)	Bond	Angle (°)
N2-Co1-N4	88.99(5)	N3-Co1-N5	89.719(4)	N5-Co1-N3	89.1(3)
N2-Co1-N4'	91.01(5)	N3-Co1-N5'	90.281(4)	N3-Co1-N12	90.1(3)
N2-Co1-N2'	180.00(6)	N3-Co1-N3'	180.00(7)	N12-Co1-N10	89.8(3)
N4-Co1-N4'	180.00(6)	N5-Co1-N5'	180.00(7)	N10-Co1-N5	90.6(3)
		N10-Co3-N12	89.656(4)	N5-Co1-N12	175.2(4)
		N10-Co3-N12'	90.344(4)	N10-Co1-N3	175.0(4)
		N10-Co3-N10'	180.00(7)	Cl4-Co1-N5	92.7(3)
		N12-Co3-N12'	180.00(7)	Cl4-Co1-N3	93.4(3)
		N2-Co2-N4	76.970(3)	Cl4-Co1-N12	92.1(3)
		N2-Co2-N6	154.494(2)	Cl4-Co1-N10	91.7(3)
		N4-Co2-N6	77.849(5)	N2-Co2-N4	77.0(3)
		Cl1-Co2-Cl2	112.279(5)	N2-Co2-N6	149.1(3)
		Cl1-Co2-N4	132.8804(18)	N4-Co2-N6	77.1(3)
		Cl2-Co2-N4	114.841(4)	Cl1-Co2-Cl2	112.24(14)
		N9-Co4-N11	77.915(4)	Cl1-Co2-N4	103.9(2)
		N9-Co4-N13	154.4075(17)	Cl2-Co2-N4	143.7(2)
		N11-Co4-N13	76.747(5)	N9-Co3-N11	76.5(3)
		Cl3-Co4-Cl4	111.358(5)	N9-Co3-N13	151.5(3)
		Cl3-Co4-N11	118.083(4)	N11-Co3-N13	78.0(3)
		Cl4-Co4-N11	130.396(2)	Cl3-Co3-Cl4	106.89(10)
				Cl3-Co3-N11	109.6(2)
				Cl3-Co3-Cl4	106.89(10)

Table B.12. List of hydrogen bonds in the structures presented in the fourth chapter.

D-H···*A*	Type	*D*-H	H···*A*	*D*···*A*	<(DHA)
$[Co^{II}(Py_2ImAm)_2]$					
N2-H2A···N1	Intra	0.86(2)	2.17(2)	2.694(2)	119.1(13)
N4-H4···N5	Intra	0.84(2)	2.20(2)	2.72(1)	118.9(14)
$[Co^{II}_3(Pm_2ImAm)_2Cl_4]\cdot 5H_2O$					
N3-H3···N1	Intra	0.81(2)	2.38(2)	2.800(3)	113(2)
N5-H5···N7	Intra	0.81(2)	2.39(2)	2.801(3)	113(2)
N10-H10···N8	Intra	0.82(2)	2.36(3)	2.779(3)	113(2)
N12-H12···N14	Intra	0.81(3)	2.43(3)	2.821(3)	111(2)
O1-H1A···Cl1^{i}	Inter	0.85(3)	2.55(4)	3.338(2)	155(4)
O1-H1A···N8^{i}	Inter	0.85(3)	2.59(4)	3.010(3)	112(3)
O1-H1B···Cl2^{ii}	Inter	0.84(3)	2.49(3)	3.288(2)	161(4)
O2-H2A···Cl4^{ii}	Inter	0.85(3)	2.47(3)	3.258(2)	154(4)
O2-H2A···N7^{ii}	Inter	0.85(3)	2.60(4)	3.040(3)	113(3)
O2-H2B···Cl3^{i}	Inter	0.82(3)	2.77(4)	3.412(2)	137(4)
O2-H2B···N1^{iii}	Inter	0.82(3)	2.50(4)	3.062(3)	127(4)
N3-H3···O2^{iii}	Inter	0.81(2)	2.23(2)	3.019(3)	164(2)
N5-H5···O2^{iv}	Inter	0.81(2)	2.21(2)	2.994(3)	164(2)
N10-H10···O1^{i}	Inter	0.82(2)	2.19(2)	2.991(3)	165(3)
N12-H12···O1^{iii}	Inter	0.81(3)	2.19(3)	2.987(3)	166(2)
C1-H1···Cl3^{iii}	Inter	0.95	2.78	3.606(3)	146
C2-H2···Cl1^{v}	Inter	0.95	2.72	3.663(3)	172
C11-H11···Cl2^{vi}	Inter	0.95	2.82	3.615(3)	142
C19-H19···Cl3^{vii}	Inter	0.95	2.70	3.545(3)	148
$[Co^{II}_6(\mu\text{-}Cl)_2(Pm_2ImAm)_4Cl_6]\cdot 2CH_3OH\cdot 2CH_2Cl_2$					
N3-H3···N1	Intra	0.84(4)	2.30(7)	2.760(12)	115(6)
N5-H5···N7	Intra	0.84(6)	2.30(7)	2.782(11)	117(7)
N10-H10···N8	Intra	0.84(5)	2.25(9)	2.805(11)	124(8)
N12-H12···N14	Intra	0.85(6)	2.29(7)	2.741(10)	114(7)
N5-H5···O1^{i}	Inter	0.84(6)	2.27(7)	3.013(12)	149(7)
N10-H10···O1^{i}	Inter	0.84(5)	2.32(7)	3.047(12)	145(10)
O1-H1A···Cl1^{viii}	Inter	0.84	2.39	3.220(9)	170
C3-H3A···Cl4^{iv}	Inter	0.95	2.61	3.407(13)	142
C8-H8···Cl3^{ix}	Inter	0.95	2.79	3.603(12)	144
C10-H10A···Cl1^{x}	Inter	0.95	2.70	3.532(11)	147
C13-H13··Cl2^{ii}	Inter	0.95	2.55	3.391(11)	147
C20-H20···Cl3^{xi}	Inter	0.95	2.69	3.476(9)	140

Symmetry codes: ^{i} x, y, z; ^{ii} 1 +x, y, z; ^{iii} 1 -x, 1 -y, 1 -z; ^{iv} -1 +x, y, z; ^{v} 1 -x, -y, 1 -z; ^{vi} -x, 1 -y, 1 -z; ^{vii} 1 -x, 1 -y, -z; ^{viii} -x, -½ +y, ½ -z; ^{ix} -1 +x, 3/2 -y, -½ +z; ^{x} x, 3/2 -y, -½ +z; ^{xi}

Table B.13. List of intra stack cobalt to cobalt distances within **[Co^{II}_3(Pm$_2$ImAm)$_2$Cl$_4$]·5H$_2$O** at 200 K.

Connectivity	Distance (Å)
Co1-Co3	3.6268(3)
Co1-Co2	5.2932(4)
Co1-Co4	5.7287(4)
Co1-Co4	7.0448(4)
Co1-Co1	7.2535(6)
Co1-Co2	7.9347(5)
Co1-Co2	9.9148(6)
Co2-Co3	5.6865(3)
Co2-Co3	7.0716(4)
Co2-Co4	7.2028(5)
Co2-Co2	7.2535(6)
Co2-Co4	8.3024(5)
Co3-Co4	5.2981(4)
Co3-Co3	7.2535(6)
Co4-Co4	7.2535(6)

Table B.14. List of inter stack cobalt to cobalt distances within **[Co^{II}_3(Pm$_2$ImAm)$_2$Cl$_4$]·5H$_2$O** at 200 K.

Connectivity	Distance (Å)
Co2-Co2	7.0704(4)
Co2-Co2	8.3087(4)
Co2-Co4	8.6895(6)
Co2-Co4	9.0765(6)
Co4-Co4	7.2300(4)
Co4-Co4	7.8947(4)

Table B.15. List of intermolecular cobalt to cobalt distances at 200 K within **[Co^{II}_6(μ-Cl)$_2$(Pm$_2$ImAm)$_4$Cl$_6$]·2MeOH·2DCM**.

Connectivity	Distance (Å)
Co1-Co2	6.628(2)
Co1-Co2	7.2427(18)
Co1-Co2	8.6454(18)
Co1-Co1	8.8644(12)
Co1-Co2	9.2029(18)
Co1-Co3	9.2543(17)
Co2-Co3	6.2523(15)
Co2-Co2	6.315(3)
Co2-Co3	6.968(2)
Co2-Co2	8.210(2)
Co2-Co2	8.3211(8)
Co2-Co2	9.414(3)
Co3-Co3	8.4163(8)
Co3-Co3	9.321(2)

Table B.16. List of intramolecular cobalt to cobalt distances at 200 K within **[Co^{II}_6(μ-Cl)$_2$(Pm_2ImAm)$_4Cl_6$]·2MeOH·2DCM**.

Connectivity	Distance (Å)
Co1-Co3	4.1545(17)
Co1-Co3	5.2881(16)
Co1-Co2	5.2969(17)
Co1-Co1	7.0448(4)
Co2-Co3	7.897(2)
Co2-Co3	8.5607(16)
Co3-Co3	5.299(2)

Table B.17. Experimental crystallographic details for the complexes discussed in the fifth chapter.

Abbreviation	**5.3b**	**5.1b**	**5.2b**
Empirical formula	$C_{24}H_{20}CuN_{10}$	$C_{20}H_{20}Cl_4CuMn_2N_{14}O_2$	$C_{44}H_{44}Cl_{12}Cu_2Mn_4N_{28}O_2$
Formula weight	512.04	803.72	1769.31
Temperature (K)	210	295	200
Crystal System	Monoclinic	Triclinic	Triclinic
Space group	*C2/c*	*P*-1	*P*-1
a (Å)	25.2091(17)	7.330(7)	10.7428(3)
b (Å)	9.6288(7)	15.001(13)	11.6906(4)
c (Å)	18.4270(12)	15.758(13)	14.4711(5)
α (°)	90	89.794(16)	104.092(3)
β (°)	92.285(2)	83.035(17)	96.428(3)
γ (°)	90	89.979(16)	106.239(3)
Volume (Å^3)	4469.3(5)	1720(3)	1660.48(10)
Z	8	2	1
ρ_{calc} (g/mL)	1.522	1.552	1.769
μ (mm^{-1})	1.014	1.688	1.910
F(000)	2104.0	802.0	882.0
data collection range (°)	3.2 to 62.2	2.6 to 55.9	2.9 to 64.0
Reflections collected	91917	8262	52197
Independent reflections	7173	8262	11519
Goof on F^2	1.035	1.049	1.044
R_1 [I>=2σ (I)]	0.0398	0.0472	0.0647
wR_2 all reflections	0.1053	0.1272	0.1840
H atom treatment	Mixed	Mixed	Mixed

Table B.18. List of hydrogen bonds in the structures presented in the fifth chapter.

D-H···*A*	Type	*D*-H	H···*A*	*D*···*A*	<(DHA)
$[Cu^{II}(Py_2ImAm)_2]$					
N2-H2···N1	Intra	0.82(2)	2.18(2)	2.687(2)	120(2)
N4-H4···N5	Intra	0.82(2)	2.28(2)	2.749(2)	117(2)
N7-H7···N6	Intra	0.81(2)	2.20(2)	2.693(2)	120(2)
N9-H9···N10	Intra	0.81(2)	2.18(2)	2.679(2)	120(2)
N4-H4···N5^{i}	Inter	0.82(2)	2.49(2)	3.220(2)	148(2)
$[Mn^{II}_2Cu^{II}(Pm_2ImAm)_2Cl_4]\cdot 2H_2O$					
N3-H3···N1	Intra	0.83(3)	2.31(4)	2.742(4)	113(3)
N5-H5···N7	Intra	0.84(3)	2.29(4)	2.783(4)	118(3)
N10-H10···N8	Intra	0.83(3)	2.35(4)	2.770(4)	112(4)
N12-H12···N14	Intra	0.83(3)	2.35(4)	2.771(5)	112(4)
N3-H3···O1	Inter	0.83(3)	2.27(3)	3.075(5)	163(4)
N5-H5···O1^{ii}	Inter	0.84(3)	2.30(3)	3.086(5)	155(4)
N10-H10A···O2	Inter	0.83(3)	2.32(3)	3.129(5)	165(4)
N12-H12···O2^{iii}	Inter	0.83(3)	2.29(3)	3.099(4)	165(4)
O1-H1A···N7^{ii}	Inter	0.82(5)	2.88(8)	3.152(5)	102(6)
O1-H1A···Cl4^{iv}	Inter	0.82(3)	2.77(4)	3.412(2)	137(4)
O2-H2B···Cl2^{iii}	Inter	0.86(2)	2.47(2)	3.332(5)	175(6)
$[Mn^{II}_4Cu^{II}_2(\mu\text{-}Cl)_2(Pm_2ImAm)_4Cl_8]\cdot 2MeOH\cdot 2DCM$					
N3-H3···N1	Intra	0.91(2)	2.31(5)	2.763(4)	111(4)
N5-H5···N7	Intra	0.91(2)	2.20(5)	2.737(4)	117(5)
N10-H10···N8	Intra	0.91(2)	2.49(4)	2.769(4)	98(3)
N12-H12···N14	Intra	0.91(2)	2.30(8)	2.734(4)	109(6)
N5-H5···O1	Inter	0.91(2)	2.23(4)	3.045(5)	149(5)
N10-H10···O1	Inter	0.91(2)	2.12(2)	3.018(4)	167(4)
O1-H1A···Cl4^{iv}	Inter	0.84	2.37	3.204(4)	171.1
C11-H11···Cl1^{v}	Inter	0.95	2.61	3.364(4)	137.2
C3-H3A···Cl3^{vi}	Inter	0.95	2.57	3.369(4)	141.8

Symmetry codes: ^{i} 1 -x, y, ½ -z; ^{ii} 1 -x, 1 -y, 1 -z; ^{iii} -x, 1 -y, 1 -z; ^{iv} 1 +x, y, z; ^{v} 1 +x, y, 1 +z;^{vi} -1 +x, y, -1 +z.

Appendix C: Figures from Chapter 2

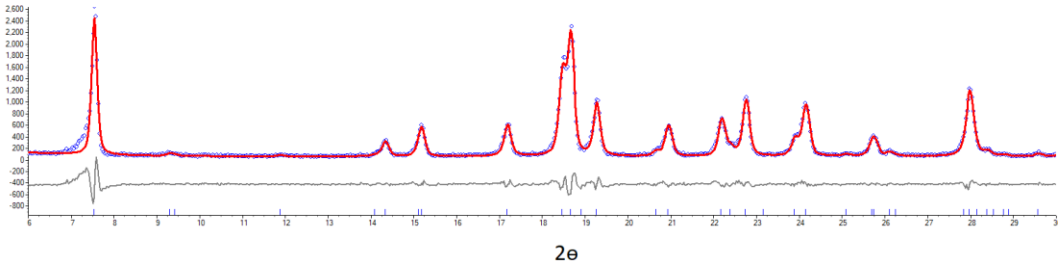

Figure C.1. Pawley fit of **[Mn^{III}(Py$_2$ImAm)$_3$]·MeCN** using the lattice parameters and space group (*R-3*) obtained from single crystal as a starting point. The lattice parameters obtained from PXRD are *a* = 14.8843(13), *c* = 28.13124(44). Blue circles are the experimental data while the red line is the predicted pattern from single crystal data.

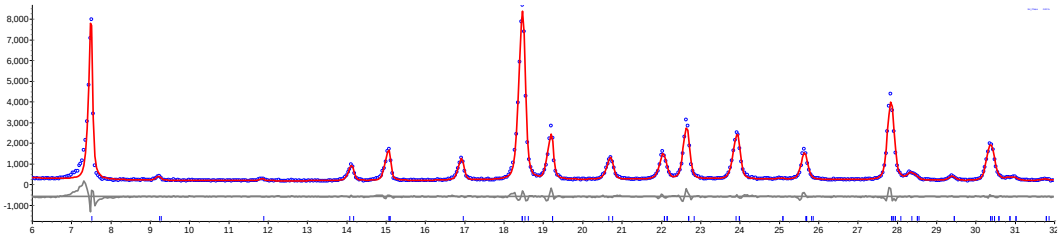

Figure C.2. Pawley fit of **[Fe^{III}(Py$_2$ImAm)$_3$]·MeCN** using the lattice parameters and space group (*R-3*) obtained from single crystal as a starting point. The lattice parameters obtained from PXRD are *a* = 14.8328(35), *c* = 28.284(11). Blue circles are the experimental data while the red line is the predicted pattern from single crystal data.

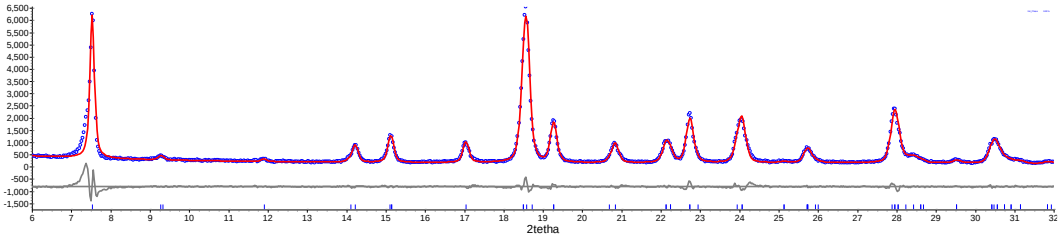

Figure C.3. Pawley fit of **[Co^{III}(Py$_2$ImAm)$_3$]·MeCN** using the lattice parameters and space group (*R-3*) obtained from single crystal as a starting point. The lattice parameters obtained from PXRD are *a* = 14.8632(26), *c* = 28.4302(66). Blue circles are the experimental data while the red line is the predicted pattern from single crystal data.

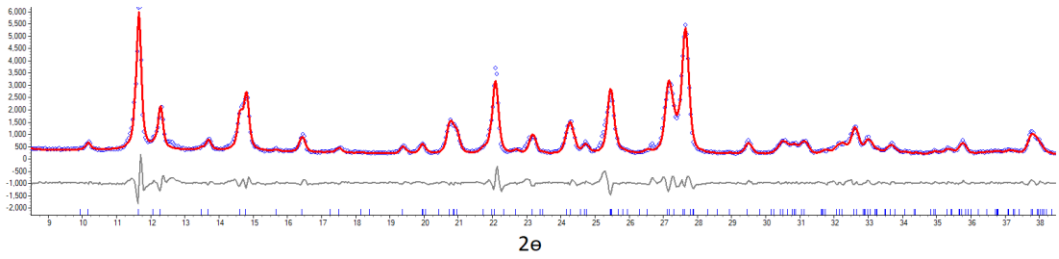

Figure C.4. Pawley fit of **[Mn^{II}(Py$_2$ImAm)Cl$_2$]** using the lattice parameters and space group (*P2$_1$/n*) obtained from single crystal as a starting point. The lattice parameters obtained from PXRD are *a* = 10.83222(91), *b* = 14.6412(15), *c* = 8.92470(83), β = 95.4867(84). Blue circles are the experimental data while the red line is the predicted Pawley pattern.

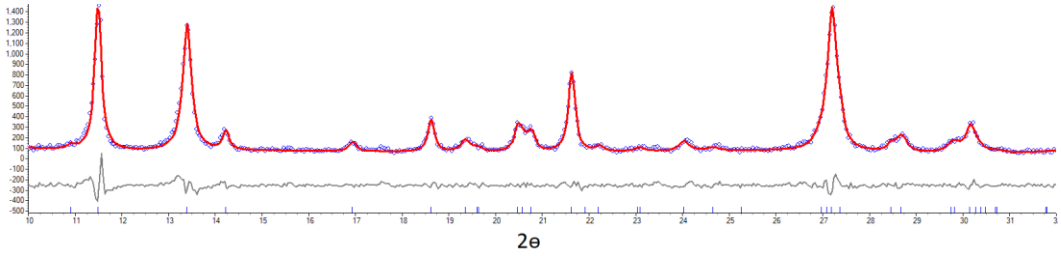

Figure C.5. Pawley fit of **[Fe^{III}(Py$_2$ImAm)Cl$_3$]** using the lattice parameters and space group (*C2/c*) obtained from single crystal as a starting point. The lattice parameters obtained from PXRD are *a* = 15.5004(29), *b* = 9.5263(19), *c* = 10.5327(22), β = 96.748(17). Blue circles are the experimental data while the red line is the predicted Pawley pattern.

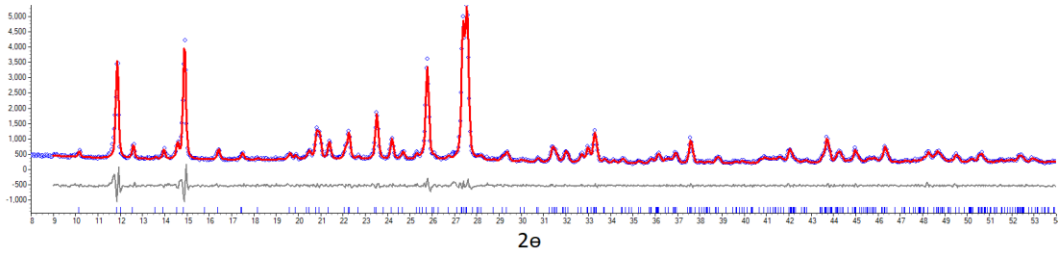

Figure C.6. Pawley fit of **[Co^{II}(Py$_2$ImAm)Cl$_2$]** using the lattice parameters and space group (*P2$_1$/n*) obtained from single crystal as a starting point. The lattice parameters obtained from PXRD are *a* = 8.69376(91), *b* = 14.7186(18), *c* = 10.8397(17), β = 94.525(11). Blue circles are the experimental data while the red line is the predicted Pawley pattern.

Appendix D: Figures from Chapter 3

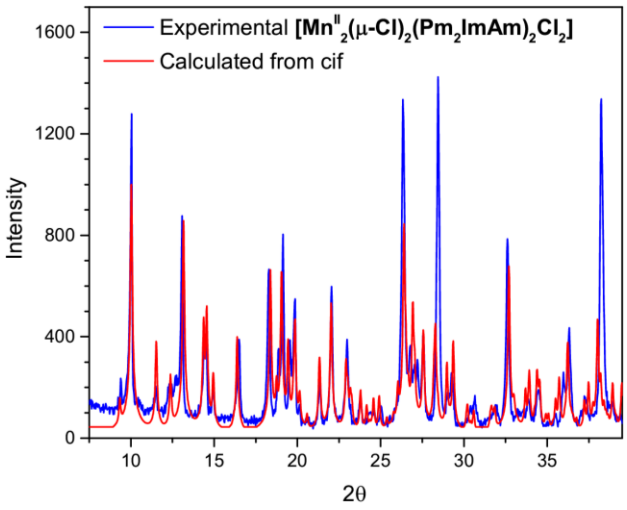

Figure D.1. PXRD pattern overlay of experimental microcrystalline **[Mn^{II}_2(μ-Cl)$_2$(Pm$_2$ImAm)$_2$Cl$_2$]** complex with its predicted pattern from single crystal using Mercury.[4]

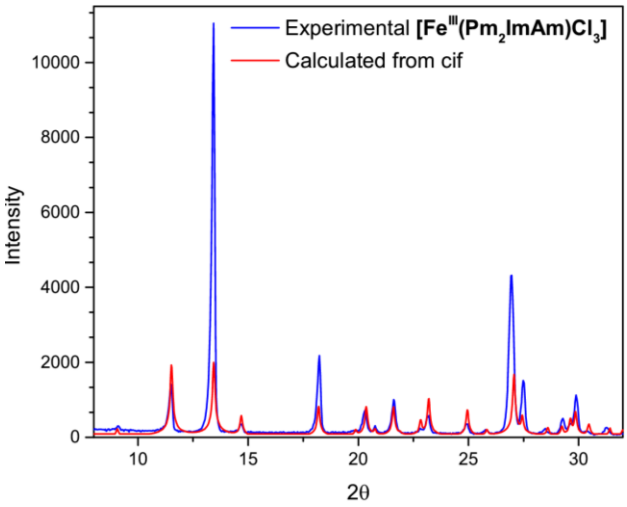

Figure D.2. PXRD pattern overlay of experimental microcrystalline **[Fe^{III}(Pm$_2$ImAm)Cl$_3$]** complex with its predicted pattern from single crystal using Mercury.[4]

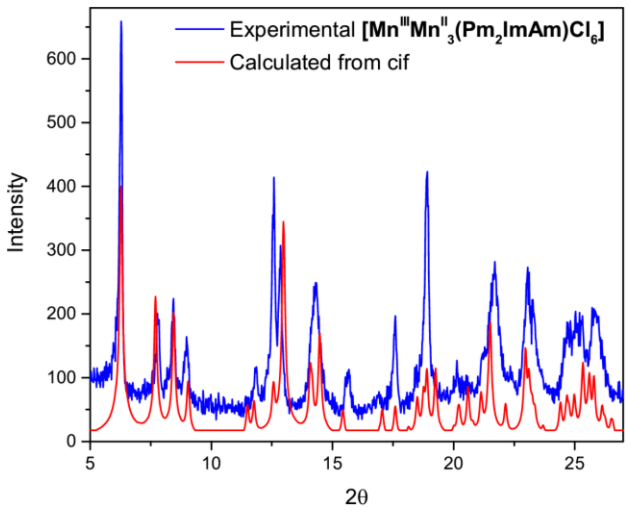

Figure D.3. PXRD pattern overlay of experimental microcrystalline **[Mn^{III}Mn$^{II}_3$(Pm$_2$ImAm)$_3$Cl$_6$]** complex with its predicted pattern from single crystal using Mercury.[4]

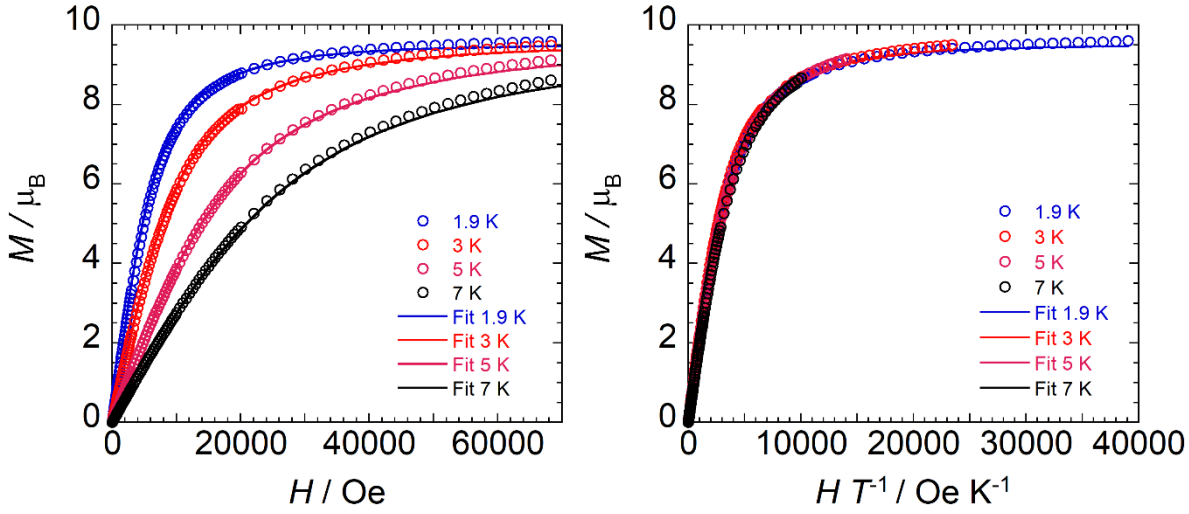

Figure D.4. Solid state field dependence of the magnetization (left) and the reduced magnetization (right) for **[Mn$^{II}_2$(μ-Cl)$_2$(Pm$_2$ImAm)$_2$Cl$_2$]** at the indicated temperatures. Solid lines represent best-fits to the experimental data; parameters are provided in Chapter 3 (Table 3.4).

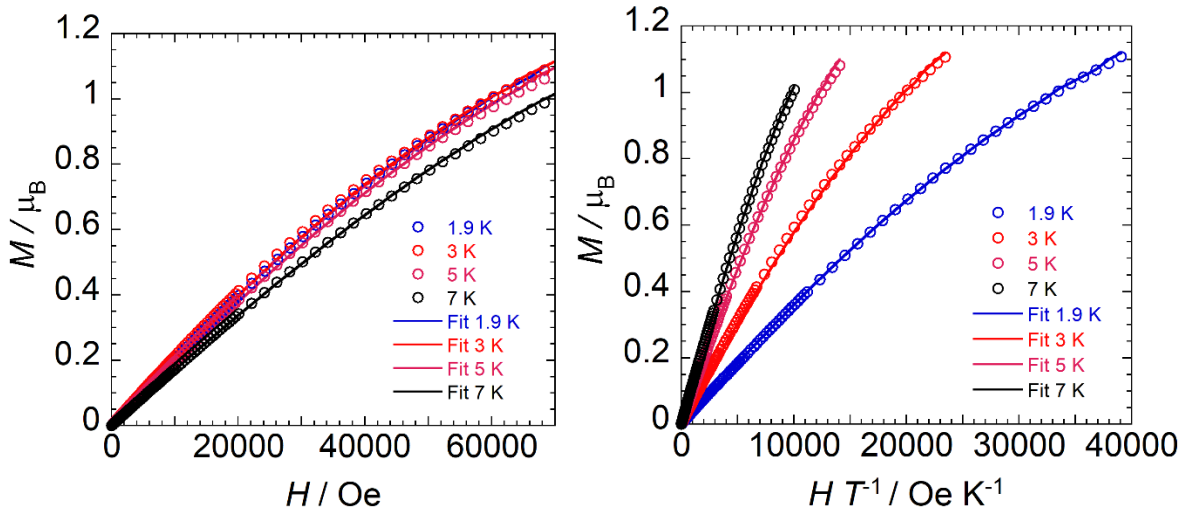

Figure D.5. Solid state field dependence of the magnetization (left) and the reduced magnetization (right) for **[Mn^{III}(Py$_2$ImAm)$_3$]** at the indicated temperatures. Solid lines represent best-fits to the experimental data; parameters are provided in the main text (Table 1).

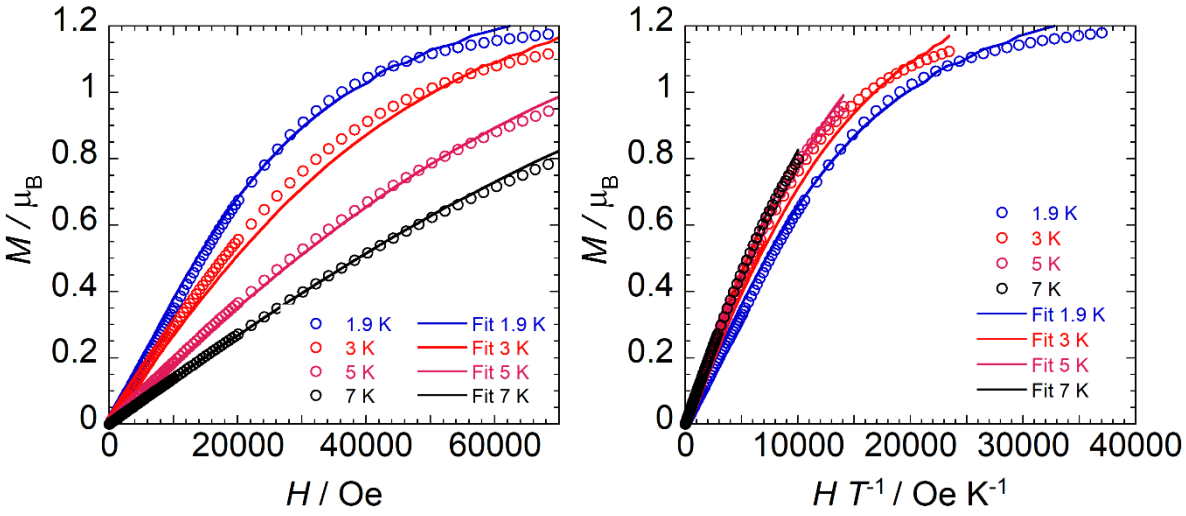

Figure D.6. Solid state field dependence of the magnetization (left) and the reduced magnetization (right) for **[Fe^{III}(Py$_2$ImAm)$_3$]** at the indicated temperatures. . Solid lines represent best-fits to the experimental data; parameters are provided in the main text (Table 1).

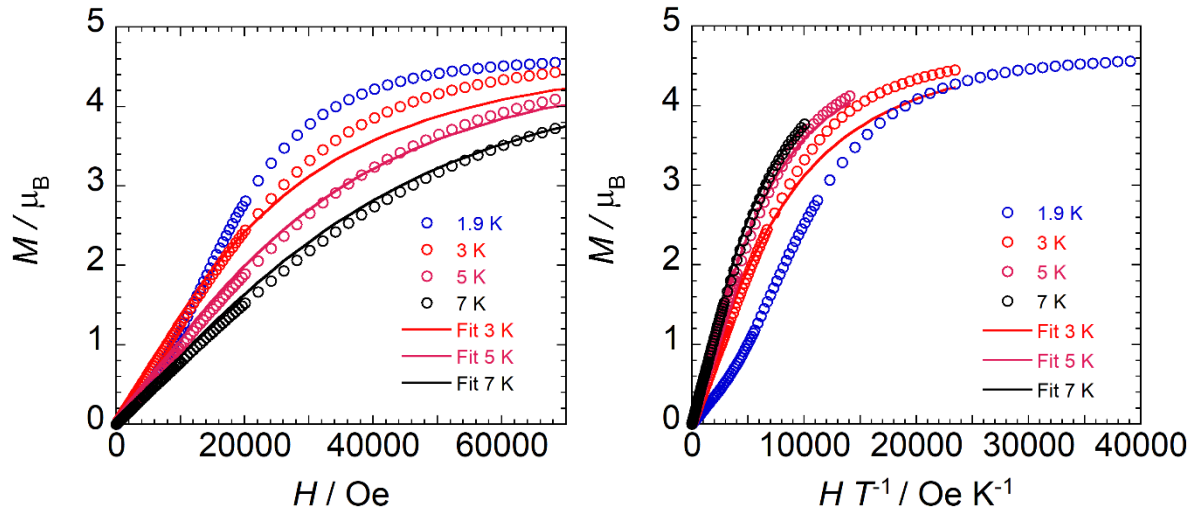

Figure D.7. Solid state field dependence of the magnetization (left) and the reduced magnetization (right) for **[Fe^{III}(Pm2ImAm)Cl3]** at the indicated temperatures. Solid lines represent best-fits to the experimental data; parameters are provided in Chapter 3 (Table 3.4).

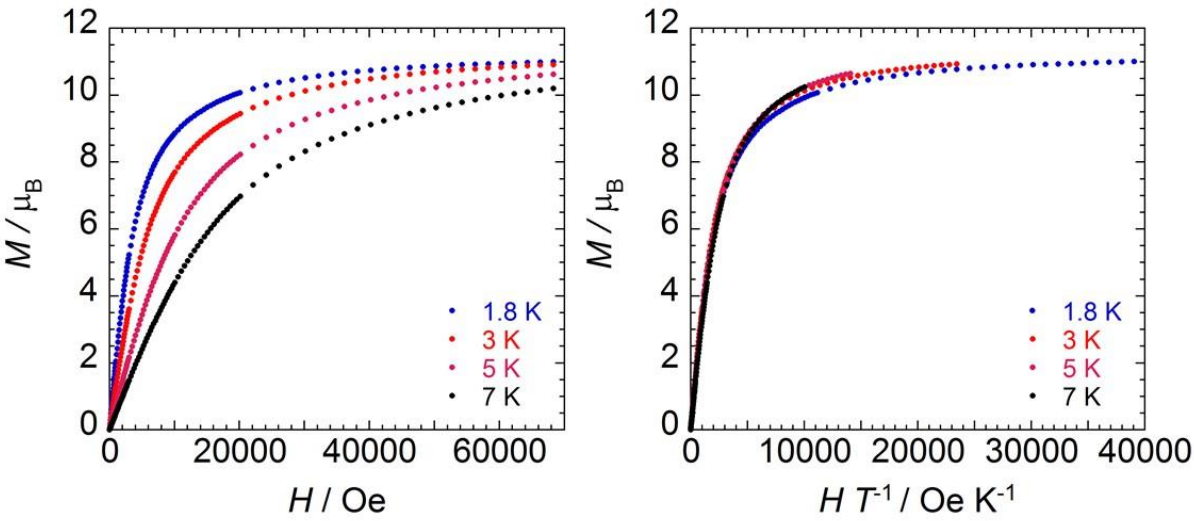

Figure D.8. Solid state field dependence of the magnetization (left) and the reduced magnetization (right) for **[$Mn^{III}Mn^{II}_3$(Pm2ImAm)3Cl6]** at the indicated temperatures.

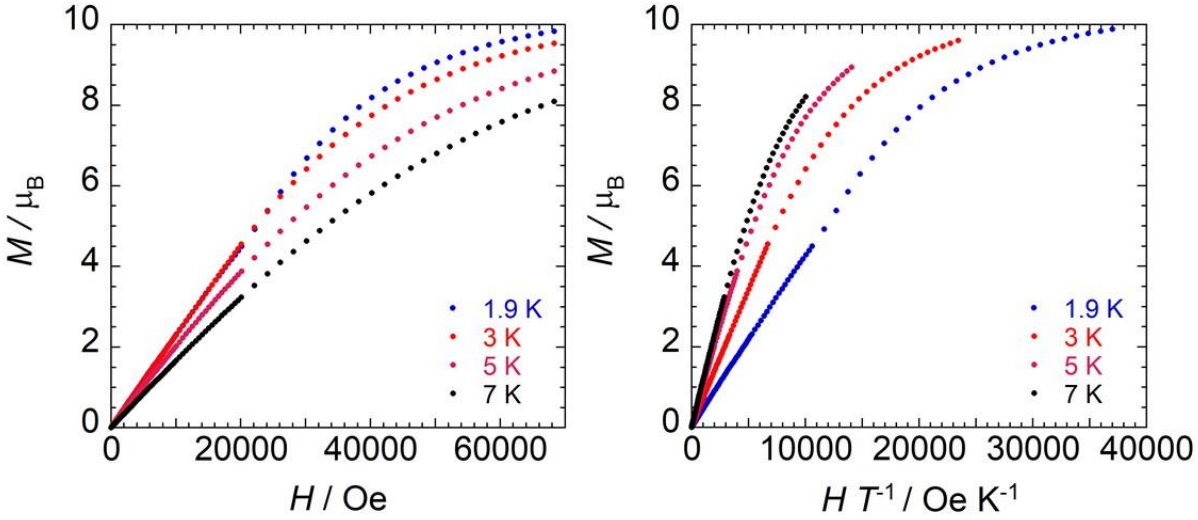

Figure D.9. Solid state field dependence of the magnetization (left) and the reduced magnetization (right) for **[$Fe^{III}_4(Pm_2ImAm)_3Cl_9$]** at the indicated temperatures.

Appendix E: Figures from Chapter 4

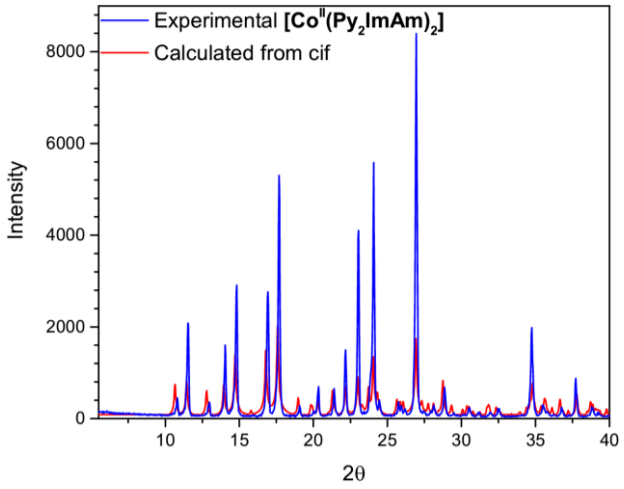

Figure E.1. PXRD pattern overlay of experimental microcrystalline **[Co^{II}(Py$_2$ImAm)$_2$]** complex at room temperature with its calculated pattern from single crystal at 200 K using Mercury.[4]

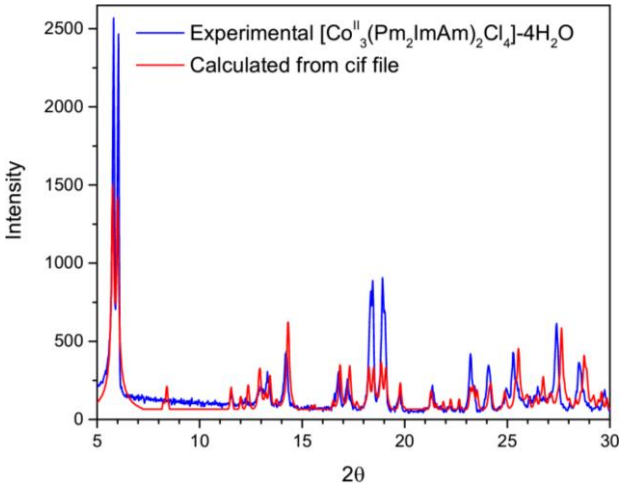

Figure E.2. PXRD pattern overlay of experimental microcrystalline **[Co$^{II}_3$(Pm$_2$ImAm)$_2$Cl$_4$]·5H$_2$O** trinuclear complex at room temperature with its calculated pattern from single crystal at 200 K using Mercury.[4]

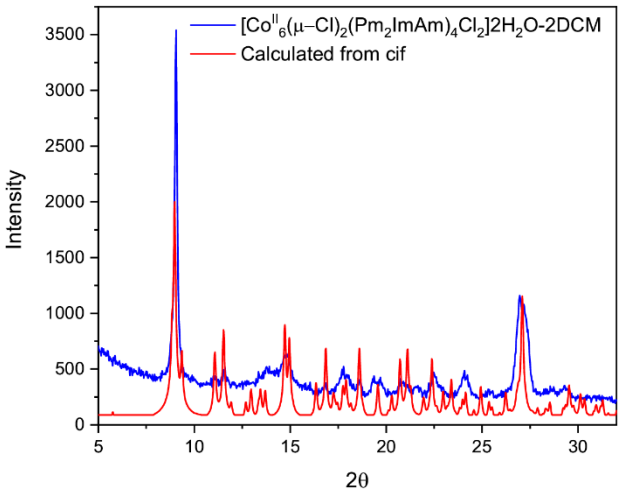

Figure E.3. PXRD pattern overlay of the experimental microcrystalline **[Co$^{II}_6$(μ-Cl)$_2$(Pm$_2$ImAm)$_4$Cl$_6$]·2MeOH·2DCM** hexanuclear complex at room temperature with its calculated pattern from single crystal at 200 K using Mercury.[4]

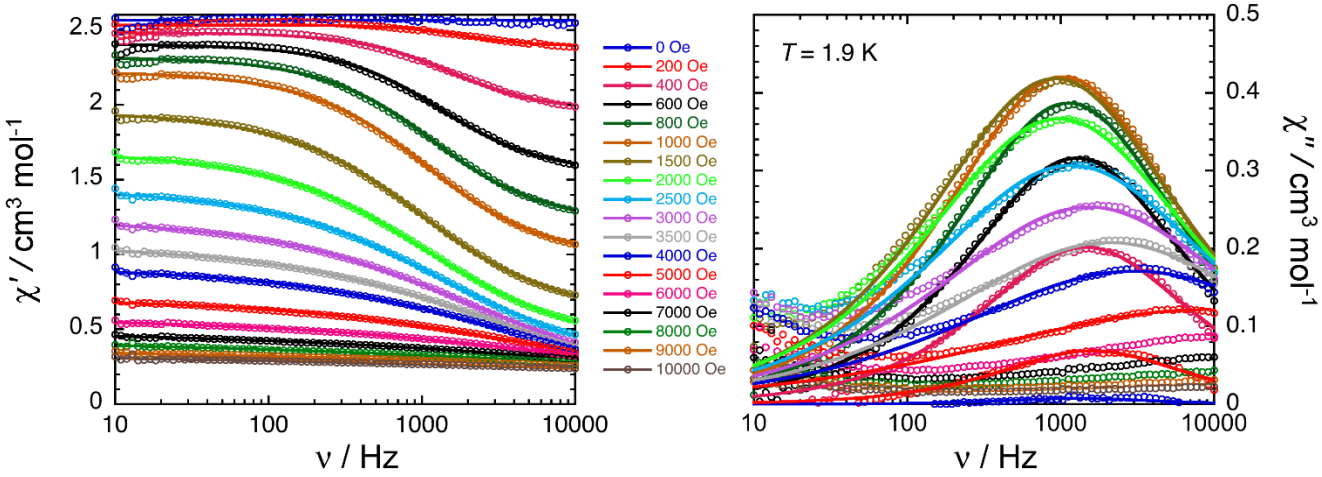

Figure E.4. Frequency dependence of the real (χ', left) and imaginary (χ'', right) parts of the ac susceptibility (normalized per [Co$^{II}_6$(μ-Cl)$_2$(Pm$_2$ImAm)$_4$Cl$_6$] unit) for **[Co$^{II}_6$(μ-Cl)$_2$(Pm$_2$ImAm)$_4$Cl$_8$]·2MeOH·2DCM** collected at 1.9 K and varying dc fields. Solid lines are the best fits obtained with the Debye generalized model.

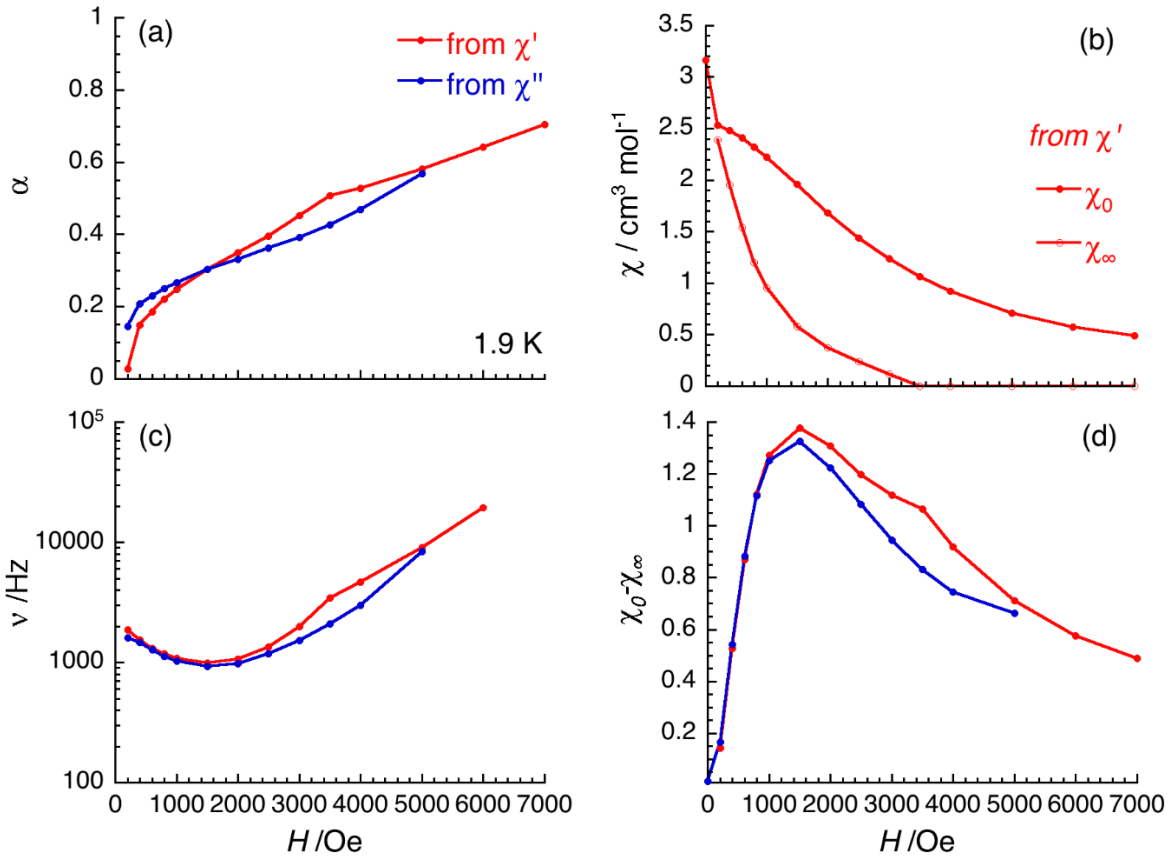

Figure E.5. Field dependence of the parameters, α, ν, χ_0, χ_∞ and χ_0-χ_∞, between 0 and 0.7 T deduced from the generalized Debye fit of the frequency dependence of the real (χ') and imaginary (χ'') components of the ac susceptibility at 1.9 K, shown in Figure A18, for **$[Co^{II}_6(\mu\text{-}Cl)_2(Pm_2ImAm)_4Cl_8]\cdot 2MeOH\cdot 2DCM$**.

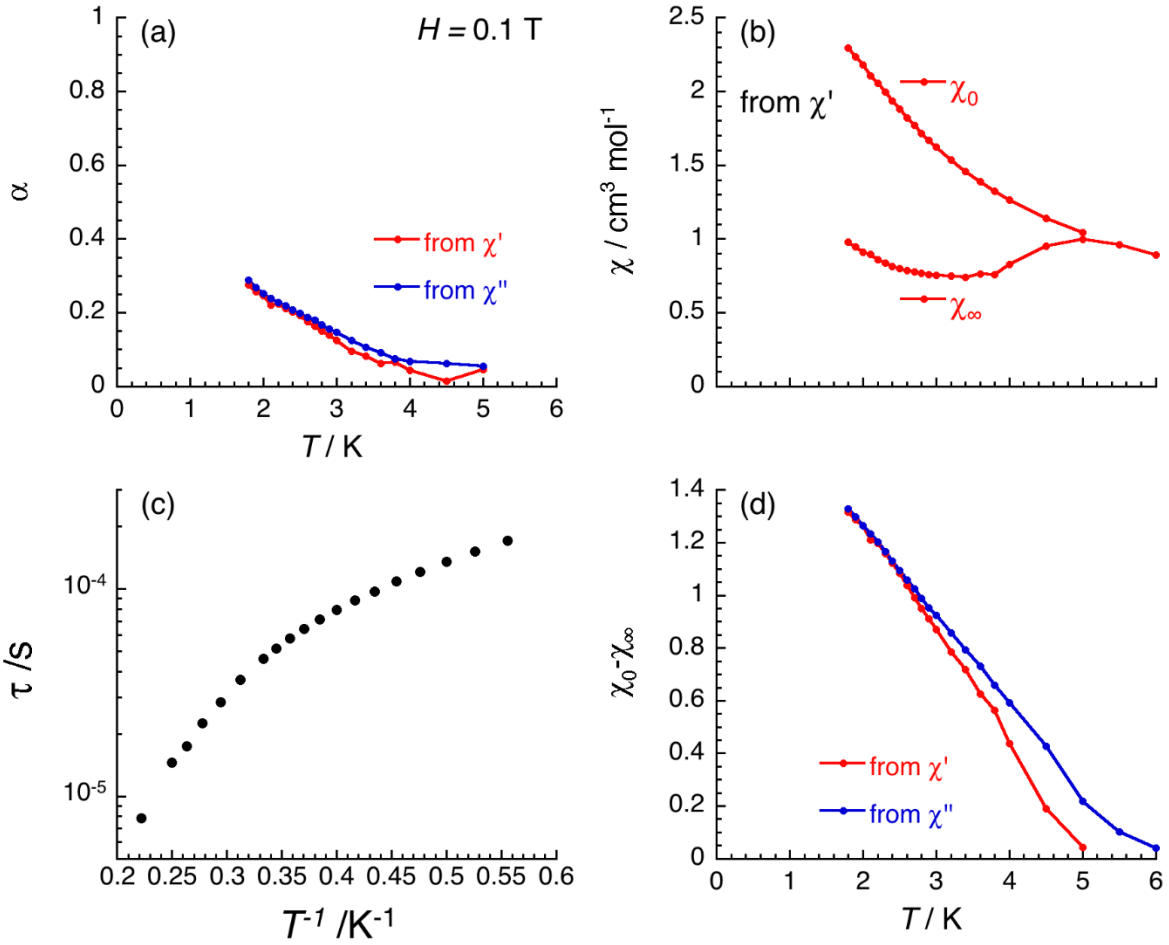

Figure E.6. Temperature dependence of the parameters, α (a), χ_0 & χ_∞ (b), τ(c) and χ_0-χ_∞ (d) between 1.8 and 6 K deduced from the generalized Debye fit of the frequency dependence of the real (χ') and imaginary (χ'') components of the ac susceptibility at 0.1 T, shown in Figure 4.12 of the main text for **$[Co^{II}_6(\mu\text{-}Cl)_2(Pm_2ImAm)_4Cl_8]\cdot 2MeOH\cdot 2DCM$**. On the bottom left figure, the temperature dependence of the relaxation time of **$[Co^{II}_6(\mu\text{-}Cl)_2(Pm_2ImAm)_4Cl_8]\cdot 2MeOH\cdot 2DCM$** is shown at 0.1 T between 1.8 and 4.5 K (treatment of χ' *versus* ν and χ'' *versus* ν curves gives undistinguishable results; both sets of data were averaged and plotted

Appendix F: Figures from Chapter 5

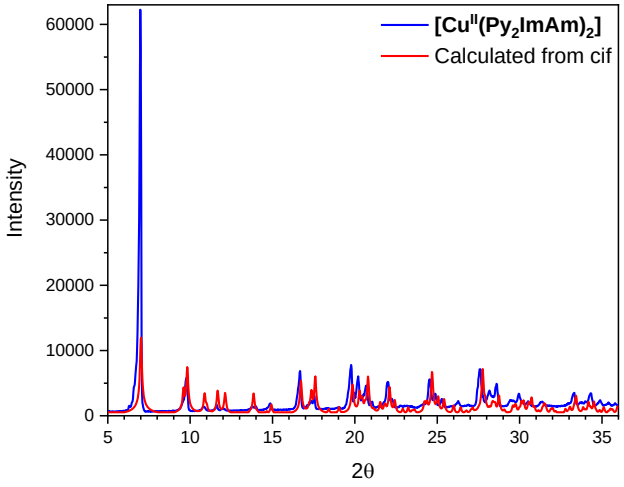

Figure F.1. PXRD pattern overlay of experimental microcrystalline **[Cu^{II}(Py$_2$ImAm)$_2$]** complex at room temperature with its calculated pattern from single crystal at 200 K using Mercury.[4]

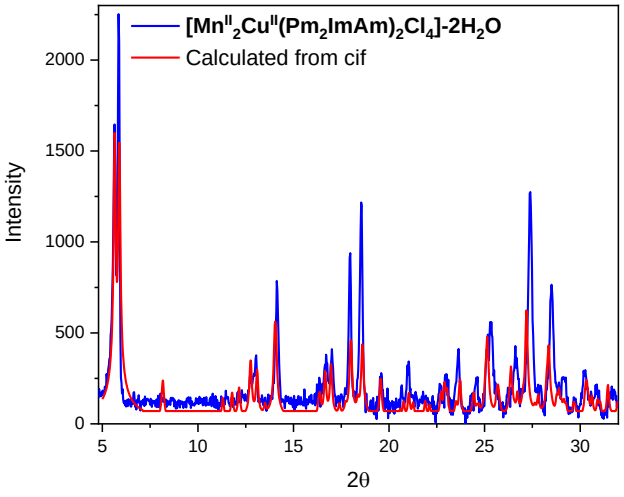

Figure F.2. PXRD pattern overlay of experimental microcrystalline **[Mn$^{II}_2$Cu^{II}(Pm$_2$ImAm)$_2$Cl$_4$]·2H$_2$O** complex at room temperature with its calculated pattern from single crystal at 200 K using Mercury.[4]

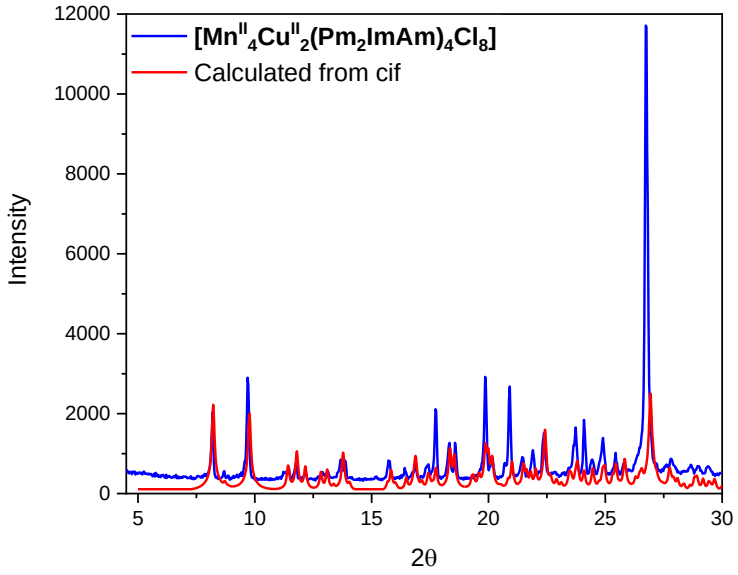

Figure F.3. PXRD pattern overlay of experimental microcrystalline **[Mn$^{II}_4$Cu$^{II}_2$(μ-Cl)$_2$(Pm$_2$ImAm)$_4$Cl$_6$]·2MeOH·2DCM** complex at room temperature with its calculated pattern from single crystal at 200 K using Mercury.[4]

Appendix G: Equations

Spin Hamiltonians

Compounds **$[Mn^{II}_2(\mu\text{-}Cl)_2(Pm_2ImAm)_2]$**, **$[Mn^{III}(Py_2ImAm)_3]$**, **$[Fe^{III}(Py_2ImAm)_3]$**, **$[Fe^{III}(PmImAm)Cl_3]$**, **$[Mn^{III}Mn^{II}_3(Pm_2ImAm)_3Cl_6]$** and **$[Fe^{III}_4(Pm_2ImAm)_3Cl_9]$** were all fit with PHI software to the below spin Hamiltonians. Due to the summative nature of the Hamiltonians (Equation F.1), all compounds were fit considering the general Zeeman interaction (Equation F.2) as well as the axial zero field splitting (ZFS) (Equation F.3). The magnetic behavior of some of the complexes is best described by the inclusion of a spin-orbit coupling term (Equation F.4), and in the case of the dinuclear compound and the tetranuclear systems, an exchange Hamiltonian, Equation F.5 and Equation F.6 respectively. Hamiltonians for each complex are described below:

$[Mn^{II}_2(\mu\text{-}Cl)_2(Pm_2ImAm)_2]$ was fit including the Zeeman (Equation F.2), exchange (Equation F.5), and inter-complex interactions (Equation F.7, *vide infra*).

$[Mn^{III}(Py_2ImAm)_3]$ was fit considering only the Zemman interaction (Equation F.2), the axial component of the ZFS (Equation F.3), and an inter-complex interactions (Equation F.7, *vide infra*).

$[Fe^{III}(Py_2ImAm)_3]$ was fit with a spin-orbit term (Equation F.4) in addition to the Zeeman (Equation F.2) and axial ZFS (Equation F.3) components.

For **$[Fe^{III}(PmImAm)Cl_3]$**, an inter-complex interaction (Equation F.7, *vide infra*) was used to fit the data in addition to the Zeeman (Equation F.2) and axial ZFS (Equation F.3) components.

For **$[Mn^{III}Mn^{II}_3(Pm_2ImAm)_3Cl_6]$**, the spin Hamiltonian included the Zeeman (Equation F.2) and axial ZFS (Equation F.3) components as well as the exchange Hamiltonian (Equation F.6).

$[Fe^{III}_4(Pm_2ImAm)_3Cl_9]$ was fit considering the Zeeman interaction (Equation F.2), the axial ZFS (Equation F.3), as well as the exchange Hamiltonian (Equation F.6). An inter-complex interaction was also utilized (Equation F.7, *vide infra*).

$$\mathbb{H} = \mathbb{H}_{Zeeman} + \mathbb{H}_{axial} + \mathbb{H}_{spin\text{-}orbit} + \mathbb{H}_{exchange} \quad \text{(Equation G.1)}$$

$$\mathbb{H}_{Zeeman} = g\mu_B SH \quad \text{(Equation G.2)}$$

$$\mathbb{H}_{axial} = D[\hat{S}_z^2 - 1/3S(S+1)] \quad \text{(Equation G.3)}$$

$$\mathbb{H}_{spin\text{-}orbit} = \xi(r)\hat{L}\cdot\hat{S},\ \xi = \pm\lambda\cdot 2S \quad \text{(Equation G.4)}$$

$$\mathbb{H}_{exchange} = -2J_1(\hat{S}_1\hat{S}_2), \text{ where } S_1 = S_2 \quad \text{(Equation G.5)}$$

$$\mathbb{H}_{exchange} = -2J_2(\hat{S}_1\hat{S}_2 + \hat{S}_1\hat{S}_3 + \hat{S}_1\hat{S}_4), \text{ where } S_1 \neq S_2 = S_3 = S_4 \quad \text{(Equation G.6)}$$

Inter-complex interactions were used to describe the low temperature susceptibilities for **[Mn^{II}_2(μ-Cl)$_2$(Pm$_2$ImAm)$_2$]**, **[Mn^{III}(Py$_2$ImAm)$_3$]**, **[Fe^{III}(Pm$_2$ImAm)Cl$_3$]** and **[Fe^{III}_4(Pm$_2$ImAm)$_3$Cl$_9$]**, which were described in the frame of the mean field approximation as per the below definition of susceptibility:

$$\chi = \frac{\chi_0}{\frac{2zJ'}{Ng^2\mu_B^2}\chi_0} \quad \text{(Equation G.7)}$$

Appendix H: Copyright Permissions

All the images used for Chapter 1 are original images and have not being copying from any source. The copyright permission for the reproduction of material from the articles “Probing the coordination chemistry of *N*-2-pyridylimidoyl-2-pyridylamidine: a versatile ligand with multiple coordination sites” and “Rational design of tetranuclear complexes employing N-imidoylamidine based ligands” can be seeing bellow.

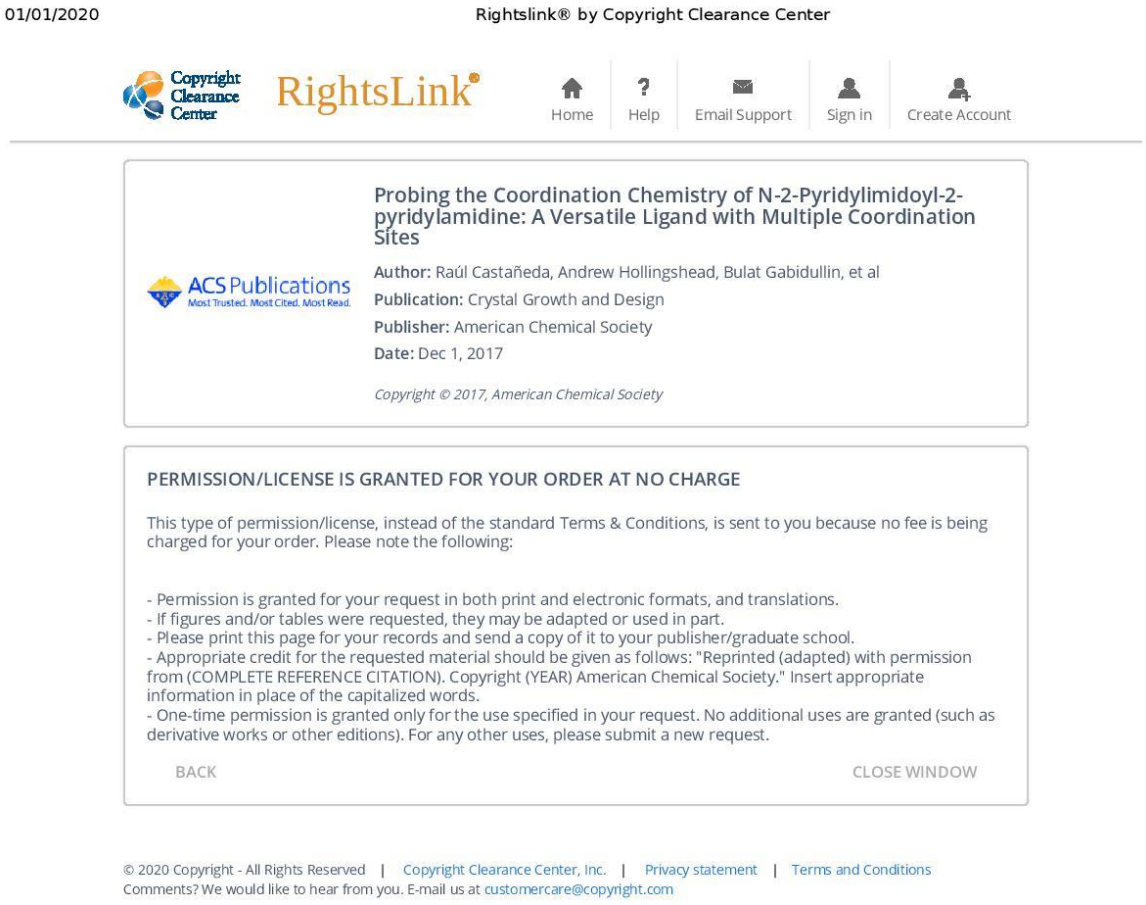

JOHN WILEY AND SONS LICENSE
TERMS AND CONDITIONS

Jan 01, 2020

This Agreement between Luis Raul Castaneda Perea ("You") and John Wiley and Sons ("John Wiley and Sons") consists of your license details and the terms and conditions provided by John Wiley and Sons and Copyright Clearance Center.

License Number	4740510746655
License date	Jan 01, 2020
Licensed Content Publisher	John Wiley and Sons
Licensed Content Publication	European Journal of Inorganic Chemistry
Licensed Content Title	Rational Design of Tetranuclear Complexes Employing N-Imidoylamidine Based Ligands
Licensed Content Author	Jaclyn L. Brusso, Muralee Murugesu, Bulat Gabidullin, et al
Licensed Content Date	Jan 30, 2019
Licensed Content	2019

Volume	
Licensed Content Issue	7
Licensed Content Pages	10
Type of use	Dissertation/Thesis
Requestor type	University/Academic
Format	Electronic
Portion	Figure/table
Number of figures/tables	4
Original Wiley figure/table number(s)	Figure 1, Figure 2, Figure 3, Figure 4
Will you be translating?	No
Title of your thesis / dissertation	Imidoyl amidine ligands: A versatile framework to build homo and heterometallic complexes
Expected completion date	Jan 2020

Expected size (number of pages)	200
	Luis Raul Castaneda Perea [redacted]
Requestor Location	[redacted] Canada Attn: Luis Raul Castaneda Perea
Publisher Tax ID	EU826007151
Total	0.00 USD

Terms and Conditions

TERMS AND CONDITIONS

This copyrighted material is owned by or exclusively licensed to John Wiley & Sons, Inc. or one of its group companies (each a"Wiley Company") or handled on behalf of a society with which a Wiley Company has exclusive publishing rights in relation to a particular work (collectively "WILEY"). By clicking "accept" in connection with completing this licensing transaction, you agree that the following terms and conditions apply to this transaction (along with the billing and payment terms and conditions established by the Copyright Clearance Center Inc., ("CCC's Billing and Payment terms and conditions"), at the time that you opened your RightsLink account (these are available at any time at http://myaccount.copyright.com).

Terms and Conditions

- The materials you have requested permission to reproduce or reuse (the "Wiley Materials") are protected by copyright.

Appendix References

[1] Kahn, O., *Molecular Magnetism.* ed.; VCH: **1993**.

[2] Van Vleck, J. H., *The theory of electric and magnetic susceptibilities.* ed.; Clarendon Press: Oxford, **1932**.

[3] Pedersen, K. S.; Bendix, J.; Clérac, R., *ChemComm* **2014**, 50, (34), 4396-4415.

[4] Macrae, C. F.; Bruno, I. J.; Chisholm, J. A.; Edgington, P. R.; McCabe, P.; Pidcock, E.; Rodriguez-Monge, L.; Taylor, R.; van de Streek, J.; Wood, P. A., *Journal of Applied Crystallography* **2008**, 41, (2), 466-470.